Enhancing the Measurement of Spin-Orbit Torque Using the Harmonic Hall Method

Simon Valentin Lucas Lenne

School of Physics and CRANN

Trinity College Dublin, the University of Dublin

Magnetism and Spin-Electronics Group

Supervisor

Prof. Plamen Stamenov

Co-Supervisor

Dr. Karsten Rode

A thesis submitted to Trinity College Dublin, the University of Dublin

in partial fulfilment of the requirements for the degree of

Doctor of Philosophy

2025

Declaration

I declare that this thesis has not been submitted as an exercise for a degree at this or any other university and it is entirely my own work.

I agree to deposit this thesis in the University's open access institutional repository or allow the Library to do so on my behalf, subject to Irish Copyright Legislation and Trinity College Library conditions of use and acknowledgement.

I consent to the examiner retaining a copy of the thesis beyond the examining period, should they so wish (EU GDPR May 2018).

Simon Lenne

Summary

Spin-orbit torques show potential for magnetic random access memory applications due to their ability to control magnetic states with electrical current. The majority measurements of SOT have been performed on bilayer samples. However, more competitive options may exist, utilising alternative mechanisms at the origin of spin-orbit torque, such as intrinsic effects in single-layer materials. The harmonic Hall method has become one of the standards for the evaluation of spin-orbit torque. However, this method suffers from spurious contributions, including thermoelectric effects, which limit its accuracy. These issues often present within bilayer systems and may potentially be stronger in new systems. There is a need to develop new methodologies that are able to remove these spurious contributions to allow precise and accurate measurement of spin-orbit torques.

The aim of this thesis was to develop these new methodologies for accurate measurement of spin-orbit torque in novel materials, based on the harmonic Hall principle. A single-layer ferrimagnetic material, Mn_2Ru_xGa, was investigated, as it has shown promise in spintronics applications. This research used a combination of the symmetry and microscopic approaches. Symmetry arguments were used to determine a magnetogalvanic tensor which was able to model any material and that respects the symmetry of a sample. A derivation of the harmonic Hall method was performed using a microscopic approach by solving the balance of torques, including the SOT field.

The first research chapter investigated the reliability and validity of published harmonic

Hall analytical techniques to determine spin-orbit torque. An evaluation of these analytical methods was performed to determine the effectiveness of analysing harmonic Hall signals that do not meet the initial derivation assumptions of these published methods. A numerical simulation of the harmonic Hall signals was developed based on a single macrospin approximation. This model considers a wide range of factors, including both sample and experimental setup conditions. A dataset of one million simulated harmonic Hall signals under varying conditions was generated. These simulated signals were analysed using the different published analytical methods and the error of the estimation was determined. Using methods of machine learning, a linear model based on an extended set of parameters was used to calculate the estimation error. A genetic algorithm was used to select influential parameters and their interactions, which were applied to a training dataset and verified using a test dataset, to ensure that no over fitting occurred. All analytical methods investigated showed high inaccuracies in the determination of spin-orbit torques. High-field analytical methods were significantly affected by the sample positioning, with a greater than 80% error for a 5° offset in the field direction. Offsets of this magnitude are necessary to ensure a single magnetic domain is present in the sample. They are standard within the method, rendering the high-field analytical method highly inaccurate. Low-field analytical methods showed thermoelectric and planar hall effect corrections are mandatory. Even with these corrections, there were large errors; they were primarily caused by the rotation of the sample along the z-direction, second-order anisotropy and magnetoresistance effects. A complete numerical model was required to obtain high accuracy in the estimation of spin-orbit torques.

The second research chapter investigated the potential crystallographic origin of the SOT in a single-layer MRG thin film, originating from the lack of inversion symmetry in the crystallographic structure. This involved distinguishing between the SOT arising from the crystal structure and from that caused by the interfaces, as well spurious contributions to the harmonic Hall signal. Symmetry analysis was used to derive the tensor expression

for both of the SOT effective fields. The numerical model was then used to analyse the harmonic Hall signal, taking into account both effective fields and including spurious contributions. Multiple measurements were conducted with a rotating field up to 1.9 T at room temperature, recording both transverse and longitudinal harmonic signals. A second set of measurements was performed in a Quantum Design PPMS system up to 14 T, recording the transverse signal. The transport coefficients and SOTs were extracted. The numerical model developed within this thesis accurately measured the spin-orbit torque of Mn_2Ru_xGa. There was no spin-orbit torque with a crystallographic origin while the interfacial contribution was found to be small. When estimating SOT for Mn_2Ru_xGa, if thermal effects were inadvertently ignored, as per the standard methodology, the absolute error on the damping-like spin efficiency would be of 0.15.

The third research chapter focused on improving the pattern device design to eliminate thermal effects in Harmonic Hall measurements. The aim was to use a rotating current instead of the traditionally employed oscillating current. This was achieved by inducing a rotating current by using two sources for the x- and y-directions, respectively, with a phase offset of 90°. Based on the analytical and numerical solutions, modelling demonstrated that SOT was present in the harmonic hall signal, while thermoelectric contributions were ideally absent. The new pattern was then tested experimentally. First, a finite element analysis was performed to determine the current distribution and validate the new geometry's conformity with a rotating current. Second, a cobalt-platinum multilayer was measured with the standard and new geometries. Finally, a noise analysis and budgeting were conducted to quantify the added noise in the new configuration caused by the presence of two current sources. Experimentally, the SOT signal was present in both geometries, while there was no substantial thermoelectric contribution measured in the new geometry, eliminating the need for corrections. There was a small increase in electronic noise due to the use of a rotating current, but this did not affect the accuracy of the spin-orbit torque determination. This new geometry presents a further advantage in the

ability to record both the field-like and damping-like torques in a single scan. It allows measurement of any anisotropic transport effect, as the current rotates in the xy-plane. This method can be widely used and is essentially independent of any specificity of the sample.

Acknowledgements

First of all, I would like to thank both of my supervisors, Prof. Plamen Stamenov and Dr. Karsten Rode, for all their support during this PhD. We met for the first time, when I was a summer student, and my main motivation was to come to Ireland to learn English while still doing some physics. Thanks to your warm welcome, I decided to return for my PhD. Plamen, I thoroughly enjoyed working with you; I appreciate all the knowledge and support you gave me. Your knowledge of physics, coupled with your expertise with the lab equipment, allowed me to carry out this PhD. Karsten, even before my PhD, despite your perfect French, you kept speaking to me in English during my time as a summer student, just for me to be able to learn it. I know how difficult this must have been! I enjoyed that we could speak French during the PhD, while you continued to teach me English. You provided great support during my PhD. Thank you for your constant motivation, your passion for the details, the time you spent with me in the lab and your genuine curiosity about my thoughts on various physics topics. This helped me to reach a deeper understanding of the field. Thank you for tolerating my stubbornness, even if this meant, on some occasions, that I had to do extensive reading before I agreed with you. You're an excellent supervisor, both in your human and scientific aspects.

Next in line is Dr. Gwenaël Atcheson, who has been a great support for all the deposition process. You are one of the most patient people I know. You understood MRG perfectly, answering all my questions and providing any samples needed for my PhD. You quickly became a very good friend, even offering me a place to stay at your home during my

summer internship. Then, you invited me to dinner parties regularly during my PhD. It has been truly nice to have you as a friend, housemate, and colleague. Thank you very much, Dr. Jean Besbas for all the time we spent together chatting around and for your friendship. I had an excellent and insightful time working with you in the optics lab and talking during the numerous breaks. I learnt so much from you about fast optics and magnetism. Then, I would like to thank Lucy and Brian, who completed their PhDs alongside mine. You became my closest friends in Ireland. Thank you for putting up with the time I spent chatting in the office, whether the topic was physics or something else. You both have always been supportive, and I hope I was able to help you as much as you gave to me. I would also like to acknowledge all the other past and present postdocs of the group, in particular, to Dr. Chandrima Banerjee, Dr. Yangkun He, Dr. Pilar Jiménez and Dr. Zsolt Gercsi for all the interesting discussions. I would also like to thank all the other students I spent time with in the office, particularly Tim, Ross, Jack, and Orrie. Sharing our office was a great time. I wish you all the best.

A great thanks to my family, who have always supported me throughout my life, from when I was small to when I was far away. I would not have gone so far without your constant support. A huge thanks to Rochelle for your support since we met. I apologise that you had to endure a second, by proxy this time, PhD writing process. I look forward to the future. Finally, thanks to all my long-lasting friends, whom I have stayed in contact with during all those years, even if we rarely get to see each other. Keeping in touch via calls and the occasional time that we could meet up was really great.

List of Publications and Presentations

- **Publication:** S. Lenne, Y.-C. Lau, A. Jha, G. Y. P. Atcheson, R. E. Troncoso, A. Brataas, J. M. D. Coey, P. Stamenov, and K. Rode, "Giant spin-orbit torque in a single ferrimagnetic metal layer", arXiv Preprint (2019)

- **Publication:** C. Banerjee, K. Rode, G. Atcheson, S. Lenne, P. Stamenov, J. M. D. Coey, and J. Besbas, "Ultrafast double pulse all-optical reswitching of a ferrimagnet", Phys. Rev. Lett. **126**, 177202 (2021)

- **Publication:** K. E. Siewierska, G. Atcheson, A. Jha, K. Esien, R. Smith, S. Lenne, N. Teichert, J. O'Brien, J. M. D. Coey, P. Stamenov, and K. Rode, "Magnetic order and magnetotransport in half-metallic ferrimagnetic Mn_yRu_xGa thin films", Phys. Rev. B **104**, 064414 (2021)

- **Publication:** Y. He, S. Lenne, Z. Gercsi, G. Atcheson, J. O'Brien, D. Fruchart, K. Rode, and J. M. D. Coey, "Noncollinear ferrimagnetism and anomalous hall effects in Mn_4N thin films", Phys. Rev. B **106**, L060409 (2022)

- **Publication:** A. Jha, S. Lenne, G. Atcheson, K. Rode, J. M. D. Coey, and P. Stamenov, "Quasistatic magnetization evolution in the compensated ferrimagnetic half-metal Mn_2Ru_xGa", Phys. Rev. B **108**, 224413 (2023)

- **Talk:** S. Lenne, Y. C. Lau, J. M. D. Coey, P. Stamenov, and K. Rode, "Single-layer spin-orbit-torque: filling the terahertz gap", SPIE Optics + Photonics, 2019

- **Poster:** S. Lenne, G. Atcheson, and P. Stamenov, "Transport properties and spin orbit torque in single layers of $Mn_2Ru_{0.9}Ga$", MagnEFi Conference, 2022
- **Talk/Publication:** S. Lenne, G. Atcheson, R. Smith, P. Stamenov, and K. Rode, "Single layer spin-orbit torque in $Mn_2Ru_{0.9}Ga$", in 2023 ieee international magnetic conference - short papers (2023), pp. 1–2
- **Seminar:** S. Lenne, "Separation of spin-orbit torque and thermal effects in $Mn_2Ru_{0.9}Ga$", IPCMS Seminar, Strasbourg, 12/01/2024, 2024
- **Seminar:** S. Lenne, "Separation of spin-orbit torque and thermal effects in $Mn_2Ru_{0.9}Ga$", l'Institut Jean Lamour Seminar, Nancy, 11/01/2024, 2024
- **Poster:** S. Lenne and P. Stamenov, "Elimination of thermal effects in harmonic hall measurements", 22nd International Conference on Magnetism, 2024

Table of contents

List of acronyms

AC alternating current

AFM anti-ferromagnetic

AHE anomalous Hall effect

AMR anisotropic magnetoresistance*

**Defined as the additional, longitudinal only, contribution which appears when reducing the symmetry from isotropic to ∞m (Section 1.3.3.3)*

ANE anomalous Nernst effect

DL damping-like

DMI Dzyaloshinskii-Moriya interaction

DOS density of state

EXAFS X-ray absorption fine structure spectroscopy

FEM finite element method

FL field-like

FMR ferromagnetic resonance

GLM generalised linear model

GMR giant magnetoresistance

GST generalised Sucksmith-Thompson

HE Hall effect

ISGE inverse spin galvanic effect

ISHE inverse spin Hall effect

LIA lock-in amplifier

LLG Landau-Lifshitz-Gilbert

LMR linear magnetoresistance

MBE molecular-beam epitaxy

NE Nernst effect

PHE planar Hall effect

PMA perpendicular magnetic anisotropy

PPMS® Quantum Design physical property measurement system

RKKY Ruderman-Kittel-Kasuya-Yosida

SHE spin Hall effect

SMR spin Hall magnetoresistance

SOC spin orbit coupling

SOT spin orbit torque

SQUID superconducting quantum interference device

SSE spin Seebeck effect

ST-FMR spin torque ferromagnetic resonance

STT spin transfer torque

SVD single variable dependence

TEM transmission electron microscopy

TMR tunnel magnetoresistance

UHV ultra high vacuum

List of Figures

List of Tables

CHAPTER 1

Introduction

There is growing interest in discovering new materials with strong spin orbit torque (SOT), leading to the study of a wider range of magnetic materials [2–4]. The harmonic Hall method is a widely used technique for measuring SOT [5]. However, SOT values reported in the literature do not always agree with each other. This is most likely due to two factors. First the approximations assumed when deriving analytical expressions to extract the SOT are often not valid. Second, the contributions from the thermogalvanic effects are set to zero without justification. The thesis aims to assess the current models and techniques for determining SOT using the harmonic Hall method and to explore methods for enhancing the measurement of this in novel materials, with a particular focus on single-layer films.

In this chapter, we outline the approach used to construct analytical models of SOT. This combines the microscopic origin of magneto- and thermogalvanic effects under the constraint that the spatial and temporal symmetry of the resulting signals must reflect the symmetry of the sample under investigation. This includes both symmetry on the level of the crystallographic point- and spacegroup, as well as the geometrical symmetry of the sample itself, i.e. it consists of a thin film on a substrate with symmetry ∞m. First, we compare the top-down method of symmetry analysis to the bottom-up, microscopic

approach. Then, we provide a brief overview of fundamental concepts in magnetism and magnetic materials. We then describe the pertinent magneto- and thermogalvanic effects, their microscopic origin, when known, and their symmetry. This is followed by a description of the material studied in this thesis, Mn_2RuGa. The second part of the introduction focuses briefly on the origins and different methods used to measure the SOT.

The Harmonic Hall method is then described in detail, starting with the magnetisation oscillation around its equilibrium position due to an oscillating SOT effective field, which is induced by the sine current flowing through the sample. We then discuss how this results in a second harmonic signal. The different magneto transport effects combine the sine source current with the oscillating magnetisation. This results in a second-order non-linear signal that contains the SOT, which is recorded using a lock-in amplifier. Different versions of the harmonic Hall method are presented, including variations in the direction and intensity of the applied field. Additionally, typical artefacts, such as the signal arising from thermoelectric effects, are discussed. This is followed by an outline of the thesis and a summary of the research chapters.

1.1 There's more than one way to skin a cat: microscopic origin versus symmetry arguments

While the microscopic approach examines the mechanisms of an observed effect, symmetry analysis provides the minimal number of parameters necessary to model the system without including details regarding their origins. Symmetry approach is valid in all fields of science, but is most beneficial when the system under study exhibits known, high symmetries that allow one to reduce the number of free (or unknown/phenomenological) parameters. It is important to note here that the two are not mutually exclusive. A large portion of modern science (e.g. atomic and high-energy physics) relies on both to build

robust models.

The microscopic approach relies on detailed knowledge of the mechanisms behind the different effects. For example, how scattering affects the transport properties, or how the crystal field affects the atomic spins' orbitals and thus the anisotropy. The microscopic approach can produce quantitative values if the band structure of the material is known. By designing models of these effects, using an understanding of the mechanism of each effect, one can determine the overall contribution to the signals recorded. However, this method has its limitations. Some microscopic theories are not fully understood (i.e. the side jump in the anomalous Hall effect (AHE) or spin Hall effect (SHE), see Section 1.3.2.1, Section 1.3.2.2). Additionally, the microscopic approach relies on a full (or at least sufficient) description of the system, including its defects, many of which are not easily determined (i.e. the detailed interface between two layers in a bilayer structure).

In contrast, the symmetry approach relies on the Neumann principle, which states that effects should have the same symmetry as their causes. First, the system's relevant symmetries are identified. This includes the point group and space group for crystallographic effects or by considering a fully isotropic material to determine which effects are present in any given material. However, this comes at a cost. If several microscopic origins obey the same symmetry, they will be mapped to a single phenomenological parameter. We note that this is experimentally valid, as it is impossible to distinguish between effects that share the same symmetry. To distinguish between contributions with the same symmetry, it is necessary to have an understanding of their underlying microscopic mechanisms. By manipulating a specific parameter, such as the material's composition, thickness, probing technique, or the measurement's temporal resolution, one can influence an effect over another.

In this thesis, the symmetry approach was used extensively to describe and define relevant tensors that were not directly related to the SOT measurement, including all transport

properties and the SOT effective field. Thereafter, using a microscopic approach, determination of the SOT field was achieved using the harmonic Hall method. This was based on the magnetisation response to the effective SOT field. Then the harmonic Hall signal was determined from this response via the transport properties.

We now give further detail on the mathematical and physical foundations of symmetry analysis, followed by brief descriptions of the microscopic magneto- and thermogalvanic effects considered. In the latter we highlight the simplifications made possible by symmetry analysis.

1.1.1 Symmetry analysis

The understanding of the micro-mechanism at the origin of the SOT effect (or any other physical effect) is not trivial and relies on a correct description of all the different mechanisms occurring in condensed matter. This implies that a predominant part of these effects is difficult to describe *ab initio*, due to a lack of information on the mechanism or system.

Instead of using this bottom-up strategy, where the understanding of the mechanism leads to the expression of the effect, a more general approach can be used, which is based on symmetry analysis. Symmetry is a powerful tool and can be summarised by the Neumann principle, paraphrased above, which states that:

> *Any type of symmetry which is exhibited by the point group of the crystal is possessed by every physical property of the crystal [6].*

Through symmetry, we understand any operation that transforms the system under investigation to itself. These operations can be (n-fold) rotations around a given axis, spatial inversion, or time reversal. A concrete example is encountered in crystallography. Any symmetry operation that leaves the crystal invariant, which is the ensemble of those cor-

responding to its point group symmetry, also has to be expressed in any of the properties exhibited by this material. We note here that we focus on the point group rather than the space group, as the galvanic effects we will discuss later do not depend on the translational symmetries that differentiate the space- from the point group.

A simple example can be made with the Hall effect in two dimensions, assuming a sample that is otherwise isotropic. Here, the magnetic field at the origin of the Hall effect is contained in the ρ_{xy} coefficient. From Ohm's law:

$$\begin{pmatrix} E_x \\ E_y \end{pmatrix} = \begin{pmatrix} \rho_{xx} & \rho_{xy} \\ \rho_{yx} & \rho_{yy} \end{pmatrix} \begin{pmatrix} J_x \\ J_y \end{pmatrix}, \tag{1.1}$$

and the simple symmetry of rotation by 90°, which can be represented by the matrix:

$$R = \begin{pmatrix} 0 & -1 \\ 1 & 0 \end{pmatrix}. \tag{1.2}$$

If we physically rotate the sample by 90° then $R^{-1}\mathbf{E} = \rho R^{-1}\mathbf{J}$ and so $\mathbf{E} = R\rho R^{-1}\mathbf{J}$. According to the Neumann principle, we found that $\rho_{xx} = \rho_{yy}$ and $\rho_{xy} = -\rho_{yx}$. This includes here that for a cubic system, where the rotation by 90° is a symmetry operation (or for any higher symmetry), there should not be a difference between the conductivity along x and y, and that the Hall effect is antisymmetric when exchanging the position of current and voltage contacts.

The symetry approach can simplify any tensor quantity [6]. Only its order and nature, such as axial or polar, needs to be considered. The axial vector, sometimes called the pseudo-vector, does not transform naturally under a symmetry operation. For example, a sign flip is required when applying a mirror operation to the axial vector. The presence of the sign flip operation is written mathematically as the determinant of the symmetry operation $|\sigma|$. These axial vectors are usually defined as the cross product of two polar vectors. Thus, angular momentum, $\mathbf{L} = \mathbf{r} \times \mathbf{p}$, is an axial vector. As such, any vector

representing the magnetic field or magnetisation is also axial. To identify whether a given tensor is axial or polar, one can establish a connection with other well-known quantities. The nature of a tensor can then be determined using the multiplication rule (Table 1.1).

Table 1.1: Multiplication rules for polar and axial tensors.

	axial	polar
axial	polar	axial
polar	axial	polar

For example, we know that for Ohm's law the electric field **E** and the current density **J** are polar and so the resistivity tensor $\hat{\rho}$ is also polar. The Neumann principle is then written for a polar tensor $\hat{d}$:

$$\hat{d}_{ijk...n} = \sigma_{ip}\sigma_{jq}\sigma_{kr}...\sigma_{nu}\hat{d}_{pqr...u}\,, \tag{1.3}$$

and for an axial tensor $\hat{d}$:

$$\hat{d}_{ijk...n} = |\sigma|\sigma_{ip}\sigma_{jq}\sigma_{kr}...\sigma_{nu}\hat{d}_{pqr...u}\,, \tag{1.4}$$

where σ is the matrix representing the symmetry. Einstein notation for the implicit summation over repeated indices is used. Continuing on the example of Ohm's law above, and developing the expression in orders of **b**, the reduced applied magnetic field, we find that even a system where inversion is an allowed symmetry operation can exhibit finite ρ_{xy} as now the tensor in the first-order of **b** is axial.

The equation system from Equation 1.3 and 1.4 can be solved for each new system or we can directly use the table of the tensor [6] using the generality of this approach, depending only on the tensor rank and type and symmetry operation.

Here, we consider an example for the SOT. From an experimental point of view, the SOT is expressed as an effective field $\mathbf{H}_{\mathrm{SOT}}^{\mathrm{FL(DL)}}$:

$$\mathbf{H}_{\mathrm{SOT}}^{\mathrm{FL}} = \xi^{\mathrm{FL}}\mathbf{J} \quad \text{and} \quad \mathbf{H}_{\mathrm{SOT}}^{\mathrm{DL}} = \xi^{\mathrm{DL}} : \mathbf{mJ}\,, \tag{1.5}$$

where $\mathbf{m}$ is the reduced magnetisation of the sample, $\mathbf{J}$ the current density and $\xi^{\mathrm{FL(DL)}}$ are the tensors linking the field-like (FL) and damping-like (DL) effective fields to the current density. As previously stated, magnetisation and magnetic fields consist of axial vectors. The current density naturally transforms under symmetry operations and is therefore a polar vector. Using the multiplication rules (Table 1.1), we determine that ξ^{FL} is axial and ξ^{DL} is polar. We can now consider a simple amorphous bilayer system, where the only symmetry is ∞m, and any rotation around the z-axis is a symmetry operation. The symmetry tensor can then be expressed as:

$$\sigma^{\theta} = \begin{pmatrix} \cos(\theta) & -\sin(\theta) & 0 \\ \sin(\theta) & \cos(\theta) & 0 \\ 0 & 0 & 1 \end{pmatrix} . \tag{1.6}$$

Therefore, we can write the system of equations for ξ^{FL} using Equation 1.4:

$$\hat{\xi}^{\mathrm{FL}}_{ij} = |\sigma^{\theta}| \sigma^{\theta}_{ip} \sigma^{\theta}_{jq} \hat{\xi}^{\mathrm{FL}}_{pq} , \tag{1.7}$$

and for ξ^{DL} following Equation 1.3:

$$\hat{\xi}^{\mathrm{DL}}_{ijk} = \sigma^{\theta}_{ip} \sigma^{\theta}_{jq} \sigma^{\theta}_{kr} \hat{\xi}^{\mathrm{DL}}_{pqr} . \tag{1.8}$$

This yields a linear system of 9 and 27 equations, respectively. By solving these using symbolic computational tools, we find that:

$$\xi_{\mathrm{FL}} = \begin{pmatrix} 0 & x_1 & 0 \\ -x_1 & 0 & 0 \\ 0 & 0 & 0 \end{pmatrix} , \quad \xi_{\mathrm{DL}} = \begin{pmatrix} x_3 m_z & 0 & x_2 m_x \\ 0 & x_3 m_z & x_2 m_y \\ x_1 m_x & x_1 m_y & x_4 m_z \end{pmatrix} , \tag{1.9}$$

where the different x_i are independent variables. m_α represents the components of the magnetisation vector, which have been contracted into the DL tensor, resulting in a matrix notation for the effective SOT field $\mathbf{H}^{\mathrm{FL(DL)}}_{\mathrm{SOT}} = \xi^{\mathrm{FL(DL)}} \mathbf{J}$. Symmetry analysis allows us to

reduce the ξ^{FL} tensor from nine to a single variable, and the ξ^{DL} tensor from 27 to four variables. Further simplification is possible, as discussed in Section 1.5.2.

1.2 Magnetic materials

In non-magnetic materials, a magnetic field is generated by the time variation of an electric field or a charge current, as described by the Maxwell equations:

$$\nabla \cdot \mathbf{E} = -\frac{\rho}{\varepsilon_0}, \quad \nabla \cdot \mathbf{B} = 0, \quad \nabla \wedge \mathbf{E} = -\frac{\partial \mathbf{B}}{\partial t}, \quad \nabla \wedge \mathbf{B} = \mu_0 \left(\mathbf{J} + \varepsilon_0 \frac{\partial \mathbf{E}}{\partial t} \right), \tag{1.10}$$

where $\mathbf{E}$ is the electric field, $\mathbf{B}$ the magnetic flux density, ρ the charge density and $\mathbf{J}$ the current density. μ_0 and ε_0 are vacuum permeability and vacuum permittivity, respectively.

The charge current produces the magnetic field of the electromagnet in both resistive coils and superconducting magnets. On the other hand, in matter the magnetic moment has two different origins [7]: i) the orbital moment originating from the orbital motion of the electron around the nucleus, corresponding to a current loop, and ii) the electron spin, an intrinsic property of particles. In solids, electrons, neutrons and protons have a spin. However, the contribution of neutrons and protons to a magnetic material is usually neglected, as their mass is $\sim$ 1000 times greater than that of the electron. A notable exception is nuclear magnetic resonance, where the configuration of molecules leads to different absorption spectra allowing the identification of chemical species. A well-known application is magnetic resonance imaging, which uses hydrogen resonance to image organic materials.

The second Maxwell Equation 1.10 states that there is no magnetic charge at the source of the magnetic field. Ampère's approach was to consider that magnetisation originates from a small permanent current loop in the material. This description is unphysical, as such currents will dissipate. The source of magnetisation is the magnetic dipoles created by spin and orbital angular momentum [7]. However, Ampère's description highlights

that a magnetic moment is always associated with angular momentum. This link was confirmed experimentally by the Einstein de Haas experiment [8].

The orbital magnetic momentum can be computed from a classical Bohr atomic model approach using Ampère's law:

$$\mathbf{m} = I\mathbf{A} = -\frac{\pi r_e^2 \mathbf{n} e v_e m_e}{2\pi r_e m_e} = -\frac{e}{2m_e}\boldsymbol{\ell}\,, \tag{1.11}$$

with $\mathbf{A} = \pi r^2 \mathbf{n}$ the oriented surface from the orbital, m_e the electron mass and $\boldsymbol{\ell} = \mathbf{n} r m_e v_e$ the orbital angular momentum. As the orbital angular momentum of the electron is quantised in units of $\hbar$ (the reduced Plank constant), we can define an quantisation unit for the magnetic moment, the Bohr magneton:

$$\mu_B = \frac{\hbar|e|}{2m_e} \approx 9.274 \times 10^{-24}\,\mathrm{A\,m^2}. \tag{1.12}$$

More generally,

$$\mathbf{m} = g\mu_B \mathbf{l}\,, \tag{1.13}$$

where g is the g-factor, the unit less ratio of magnetic moment to angular momentum. In the case where the nucleus is fixed, i.e. $m_{\text{nucleus}} \gg m_e$, $g = 1$, for the orbital moment. The expectation value of $\mathbf{l}$ is $\sqrt{l(l+1)}$ and that of its z-projection $-l \leq m_l \leq l$, in steps of one and without units as $\hbar$ is now included in μ_B.

The spin angular momentum is an intrinsic property of the electron, which appears when solving the Dirac's equations and which does not have a classical equivalent. The spin angular momentum is quantised in units of $\frac{\hbar}{2}$ (half of the value of the orbital momentum). The g-factor of the spin is $g_e \approx 2$ and so the spin magnetic moment of the electron also varies in steps of μ_B.

The description above addresses the one-electron contributions to the magnetic moment of the atom. In magnetism we are generally interested in the ground state of the multi-electron atom (in a solid), and most often in cases where there is only one partially filled

electronic shell, or when two shells are partly filled but one of them is an s-orbital ($l = 0$). In these cases, one can show [9] that electrostatic interaction between equivalent electrons (fermions) leads to partial positional correlation between them and thus a lowering of the potential energy if their spins are parallel. Likewise, among the states of maximum $S = \sum_i s_i$, the lowest term is that of maximum $L = \sum_i l_i$. These are the first and second Hund's rules.

From here, the total angular momentum can be computed by vector coupling of S with L ($\mathbf{L} + \mathbf{S} \geq \mathbf{J} \geq |\mathbf{L} - \mathbf{S}|$) along with the associated g-factor (the Landé g-factor):

$$g_L = \frac{3}{2} + \frac{S(S+1) - L(L+1)}{2J(J+1)}\,, \tag{1.14}$$

where S, L and J correspond to the quantum number for, respectively, the spin, orbital and total momentum operator. The ground state is that of the lowest J for more than half-filled shells, and the highest J for less than half filled. This is Hund's third rule. Note that we have treated the description of atomic magnetism in the Russell-Saunders (LS) coupling scheme. This is the easiest approach and justified in most cases for both $3d$ transition elements and $4f$ rare earths in their ground state.

In an external magnetic field $\mathbf{B}$ along the z-direction, the interaction energy is:

$$E_Z = -\mathbf{M} \cdot \mathbf{B} = g_L \mu_B m_j B\,, \tag{1.15}$$

where $\mathbf{M}$ is the magnetisation, $\mathbf{B}$ the external field, g_L the Landé g-factor, μ_B the Bohr magnetron and m_j the total angular momentum number. This is the Zeeman energy.

The different Landé g-factors for different atoms are particularly important in multi-magnetic-lattice systems, where the net angular momentum and the net magnetic moment are no longer proportional.

1.2.1 Exchange interaction

In the previous section, we focused on the magnetism of atoms isolated in space, for which the wave functions can be described as a linear combination of anti-symmetrised products of the spherical harmonics and the radial functions of the electrons in an electrical field ('central field' of spherical symmetry) created by the nucleus. Here, we address the origin of collective effects, such as ferromagnetism and antiferromagnetism. In matter, the electrical potential seen by the electrons is no longer a central field, and furthermore, when atoms are sufficiently close, their orbitals can overlap. The exchange interaction then appears, as for the partial correlation responsible for parallel spins in the ground state described above, due to electron-electron Coulomb interaction. This exchange interaction associates an energy to the relative orientation of two electron spins and is the strongest interaction in most magnetic materials [7]. Considering spin localised on a lattice and the exchange interaction, we can define the Heisenberg Hamiltonian as:

$$E_{\text{ex}} = \sum_{i,j} J_{ij} \mathbf{S_i} \cdot \mathbf{S_j} \,, \tag{1.16}$$

where J_{ij} is the exchange constant between the spin i and j. As the individual atoms are no longer strictly described by a central field problem, and because the electrons from two different ions are not necessarily completely indistinguishable, J_{ij} can be of either sign. For metallic systems, the sum in Equation 1.16 can be limited to the nearest neighbours. Rare earths interact via the Ruderman-Kittel-Kasuya-Yosida (RKKY) interaction of a longer range. Other exchange interactions can exist, for example in oxides, such as super-exchange [10] and double-exchange.

Research in magnetism focuses on these materials and their diverse magnetic properties. The presence of ferromagnetic order is particularly interesting for the creation of permanent magnets or recording devices [7]. Anti-ferromagnetic (AFM) order was discovered later, with the first explanation given by L. Néel in 1936 [7]. In AFMs, two or more

magnetic sublattices in the crystal compensate each other perfectly, resulting in zero net magnetisation. As a consequence, they are insensitive to external magnetic fields. The strong exchange between the sublattices gives rise to high-frequency magnetisation dynamics, which could be exploited in electronic devices [11]. However, AFM order is more difficult to modify and measure due to the absence of a net magnetic moment and the perfect symmetry of the band structure cancels the first-order effect of magnetisation in transport.

Ferrimagnetism combines properties of both ferromagnetism and antiferromagnetism. A ferrimagnet has two **inequivalent** magnetic sublattices. Each of these is a ferromagnetically coupled intra-sublattice, while intersublattice coupling is antiferromagnetic. As the sublattices are inequivalent, they partially compensate each other, so the total net moment is usually small and can be zero: the case for perfect compensation. Due to their crystallographic in-equivalence, the thermal evolution of both sublattices is usually different and compensation occurs only for one particular temperature, T_{comp}. For a ferrimagnet, the spin-resolved band structure does not need to be symmetric. This allows for a significant magnetic contribution in transport measurements, which raises the prospects of combining the advantages of the ferromagnets (i.e. strong signal in transport properties) with those of the antiferromagnets (i.e. high frequency dynamics and robustness to external field perturbation)[12].

1.2.2 Stoner model

In the Heisenberg exchange model, we considered the local atomic moment to be sufficiently close to that of an isolated atom. This approximation holds true for $4f$-electrons, as their bands are considerably lower than the Fermi level. However, this is not the case for $3d$ transition metals, for which the $3d$-electrons are to a certain degree delocalised. A band approach to magnetism is more appropriate and a Stoner theory provides a suitable

model [13].

The Stoner model introduces an interaction (I) that favours a magnetic state by adding a molecular field (H_m) term to the Hamiltonian:

$$H_m = I(n_\uparrow - n_\downarrow)\,, \tag{1.17}$$

where n_i corresponds to the number of electrons with a spin orientation i and so $n_\uparrow - n_\downarrow$, proportional to the magnetisation.

The Pauli exclusion principle forbids having more than one electron per quantum state. Next, by looking at the distribution of states in the absence of a molecular field, the net magnetisation will be zero. Here, it will be advantageous to have two electrons (one for each spin) per state. The introduction of the molecular field lifts the degeneracy between the two different spin orientations. To have the appearance of a magnetic order, the gain of energy by having a finite magnetisation needs to be larger than the increase due to the population of a higher kinetic energy state. The instability of the zero magnetisation state is given by the Stoner criterion [13]:

$$IN_0 > 1\,, \tag{1.18}$$

where N_0 is the density of state (DOS) at the Fermi level. Contrary to the spin localised on a lattice model, which predicts any exchange interaction will result in a magnetic order at 0 K, the Stoner criteria indicate that, in the case of band magnetism, both the strength of the interaction and the DOSs at the Fermi level matter for the emergence of magnetism. An understanding of this criterion is that the larger the density of the state is at the Fermi level, the less increase in energy will be needed to be paid per electron, changing its spin orientation and so the more effective the molecular field will be to bias the system into reaching a net magnetisation. Computation done by Janak in 1977 [14] shows (Figure 1.1) that this criterion for elements of the $3d$-group. It first

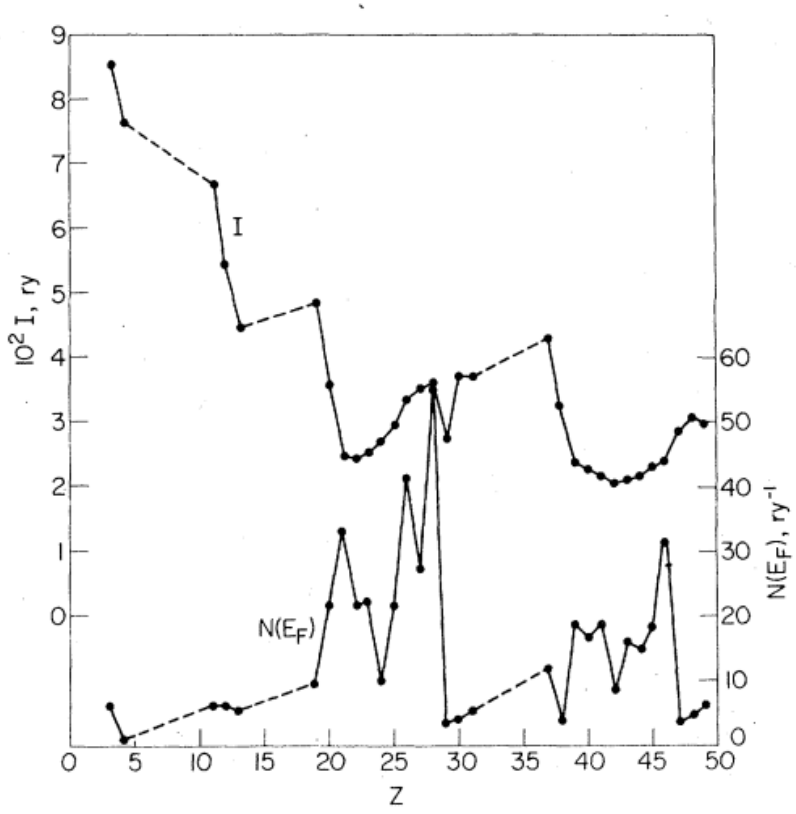

Figure 1.1: DOS and interaction strength as a function of the atomic number. The dashed line represents the range for which no calculations were performed. Focusing on the transition metals between 21 and 30, we see that the main driver for the Stoner criterion holding for Ni, Fe and Co comes from the increase in the DOSs at the Fermi level, while the interaction strength remains largely unchanged. Reuse of figure with permission from [14], ©1977 by the American Physical Society.

appears that the interaction molecular field (I) is relatively constant over the range of elements. However, the DOS is much larger for cobalt, nickel and iron, which explains why those three materials in particular are ferromagnetic.

1.2.3 The *s-d* model

The *s-d* model allows us to understand how localised electrons, such as *d*-electrons, which only slightly participate in transport, can interact with the conduction electrons. This is fundamental for *f*-electrons, which are fully localised and are deep below the Fermi level. The *s-d* model states that there is a local exchange interaction between the localised *d*-electrons and the conductive *s-p*-electrons. The Fermi level is then polarised either

parallel or antiparallel to the local moment, depending on the sign of the interaction with the localised electrons. This interaction is simplified and can be used to understand the mechanism behind multiple transport effects, such as anisotropic magnetoresistance (AMR) (further details in Section 1.3.3.1).

The *s-d* model corresponds to a Hamiltonian term following [10]:

$$H_{sd} = -2J_{sd} \sum_i \delta(\mathbf{r_i})(\mathbf{s_i} \cdot \mathbf{S}) \,, \tag{1.19}$$

where $\mathbf{s_i}$ and $\mathbf{r_i}$ are respectively the spin and position vector of the conduction electrons. $\mathbf{S}$ is the local spin (at the origin of the coordinate system). J_{sd} is the exchange associates with the local spin. δ is the Dirac δ function, which forces the exchange to be local.

As the interaction is local, the exchange is strong with $J_{sd} \approx 1\,\text{eV}$ [7]. This interaction strongly coupled the localised spin and the conduction electrons spin, allowing the local magnetisation to affect any properties at the Fermi level. One of the consequences is to induce a spin polarisation of the Fermi level affecting the scattering rate of the conduction electrons and leading to the two current model, which will be discussed more in Section 1.3.1. The *s-d* model also helps to explain how spin polarisation, which is injected or induced at the Fermi level in spin transfer torque (STT) and SOT systems, can generate torque on the local magnetisation. A change in the spin direction of the conduction electron $\mathbf{s_i}$ will exert a torque on the local spin $\mathbf{S}$, allowing a reversal of the local magnetisation.

1.2.4 Spin-orbit coupling

The spin-spin interaction described above originates from electrostatic interactions that are sufficiently strong to allow collective order at and above room temperature. Furthermore, as the spin is an intrinsic property of the electron, it does not interact directly with real space, making the spin magnetic moment very robust to perturbations from the

lattice. So far, the only interaction we have explicitly addressed is the Zeeman energy, the energy of a magnetic dipole in an externally applied magnetic field.

A second interaction is spin orbit coupling (SOC) which we implicitly assumed when coupling S to L to form J above. We saw that both orbital and spin generate a magnetic moment. These two moments interact, thus coupling the spin to the real space. Hence, magnetic effects visible in transport measurements always involve SOC, even when this is not explicitly specified in the models used.

The interaction energy is calculated using classical arguments [7]:

$$\epsilon_{SO} = -\frac{1}{2}\frac{\mu_0 \mu_B^2 Z^4}{4\pi a_0^3}\,, \tag{1.20}$$

where μ_0 is the magnetic permeability, μ_B the Bohr magnetron, Z the atomic number and a_0 the Bohr radius. The factor $\frac{1}{2}$ corresponds to the Thomas correction, which takes into account the correct relativistic transformation of the coordinate system. If instead of classical arguments, the Dirac equation is used to derive the SOC, the correct expression, including the factor $\frac{1}{2}$, is found [10]. Note, the scaling is in Z^4, which indicates that the SOC is larger in heavy elements.

This expression gives the SOC for a single electron in the atom. The interaction between the different electrons reduced the SOC value by screening the electric potential. Consequently, the SOC value depends on the orbital. Electrons closer to the nucleus will have a larger SOC. Furthermore, s-electrons are spherically symmetric and exhibit little or no SOC. The electrons responsible for the atomic moments are d- or f-like, which subsequently affects the magnetic anisotropy (see Section 1.2.5). The outermost electrons, corresponding to the conduction electrons in metals, are primarily responsible for transport and the single-layer intrinsic SOT effect. The strength of the SOC in the outermost electrons was computed using the Hartree Fock method [15]. These values are represented in the periodic table in Figure 1.2. Here, the SOC increases as a square for element in the

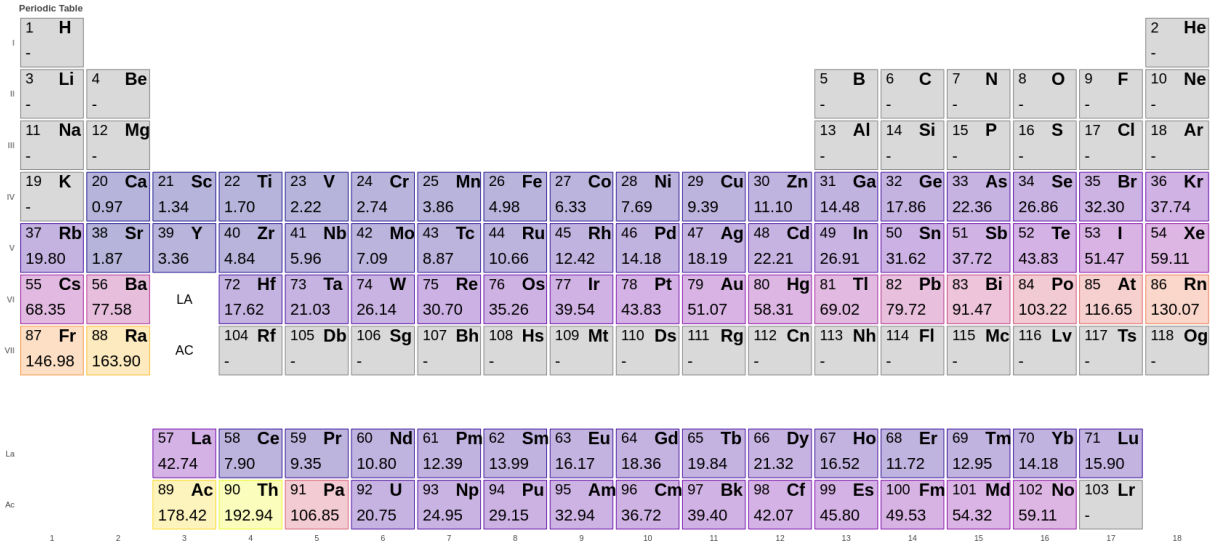

Figure 1.2: Periodic table showing the SOC strength of the different elements, grey elements denote the absence of data. Unit of the SOC is 10^{-3} R_y. *The values were extracted from [15].*

same family and to the Z^4 for the one in the same period. The difference being due to the screening of the electric potential depending on the filling of the orbital.

1.2.5 Magnetic anisotropy

When magnetic order is present, all the spins tend to align in the same direction. When only the exchange is present, all directions are equivalent and the magnetisation direction will follow the external field. However, it is well known that the magnetisation of permanent magnets cannot be modified easily. Resistance to the change in magnetisation direction is due to magnetic anisotropy.

Generally, magnetic materials are not isotropic and are easier to magnetise along certain axes, which are called the axes of easy magnetisation. The anisotropy has multiple origins [7]: shape anisotropy, magnetocrystalline anisotropy and induced anisotropy. We will first briefly discuss the shape and induced anisotropy, before giving more detail on magnetocrystalline anisotropy.

The stray field generated by the material is at the origin of the shape anisotropy. The

energy cost associated with the stray field must be minimised. The stray field depends on the shape of the magnetised object and the presence of domains. If the magnetisation of the sample is small, the demagnetisation field (proportional to M_s^2) can be neglected. This is the case for the Mn_2Ru_xGa studied in this thesis (Section 1.4).

The induced anisotropy is due to the presence of micro-texture in the material and the interaction between different interfaces. Because the exact texture of the materials is generally unknown, it is usually difficult to treat with a microscopic model. It is the parameter that allows creating permanent magnets with coercive fields approaching the anisotropy field in e.g. NdFeB. We do not discuss it further here, as it is not relevant to quasi-single crystal thin film samples.

The magnetocrystalline anisotropy stems from the interaction between the orbital and the spin moment via the SOC. This is related to the crystal structure and the angular shape of the electron orbitals. Intuitively, we see that aligning the orbitals with the positions of the crystal atoms in the cell will reduce the Coulomb energy, i.e. be more stable. The SOC forces the spin moment to align with the orbital moment. The magnetocrystalline anisotropy can be tuned by changing the crystal structure and, in the case of thin films, a distortion (e.g. tetragonal) can be induced by the substrate and can change the anisotropy constant.

The most used model for the calculation of the magnetocrystalline anisotropy is the point-charge model of the crystal field. In this model the magnetic ion is assumed to be coordinated by a number (four, six or eight) of point charges (or ligands). The magnetocrystalline energy is then calculated as the energy-density-dependence on the direction of magnetisation in real space due to SOC. This model is clearly approximate; the ligands are not point charges, and the distances involved may not be constant. However, if the symmetry of the site of the magnetic ion is known, the energy functional must, as explained above, respect this symmetry. This allows the establishment of general phe-

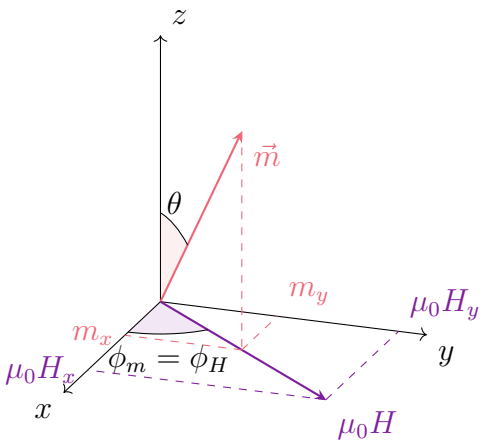

Figure 1.3: Polar coordinate used for the representation of the tetragonal anisotropy. For thin-film system, z corresponds to the out-of-plane direction.

nomenological models of anisotropy for the seven Laue classes. We note that to respect time-reversal symmetry, the anisotropy energy has to be even functions of m, i.e. functions of m^i, where $i = 2, 4, 6$ and that $i_{\max} = 2l$ (l the orbital quantum number of the electrons, 1 for p, 2 for d and 3 for f-electrons) as otherwise the resultant energy would depend on the choice of axis, which is unphysical. We treat the case of cubic anisotropy with a small tetragonal distortion next.

1.2.5.1 From cubic to tetragonal anisotropy

In a cubic system, the first-order cubic anisotropy is given by [7]:

$$E_{\text{cubic}} = k_1(\alpha^2\beta^2 + \beta^2\gamma^2 + \gamma^2\alpha^2)\,, \tag{1.21}$$

where α, β, γ are respectively the projections of the reduced magnetisation vector on the x-, y- and z-axis.

To start the transition toward a tetragonal anisotropy, we change the Cartesian coordinate system to a polar one Figure 1.3. In this coordinate system, the magnetisation is given

by:

$$\alpha = m_x = \sin(\theta)\cos(\phi)\,, \tag{1.22}$$

$$\beta = m_y = \sin(\theta)\sin(\phi)\,, \tag{1.23}$$

$$\gamma = m_z = \cos(\theta)\,. \tag{1.24}$$

Rewriting the cubic anisotropy energy given in the Equation 1.21 we obtain:

$$E_{\text{cubic}} = k_1\left(\sin^2(\theta) - \left(\frac{7}{8} + \frac{1}{8}\cos(4\phi)\right)\sin^4(\theta)\right)\,. \tag{1.25}$$

Now when reducing the symmetry of the system to tetragonal, we obtain [7]:

$$E_{\text{tetragonal}} = k_1\sin^2(\theta) + (k_2 + k_2'\cos(4\phi))\sin^4(\theta)\,, \tag{1.26}$$

where now k_1, k_2 and k_2' are independent parameters. As usual, reducing the symmetry of the system increases the number of independent parameters. If the symmetry of a sample is reduced due to strain, only the first-order will be perturbed and so k_2 and k_2' still originate from the cubic anisotropy. This can be verified by checking if experimentally $k_2 = 7k_2'$. We then expect that if the degree of tetragonal distortion is low, $8k_2 \approx -7k_1$.

1.2.5.2 Anisotropy determination using the Generalised Sucksmith-Thompson method

The anisotropy coefficients, k_1 and k_2, are experimentally determined using the generalised Sucksmith-Thompson (GST) method [16]. After saturating the sample along the easy axis (out-of-plane direction) to ensure $\theta = 0$, the magnetic field is applied along a hard axis (in the hard plane of the sample in the case of an easy, perpendicular to the film surface axis) and the angle θ is recorded.

The magnetic free energy for tetragonal anisotropy is obtained by adding the Zeeman

energy to the previous expression:

$$\begin{aligned} E =& k_1 \sin^2(\theta) + (k_2 + k_2' \cos(4\phi)) \sin^4(\theta) \\ & - \mu_0 H (\cos(\theta_H)\cos(\theta) + \sin(\theta_H)\sin(\theta)\cos(\phi_H - \phi)) \,, \end{aligned} \tag{1.27}$$

where k_1, k_2 and k_2' correspond to the anisotropy field for the uniaxial first, second-order and second-order in-plane components, respectively. μ_0 is magnetic permeability, H the external field, θ and ϕ (resp. θ_H and ϕ_H) are the magnetisation (resp. field) vector angles expressed in spherical coordinates.

Assuming the field is applied along a hard axis ($\theta_H = \frac{\pi}{2}$) and that $\phi = \phi_H$ (k_2' is small), the minimum energy should respect:

$$\frac{\partial E}{\partial \theta} \stackrel{!}{=} 0 = 2k_1 \sin(\theta)\cos(\theta) + 4(k_2 + k_2' \cos(4\phi)) \sin^3(\theta)\cos(\theta) - \mu_0 H(\cos(\theta)) \,. \tag{1.28}$$

There is no easy expression of θ versus H. By dividing by $\cos(\theta)\sin(\theta)$ we obtain:

$$\frac{\mu_0 H}{\sin(\theta)} = 2k_1 + 4(k_2 + k_2' \cos(4\phi)) \sin^2(\theta) \,. \tag{1.29}$$

This expression is inconvenient, as both the measured quantity (θ) and the controlled quantity (H) are not independent. However, we recognise the equation of a straight line in Equation 1.29, $y = ax + b$, where $x = \sin^2(\theta)$ and $y = \frac{\mu_0 H}{\sin(\theta)}$, from which k_1 and k_2 easily determined from the intercept and slope, respectively. A final refinement of the constants is achieved by fitting the data using the numerical solution of Equation 1.28 with the GST result as initial parameters.

1.3 Transport properties

Transport here refers to the movement of charge, spin and heat through the sample. Each of these currents is associated with a potential: the electric potential associated with a charge current, the temperature associated with a heat current, and the spin

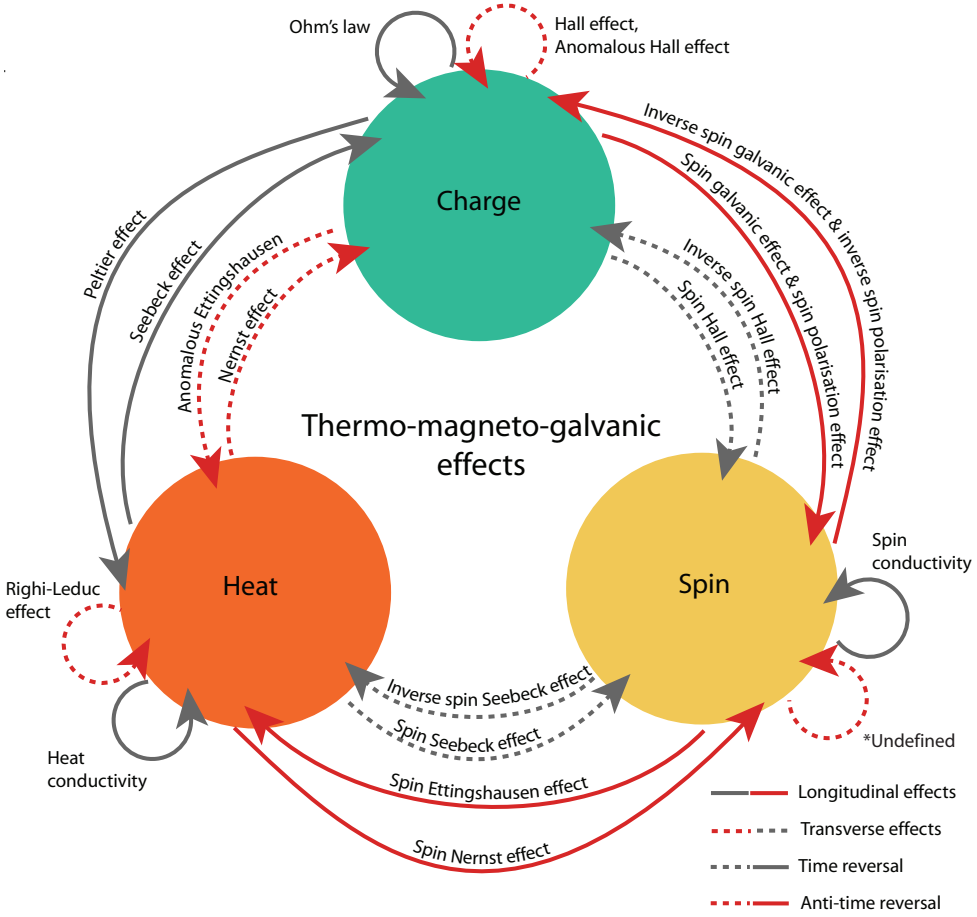

*Figure 1.4: Illustration of transport effects involving charge, spin and heat. *Undefined: theoretically a transverse effect will exist on the spin current, however this effect was not yet studied.*

potential associated with a spin current. Experimentally, only the charge current and electric potential can be controlled and measured with ease; others, such as heat current, require a more dedicated setup. The spin current must be generated and detected at the sample level. The resulting signal is the sum of those interactions. If we consider the SOT in bilayers, measured with the harmonic Hall method, we expect the creation of a spin current via the spin Hall effect. When this spin current acts on magnetisation, the change in magnetisation is recorded via the anomalous Hall effect. Hence, by focusing only on the direction of the effects, we can determine that the interface between the non-magnetic and magnetic layers need to be perpendicular to the current flow. We know that a heat current exists as the charge current results in Joule heating. As the Nernst effect

and the anomalous Hall effect possess the same symmetry, we must consider both effects. Figure 1.4 illustrates the different first-order interactions between the spin, charge and heat current. All of these interactions contribute to the final signal. Therefore, they must be taken into account when designing an experiment to distinguish between the desired signal and potential artefacts.

Possible microscopic origins of the effects relevant to this work are detailed below. The tensor finally used to represent the transport effects was determined by symmetry, which groups effects that obey the same symmetry. This is in particular true for the second-order (in magnetisation) tensor, where anisotropic magnetoresistance and spin Hall magnetoresistance are described by the same phenomenological parameter (Section 1.3.3.3).

1.3.1 Spin polarisation and spin current

The current at the Fermi level in a magnetic metal can be spin polarised [17]. This can occur both due to d character of the conduction band or through sd-exchange (Section 1.2.3). The spin of an electron is generally conserved and the spin-scattering length λ_s (average distance before a spin-flip scattering event) tends to be much larger than the electron's phase or charge scattering length because of the weak (SOC) coupling with real space and the requirement that angular momentum must be conserved. λ_s is of the order of 350 nm for aluminium and 200 nm for copper, both non-magnetic light elements. In ferromagnetic material this quantity is reduced to respectively 50 nm and 40 nm for iron and cobalt and to 10 nm for nickel [7]. This distance exceeds, however, the vertical dimensions of individual layers in a multilayer stack manufactured by thin film deposition and lithography. It is thus appropriate to consider a two-current model with a spin-up and -down channel. In agreement with our description above, these two channels can be considered independent with, if required, a spin-mixing conductance describing the interaction between the two. We now turn to the microscopical foundation for the two-current model.

The current is carried by all electrons present at the Fermi level. This includes mainly *sp* and some *d*-electrons. As the effective mass of the *d*-electron is much higher than that of *sp* electrons, most of the conduction is carried by the *sp* electrons. The conduction is then determined mainly by the average time between scattering events of the *sp*-electrons. The scattering process can involve either two *sp*-electrons or a *sp*-electron can be scattered with a *d*-electron. The last one is by far the most efficient and so determines resistance when present [18]. This scattering is also spin-dependent and can occur only between *sp*-electrons and *d*-electrons of the same spin, thus neglecting any spin-flip process. Hence, two conduction channels appear corresponding to the majority and minority spin. This is the basis of the two current spin model was introduced in those words by Fert and Campbell in 1968 [18, 19].

The resistance of each channel is described by the Matthiessen's rule [19].

$$\rho^S = \rho_0^S + \rho_{dS}^S + \rho_{d\varsigma}^S \,, \tag{1.30}$$

where ρ^S is the resistivity of the spin channel S, ρ_0^S is the part of the resistivity that includes *s*-*s*-electron scattering, defects and impurities. ρ_d^S is the scattering between the *s* and *d*-electrons of the same spin and $\rho_{d\varsigma}^S$ is the scattering between the *s*-electron of spin S with the *d*-electrons of spin $\varsigma \neq S$. The scattering probability between the *s*- and *d*-electrons follows the Fermi golden rule and so $\rho_d^S \propto \mathcal{N}_d^S$ where $\mathcal{N}_d^S$ represent the number of *d* states with spin S [18].

In the absence of SOC, only spin-conserving scattering is allowed ($\rho_{d\varsigma}^S = 0$); the density of states corresponds to the one illustrated in Figure 1.5a. The resistivity is described by the equivalent circuit in Figure 1.5c with the associated resistivity:

$$\rho_{\text{tot}} = \frac{\rho_\uparrow \rho_\downarrow}{\rho_\uparrow + \rho_\downarrow} \,, \tag{1.31}$$

where ρ_{tot} is total equivalent resistivity and ρ_S is resistivity associated with spin channel S.

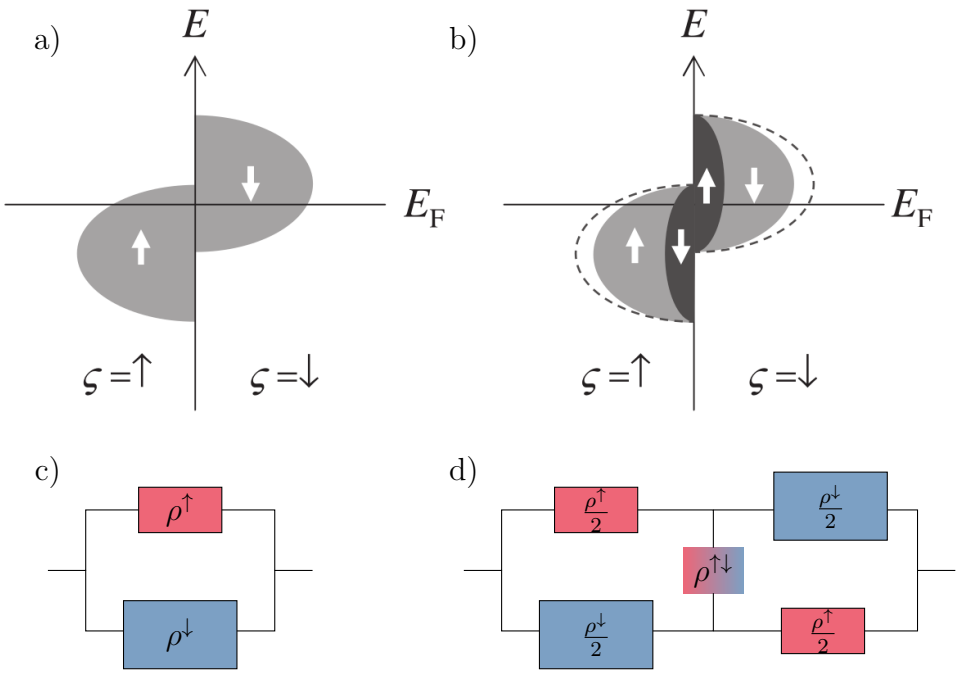

Figure 1.5: a) schematic DOS in the absence of SOC, b) schematic DOS when mixing occurs due SOC, c) equivalent circuit in the absence of SOC, the two channels are fully independent, d) equivalent circuit in the presence of SOC which introduced a term $\rho^{\uparrow\downarrow}$ allowing mixing between the spin up and down. Figures a-b reproduced from [20], CC-BY-4.0 ©2012, Kokado et al., figure d: reproduced with permission from [21] ©2023, EDP Sciences.

When SOC is included, mixing occurs between the *d*-orbital with a portion taking the characteristic of the opposite spin direction as sketched in Figure 1.5b, this opens a new scattering channel between the *s*-electron with spin ς and *d*-electron with spin S where $S \neq \varsigma$ ($\rho^{S}_{d\varsigma} \neq 0$). The equivalent circuit is then changed to Figure 1.5d with the associated resistivity:

$$\rho_{\text{tot}} = \frac{\rho_{\uparrow}\rho_{\downarrow} + \rho_{\uparrow\downarrow}(\rho_{\uparrow} + \rho_{\downarrow})}{\rho_{\uparrow} + \rho_{\downarrow} + 4\rho_{\uparrow\downarrow}}, \tag{1.32}$$

where the $\rho_{\uparrow\downarrow}$ has been added, representing the new scattering channel. The scattering channel opens due to hybridisation of the orbital and does not require a spin-flip scattering event.

As the Fermi surface is composed of electrons of both spins, it is useful to define the spin polarisation, which corresponds to the proportion of each spin at the Fermi level.

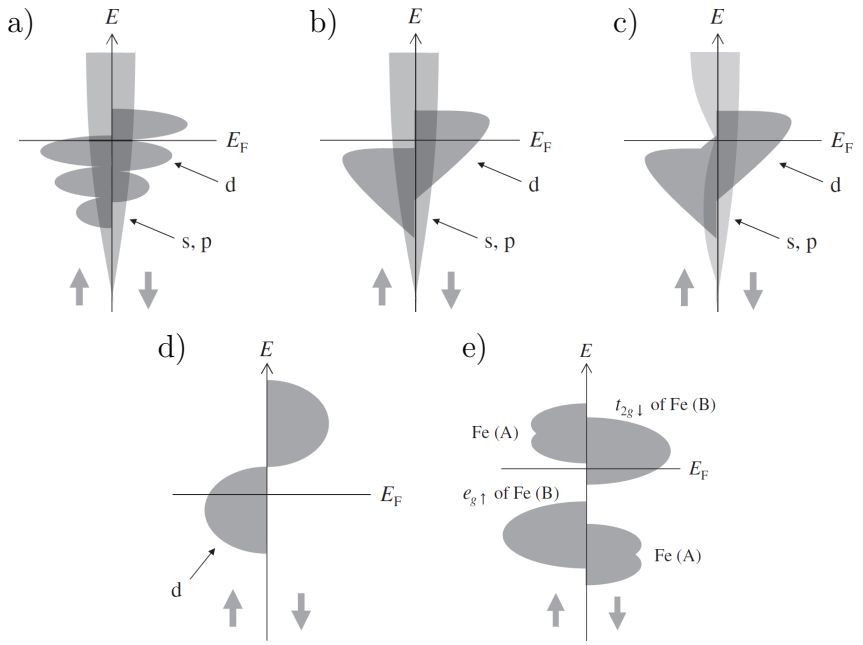

Figure 1.6: Simplified density of states for a weak ferromagnet bcc Fe (a), a strong ferromagnet fcc Co or fcc Ni (b) and Fe_4N (c), and half-metallic ferromagnet $Co_2MnAl_{1-x}Si_x$ (d) and Fe_3O_4 (e). The dominant $s-d$ scattering is: a) $s_\downarrow \rightarrow d_\uparrow$, b) $s_\uparrow \rightarrow d_\downarrow$, c) $s_\downarrow \rightarrow d_\downarrow$, d) $s_\uparrow \rightarrow d_\uparrow$, and e) $s_\downarrow \rightarrow d_\downarrow$. Reproduced from [20], CC-BY-4.0 ©2012, Kokado et al.

Unfortunately, this polarisation is not always well defined and depends on the method used to measure it, and, consequently, the detail of the band structure [22]. In practice, different definitions depending on their dependencies on the Fermi velocity associated with each band coexist and are adapted to different experimental configurations.

The schematic spin-resolved densities of states for different materials are represented in Figure 1.6. The densities associated with a non-magnetic metal would be perfectly symmetric. Each of these configurations results in distinct scattering events, leading to unique transport properties.

Depending on the spin polarisation of the lower energy band, the magnetic material could be either a ferromagnet or a ferrimagnet, but not an antiferromagnet. Antiferromagnets have two magnetic sublattices with opposite moments, but both sublattices are equivalent in terms of crystallographic environment. This equivalence explains the perfect compensation of magnetic moments for all temperatures. However, this symmetry is imposed

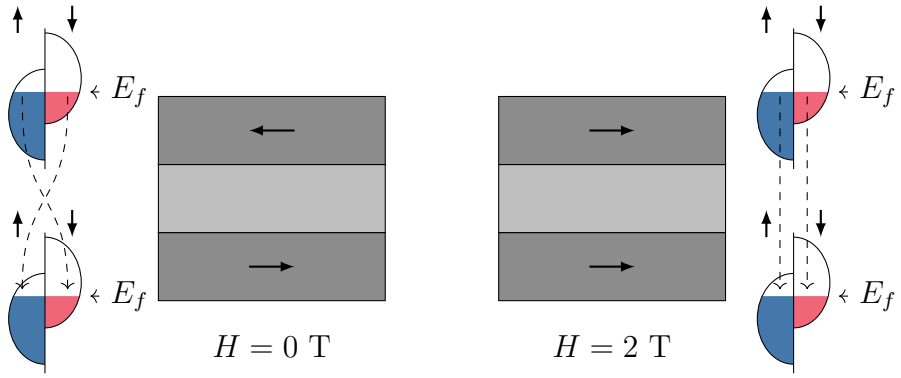

Figure 1.7: The GMR and tunnel magnetoresistance (TMR) structures. Two magnetic layers are spaced by a non-magnetic metal (GMR) or an insulator (TMR), respectively. In zero field, the configuration is antiparallel, and in a magnetic field, all the moments align. In the antiparallel state, the majority spin orientation of one layer corresponds to the minority spin orientation of the other, which leads to a large resistance. In the parallel example, both layers have the same spin orientation for the minority and majority states, which lead to low resistance.

on the band structure. In other words antiferromagnets cannot be spin polarised, unlike compensated ferrimagnets.

The spin polarisation and the two current model have a direct application when a charged current propagates through multiple ferromagnetic layers with the appearance of the giant magnetoresistance (GMR). The GMR was discovered simultaneously by Albert Fert and Peter Grünberg in 1988 in a multilayer system made of iron (magnetic) and chromium (non-magnetic)[23]. For certain thicknesses of the Cr spacer, the coupling leads to an antiparallel alignment of the different magnetic layers. The resistance of the sample at 4.2 K decreased almost by a factor two when a field of 2 T was applied, resulting in a parallel alignment of both layers. This change in resistance can be understood in terms of the two current models (Figure 1.7) as the structure is smaller than the spin scattering length. The spin is conserved during the propagation between the different layers. Thus, when the magnetisation state is antiparallel, each independent channel encounters low and high resistance in one of the layers, resulting in an overall high resistance state. When the magnetisation of both layers is aligned, one spin channel is always associated with low resistance, while the second is always associated with high resistance leading to an overall low resistance state.

1.3.2 First-order effects in magnetisation

1.3.2.1 Anomalous Hall effect and Hall effect

The Hall effect (HE), first observed by Edwin H. Hall in 1879 [24], describes the buildup of electric charge on one side of a conductor as a current flows through it under the influence of a magnetic field. Its origin can be explained by the Lorentz force on the carriers. Soon after, the HE was discovered to be much stronger in magnetic materials [25], which refuted that it was solely a contribution from the Lorentz force, due to a magnetic field induced by magnetisation but a new effect, the anomalous Hall effect (AHE), sometimes referred to as the extraordinary Hall effect. Its microscopic origin is different and does not rely on the Lorentz force [26]. The AHE signal has multiple microscopic origins. Three distinct contributions can be distinguished: skew scattering, side jump and intrinsic deflections [26].

In skew scattering, the scattering process depends on spin, which will deflect, on average, the electron in different directions depending on its spin. In ferromagnetic materials, its net spin polarisation at the Fermi level results in more electrons being scattered in one direction, resulting in a charge accumulation similar to that of the HE.

A different mechanism drives the side jump, where the electron doesn't change its propagation direction (k is conserved), but its position is shifted transverse to the propagation direction. Once again, the direction of the side jump depends on the spin direction and so leads to a charge accumulation.

With intrinsic deflection, no scattering process occurs. This mechanism corresponds to the evolution of an electron spin in evolving adiabatically in a varying potential. It acts as a non-constant magnetic field distribution in the unit cell. This field is in the order of the SOC interaction. For $3d$ metals, it is $\approx 30\,\mathrm{meV}$, corresponding to a field of $\approx 300\,\mathrm{T}$. The intrinsic contribution often dominates the AHE. Interestingly, the localised spins at

the origin of magnetism don't have to be aligned for this to occur; even a coplanar (but not collinear) antiferromagnet can display AHE due to the intrinsic contribution, provided the spin structure breaks time-reversal symmetry [27].

The total Hall effect can be then written phenomenologically as:

$$\mathbf{E}_{\text{Hall}} = R_{\text{HE}}(\mathbf{J} \times \mathbf{B}) + R_{\text{AHE}}(\mathbf{J} \times \mathbf{M}) \,, \tag{1.33}$$

with $\mathbf{M}$ being the magnetisation of the material, $\mathbf{B}$ the magnetic field, $\mathbf{J}$ the current density, R_H the Hall coefficient and R_{AHE} the Anomalous Hall effect coefficient, which groups the three effects described above.

Despite the complicated microscopic origin of AHE, its expression remains simple for ferromagnetic or ferrimagnetic materials, where the AHE voltage is proportional to the cross product of the current and magnetisation ($\mathbf{J} \times \mathbf{M}$). All the microscopic contributions can be factored together in the R_{HE} coefficient. However, as the skew scattering ($\sigma_{xy}^{\text{skew}}$) process depends on the quasi-particle scattering rate (τ) which is related to the conductivity $\sigma_{xx} \sim \tau$ we have $\sigma_{xy}^{\text{skew}} \sim \tau \sim \sigma_{xx}$, while the side jumps and intrinsic contributions ($\sigma_{xy}^{\text{intrinsic, side-jump}}$) are unaffected by this scattering rate i.e. $\sigma_{xy}^{\text{intrinsic, side-jump}} \sim \tau^0 \sim (\sigma_{xx})^0$. R_H depends on temperature or defect as dictated by its dominant microscopic origin [26]. This description concerns the contribution to the AHE and is valid only if $\|\mathbf{M}\|$ is constant otherwise. Consequently, changing the temperature of the sample can be used to determine the type of contribution present only if the magnetisation itself doesn't depend strongly on the temperature. For a simple ferromagnet, this corresponds to staying much lower than the Curie temperature [26].

The AHE is an ideal tool for electrically measuring the magnetisation of a sample. When the measurements are conducted at a constant temperature, the R_{AHE} coefficient is obtained by performing a field loop where the magnetisation is saturated in both directions along its easy axis. This allows to experimentally obtain the R_{AHE} coefficient for a given

temperature without the need of knowing the different microscopic contributions behind the value.

1.3.2.2 Spin Hall effect

The SHE corresponds to the creation of a spin current transverse to the charge current. It is the primary mechanism of SOT in bilayer systems composed of a ferromagnetic layer adjacent to a heavy metal. Predicted by Dyakonov and Perel, this effect is based on Mott scattering [28]. They postulate that scattering events are asymmetric due to SOC. As a result, when a charge current flows, an opposing spin polarisation will appear at the opposite edges of the conductor. This spin accumulation was observed experimentally in 2004 by Kerr microscopy in a semiconductor [29]. Even though heavy metals are the most efficient sources of spin current via SHE due to the Z^4-dependence of the SOC, optical detection was only achieved in 2017, due to the low magneto-optical signal associated with spin accumulation [30].

Based on drift diffusion theory, an expression can be given [31, 32]:

$$\mathbf{j}^c = e\mu n\mathbf{E} + D\nabla n + e\alpha_{\mathrm{SH}}\mu\left(\mathbf{E}\times\mathbf{P}\right) + e\alpha_{\mathrm{SH}}D\left(\nabla\times\mathbf{P}\right), \tag{1.34}$$

$$\mathbf{j}^s_{ij} = -\hbar\mu n E_i P_i + D\frac{\partial P_j}{\partial x_i} - \hbar\alpha_{\mathrm{SH}}\epsilon_{ijk}\left(\mu n E_k + D\frac{\partial n}{\partial x_k}\right), \tag{1.35}$$

where $\mathbf{j}^c$ is the charge current along j, $\mathbf{j}^s_{ij}$ the spin current along i with the j component of the spin polarisation, e the electrons charge, μ the electron mobility, E the electric field, n the electron density, D the electron diffusion constant, $\mathbf{P}$ is the spin polarisation, and α_{SH} the phenomenological spin Hall angle.

The first two terms in Equations 1.34 and 1.35 correspond to the uncoupled charge- and spin currents. The third term in Equation 1.34 corresponds to AHE, the fourth term to inverse spin Hall effect (ISHE). In Equation 1.35, the third term corresponds to the generation of a spin current from an electric field and the fourth term to the contribution from

diffusion. The Levi-Civita tensor, ϵ_{ijk}, indicates that the spin polarisation is transverse to both the charge and spin current directions. Contrary to the AHE, this effect also appears in non-magnetic materials in the absence of any external field.

In thin films, the SHE is usually represented as the creation of a spin current along the z-axis, as the x- and y-directions don't have significant importance due to the sample shape. This spin current can then diffuse into an adjacent material, creating SOT as its angular momentum is transferred. In Equations 1.35 and 1.34, the only contribution considered is scattering. As with the AHE there is also an intrinsic contribution to the SHE [31].

1.3.2.3 Linear magnetoresistance

The linear magnetoresistance (LMR) does not appear immediately in a symmetry analysis. This type of analysis assumes a power expansion of the variable of interest (x, x^2, $x^3, \dots$) while ignoring terms such as $\|x\|$. When the magnetic field is applied to the material, a linear decrease in the longitudinal resistance may be observed. This decrease is assumed to be linked to the stabilisation of the magnetic structure. As the field increases, the number of magnons decreases, reducing the number of scattering events, which in turn reduces resistance. This reduction appears linear under low fields. It is different from the magnetoresistance found in non-magnetic metals, proportional to B^2 and positive.

1.3.2.4 Nernst and anomalous Nernst effects

The Nernst effect (NE) corresponds to the generation of a transverse charge accumulation, and so an electric field when a thermal gradient is applied to a material in the presence of a magnetic field. The anomalous Nernst effect (ANE) works similarly, but replaces the external magnetic field with magnetisation [33].

The origin of the ANE is as complex as that of the AHE, with both intrinsic origins linked to the Berry phase curvature and scattering contributions [33]. From a symmetry

standpoint, the Onsager relations establish the existence of NE and ANE, and their relation to the Ettingshausen effect [34].

For the analysis of SOT at constant temperature, we do not need to know the detailed origin of the NE and ANE. It is sufficient to determine a general expression for the Nernst voltage for inclusion in the harmonic Hall method, which is given as:

$$\mathbf{E}_{\text{Nernst}} = R_{\text{NE}}(\nabla T \times \mathbf{B}) + R_{\text{ANE}}(\nabla T \times \mathbf{M}) \,, \tag{1.36}$$

where ∇T is the temperature gradient in the material, R_{NE} and R_{ANE} are the NE and ANE coefficients respectively, $\mathbf{B}$ the external field and $\mathbf{M}$ the material magnetisation.

1.3.2.5 Symmetry determination of first-order effects

Generally, one can determine the different first-order effects presented here through symmetry arguments. The interest in using symmetry arguments is that they ensure obtaining a tensor fully representing the sample.

From a symmetry approach, the first-order effects for the galvano-magnetic tensor can be expressed using isotropic (spherical) sample symmetry, with the applied magnetic field $\mathbf{H}$ and reduced magnetisation m along the Cartesian axis $i = x, y, z$. The following tensor describes the first-order effects used in the model:

$$\rho^{1m} = \begin{pmatrix} -\rho^{\text{LMR}}\|\mathbf{H}\| & \rho^{\text{AHE}}m_z + \rho^{\text{HE}}H_z & -\rho^{\text{AHE}}m_y + \rho^{\text{HE}}H_y \\ -\rho^{\text{AHE}}m_z + \rho^{\text{HE}}H_z & -\rho^{\text{LMR}}\|\mathbf{H}\| & \rho^{\text{AHE}}m_x + \rho^{\text{HE}}H_x \\ \rho^{\text{AHE}}m_y + \rho^{\text{HE}}H_y & -\rho^{\text{AHE}}m_x - \rho^{\text{HE}}H_x & -\rho^{\text{LMR}}\|\mathbf{H}\| \end{pmatrix}, \tag{1.37}$$

where ρ^{LMR} represents the negative linear coefficients, ρ^{AHE} the AHE coefficient and ρ^{HE} the Hall effect coefficient.

The temperature gradient in the sample is due to Joule heating. We add the ANE and NE contribution *a posteriori*. The heat gradient, assumed along the z-axis, was therefore written as dependent on I^2, the square of the current. Consequently, the ANE and NE co-

efficients reported here groups the actual ANE and NE resistance and the sample/substrate thermal conductivity. The actual thermal gradient value is rather difficult to measure.

All these contributions, excluding the linear magnetoresistance, generate a voltage that is transverse to the current flow. Thus, the power dissipation $\mathbf{E} \cdot \mathbf{J}$ associated with all tensor contributions is zero. These effects are dissipationless, which agrees with time-reversal symmetry. The electric voltage doesn't change under time-reversal symmetry, but the current, magnetic field and magnetisation do change sign. ρ^{HE} and ρ^{AHE} retain their signs under time-reversal symmetry, so they cannot induce dissipation. This is not the case for ρ^{LMR}, as the absolute value cancels the sign change of $\mathbf{H}$ under time-reversal symmetry. Thus, the LMR induces dissipation, as expected.

The ANE and ISHE both connect different transport quantities transversally. ANE connects heat current to transverse electric potential, while ISHE connects spin current to transverse electric potential. ANE requires an external field or magnetisation to break the time reversal symmetries, while ISHE does not.

The symmetry determination of the tensor used here respects the expressions given in the above sections. In this thesis, the influence of a particular crystal structure on the first-order effects has not been taken into account. When we reduce the symmetry to ∞m, or to the crystallographic structure $4\bar{2}m$ used for Mn_2Ru_xGa (Section 1.4), we find that only the ρ^m_{ij} with $i > 2$ or $j > 2$ are affected. Thus, in order to take advantage of a choice of symmetry closer to the actual sample, we need the current or probing directions to include the z-direction, perpendicular to the sample plane. The thin film nature of the sample excludes applying or measuring any current or voltage along z. We therefore retain spherical (isotropic) symmetry for the first-order effects.

The fact that the effects described above are allowed by symmetry does not guarantee that they always occur or are measurable. An example to the contrary is e.g. the magnetic oxides, where all charge effects are allowed, but will not occur as the oxides are mostly

insulating. The optical analogues of these effects (e.g. magneto-optic Kerr effect) can be measured.

1.3.3 Second-order effects in magnetisation

1.3.3.1 Anisotropic magnetoresistance

Anisotropic magnetoresistance (AMR) is a second-order effect, corresponding to a difference in resistance when the current flow is changed from parallel to transverse to the magnetisation direction. It can be expressed as:

$$\frac{\Delta\rho}{\rho} = \frac{\rho_{\parallel} - \rho_{\perp}}{\rho_{\perp}}, \tag{1.38}$$

where $\rho_{\parallel(\perp)}$ is the resistivity when the magnetisation is parallel (perpendicular) to the current flow and the value Δ_{ρ} corresponding to the AMR value.

Thomson first measured AMR in Fe and Ni [35]. It is a relatively weak effect, usually a few percent [36], but can reach up to 16 to 25 % in $Ni_{80}Fe_{20}$ [37, 38]. The direction dependence doesn't correspond to the particular crystallographic structure but to a change in scattering time depending on the magnetisation direction. Consequently, any magnetic material can present magnetoresistance, including antiferromagnets, even if the microscopic origins remain unclear [36].

Microscopically, both intrinsic and extrinsic contributions give rise to the AMR [36]. Extrinsic contributions are explained mainly using scattering theory and have been discussed by Smit [39]. In a system without SOC the orbital should follow the spherical atomic orbital preventing any directional preference. As the SOC is included, the degeneracy of the *d*-orbital is lifted, which results in a different scattering depending on the orientation of the magnetisation and therefore anisotropic magnetoresistance [40].

There is also an intrinsic contribution to AMR which doesn't depend on scattering. It

originates from band effects [36]. Hence, they can be separated using high-frequency measurements (up to 28 THz) as shown by [41]. Calculations can be performed for the intrinsic magnitude of the AMR. However, the difference between the calculated and experimental value is often large, and is attributed to the extrinsic part of the scattering, thereby making direct comparison difficult [36]. Finally, an interesting observation from the models of the microscopic origin of AMR is that the sign can be inferred from the DOS and the main scattering channel, as shown by [20]. For example, for a half-metallic system, the AMR must be negative. The opposite is not true; a negative AMR doesn't indicate half-metallicity.

Note that the resistivity tensor associated with the AMR does not have any off-diagonal component when it is expressed on the basis of $\parallel \mathbf{m}$ and $\perp \mathbf{m}$; it is a true magnetoresistance. However, if we express it in the sample coordinates, where the current is applied along x, we obtain:

$$R(\phi)\rho R^T(\phi) = \begin{pmatrix} \cos(\phi) & -\sin(\phi) \\ \sin(\phi) & \cos(\phi) \end{pmatrix} \begin{pmatrix} \rho_\parallel & 0 \\ 0 & \rho_\perp \end{pmatrix} \begin{pmatrix} \cos(\phi) & \sin(\phi) \\ -\sin(\phi) & \cos(\phi) \end{pmatrix} \tag{1.39}$$

$$= \begin{pmatrix} \rho_0 + \frac{\Delta\rho}{2}\cos(2\phi) & \frac{\Delta\rho}{2}\sin(2\phi) \\ \frac{\Delta\rho}{2}\sin(2\phi) & \rho_0 - \frac{\Delta\rho}{2}\cos(2\phi) \end{pmatrix}, \tag{1.40}$$

where $\Delta\rho = \rho_\parallel - \rho_\perp$ and $\rho_0 = \frac{\rho_\parallel + \rho_\perp}{2}$. The off-diagonal coefficient originates from the change of basis; thus it is different to that of the AHE. This traverse contribution is usually called planar Hall effect (PHE). It is not a new or different Hall effect, only a representation of AMR in the coordinates of the sample.

1.3.3.2 Spin Hall magnetoresistance

The spin Hall magnetoresistance (SMR) is often present in bilayer samples composed of a ferromagnetic material and an adjacent heavy metal. Its origin is strongly related to the SHE, which is generated in heavy metal due to the path of the charge current [42].

This spin current propagates into the ferromagnetic layer, while a portion is reflected at the interface. The reflection is dependent on the relative orientation of the spin current and the local magnetisation. This reflected spin current is converted back into a charge current by the ISHE, resulting in a change in resistance.

In (anti)ferromagnetic oxide heavy metal bilayers, no current can flow in the magnetic layer, preventing the appearance of the aforementioned effect. The SMR, necessitating no charge current in the magnetic layer, is by consequence one of the dominant transport effects in those systems. It is then, often considered to electrically measure magnetisation [43, 44]. On the other hand, magnetic oxides allow to study the SMR effect itself in the absence of other magnetoresistive effects present in magnetic metals.

SMR also has a transverse contribution for the same reason as described in the AMR (Section 1.3.3.1). When working in the sample coordinate system, where the current direction is along x, dependence on the magnetisation angle appears, and off-diagonal components appear in the tensor. Its expression in the sample coordinate systems is [45]:

$$\rho_{xx} = \rho_0 - \Delta\rho_s m_y^2 \,, \tag{1.41}$$

$$\rho_{xy} = \Delta\rho_s m_x m_y \,, \tag{1.42}$$

where ρ_0 is isotropic resistivity, $\Delta\rho_s$ is the SMR, and m_i the magnetisation along i. We note that the expression for the transverse contribution is similar to that of AMR (Equation 1.40), but different from the longitudinal contribution.

1.3.3.3 Symmetry determination of second-order effects

This thesis uses a tensor determined by symmetry analysis considering the second-order effects on magnetisation (m). We saw, in the previous sections, that the AMR exists in any magnetic material and doesn't require any symmetry reductions. This differs for the SMR, which requires an interface for the spin current to be injected and/or reflected. In

the first case, the symmetry is isotropic, while in the second case, it is reduced to ∞m.

For the isotropic symmetry, the second-order tensor is:

$$\rho^{m^2} = \begin{pmatrix} x_0\|\mathbf{m}\|^2 - x_1(m_y^2 + m_z^2) & x_1 m_x m_y & x_1 m_x m_z \\ x_1 m_x m_y & x_0\|\mathbf{m}\|^2 - x_1(m_x^2 + m_z^2) & x_1 m_y m_z \\ x_1 m_x m_z & x_1 m_y m_z & x_0\|\mathbf{m}\|^2 - x_1(m_x^2 + m_y^2) \end{pmatrix}, \tag{1.43}$$

where m_i is the magnetisation along i, and x_j are the different parameters representing the transport contributions. Only two coefficients appear: the first one, x_0, appears only on the diagonal elements and always appears in products with $\|\mathbf{m}\|^2$. As the expression is given in the function of normalised magnetisation, in other words we only consider the variation of the magnetisation direction; we have $\|\mathbf{m}\|^2 = 1$. This term appears as an addition to the isotropic resistance. It is a magnetic effect that does not depend on the magnetisation *direction*. The second term, x_1, depends on the magnetisation direction and matches the expression of the AMR given in the Equation 1.40.

When the symmetry of the system reduces to ∞m, the second-order tensor becomes:

$$\rho^{m^2} = \begin{pmatrix} x_0(m_x^2 + m_y^2) - x_1 m_y^2 + x_2 m_z^2 & x_1 m_x m_y & x_3 m_x m_z \\ x_1 m_x m_y & x_0(m_x^2 + m_y^2) - x_1 m_x^2 + x_2 m_z^2 & x_3 m_y m_z \\ x_3 m_x m_z & x_3 m_y m_z & x_4(m_x^2 + m_y^2) + x_5 m_z^2 \end{pmatrix}. \tag{1.44}$$

The degeneracy was lifted in all terms, including m_z, and so increased the number of parameters from two to six. Since the current does not flow along the z-direction for thin films, this tensor was simplified by setting $x_0 = x_4$, $x_1 = x_3$ and $x_2 = x_5$. After this simplification, we note that $m_z^2 = 1 - m_x^2 - m_y^2$. Therefore, the coefficients of x_0 and x_2 are redundant and we can set $x_2 = -x_1$. The constant offset will be incorporated into the isotropic resistivity.

The final second-order tensor used for this thesis is then:

$$\rho^{\mathbf{m^2}} = \begin{pmatrix} -\rho^{\mathrm{AMR}}(m_x^2+m_y^2) & 0 & 0 \\ 0 & -\rho^{\mathrm{AMR}}(m_x^2+m_y^2) & 0 \\ 0 & 0 & -\rho^{\mathrm{AMR}}(m_x^2+m_y^2) \end{pmatrix} + \begin{pmatrix} \rho^{\mathrm{PHE}}(m_y^2+m_z^2) & -\rho^{\mathrm{PHE}}m_xm_y & -\rho^{\mathrm{PHE}}m_xm_z \\ -\rho^{\mathrm{PHE}}m_xm_y & \rho^{\mathrm{PHE}}(m_x^2+m_z^2) & -\rho^{\mathrm{PHE}}m_ym_z \\ -\rho^{\mathrm{PHE}}m_xm_z & -\rho^{\mathrm{PHE}}m_ym_z & \rho^{\mathrm{PHE}}(m_x^2+m_y^2) \end{pmatrix}. \tag{1.45}$$

This symmetry determined tensor and the one defined by the AMR and SMR effects (Section 1.3.3.1 and Section 1.3.3.2 respectively) are equivalent provided $\rho^{\mathrm{PHE}} = -\Delta\rho_S - \Delta\rho_A$ and $\rho^{\mathrm{AMR}} = -\Delta\rho_S$. However, the symmetry determined one is, by definition, more generic and is suitable for any sample following ∞m symmetry, i.e. it is not limited to the AMR and SMR effects.

We chose this specific expression for the second-order tensor, as this allows us to recover the tensor following the isotropic symmetry by setting $\rho_{\mathrm{AMR}} = 0$. By defining the AMR in this way, it corresponds only with the longitudinal contribution, which appears from the degeneracy lift due to the symmetry reduction from isotropic to ∞m. This will be the working definition of this thesis. Please note, this is not the more widely used definition of AMR (as in Section 1.3.3.1).

1.4 Mn_2Ru_xGa

The Heusler alloy, Mn_2Ru_xGa (MRG), serves as the material of interest in this thesis. As a compensated ferrimagnet with a large spin polarisation and broken inversion symmetry, it's a good candidate for current-induced SOT. Heusler alloys have gained interest since the prediction of ferromagnetic half-metallicity in 1993 by de Groot *et. al* [47], followed by the prediction of a half-metallic ferrimagnet two years later [48]. In 2014, Kurt *et. al* [46]

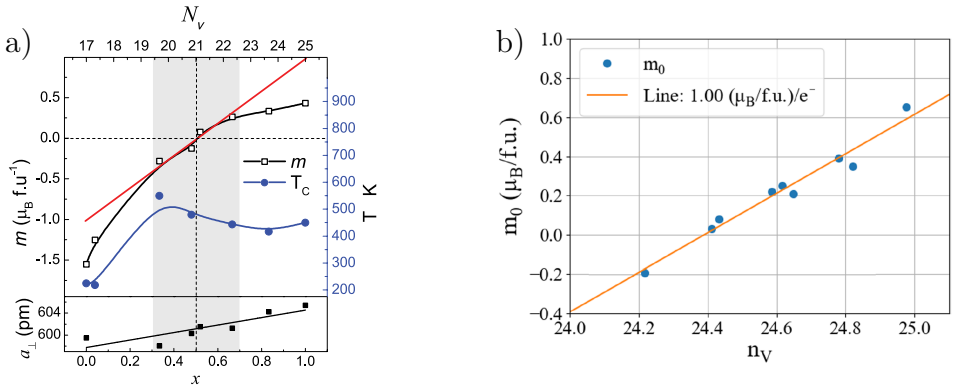

Figure 1.8: a) Magnetisation dependence of Mn_2Ru_xGa in the function of Ru content. MRG follows the Slater Pauling Rule, with a slope of $2\mu_B$ per Ru atom. Due to the in-equivalence of the lattice, the moment at 0 K also impacts the compensation temperature. b) Magnetisation dependence of Mn_2Ru_xGa as a function of the number of valence electrons associated with a change in composition. Both figures represent the same range of compositions. However, a reduction in Ru was assumed to create vacancies in (a), while disorder, with no vacancies, was considered in (b). The latter provides a better agreement with the theory. Reuse of figure (a) with permission from [46], ©2014 by the American Physical Society. Reuse of figure (b) with permission from [1], ©2021 by the American Physical Society.

found that the addition of Ruthenium to Mn_2Ga resulted in a ferrimagnet with a high spin polarisation of 54% and a Curie temperature around 550 K.

Full Heusler alloys comprise a rich family of magnetic materials that often have a gap at the Fermi level of the minority electron band [49]. Half-metallicity implies that these materials (should) follow the Slater-Pauling Curve, which allows one to predict the magnetisation of the compound from the number of valence electrons. According to this rule, the magnetic moment of Mn_2Ru_xGa is $M = (-1 + 2x)\mu_B(\mathrm{f\,u})^{-1}$ which has been verified experimentally [1, 46, 50] (Figure 1.8). As predicted, the magnetic moment is zero for a value of $x = 0.5$ and the variation of the moment as a function of ruthenium content is linear with a slope of 2.

MRG has a cubic crystal structure (Figure 1.9) and is composed of four sublattices whose Wyckoff positions are labelled $4a$, $4b$, $4c$ and $4d$. The magnetic moment is carried by Mn atoms on $4a$ and $4c$. The Mn^{4a} moments couple ferromagnetically between each other, as do the Mn^{4c} moments. However, the coupling between moments on different sublattices is antiferromagnetic, i.e. the coupling between Mn^{4a} and Mn^{4c}.

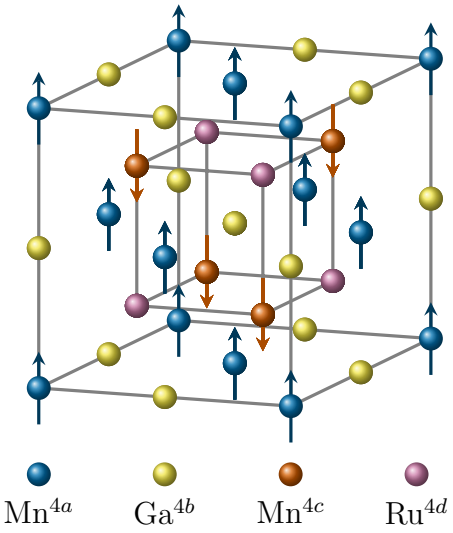

Figure 1.9: Cubic representation of the MRG crystal lattice structure. Magnetic moments reside on both Mn 4a and 4c sub-lattices and couple antiferromagnetically.

Turning to the symmetry of the Mn_2Ru_xGa crystal, a symmetry operation can be a rotation, inversion, mirror or translation that leaves the crystal structure unchanged. The space group of the crystal is the group of all symmetry operations. When excluding the translation, we obtain the point group subgroup of the crystal (as discussed in Section 1.1.1). The Wychoff positions, introduced previously, correspond to the set of positions which are linked by one or more symmetry operations. The details of the different symmetries can be found in the International Tables for Crystallography [51].

Cubic MRG has a point group of $\bar{4}3m$, using Hermann-Mauguin notation. The cell represented here for MRG is cubic; however, the thin-film MRG samples studied here have a small tetragonal distortion (elongation of order 1 %) along the c-axis. This distortion is due to the epitaxial growth on the MgO substrate, which compresses the in-plane lattice parameters. This distortion is large enough to give rise to axial magnetocrystalline anisotropy with an easy axis along the c-axis. Previous studies indicate that only the $4c$ sub-lattice contributed to the transport properties, and so phenomena such as the anomalous Hall effect depend only on the $4c$ sub-lattice magnetisation rather than net magnetisation.

The tetragonal distortion of the unit cell reduces the symmetry of Mn_2Ru_xGa to $\bar{4}m2$. However, the crystal structure remains very close to cubic, and we expect that the most prominent features in both magnetisation (anisotropy) and transport can be described in the cubic representation, with a small correction due to distortion. We found, for example, that $k_2 = 7k_2'$ and so the correction is due to distortion effects are near-exclusively first-order terms.

1.5 Spin-torque phenomena

We previously saw that interactions of local magnetisation with the conduction electron through the *s-d* interaction (Section 1.2.3) lead to a large number of magneto- and thermogalvanic effects (Section 1.3). In particular the two-current model and the concept of a spin current allow for an understanding of the GMR and TMR effects (Section 1.3.1). Magnetic sensors use these effects to read the relative magnetisation direction of a thin, free-to-rotate magnetic layer. The idea postulated by Slonczewski and Berger [52, 53] was that the effect inducing a change in resistance will also cause a torque on the local magnetisation as its reciprocal. It should be possible to manipulate the magnetisation direction using a charge current. Spintronics research thereafter pursued this idea.

In spin-transfer torque, a charge current is spin-polarised as it passes through a ferromagnetic layer. When it enters a nearby magnetic layer where the local magnetisation is not collinear with the polarisation of the spin current, it exerts a torque on the local magnetisation through *s-d* exchange. We note that the charge current through the ferromagnetic layer is decoupled from the effect. It is only required as a source of a spin polarised charge current and more accurately, only the spin current is necessary to generate torque. The spin current can be produced using different mechanisms. We now describe the most common approaches used to this effect.

The SHE produces a particularly strong transverse spin current in heavy metals. If a

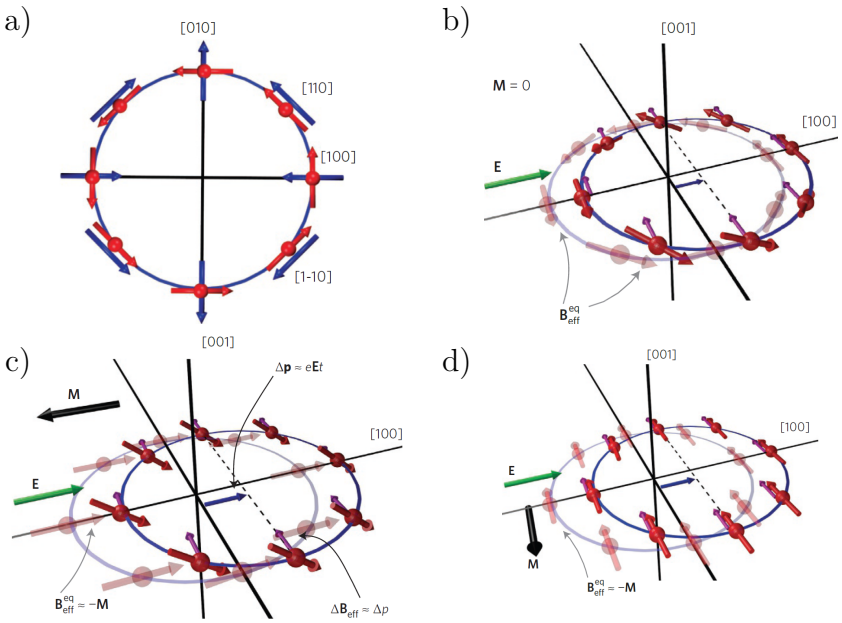

Figure 1.10: Fermi surface associated with Rashba and Dresselhaus Hamiltonian for: a) Spin polarisation of the Fermi surface for a Rashba (red) and Dresselhaus (blue) spin-orbit coupled system in equilibrium and in the absence of an exchange field (zero magnetisation). b) For a Rashba system, in the presence of an electric field (E) which shifts the Fermi surface (blue arrow), a torque appears (purple arrow). This gives the spin an out-of-plane component, in agreement with the intrinsic contribution of the SHE. The equilibrium direction reference is represented as transparent. c) This is the same as b*, with an exchange field along the x-direction much greater than the SOC field. In equilibrium, the spin nearly aligns with the exchange field. When the electric field is applied, a torque component appears (purple), which changes the direction of the conduction spin and, via the exchange interaction, exerts a torque on the local magnetisation. d) This is the same as* c *except with an exchange field transverse to the current direction. This results in a torque which is aligned with the magnetisation; so this does not change the direction of the spin. Reproduced with permission from Springer Nature from [54]*

bilayer system consists of a ferromagnetic and an adjacent heavy metal layer, a charge current through the heavy metal produces by SHE a spin current that can propagate into the ferromagnetic layer. As the injected spins either relax to the local magnetisation there, or accumulate close to the interface, it exerts a torque on the magnetisation. As the spin current is generated in the adjacent layer, the ferromagnetic layer needs to be relatively thin to have large torque density (torque per unit volume of the magnetic layer), ideally just thick enough to fully absorb the spin current $\approx \lambda_{sf}$.

Above, we have used the concept of spin current and the conservation of angular momentum to explain the origin of SOT. Microscopically, this spin current enters the magnetic

layer at (or at least close to) the Fermi level. Any 'excess' torque there could generate SOT [4]. This can be achieved via an intrinsic process in materials with broken inversion symmetry [55, 56]. In these materials, in the presence of SOC, a new contribution appears, which couples the spin of the electrons with the wave vector **k** (Figure 1.10), leading to the Edelstein effect [57] also called the inverse spin galvanic effect (ISGE) [58]. If inversion symmetry is broken by an interface, the Rashba Hamiltonian [4, 59] gives the coupling between the electron momentum p and the spin operator σ via the phenomenological parameter α_r:

$$H_R = \alpha_r \sigma \cdot (\mathbf{p} \times \mathbf{z}) \,. \tag{1.46}$$

Inversion symmetry can be broken by other means. For example, in the zinc-blend crystallographic structure, which is that of the inverse and half-Heusler crystals (space group $F\bar{4}3m$), the Hamiltonian is that of Dresselhaus coupling [4, 60]:

$$H_D = \beta(\sigma_x p_x - \sigma_y p_y) \,, \tag{1.47}$$

where α and β are respectively the Rashba and Dresselhaus parameters, σ the spin operator, **p** the momentum operator and **z** the direction normal to the interface. Both of those terms couple the momentum (and thus real space) with spin polarisation. The effect on the spin polarisation of the Fermi surface is shown in Figure 1.10. Thus, under the influence of a (non-equilibrium) charge current, a shift of the Fermi surface in k space induces a spin-momentum locking and therefore a spin polarisation. Due to the s-d exchange, this spin polarisation associated with the conduction electrons also generates a torque on the local magnetic moment.

While we have discussed the SOT contributions originating from the SHE in bilayers, the interface breaks inversion symmetry, allowing intrinsic contributions to the SOT. The interface between the two materials leads to the Rashba effect (Figure 1.10), coupling the spin polarisation with the momentum. This results in a SOT contribution from the ISGE.

It was initially considered that the SHE contribution to the SOT was the DL torque, while the ISGE was at the origin of the FL torque [4, 61]. However, when contributions from SOC and exchange coupling are taken into account, both FL and DL can originate from ISGE or SHE [61, 62]. The separation of the ISGE from the SHE contributions is therefore not trivial and requires modelling the dependence of both effects as a function of e.g. the material thickness [63–65], or imposing a lower symmetry by carefully selecting an appropriate material [61].

The induced spin polarisation becomes a property of the bulk material when there is a lack of inversion symmetry in the crystallographic structure. This eliminates the need for a bilayer structure and makes it possible to study single-layer SOT. Since this is a bulk effect, the SOT will scale naturally with the layer thickness. This allows for the use of thicker ferromagnetic layers, which is advantageous because the thermal stability of the magnetisation scales as the volume of the magnetic element. Applications that require high-output power also become feasible, as higher currents can be pass through the device without damage to the active layers.

1.5.1 From a torque to an effective field

We have seen various microscopic origins of the torque. To formalise this, we can use the expression from Slonczewski [4, 52] and write the Landau-Lifshitz-Gilbert (LLG) equation with the inclusion of the SOT torque, explicit in FL and DL components:

$$\frac{\mathrm{d}\mathbf{m}}{\mathrm{d}t} = -\gamma \mathbf{m} \times \mathbf{B}_{eff} + \alpha \mathbf{m} \times \frac{\mathrm{d}\mathbf{m}}{\mathrm{d}t} + \frac{\gamma}{M_s}\mathbf{T}\,, \tag{1.48}$$

where $\mathbf{m}$ is the magnetisation unit vector, γ is the electron gyromagnetic ratio and α the damping parameter.

The SOT $\mathbf{T}$ is given by:

$$\mathbf{T} = \tau_{\mathrm{FL}} \mathbf{m} \times \xi + \tau_{\mathrm{DL}} \mathbf{m} \times (\mathbf{m} \times \xi)\,, \tag{1.49}$$

where τ_{FL} and τ_{DL} are the FL and DL parameters, ξ is the direction normal to the plane between the two bilayers.

A comment on the naming of the two torque components is required: their names, field- and damping-like, are motivated by their similarity to the expression of the field-driven and damping effects in the LLG equation. This becomes apparent when Equation 1.48 is rewritten to obtain the Landau-Lifshitz equation. The $\frac{\mathrm{d}m}{\mathrm{d}t}$ term on the right-hand side of the equation is then added to that on the left, with the appropriate prefactor. The detail of the derivation is given in Appendix B.1. The Landau-Lifshitz equation is then given by:

$$\begin{aligned}\frac{\mathrm{d}\mathbf{m}}{\mathrm{d}t} =& -\frac{\gamma}{1+\alpha^2}\mathbf{m}\times\mathbf{B}_{\mathrm{eff}} + \frac{\gamma}{M_s(1+\alpha^2)}\mathbf{T} \\ & -\frac{\gamma\alpha}{1+\alpha^2}\mathbf{m}\times\mathbf{m}\times\mathbf{B}_{\mathrm{eff}} + \frac{\alpha\gamma}{M_s(1+\alpha^2)}\mathbf{m}\times\mathbf{T} \qquad (1.50)\\ =& -\frac{\gamma}{1+\alpha^2}\mathbf{m}\times\left(\mathbf{B}_{\mathrm{eff}} - \frac{\tau_{\mathrm{FL}}\xi - \alpha\tau_{\mathrm{DL}}\xi}{M_s}\right) \\ & -\frac{\gamma\alpha}{1+\alpha^2}\mathbf{m}\times\mathbf{m}\times\left(\mathbf{B}_{\mathrm{eff}} - \frac{\tau_{\mathrm{DL}}\xi + \alpha\tau_{\mathrm{FL}}\xi}{M_s\alpha}\right). \qquad (1.51)\end{aligned}$$

In the absence of FL and DL torques ($\tau_{\mathrm{FL}} = \tau_{\mathrm{DL}} = 0$), we find the two terms of the Landau-Lifshitz which correspond respectively to precession in a field and damping. Both the FL and DL terms contribute to the precession and damping dynamics. However, as $\alpha \ll 1$ the DL contribution to the precession and the FL contribution to the damping can be neglected. Depending on the symmetry of the crystallographic structure, the intrinsic contribution can lead to terms depending on the magnetisation, which cannot be written in the form $\mathbf{m}\times\hat{\sigma}$. These differ from the usual bilayer DL torque.

In the quasi-static approximation, where the frequency involved in the measurement are significantly lower than the one of the magnetisation dynamics, this distinction is less

important. Then $\frac{\mathrm{d}\mathbf{m}}{\mathrm{d}t} = 0$ and so Equation 1.48 becomes:

$$0 = -\gamma \mathbf{m} \times (\mathbf{H}_{\text{eff}} + \mathbf{H}_{\text{FL}} + \mathbf{H}_{\text{DL}}), \tag{1.52}$$

where we define the equivalent field-like ($\mathbf{H}_{\text{FL}}$) and damping-like ($\mathbf{H}_{\text{DL}}$) fields as:

$$\mathbf{H}_{\text{FL}} = \frac{\tau_{\text{FL}}}{M_s}\xi\,, \quad \text{and} \quad \mathbf{H}_{\text{DL}} = \frac{\tau_{\text{DL}}}{M_s}(\mathbf{m} \times \xi). \tag{1.53}$$

In this approximation, the SOT field is equivalent to an external field being applied to the sample. The only difference between the FL and DL torque arises from the direction of the effective field and the magnetisation dependence on the DL torque. This approximation is always valid when using the harmonic Hall method, where the frequency of the injected current is lower than a few kHz, far below the natural frequency of the magnetisation precession, which is in the GHz range, or higher depending on which mode is excited and the magnitude of its **k** vector.

1.5.2 Determination of the effective field tensor

The expression of the effective field can be determined from the microscopic origin [4, 66, 67]. However, as mentioned previously (Section 1.5) the origin and number of effects contributing to the SOT render the microscopic approach extremely complex. We therefore resort to a symmetry argument, as the SOT field also obeys the Neumann principle. This argument allowed us to determine an SOT effective field tensor based on the principles detailed in Section 1.1.1.

The general tensor for an effective field is then given by:

$$\mathbf{H}_{\text{SOT}} = \xi_{\text{FL}} \cdot \mathbf{J} + \xi_{\text{DL}} \cdot \mathbf{J}, \tag{1.54}$$

with ξ_{FL} a tensor rank 2 axial and ξ_{DL} rank 3 polar, corresponding to the FL and DL fields.

In the case of a fully isotropic material, both tensor are null; thus no torque can appear. In order to have SOT, inversion symmetry needs to be broken. The most common case of this is in a bilayer sample, corresponding to the ∞m symmetry where applying the Neumann principle gives:

$$\xi_{\mathrm{FL}} = \begin{pmatrix} 0 & x_1 & 0 \\ -x_1 & 0 & 0 \\ 0 & 0 & 0 \end{pmatrix}, \quad \xi_{\mathrm{DL}} = \begin{pmatrix} x_3 m_z & 0 & x_2 m_x \\ 0 & x_3 m_z & x_2 m_y \\ x_1 m_x & x_1 m_y & x_4 m_z \end{pmatrix}, \tag{1.55}$$

where x_i are different independent factors. This expression of the SOT is different from the one commonly found in the experimental literature. A derivation of the SOT tensor for the bilayer system considering symmetry argument was provided by Garello *et al.* [66]. Based on the spin accumulation in the magnetic layer, they consider a possible SOT anisotropy (or asymmetry); their expression of the torque, keeping here only terms up to the second-order in magnetisation ($\mathbf{m}$) is then [66]:

$$\mathbf{T}^{\perp} = (\mathbf{y} \times \mathbf{m}) T_0^{\perp}, \tag{1.56}$$

$$\mathbf{T}^{\parallel} = \mathbf{m} \times (\mathbf{y} \times \mathbf{m}) T_0^{\parallel} + (\mathbf{z} \times \mathbf{m})(\mathbf{m} \cdot \mathbf{x}) T_2^{\parallel}, \tag{1.57}$$

where $\mathbf{T}^{\perp}$ corresponds to the FL torque and $\mathbf{T}^{\parallel}$ corresponds to the DL torque, the indices n in T_n correspond to the order for the anisotropy of the SOT. The expression of the DL is equivalent to Equation 1.55, if we set $x_1 = -T_0^{\parallel} - T_2^{\parallel}$ and $x_3 = T_0^{\parallel}$.

In the model presented by Garello *et al.* the higher order of the SOT anisotropy can be neglected to obtain the usual expression given by experiment and microscopic models [4, 66]. This simplification is not as obvious in the tensor given in Equation 1.55 Adding, 'by hand', a supplementary asymmetry reduces the symmetry of all effects simultaneously and doesn't allow disentangling the contribution of the different microscopic mechanisms, i.e. the effect of the anisotropic SOC only. To obtain the same DL tensor as reported in the literature, we need to increase the symmetry of the sample (as this is the only option

to reduce the number of free parameters).

To do so, we can focus only on the ferromagnetic layer and consider a fully isotropic system where a spin current is injected from the surroundings:

$$\mathbf{H}_{\mathrm{SOT}} = \xi^S_{\mathrm{FL}} \cdot \mathbf{J}^{\mathbf{S}} + \xi^S_{\mathrm{DL}} \cdot \mathbf{J}^{\mathbf{S}}, \tag{1.58}$$

where $\mathbf{J}^{\mathbf{S}}$ is a spin current with polarisation $\mathbf{S}$. Then, ξ^S_{FL} is a polar tensor of rank 2 and ξ^S_{DL} is an axial tensor of rank 3:

$$\xi^S_{\mathrm{FL}} = \begin{pmatrix} x_0 & 0 & 0 \\ 0 & x_0 & 0 \\ 0 & 0 & x_0 \end{pmatrix}, \quad \xi^S_{\mathrm{DL}} = \begin{pmatrix} 0 & -x_1 m_z & x_1 m_y \\ x_1 m_z & 0 & -x_1 m_x \\ -x_1 m_y & x_1 m_x & 0 \end{pmatrix}. \tag{1.59}$$

Considering the origin of the spin current being the SHE, then:

$$\mathbf{J}^{\mathbf{S}} \propto \mathbf{J} \times \mathbf{z} = \begin{pmatrix} J_y \\ -J_x \\ 0 \end{pmatrix}, \tag{1.60}$$

where J_i is the charge current along i and z is the direction normal to the interface between the ferromagnetic layer and the heavy metal layer.

Thus, the DL tensor expressed in terms of charge current becomes:

$$\xi_{\mathrm{DL}} = \begin{pmatrix} x_1 m_z & 0 & 0 \\ 0 & x_1 m_z & 0 \\ -x_1 m_x & -x_1 m_y & 0 \end{pmatrix}, \tag{1.61}$$

which is identical to the one most commonly found in literature when the current along z is not considered (or cannot be measured).

When the origin of the SOT is intrinsic, i.e. originating from the crystallographic structure, the expression of the effective field can be widely different and the microscopic calculation

to find its expression not trivial. In this situation, relying on the symmetry argument is advantageous and possibly the only option for the experimentalist. This has been performed and tabulated for all the point groups breaking inversion symmetry [56]. The tensors are furthermore easily found using the Neumann principle. For the symmetry of Mn_2Ru_xGa we start from its cubic point group $\bar{4}3m$:

$$\xi_{\mathrm{FL}} = \begin{pmatrix} 0 & 0 & 0 \\ 0 & 0 & 0 \\ 0 & 0 & 0 \end{pmatrix}, \quad \xi_{\mathrm{DL}} = \begin{pmatrix} 0 & x_1 m_z & x_1 m_y \\ x_1 m_z & 0 & x_1 m_x \\ x_1 m_y & x_1 m_x & 0 \end{pmatrix}. \tag{1.62}$$

When the substrate induces a distortion, the symmetry is reduced to $\bar{4}m2$ and the tensor becomes:

$$\xi_{\mathrm{FL}} = \begin{pmatrix} 1 & 0 & 0 \\ 0 & -1 & 0 \\ 0 & 0 & 0 \end{pmatrix}, \quad \xi_{\mathrm{DL}} \begin{pmatrix} 0 & x_3 m_z & x_2 m_y \\ x_3 m_z & 0 & x_2 m_x \\ x_1 m_y & x_1 m_x & 0 \end{pmatrix}. \tag{1.63}$$

This reduction of the symmetry allows an FL torque to appear and lift the degeneracy between the different DL torque coefficients. As the distortion is small, it is sensible to consider that the difference due to a symmetry reduction is also small. Finally, considering the expression of the DL in the $\bar{4}3m$ symmetry, we notice that this term doesn't correspond to the damping terms presented in the Landau-Lifshitz equation, as it cannot be written as a $\mathbf{m} \times \mathbf{u}$ product with $\mathbf{u}$ being a unit vector.

1.5.3 Spin orbit torque measurements

SOT cannot be measured directly. In some cases, the spin accumulation resulting from e.g. SHE can be detected optically, such as in GaMnAs [29] or in Pt and W [30]. Furthermore, spin, unlike charge, is not conserved due to dephasing and spin-flip scattering events. The measurement needs to be local, and therefore indirect.

Quantifying the effect of SOT on a ferromagnetic layer typically involves multiple approximations. The first being that both the SOT and the ferromagnetic layer are completely uniform, so that a uniform rotation of the magnetisation results from the torque. However, looking at the microscopic origin of the torque, i.e. a spin current injected into the ferromagnetic layer, we know that the effect will decay over the spin diffusion length. Therefore, the torque will be stronger near the interface. The same applies to the Rashba effect, which is a localised interface effect. Intrinsic effects, such as the Dresselhaus spin-orbit torques differ, as they originate from the lack of inversion symmetry in the crystallographic structure, and thus will act uniformly over the entire magnetic volume. This approximation can be considered valid if the ferromagnetic layer is relatively thin, taking into account the fact that the exchange interaction will propagate any torque through the full layer. We note that this is often referred to as 'exchange averaging' when discussing the effect of a local anisotropy axis changing direction throughout the magnetic sample.

The second approximation consists of inferring the SOT from its effect on the magnetisation. For low-field methods, such as the harmonic Hall method, we do not measure the torque. Instead, we compare the change in magnetisation due to the SOT with its variation due to the externally applied field (considered to be known). In this fashion, we can express the SOT in terms of an effective field. Therefore, the SOT field derived from the harmonic Hall approach is calibrated against the influence of an external field on magnetisation. As a result, low-magnetisation materials, including compensated ferrimagnets, exhibit a substantial SOT field, even for modest values of SOT.

Other methods attempt to measure either dynamic SOT, e.g. the effect on the ferromagnetic resonance (FMR) linewidth and resonant frequency/field, or to measure magnetisation in a non-equilibrium state. The latter could record domain wall motion or the shifting of the hysteresis loop dependent on an applied bias current, which provides SOT, linear in the current [68]. We note here that the exact shape of the magnetic hysteresis depends on

nucleation fields and domain wall propagation speeds, which are governed by microstructural quantities, usually unknown for a thin-film sample. This makes the extraction of the actual SOT complex and prone to error.

Ultimately, for memory applications, we require switching the magnetisation direction from one stable state to another. A good figure of merit for SOT efficiency is the minimum current density required to reverse the magnetisation. Unfortunately, there is no direct correlation between this minimum current density and the value of SOT obtained using other methods [69]. This is because most current switching methods require large current densities, which result in significant Joule heating. As a consequence, the magnetic switching in the SOT system is facilitated by thermal heating. Increasing the sample temperature reduces the anisotropy barrier, allowing it to nucleate a domain in the opposite direction, followed by domain wall propagation until the full sample magnetisation is reversed [70, 71]. Additionally, it has been observed that the DL torque is more efficient at inducing switching than the FL torque [72]. This could be explained by two potential mechanisms. The first of which corresponds to the transfer of the angular momentum associated with the DL torque. The second case is when the magnetic anisotropy decreases enough with increasing temperature. Then the in-plane magnetisation component becomes large due to the external bias field. In this case, the DL torque would have a component along the out-of-plane direction, which would be sufficient to bias the switching direction.

The FL torque appears to reduce the critical current, without allowing switching. At first, it may seem that the FL torque should, as the name suggests, correspond to an external field. Since an external field is required to cancel out the pinning effect of the Dzyaloshinskii-Moriya interaction (DMI) in bilayers or crystallographic structures that allow it, this should not matter during switching experiments. However, it's important to note that the FL torque is localised at the interface. During a switching event, the

magnetisation is not uniform, and there is a clear distinction between the FL and the external field.

Additionally, there are no easy direct comparisons between the two main measurements of SOT used in literature: spin torque ferromagnetic resonance (ST-FMR) and the harmonic Hall method. ST-FMR requires thicker samples, whereas the harmonic Hall method focuses on samples with a thickness comparable to the spin diffusion length. This prohibits patterning both devices on the same sample. As a result, it is not possible to directly compare the efficiency extracted using these two methods. ST-FMR occurs at relatively high frequencies, which may thus include different physical effects compared to the quasi-static harmonic Hall method. It is to be noted that the measured spin torque efficiency varies among sample configurations and experimental techniques [73].

The indirect measurement of the SOT complicates comparing different materials. During a measurement, the SOT value is given as an effective field. This effective field is to be understood as the external field that should be applied to obtain the same effect on magnetisation. The effective SOT field is highly dependent on the saturation magnetisation of the sample and its thickness. Consequently, the spin torque efficiency is defined to take this into account to enable comparison between materials [4]:

$$\xi_{\mathrm{DL,(FL)}} = \frac{2e}{\hbar} M_s t_{\mathrm{FM}} \frac{B_{\mathrm{DL,(FL)}}}{j_c}\,, \tag{1.64}$$

where e is the electron charge, $\hbar$ the reduced Plank constant, M_s the saturation magnetisation, t_{FM} the thickness of the magnetic layer, $B_{\mathrm{DL,(FL)}}$ is the SOT FL (DL) effective fields, respectively, and j_c the current density applied to the sample. This spin-torque efficiency is unitless, with higher values corresponding to higher SOT. One should keep in mind that this metric is still imperfect as it has been shown to correlate with material resistivity [74].

In bilayer systems, the total SOT exerted on the magnetisation remains constant as the

magnetic layer thickness increases. In contrast, the total torque from the external field increases linearly with the thickness. The t_{FM} factor in Equation 1.64 corrects for this discrepancy. The situation is different in a single-layer system as the torque from the SOT now scales linearly with increasing thickness. Therefore, we expect the spin torque efficiency to scale with thickness. Nerveless, we use the Equation 1.64 in this thesis to allow for a direct comparison with the values reported for bilayer systems in the literature.

Finally, since we only have an indirect measure of the SOT, many concurrent effects can happen in the sample at once. Some of these concurrent effects can be avoided, but most measurement methods induce a thermoelectric effect, as they rely on spin rectification, both in ST-FMR and harmonic Hall. This means that these methods have difficulty distinguishing between different contributions present in the material. A global overview of these different measurement methods can be found in Nguyen's review article [5]. For the purposes of this thesis, we focus on the harmonic Hall method, and describe the derivation of the relation between the observed signals (V_{xy} and V_{xx} at the first and second harmonic of the AC bias current) and the extracted SOT efficiency in the next section.

1.6 The harmonic Hall method

The harmonic Hall method has become a standard technique for determining the symmetry and magnitude of the SOT [5, 75]. Here an alternating current modulates the magnetisation direction via SOT. This generates a change in the voltage following the magnetogalvanic response of the sample. Since the current acts both as a modulator of the magnetisation and as a probe of the magnetic state, the electric signal appears on the second harmonic.

On the other hand, any effect that depends on the square of the current will appear in the second harmonic. This includes thermoelectric effects, such as the ANE, which contribute to the harmonic signal with a similar symmetry to the DL torque contribution.

To distinguish between the thermoelectric component and the SOT signal, we can rotate the external magnetic field at different magnitudes. The decay of the SOT response allows separation from the ANE response [76].

The harmonic Hall method uses an alternating current (AC) current at a low frequency, typically in the order of 1 kHz or lower. This suggests that the measurement of harmonic Hall detects the effective field generated from the SOT, as discussed above. The harmonic Hall method captures the effect of SOT on the magnetisation via galvanomagnetic signals, which appear as a second harmonic signal.

Considering a simple case, with only the AHE involved, the traverse voltage is given by:

$$\begin{aligned} V_{xy} &= R_{\mathrm{AHE}} m_z(t) I_0 \sin(\omega t) && (1.65)\\ &= R_{\mathrm{AHE}} \left(m_z^0 + \Delta m_z I_0 \sin(\omega t) \right) I_0 \sin(\omega t) && (1.66)\\ &= R_{\mathrm{AHE}} m_z^0 I_0 \sin(\omega t) + R_{\mathrm{AHE}} \Delta m_z I_0^2 \sin^2(\omega t) && (1.67)\\ &= R_{\mathrm{AHE}} m_z^0 I_0 \sin(\omega t) + R_{\mathrm{AHE}} \Delta m_z I_0^2 \frac{1 - \cos(2\omega t)}{2}, && (1.68) \end{aligned}$$

where R_{AHE} is the anomalous Hall resistivity, m_z the z component of the magnetisation and Δm_z the change in the magnetisation due to the SOT field. From this, we can see that the first harmonic ($\propto \sin(\omega t)$) corresponds to the usual magnetic response, while the second harmonic ($\propto \cos(2\omega t)$) contains the effect of the SOT field on magnetisation. The SOT is a small effect, and so the second harmonic is a few orders of magnitude lower than the first harmonic. In order to separate the two amplitudes, a lock-in amplifier (LIA) can be used to record both the first and second harmonics simultaneously.

A Taylor expansion can be used to represent a harmonic signal under the harmonic Hall assumptions of a quasi-static magnetisation evolution and a single macro state moving coherently due to the SOT perturbation. The magnetisation variation is then given by:

$$\mathbf{m}(\mathbf{H}_{\mathrm{ext}}, t) = \mathbf{m}(\mathbf{H}_{\mathrm{ext}}) + \frac{\partial \mathbf{m}}{\partial \mathbf{H}_i} \cdot \mathbf{H}_{\mathrm{SOT}}(t). \quad (1.69)$$

If the $\mathbf{H}_{\mathrm{SOT}}$ is along $\mathbf{H}_{\mathrm{ext}}$, then this simplifies to:

$$\mathbf{m}(\mathbf{H}_{\mathrm{ext}}, t) = \mathbf{m}(\mathbf{H}_{\mathrm{ext}}) + \frac{\partial \mathbf{m}(\mathbf{H}_{\mathrm{ext}})}{\partial \|\mathbf{H}_{\mathrm{ext}}\|} \|\mathbf{H}_{\mathrm{SOT}}(t)\| \,. \tag{1.70}$$

We can now examine the transport properties. If V_{xy} only depends on the magnetisation, we obtain the harmonic Hall voltage:

$$V_{xy}^{1\omega} = V_{xy}(\mathbf{m}) \,, \tag{1.71}$$

$$V_{xy}^{2\omega} = \frac{\partial V_{xy}}{\partial \mathbf{H}_i} \mathbf{H}_{\mathrm{SOT}} \,. \tag{1.72}$$

The SOT field in a bilayer system is given by:

$$\mathbf{H}_{\mathrm{SOT}} = (h_{\mathrm{DL}} \cos(\theta), h_{\mathrm{FL}}, -h_{\mathrm{DL}} \sin(\theta) \sin(\phi)) \,. \tag{1.73}$$

When the magnetisation is close to the z-axis ($\theta \ll 1$), $\mathbf{H}_{\mathrm{SOT}}$ is along x- (respectively y) direction for the DL torque (respectively FL torque). By aligning H_{ext} along those directions, the correspond SOT field $\|\mathbf{H}_{\mathrm{SOT}}\|$ then can be found directly by writing:

$$\|\mathbf{H}_{\mathrm{SOT}}\| = \frac{V_{xy}^{2\omega}}{\frac{\partial V_{xy}^{1\omega}}{\partial H_{\mathrm{ext}}}} \,. \tag{1.74}$$

This equation does not account for the fact that both $\mathbf{H}$ and $\mathbf{M}$ are vector quantities that are not always aligned exactly along those directions. Additionally, it doesn't take into account other contributions, such as the PHE and spurious signals, such as the ANE and NE.

To obtain a more appropriate expression, we must separate the effect of the magnetisation and use the transport effect to retrieve the harmonic Hall signal. This involves taking into account the variation of magnetisation in both θ and ϕ, while considering the anisotropy field. In the next section, we discuss the expression of the variation of the magnetisation vector as a function of the SOT field, as well as how to link the harmonic response to the value of SOT.

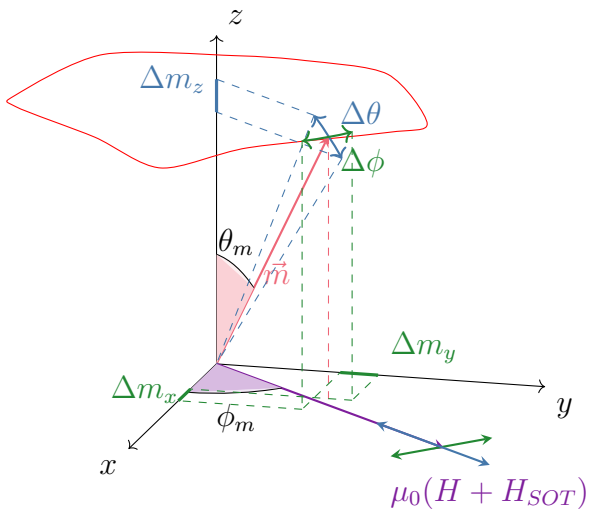

Figure 1.11: Variation of magnetisation due to the SOT associated to an AC current. The value θ_m and ϕ_m depend on the external field and anisotropy. The variation Δm_i comes from both the SOT field and Oersted field.

1.6.1 Variation of the magnetisation vector

The equilibrium position of magnetisation depends on the anisotropy energy and the Zeeman field. In this section, we will only consider a single macrospin approximation. Considering that the magnetocrystalline and Zeeman energies depend only on the magnetisation direction via the angles θ and ϕ (Figure 1.11), we can define the generic expression of the energy as $E(\theta, \phi, \mathbf{H})$ where $\mathbf{H}$ represents the external magnetic field and SOT field. At equilibrium, we know that:

$$F = \frac{\partial E}{\partial \theta} = 0\,, \quad \text{and} \quad G = \frac{\partial E}{\partial \phi} = 0, \tag{1.75}$$

where we define F and G, respectively.

In the case of small perturbation of the field, $\mathbf{H}$, $\delta\mathbf{H} = \left(\delta H_x, \delta H_y, \delta H_z\right)$, we can write this for the variation $\delta\theta$ and $\delta\phi$:

$$\frac{\partial F}{\partial \theta}\delta\theta + \frac{\partial F}{\partial \phi}\delta\phi + \frac{\partial F}{\partial H_i}\delta H_i = 0\,, \tag{1.76}$$

$$\frac{\partial G}{\partial \theta}\delta\theta + \frac{\partial G}{\partial \phi}\delta\phi + \frac{\partial G}{\partial H_i}\delta H_i = 0\,. \tag{1.77}$$

Then, we can express this as the matrix:

$$\begin{pmatrix} \frac{\partial F}{\partial \theta} & \frac{\partial F}{\partial \phi} \\ \frac{\partial G}{\partial \theta} & \frac{\partial G}{\partial \phi} \end{pmatrix} \begin{pmatrix} \delta\theta \\ \delta\phi \end{pmatrix} = - \begin{pmatrix} \frac{\partial F}{\partial H_i}\delta H_i \\ \frac{\partial G}{\partial H_i}\delta H_i \end{pmatrix}, \tag{1.78}$$

and, so

$$\begin{pmatrix} \delta\theta \\ \delta\phi \end{pmatrix} = \frac{-1}{\frac{\partial F}{\partial \theta}\frac{\partial G}{\partial \phi} - \frac{\partial G}{\partial \theta}\frac{\partial F}{\partial \phi}} \begin{pmatrix} \frac{\partial G}{\partial \phi} & -\frac{\partial F}{\partial \phi} \\ -\frac{\partial G}{\partial \theta} & \frac{\partial F}{\partial \theta} \end{pmatrix} \begin{pmatrix} \frac{\partial F}{\partial H_i}\delta H_i \\ \frac{\partial G}{\partial H_i}\delta H_i \end{pmatrix}. \tag{1.79}$$

We know that $\frac{\partial F}{\partial \phi} = \frac{\partial G}{\partial \theta}$ as the derivatives with respect to θ and ϕ commute. The Equation 1.79 is defined generically and can be used to compute the variation $\delta\theta$ and $\delta\phi$ for any energy that depends solely on the orientation of the magnetisation vector and the external field.

1.6.2 Application to tetragonal anisotropy

The anisotropy considered here is the tetragonal anisotropy (Section 1.2.5) up to the second-order, as it can be easily brought back to simple uniaxial anisotropy or cubic anisotropy by setting the parameters accordingly.

The anisotropy and Zeeman energy can then be written as:

$$\begin{aligned} E =& k_1 \sin^2(\theta) + (k_2 + k_2' \cos(4\phi)) \sin^4(\theta) \\ & - \mu_0 M_s H_\parallel \sin(\theta)\cos(\phi - \phi_H) - \mu_0 M_s H_z \cos(\theta)\,, \end{aligned} \tag{1.80}$$

where k_1 is the first-order out-of-plane anisotropy, k_2 the second-order terms, k_2' the second-order terms, including an in-plane anisotropy. M_s the saturation magnetisation, $H_\parallel$ the component of the external field in the xy-plane and H_z the component of the field out of the plane. The angle θ and ϕ represent the orientation of the magnetisation and external field vector, the basis of which is described in Figure 1.11.

The derivation based on Equation 1.79 is shown in Appendix B.2. The exact derivation is not straightforward to understand, thus another approximation is presented where the

in-plane anisotropy term is neglected ($k_2' = 0$). This simplifies the expression to the one given in [77]:

$$\delta\theta = -\frac{1}{\frac{\partial F}{\partial \theta}} \frac{\partial F}{\partial H_i} \delta H_i \tag{1.81}$$

$$= -\frac{-\cos\theta(\cos(\phi)\delta H_x + \sin(\phi)\delta H_y) + \sin(\theta)\delta H_z}{2k_1\cos(2\theta) + 4k_2\sin(\theta)\sin(3\theta) + H_{\parallel}\sin(\theta) + H_z\cos(\theta)}\,, \tag{1.82}$$

$$\delta\phi = -\frac{1}{\frac{\partial G}{\partial \phi}} \frac{\partial G}{\partial H_i} \delta H_i \tag{1.83}$$

$$= -\frac{\sin(\phi)\delta H_x - \cos(\phi)\delta H_y}{H_{\parallel}}\,. \tag{1.84}$$

Based on this finding, we can separate the effects of δH_x and δH_y by applying the external field along the x-axis ($\phi = 0°$) or y-axis ($\phi = 90°$).

1.6.3 Analytical methods

In this section, we introduce the various published analytical expressions that can be used to analyse harmonic Hall methods. To begin, the direct application of the principle introduced in Equation 1.74 is discussed in Section 1.6.3.1. The most common expression used for perpendicular magnetic anisotropy (PMA) samples with a small applied field, as developed by [78, 79], is discussed. The latter was improved by [75, 77], as described in Section 1.6.3.2. This is followed by a short description of the thermal effects, in Section 1.6.3.3. In Section 1.6.3.4, we focus on the implementation by [66, 76, 80], which allows thermal contributions to be taken into account. Finally, in Section 1.6.3.5, the rotation of the field between the hard and easy axes is discussed, taking its limitations into account.

1.6.3.1 Single derivative

Based on the principle shown in Equation 1.74, the expression for calculating the FL and DL effective fields can be derived. The details of the derivation are given in Appendix B.3.

The value of h_{DL} and h_{FL} are then given by:

$$h_{\mathrm{DL}} = \frac{\mathcal{A}_x - \xi\mathcal{A}_y}{1-\xi^2}\,, \qquad h_{\mathrm{FL}} = \frac{\mathcal{A}_y - \xi\mathcal{A}_x}{1-\xi^2}. \tag{1.85}$$

where $\xi = \frac{R_{\mathrm{PHE}}}{R_{\mathrm{AHE}}}$. The quantities $\mathcal{A}_x$ and $\mathcal{A}_y$ are then defined as:

$$\mathcal{A}_x = 2\left(V_{xy}^{2\omega}\Big/\frac{\partial V_{xy}^{1\omega}}{\partial H}\right)\Bigg|_{\mathbf{H}\parallel x} \tag{1.86}$$

$$\mathcal{A}_y = 2\left(V_{xy}^{2\omega}\Big/\frac{\partial V_{xy}^{1\omega}}{\partial H}\right)\Bigg|_{\mathbf{H}\parallel y}\,, \tag{1.87}$$

where $V_{xy}^{n\omega}$ represents the transverse signal of the n harmonic. This expression gives the FL and DL torque when the measured signals are due uniquely to AHE and PHE. The approximation that $\frac{H}{2k_1} \ll 1$ requires the external field to be small compared to the anisotropy field.

1.6.3.2 Double derivative

In this section, we derive one of the most widely used methods for analysing the harmonic Hall signal [5, 75]. This method includes both AHE and PHE contributions and is suitable for samples with PMA when the applied field is small compared to the anisotropy field, with the magnetisation direction remaining close to the z-direction. The details of the derivation are given in Appendix B.4.

The FL and DL torques are given by:

$$h_{\mathrm{DL}} = \frac{\mathcal{B}_x + \xi\mathcal{B}_y}{1-\xi^2}\,, \qquad h_{\mathrm{FL}} = \frac{\mathcal{B}_y + \xi\mathcal{B}_x}{1-\xi^2}\,. \tag{1.88}$$

where $\xi = \frac{R_{\mathrm{PHE}}}{R_{\mathrm{AHE}}}$. The quantities $\mathcal{B}_x$ and $\mathcal{B}_y$ are defined as:

$$\mathcal{B}_x = 2\left(\frac{\partial V_{xy}^{2\omega}}{\partial H} \Big/ \frac{\partial^2 V_{xy}^{1\omega}}{\partial H^2}\right)\Bigg|_{\mathbf{H}\parallel x}, \tag{1.89}$$

$$\mathcal{B}_y = 2\left(\frac{\partial V_{xy}^{2\omega}}{\partial H} \Big/ \frac{\partial^2 V_{xy}^{1\omega}}{\partial H^2}\right)\Bigg|_{\mathbf{H}\parallel y}. \tag{1.90}$$

The difference with the expression of [75] is due to the pre-factor of 2 in the definition of the PHE. Note that the result obtained in the previous section (Equation 1.85) is similar to the solution obtained here. In practice the difference is negligible, as it is not recommended to differentiate experimental signals that contain random noise for a point-by-point extraction of the SOT. Best practice is to fit a parabolic and linear curve to the first and second harmonic signals, from which the derivatives can be easily obtained.

The denominator $1-\xi^2$ causes this solution to be unstable when $\xi^2 \approx 1$. This is referred to in the literature as the PHE 'problem' [81–83]. It was suggested that the PHE correction might be detrimental when $\xi \approx 1$. Focusing on Equation B.46 and Equation B.49 in Appendix B.4, it appears that when $\xi = 1$ both equations are proportional. The matrix is then non-invertible, resulting in the "problem". This could be solved by changing the x and y direction for the measurement and re-deriving the last step of the calculation. The divergence itself appears when an error is present in the determination of $\mathcal{B}_x$ or $\mathcal{B}_y$. This could originate from random uncertainty in the recorded signal or systematic bias originating from different effects, such as ANE.

1.6.3.3 Corrections for thermal effects

The harmonic Hall measurement requires a large current to pass through the sample in order to measure any significant SOT effect. This results in considerable Joule heating, leading to a thermoelectric contribution that is dependent on the thermal gradient. In the Hall bar configuration, the primary thermal gradient is between the film (where heat generation takes place) and the substrate, serving as a heat sink. Thus, the direction of

this gradient is along the z-axis. At the modulation frequency, $\sim 1\,\mathrm{kHz}$, the dynamics of the heat dissipation are fast enough to be considered quasi-static, so that $\nabla T \propto I^2(t)$. The main contributors to the harmonic Hall signal in a single-layer are the ANE and NE (see Section 1.3.2.4). In multilayer systems, the spin Seebeck effect and the ISHE can lead to contributions that follow the same symmetry as the ANE [84]. These will be treated together.

In the case of thin film measurements, the thermoelectric contributions to the transverse (V_{xy}) and longitudinal (V_{xx}) signals are (see Section 1.3.2.4):

$$V_{xy}^{2\omega} = R_{\mathrm{ANE}} I_0^2 m_x + R_{\mathrm{NE}} H_x \tag{1.91}$$

$$= R_{\mathrm{ANE}} I_0^2 \sin(\theta)\cos(\phi) + R_{\mathrm{NE}} I_0^2 H \cos(\phi_H)\,, \tag{1.92}$$

$$V_{xx}^{2\omega} = -R_{\mathrm{ANE}} I_0^2 m_y - R_{\mathrm{NE}} H_y \tag{1.93}$$

$$= -R_{\mathrm{ANE}} I_0^2 \sin(\theta)\sin(\phi) - R_{\mathrm{NE}} I_0^2 H \sin(\phi_H)\,, \tag{1.94}$$

where R_{ANE} is the effective thermoelectric coefficient grouping the Joule heating (containing generation of the thermal gradient and the ANE or the spin Seebeck effect with the ISHE), R_{NE} is the analogue to R_{ANE} but is field dependent, m_i (H_i) is the magnetisation (external field) along $i = x, y, z$, or in spherical coordinates: θ, ϕ and ϕ_H the angles representing the magnetisation and field directions, and I_0 the current density amplitude. The $I^2(t)$ dependence indicates that the contribution is on the second harmonic and the $\sin(\theta)\cos(\phi)$ dependence of the ANE contribution to the transverse harmonic Hall signal is similar to that of the DL torque.

The presence of thermoelectric contributions can be confirmed experimentally by measuring the longitudinal second harmonic voltage ($V_{xx}^{2\omega}$). As the thermal gradient is along the z-axis, the thermoelectric effect will be present in both longitudinal and transverse voltages, rotated by 90°. We note that it is important to take into account the noise difference when comparing the longitudinal and transverse components of the thermoelectric

contribution. The V_{xx} input of the lock-in amplifier is usually set at a higher input range due to the isotropic Ohmic resistance contribution reducing the signal-to-noise ratio. The thermoelectric contribution can then be hidden by random noise leading to the wrong conclusion that there is no thermoelectric contribution.

The single and second derivative methods, as presented here, do not integrate the thermoelectric effects. However, a simple correction can be implemented by measuring both longitudinal and transverse contributions and defining the corrected first and second harmonic signals signal:

$$V_{x(y)}^{\mathrm{corr}\,1\omega} = V_{xy}^{1\omega}\Big|_{\mathbf{H}\parallel x(y)} \,, \tag{1.95}$$

$$V_{x}^{\mathrm{corr}\,2\omega} = V_{xy}^{2\omega}\Big|_{\mathbf{H}\parallel x} + \frac{w}{l}\, V_{xx}^{2\omega}\Big|_{\mathbf{H}\parallel y} \,, \tag{1.96}$$

$$V_{y}^{\mathrm{corr}\,2\omega} = V_{xy}^{2\omega}\Big|_{\mathbf{H}\parallel y} \,, \tag{1.97}$$

where $V_i^{\mathrm{corr}\,n\omega}$ are the corrected signal for the n-th harmonic and a field applied along i. $V_{xy(xx)}^{n\omega}\Big|_{\mathbf{H}\parallel i}$ is the measured signal along the transverse (xy) or longitudinal (xx) direction for the n-th harmonic and a field applied along i. w and l are respectively the width and length of the Hall bar that correct the change in signal intensity due to the Hall bar geometry. The method described above can be used without additional modification to obtain the FL and DL torque. This correction is not ideal, as it does not take into account the contribution from ρ_{AMR}, as defined in Equation 1.45 and as illustrated in Chapter 2.

Neglecting the thermoelectric effects in the differential methods, when PHE is absent, will result in an absolute error on the DL coefficient of:

$$h_{\mathrm{DL}}^{\mathrm{ANE\ neglected}} - h_{\mathrm{DL}} = \frac{2k_1 R_{\mathrm{ANE}}}{R_{\mathrm{AHE}}} \,, \tag{1.98}$$

where $h_{\mathrm{DL}}^{\mathrm{ANE\ neglected}}$ is the estimation of the DL effective field when ANE is neglected and h_{DL} is the real value.

1.6.3.4 Applied fields higher than the anisotropy field

An alternative method to determine the SOT field is to apply an in-plane field larger than the anisotropy field, $H_k = 2k_1 + 4k_2$. In this case, one can easily demonstrate from Equation B.9 and Equation B.10 in Appendix B.2 that the magnetisation is fully in-plane ($\theta = \frac{\pi}{2}$). From Equation 1.81 and Equation 1.83, the variation of the magnetisation angle becomes:

$$\delta\theta = \frac{\cos(\phi_H)h_{\mathrm{DL}}}{H_{\mathrm{ext}} - H_k}\,, \quad \delta\phi = \frac{\cos(\phi_H)h_{\mathrm{FL}}}{H_{\mathrm{ext}}}\,. \tag{1.99}$$

In this situation, both $\delta\theta$ and $\delta\phi$ are proportional to $\cos(\phi_H)$. This implies that only the field applied along the x-axis contains relevant information. The first harmonic is constant because there is no further magnetisation evolution.

The second harmonic is given by [85]:

$$\begin{aligned} V_{xy}^{2\omega} =& \frac{1}{2}R_{\mathrm{AHE}}\frac{h_{\mathrm{DL}}}{H_k - H_{\mathrm{ext}}}I_0^2 + R_{\mathrm{ANE}}I_0^2 + R_{\mathrm{NE}}H_{\mathrm{ext}}I_0^2 \\ &+ \frac{1}{2}R_{\mathrm{PHE}}\frac{h_{\mathrm{FL}}}{H_{\mathrm{ext}}}I_0^2\,, \end{aligned} \tag{1.100}$$

$$V_{xx}^{2\omega} = 0\,, \tag{1.101}$$

where the factor $\frac{1}{2}$ originates from the demodulation process. Contrary to the low-field approach, the FL contribution originates solely from the PHE, while the DL contribution depends on the AHE. It is possible to separate the FL and DL contributions based on their field dependence.

Alternatively, it is possible to apply the field along $\phi_H = 45°$ which gives:

$$V_{xy}^{2\omega} = \frac{1}{2\sqrt{2}}R_{\mathrm{AHE}}\frac{h_{\mathrm{DL}}}{H_k - H_{\mathrm{ext}}}I_0^2 + \frac{R_{\mathrm{ANE}}}{\sqrt{2}}I_0^2 + \frac{R_{\mathrm{NE}}}{\sqrt{2}}H_{\mathrm{ext}}I_0^2\,, \tag{1.102}$$

$$V_{xx}^{2\omega} = -\frac{1}{2\sqrt{2}}R_{\mathrm{PHE}}\frac{h_{\mathrm{FL}}}{H_{\mathrm{ext}}}I_0^2 - \frac{R_{\mathrm{ANE}}}{\sqrt{2}}I_0^2 - \frac{R_{\mathrm{NE}}}{\sqrt{2}}H_{\mathrm{ext}}I_0^2\,. \tag{1.103}$$

The FL and DL contributions are then conveniently separated into two independent signals.

Unlike the previous differential approach, this method naturally accounts for thermoelectric contributions without the need for additional corrections.

The applied field is usually directed at a small (typically 5°) angle from the sample surface to ensure the sample remains in a single domain state at all field magnitudes. This reduces drastically the accuracy of the extracted SOT efficiency (see Chapter 2), as the magnetisation is no longer perfectly in-plane, which is a condition assumed when deriving the analytical expression.

1.6.3.5 Rotation of magnetic field

All the above methods saturate the sample along the easy axis before applying a field perpendicular to it to measure the rotation of the magnetisation. To ensure a coherent rotation and a single domain so that the macrospin approximation remains valid, it is better to apply a large, constant in magnitude, field and rotate it from the easy to the hard axis [65, 76, 86]. This method combines the advantages of both previous methods. At $\theta_H \ll 1$ this is equivalent to the differential approach stated above, with the z-component of the applied field adding to the anisotropy. At θ angles around 90° (i.e. close to the hard plane), this method is reminiscent of the high-field approach. The main drawback of the method is that it necessitates scanning both the θ_H and field amplitudes.

In this section, we treat the case where $k_2' = 0$ and so $\phi_H = \phi_M = \phi$, where ϕ_H (ϕ_M) is the in-plane angle of the external field (magnetisation). It is then useful to rewrite the SOT field in a rotated system as described in Figure 1.12. Contrary to the previous scenario, it is not always possible to analytically calculate the position of the magnetisation θ as a function of the external field. Two independent cases can then be treated. The first is $\theta_H \ll 1$ where the magnetisation will stay close to the easy axis. The second is when the external field is large enough to almost align the magnetisation with the external field. The misalignment of the two is defined by $\Delta\theta = \theta_M - \theta_H \ll 1$.

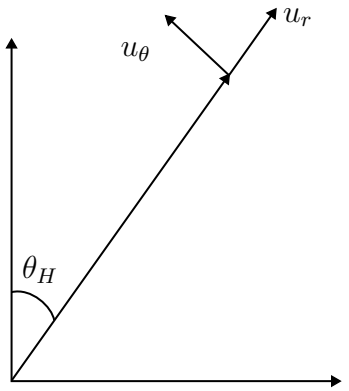

Figure 1.12: Field rotation analysis coordinate system

The first case to consider is when the field is applied close to the easy-axis (z). Taking $\theta_H \ll 1$, from Equation B.9 we obtain $\theta \ll 1$, which can be approximated by keeping only the first-order terms:

$$0 = 2k_1 - H\theta_H + H\theta\,, \tag{1.104}$$

where k_1 is the first-order anisotropy, H the external field strength, θ_H the magnetic field angle and θ the magnetisation angle. Rearranging the terms we obtain:

$$\theta = \frac{H}{2k_1 + H}\theta_H\,, \quad \text{and} \quad \Delta\theta = \theta - \theta_H = \frac{-2k_1}{2k_1 + H}\theta_H\,. \tag{1.105}$$

Using these expressions, we can express the variation of the magnetisation $\delta\theta$. Reusing Equation 1.81, we obtain:

$$\delta\theta = \frac{-\cos(\phi)\delta H_x + \sin(\phi)\delta H_y + \frac{H\theta_H}{2k_1+H}\delta H_z}{2k_1 + H}\,. \tag{1.106}$$

Injecting the expression for the bilayer SOT field (Equation 1.73):

$$H_{\mathrm{SOT}} = (\cos(\theta)h_{\mathrm{DL}}, h_{\mathrm{FL}}, -\sin(\theta)\cos(\phi)h_{\mathrm{DL}})\,, \tag{1.107}$$

the variation of θ can be written as:

$$\delta\theta = \frac{-\cos(\phi)h_{\mathrm{DL}} + \sin(\phi)h_{\mathrm{FL}}}{2k_1 + H}\,, \tag{1.108}$$

where h_{DL} and h_{FL} represent the DL and FL effective field. $\phi = \phi_H$ corresponds to the in-plane field angle and magnetisation.

The second case is $H \gg k_1, k_2$. We start by defining the difference between the magnetisation equilibrium position (θ) and the field direction (θ_H), as $\Delta\theta = \theta - \theta_H$. The details of the derivation are given in Appendix B.5.

We obtain for $\Delta\theta$:

$$\Delta\theta = -\frac{k_1 \sin(2\theta_H) + 4k_2 \sin^3(\theta_H)\cos(\theta_H)}{2k_1 \cos(2\theta_H) + 4k_2 \sin(\theta_H)\sin(3\theta_H) + H}\,. \tag{1.109}$$

The variation of the magnetisation angle due to the action of the SOT ($\delta\theta$) is given by:

$$\delta\theta = \frac{\cos(\phi)H_{\mathrm{DL}} - (\cos(\theta_H) - \Delta\theta\sin(\theta_H))\sin(\phi)H_{\mathrm{FL}}}{H_{\mathrm{eff}} - 4\Delta\theta(k_1\sin(2\theta_H) + k_2(2\sin(4\theta_H) - \sin(2\theta_H)))} \tag{1.110}$$

$$= \frac{\cos(\phi)H_{\mathrm{DL}} - (\cos(\theta_H) - \frac{k_1\sin(2\theta_H) + 4k_2\sin^3(\theta_H)\cos(\theta_H)}{H_{\mathrm{eff}}}\sin(\theta_H))\sin(\phi)H_{\mathrm{FL}}}{H_{\mathrm{eff}} - 4\frac{(k_1\sin(2\theta_H) + 4k_2\sin^3(\theta_H)\cos(\theta_H))(k_1\sin(2\theta_H) + k_2(2\sin(4\theta_H) - \sin(2\theta_H)))}{H_{\mathrm{eff}}}} \tag{1.111}$$

$$\approx \frac{\cos(\phi)H_{\mathrm{DL}}}{H_{\mathrm{eff}}} - \frac{\cos(\theta_H)\sin(\phi)H_{\mathrm{FL}}}{H_{\mathrm{eff}}}\,. \tag{1.112}$$

A simplification was performed to obtain Equation 1.112 by assuming $\Delta\theta \ll 1$, thus $\Delta\theta$ is negligible.

The expression considering all the terms is complicated and lends itself only to numerical calculations where a minimisation algorithm does a better job without approximations. The simplified expression (Equation 1.112) is easier to comprehend and highlights the contribution inversely proportional to H_{eff} of the SOT which is a result of the competition between the SOT field with the anisotropy and external fields. However, the approximation is not able to model an arbitrary combination of applied and anisotropy fields. We illustrate this in Figures 1.13 and 1.14.

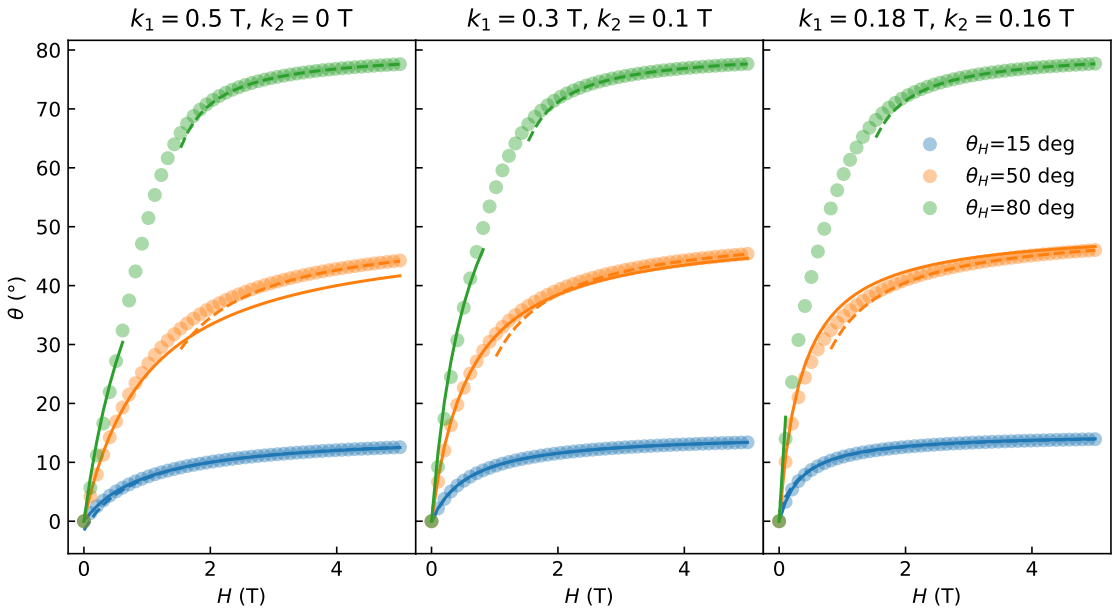

Figure 1.13: Value of magnetisation angle θ for different values of anisotropy and applied field directions. The points correspond to the numerically solved equation. The continuous lines are the analytical low angle approximations, and the dashed lines are the analytical high angle approximations. Both analytical approximations show large errors close to $H_k = 2k_1 + 4k_2 = 1\,\mathrm{T}$ when the field is applied close to the hard plane direction.

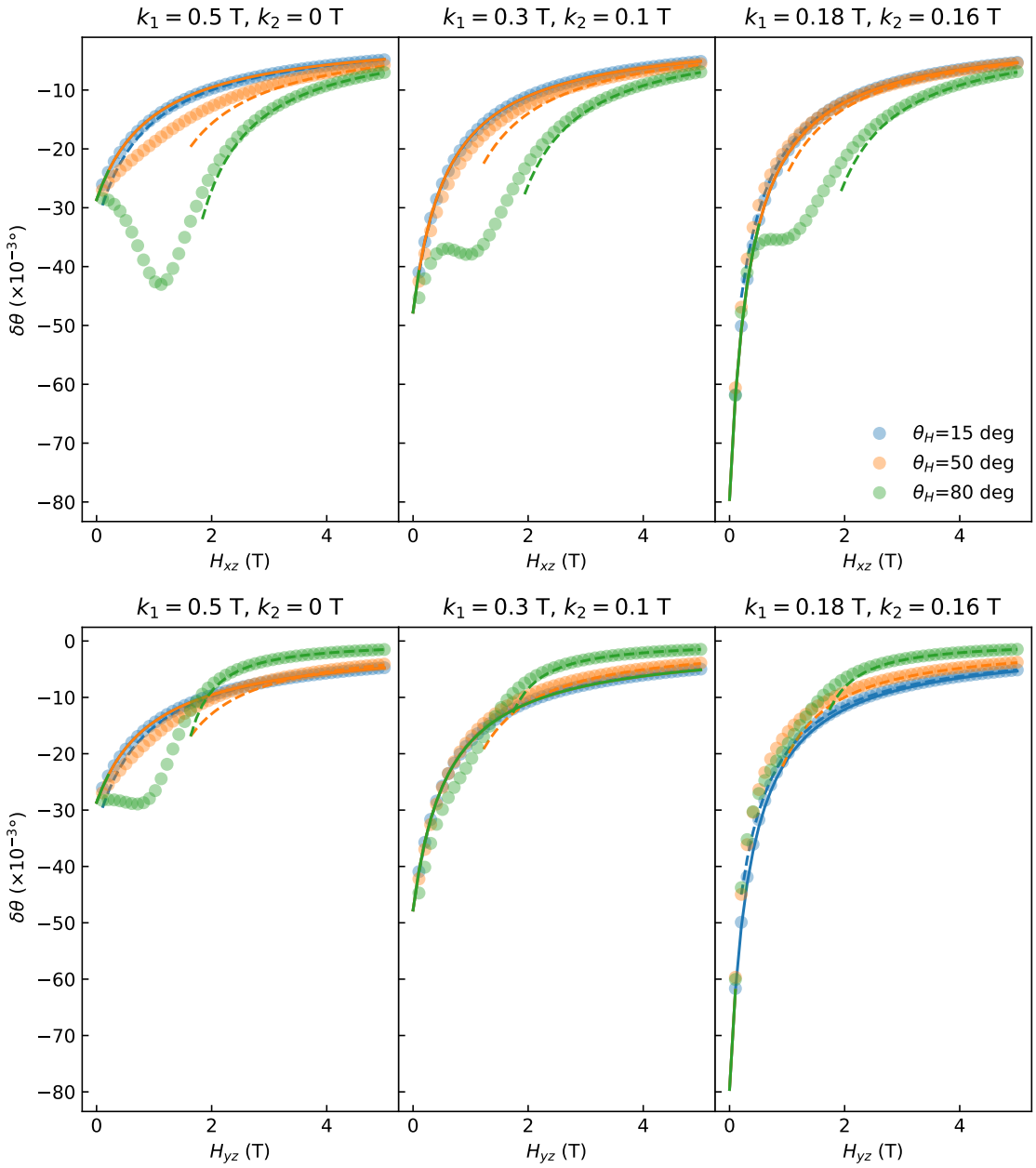

Figure 1.14: Value of variation of magnetisation angle $\delta\theta$ due to the SOT for the different values of anisotropy (k_1, k_2) and applied field angles, compared to the out-of-plane axis (θ_H). The points correspond to the numerically solved equation. The continuous lines are the analytical low angle approximations, and the dashed lines are the analytical high angle approximations. Both FL and DL efficiency were set to $0.5\,\mathrm{mT}$. *Both analytical approximations show large errors close to* $H_k = 2k_1 + 4k_2 = 1\,\mathrm{T}$ *when the field is applied close to the hard plane direction.*

1.6.3.6 Overview of the different analytical methods

We have seen in previous sections that various analytical methods exist for analysing harmonic Hall signals. In particular, for the variation of magnetisation due to the SOT field, as shown in Section 1.6.2, we can easily derive the variation of angles $\delta\theta$ and $\delta\phi$ due to the SOT field, even in the presence of the full expression for tetragonal anisotropy.

Looking at the low-field solution (Section 1.6.3.1 and Section 1.6.3.2), we were able to simplify and solve for the magnetisation position, only when the first-order anisotropy was present and when the field was applied in-plane. It remains possible to consider magnetisation variations up to the second-order. However, the equation for magnetic equilibrium is solved only up to the first-order. Applying the magnetisation variation to the second-order while solving the equilibrium position only in the first-order is not recommended. The direction of the magnetisation vector, θ, would be inaccurate, potentially introducing a larger error in the magnetisation variation.

In the case of a large field applied exactly in-plane (Section 1.6.3.4), it is possible to correctly determine the magnetisation position. This makes it possible to use the second-order expression for the variation in magnetisation due to the SOT.

The last scenario we discussed (Section 1.6.3.5) was to rotate the field between the hard and easy axes. This is preferable for multiple reasons. It will ensure a single domain and a better coherent transition of magnetisation. However, this can only be solved in two particular cases. The first is when the direction of the external field is very close to the easy axis, so $\theta_H \ll 1$. The second case is when the external field is large enough that the difference between the direction of the magnetisation and the field vector is $\Delta\theta_H \ll 1$. These are difficult to realise. For the first case, only a limited range of magnetisation variations is accessible. This causes similar problems to those encountered with the low-field method. In the second case, very high fields are required, which would

make it difficult to measure SOT-induced signals that are naturally damped by the now increased anisotropy plus applied field. The SOT contribution may be hidden in the noise. Therefore, this last method is only suitable when the magnetisation position is solved numerically.

1.7 Thesis outline

The aim of this thesis was to improve the current methods for measuring SOT in novel materials, specifically in single-layer films. The main focus was on the harmonic Hall methods, which provide a framework for measuring SOT. This was achieved by addressing gaps in current knowledge and developing new methodologies for acquiring and analysing harmonic Hall signals. The background, theory and mathematics underpinning this work were presented in the introduction. The results of this thesis are divided into three research chapters:

Chapter 2: Evaluation of contemporary analytical methods to determine SOT using the harmonic Hall measurement

To evaluate the precision and accuracy of the contemporary analytical harmonic Hall methods, a single macro-spin numerical model was compared to established analytical methods. The analysis considered a wide range of materials under different experimental conditions, taking into account both sample-specific factors (anisotropies, magneto-galvanic and thermogalvanic effects) and setup-related adjustments (sample positioning, presence of distortion in the current source). Previous studies have partially covered the sample-related effects and neglected the impact of the experimental setup-related variables. The validity ranges of each analytical method, in relation to various corrections, were also discussed.

Chapter 3: Accurate measurement of SOT in a single layer using Mn_2Ru_xGa as a test candidate

This research chapter aimed to measure the SOT contribution in a single-layer MRG sample, separating intrinsic and extrinsic contributions. Due to its compensated ferrimagnetic nature and high spin polarisation, MRG is a good candidate for spintronic applications. The MRG crystal structure presents a broken inversion symmetry, which should theoretically allow for intrinsic contributions to the SOT. The two potential origins of the SOT (interfacial and intrinsic) are separated based on the symmetry argument. This method was calibrated against a well-known material, a CoPt multilayer to ensure its accuracy. Two multilayers of CoPt were used: an asymmetric sample with a known significant SOT contribution and a symmetric layer with a known minimal SOT contribution.

Chapter 4: Elimination of thermoelectric effects in the harmonic Hall method: A new geometry pattern for spin-orbit torque measurement

A novel harmonic Hall geometry allowing rotating current was designed to eliminate thermoelectric effects at the sample level, with the aim of making it system independent. An analytical model and numerical simulation were used to investigate if using a rotating current can conserve the information originating from the SOT, while eliminating the thermoelectric contributions. A finite element model was used to determine if the proposed geometry allows the creation of a rotating current in the area of interest. Finally, this new geometry was tested experimentally against a standard Hall bar on a CoPt multilayer sample. The caveats of this new setup are discussed in relation to the noise budget and the quality of lithography required.

CHAPTER 2

Evaluation of contemporary analytical methods to determine spin orbit torque using the harmonic Hall measurement

2.1 Introduction

The harmonic Hall method has been widely used for the determination of spin orbit torque (SOT) in a variety of materials. This analytical method aims to determine the SOT effective field, e.g. the field-like (FL) and damping-like (DL) fields, by measuring the perturbation of the magnetisation vector induced by this field. Multiple iterations of this method have been implemented in the literature over the years. The first harmonic Hall method published omitted the planar Hall effect (PHE), involving only the anomalous Hall effect (AHE) and the FL torque [78]. Other transport contributions were included in further iterations to improve the accuracy of the analysis. The first of these refinements involved adding the PHE correction [66, 75]. This was followed by the addition of the spin Seebeck effect (SSE) and spin Hall magnetoresistance (SMR) [87]. Following on from this work, it became evident that thermoelectric effects were contributing with a similar order

of magnitude to the DL signal recorded. New measurement methods involving external fields higher than the anisotropy field subsequently emerged to address this, separating the thermoelectric contribution from the SOT [76, 88]. The estimation of the anomalous Nernst effect (ANE) effect is also addressed by recording the longitudinal voltage during harmonic Hall measurements [85].

Few papers in the literature have studied the efficiency of the different harmonic Hall methods for detecting the FL and DL torques. Some studies have focused on the shape of the Hall bar device, due to the width of the contact probe affecting the SOT value [89]. More recently, the need for the PHE correction has come under scrutiny, where it has been suggested that the PHE correction may be unnecessary or detrimental [82, 83]; however, this has not been substantiated with any concrete evidence. Furthermore, higher-order anisotropic coefficients and the z-component of the external field were included in the analytical method by [77]. The z-component often appears within the high-field harmonic Hall methods because the field is applied slightly off the sample-plane to maintain a single magnetic domain state. Finally, the higher order of the SOT field has been considered as well as the feed back loop existing on the DL torque due to the initial magnetisation modification [90].

Due to the wide diversity of methodologies currently used in the literature, a review of the most commonly used analytical methods was performed. These methods can be largely classified into two families: the high-field methods [88, 91–97] and the differential (low field) methods [82, 98–111]. The different variations of these methods are detailed in Table 2.1. With these numerous variations in the harmonic Hall method, there is a need to evaluate the accuracy of the FL and DL determination amongst these methods.

In order to address this problem, a numerical simulation of the harmonic Hall signal based on a single macrospin approximation was developed. This sets the validity condition, as the magnetic state needs to be simple enough to be described by a single macrospin, e.g.

Table 2.1: Summary of published analytical methods to determine harmonic Hall signals, separated into two larger families: the differential method and the high-field method.

Model	Field		Direction	Correction	
	Intensity	Direction	probed	PHE	Thermal
Differential					
initial	low	x, y	V_{xy}	✓	
no PHE	low	x, y	V_{xy}		
thermal correction	low	x, y	V_{xy}, V_{xx}	✓	✓
thermal correction no PHE	low	x, y	V_{xy}, V_{xx}		✓
High-field					
x	high	x	V_{xy}	✓	✓
xy	high	xy	V_{xy}	✓	✓
x,y	high	x, y	V_{xy}, V_{xx}	✓	✓

ferromagnetic or collinear ferrimagnetic state. Only coherent rotation can be modelled, avoiding the hysteretic region. Thus, the use of a numerical simulation allowed us to further reduce the number of assumptions in the model. This allowed a wide range of experimental conditions and transport properties to be taken into account. These transport effects include AHE, PHE, anisotropic magnetoresistance (AMR), Hall effect (HE), and linear magnetoresistance (LMR), which from a symmetry argument should occur in all magnetic thin-films. Additionally, this numerical model is capable of handling both first and second order anisotropic terms. The model also allows for the adjustment of field direction using three Euler angles in the $\theta_x, \theta_y, \theta_z$ convention. This ensures all possible orientations of the field when the field is applied along different directions during an experiment. When the field is applied along a single direction, two coefficients would be sufficient, as there are only two degrees of freedom. In this study for the differential method and the high field x, y method, the field is applied along two directions, requiring three degrees of freedom. The distortion of the current source is also taken into account. Finally, the thermoelectric effects are incorporated, e.g. ANE (which shares the same symmetry as SSE) and Nernst effect (NE). The numerical model was used to generate the harmonic Hall signals, which were subsequently analysed via each analytical method.

The estimation of the FL and DL values were then compared with the original input into the numerical model in order to establish the precision and accuracy of each analytical method. Assumptions used in the derivation of the analytical method are rarely exactly met in real experiments. While it is natural to assume that a small deviation from the approximation case will not cause a large error, this has never been tested rigorously. This work allows us to answer the question: Can common analytical methods be used when aiming for high accuracy in SOT field detection?

Additional assumptions are required for the analytical solution, as compared with the numerical simulation. For the analytical solution within the differential family, only first-order terms of the anisotropy are included. For all analytically solved solutions, the field is considered to be applied exactly in-plane. Only a handful of transport effects are usually considered, such as AHE, PHE, thermal effects, including SSE and ANE, neglecting the AMR and field-dependent effects.

The expressions for the different analytical methods are detailed below, their derivations can be found in Section 1.6.3. For the differential method family, a first harmonic signal ($V^{1\omega}$) and second harmonic signal ($V^{2\omega}$) are defined without thermal corrections:

$$V^{1\omega}_{x(y)} = V^{1\omega}_{xy}\Big|_{\mathbf{H}\parallel x(y)} \quad \text{and} \quad V^{2\omega}_{x(y)} = V^{2\omega}_{xy}\Big|_{\mathbf{H}\parallel x(y)} \,, \tag{2.1}$$

and for the differential method with thermal corrections (Section 1.6.3.3):

$$V^{1\omega}_{xy} = V^{1\omega}_{xy}\Big|_{\mathbf{H}\parallel x(y)} \,, \qquad V^{2\omega}_{x} = V^{2\omega}_{xy}\Big|_{\mathbf{H}\parallel x} + V^{2\omega}_{xx}\Big|_{\mathbf{H}\parallel y} \quad \text{and} \quad V^{2\omega}_{y} = V^{2\omega}_{xy}\Big|_{\mathbf{H}\parallel y} \,. \tag{2.2}$$

where $V^{n\omega}_{i}$ are the corrected signal for the n-th harmonic and a field applied along i. $V^{n\omega}_{xy(xx)}\Big|_{\mathbf{H}\parallel i}$ is the measured signal along the transverse (xy) or longitudinal (xx) direction for the n-th harmonic and a field ($\mathbf{H}$) applied along $i = x, y$.

As the differentiation of experimental data should be avoided, due to the resulting increase in high-frequency noise, the analysis is done by fitting the first harmonic ($V^{1\omega}$) using a

quadratic polynomial and the second harmonic ($V^{2\omega}$) with a linear polynomial. Then two coefficients are defined $\mathcal{B}_{x(y)} = \frac{a^{2\omega}_{x(y)}}{a^{1\omega}_{x(y)}}$ where a is the slope and curvature determined by linear and quadratic fit. Each of these signals is fitted independently and the four corresponding χ^2 values are then saved. The FL and DL coefficients are then defined by:

$$h_{\mathrm{DL}} = \frac{\mathcal{B}_x + \xi\mathcal{B}_y}{1-\xi^2}\,, \tag{2.3}$$

$$h_{\mathrm{FL}} = \frac{\mathcal{B}_y + \xi\mathcal{B}_x}{1-\xi^2}\,, \tag{2.4}$$

where $\xi = \frac{R_{\mathrm{PHE}}}{R_{\mathrm{AHE}}}$, in the case where the PHE is neglected, we set $\xi = 0$.

The high-field method consists of a fit of the expected signal on the second harmonic, when the field is higher than the anisotropy field:

$$\begin{aligned} V^{2\omega}_{xy} =& \frac{1}{2}R_{\mathrm{AHE}}\cos(\phi_H)\frac{h_{\mathrm{DL}}}{h_k - H} + \frac{1}{2}R_{\mathrm{PHE}}\cos(2\phi_H)\cos(\phi_H)\frac{h_{\mathrm{FL}}}{H} \\ &+ R_{\mathrm{ANE}}\cos(\phi_H) + R_{\mathrm{NE}}H\cos(\phi_H)\,, \end{aligned} \tag{2.5}$$

$$V^{2\omega}_{xx} = -\frac{1}{2}R_{\mathrm{PHE}}\sin(2\phi_H)\cos(\phi_H)\frac{h_{\mathrm{FL}}}{H} - R_{\mathrm{ANE}}\sin(\phi_H) - R_{\mathrm{NE}}H\sin(\phi_H)\,, \tag{2.6}$$

where R_{AHE}, R_{PHE} and H_k are determined independently and fixed during fitting. h_{DL}, h_{FL}, R_{ANE} and R_{NE} are left free. The full set of data are always fitted together and χ^2 is reported.

2.1.1 Research questions and approach

This study aims to investigate the reliability and validity of published analytical techniques to determine the SOT. Specifically, an evaluation of these analytical methods was performed to determine the effectiveness of analysing harmonic Hall signals that do not meet the initial derivation assumptions. The null hypothesis of this research was that the DL and FL estimations will not depend on any of the unaccounted parameters normally present in the standard magnetic materials and the experimental setup.

A numerically solvable macrospin approximation was used, which assumes a single domain ferromagnetic or ferrimagnetic state. This macrospin assumption is used in the published analytical models under study, so the use of the numerical method does not add further requirements to the samples studied. This numerical method allows for the use of a wider range of experimental conditions, allowing for field offsets, additional transport effects and other spurious signals, such as source distortion and thermoelectric effects. By adjusting these parameters, a multitude of harmonic signals can be generated, which can be analysed using the analytical methods published in the literature (Table 2.1). The null hypothesis will be tested by comparing the real and estimated FL and DL torques (the estimation error) using, first, a single variable dependence test and second, a multiple variable dependence by linear regression (generalised linear model (GLM)) on the estimation error.

2.2 Methodology

Datasets required for this evaluation were created using a numerical simulation. First, the parameter space was defined; then the numerical model (Appendix C) was used to create two series of simulated sample datasets (single variable dependences and global datasets). Harmonic Hall signals were then extracted from these simulated samples. For each method of analysis, the harmonic Hall signals were processed, in addition to the estimated FL and DL torque. The χ^2 residual was recorded. A flowchart of the process to create these datasets can be seen in Figure 2.1.

The estimation error was defined as the difference between the FL and DL estimated value and the value given to the numerical model. A correlation analysis between goodness of fit (vertical regression χ^2 value) estimation error was performed, which was repeated for each analytical method. Then examples of the possible errors arising from this approach are discussed.

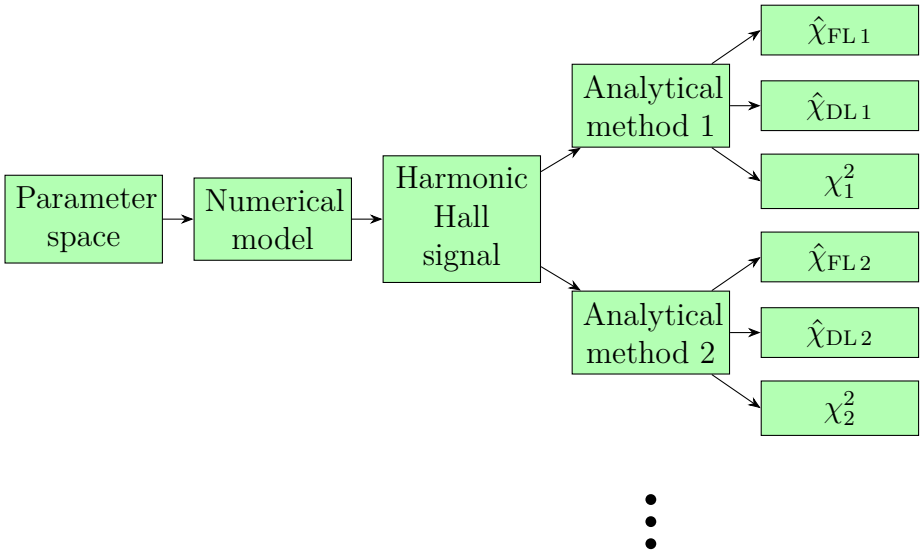

Figure 2.1: Flowchart of the process for generating the dataset series using the numerical model.

The effect of each parameter on the estimation error for each method was then analysed (Figure 2.2). First, by looking at the single variable dependencies and identifying which parameter alone can influence the estimation error. This led to a correction of the field offset compared to the sample plane being tabulated for the high-field method. Finally, the global dataset was analysed with a GLM regression. The effects of the different parameters and interactions were detailed. In this work we defined the interactions as the product of multiple parameters.

2.2.1 Creation of datasets by simulation

2.2.1.1 Parameter space specification

In order to find the different dependencies of each published analytical method on the relevant parameters, a simulation model was required to convert the parameters into harmonic Hall signals. These can then be fitted individually using the harmonic Hall methods presented in Table 2.1. These parameters reflect the vast majority of effects that are present in thin film magnetic materials. They were also defined as the requirements

for fitting Mn_2Ru_xGa within Chapter 3. Further parameters included in the simulation are related to common issues within an experimental setup that introduce error, i.e. misalignment of the sample rotation axis versus the field direction and distortion from the current source and electrical noise.

Multiple datasets were created via numerical simulation (further details in Section 2.3.2). The first dataset series were for the single variable dependence analysis. Parameters were kept at the default value presented in Table 2.2 and a single parameter was varied between its minimum and maximum value (over 50 discrete points). The second series, the global dataset, was designed to capture the different interactions between the parameters; hence a random sampling was employed using a uniform distribution for all variable parameters; a total of one million points was included in this series. This dataset was partitioned into a training dataset (800 000 points) and a test dataset (200 000 points).

To do so, an appropriate a range for each parameter was defined. This was challenging, as the range required had to be large enough to show any significant effect, as well as being representative of a large range of materials. However, the range must also be reasonable, so as not to show errors that were unlikely to occur in real experiments, while additionally being small enough to reduce the simulation space/time. The parameters and their range included within the study are shown in Table 2.2.

At first, the range of the ANE may appear to be large; however, as shown in Chapter 3, the Mn_2Ru_xGa Heusler alloys have an ANE in the magnitude of $2 \times 10^{-21}\,\Omega\,A^{-1}\,m^3$, whereas the range here is from -3 to $3 \times 10^{-21}\,\Omega\,A^{-1}\,m^3$. The range of the NE was kept similar to the parameter range of the ANE. Even though, in practice, the NE was expected to be much smaller, this illustrates how a linear dependence of the field will affect the error.

ρ_{xx0} and ρ_{AHE} were fixed respectively at $1.126 \times 10^{-6}\,\Omega\,m$ and $-1.268\,\Omega\,m$, even if these can vary drastically between samples, as this renormalised the harmonic Hall signal and consequently does not give any insight into the actual quality of the DL or FL extraction

from the harmonic Hall method.

In each sample, the current density was set to $1 \times 10^{10}\,\mathrm{A\,m^{-2}}$. The thin film thickness was set to 10 nm. The Hall bar width and length were set to 10 µm. A real Hall bar will have a longer length; however, numerically it doesn't affect the result and avoids the need to rescale the longitudinal voltage for the thermal correction in the differential method described in Section 1.6.3.3.

2.2.1.2 Numerical model

The numerical model used in this study was based on macrospin simulations, where the magnetisation direction is determined by minimising the magnetic energy:

$$E_m = k_1 \sin^2(\theta) + k_2 \sin^4(\theta) - (\mathbf{H_0} + \mathbf{H}_{\mathrm{SOT}}) \cdot \mathbf{m}\,, \tag{2.7}$$

where k_1 and k_2 represent respectively the reduced first and second order anisotropic terms express in Tesla, $\mathbf{m}$ is the reduced magnetisation, $\mathbf{H_0}$ correspond to the external magnetic field and $\mathbf{H}_{\mathrm{SOT}}$ correspond to the effective SOT field.

Next, the SOT field was added to the external field to find the new equilibrium position. The variation of magnetisation under SOT was assumed to be small enough that the DL field was kept constant despite the change in the magnetisation vector.

To obtain the harmonic Hall signal, the model starts by using a sinusoidal current. For each different value of this sine wave, it computes the new position of the magnetisation vector due to the SOT, obtaining a magnetisation vector as a function of time ($\mathbf{m}(\omega t)$). Having the current and magnetisation vector as a function of time, a magnetogalvanic tensor can then be used to obtain the electric field inside the sample at any given time. This electric field was then multiplied by the length and width of the Hall bar to obtain the longitudinal and transverse voltage. These voltages are then demodulated numerically by projecting them on cosine and sine function as defined in Equation 2.9 in order to obtain a

harmonic signal comparable to the experimental signal obtained with a lock-in amplifier, as shown here:

$$V_{\cos}^{n\omega} = \frac{1}{\pi}\int_0^1 V(t)\cos(2\pi nt)\,\mathrm{d}t \ , \tag{2.8}$$

$$V_{\sin}^{n\omega} = \frac{1}{\pi}\int_0^1 V(t)\sin(2\pi nt)\,\mathrm{d}t \ , \tag{2.9}$$

where n corresponds to the harmonic being demodulated.

2.2.2 Analysis for the evaluation

2.2.2.1 Single variable dependence

To understand the single-parameter influence of the FL and DL estimations for each of the analytical methods. All parameters were set to a default value, as shown in Table 2.2. And then one parameter was varied at a time, resulting in the creation of a sample dataset with only 50 points. All parameters which have a strong influence on both the FL and DL estimations were reported. This method does not take into account interactions between parameters, but gives an insight into which parameter on its own could significantly bias the result.

The angle offset (θ_y) for the high-field methods was found to have a strong and non-linear response. Thus a further transformation was required for the GLM analysis, which was performed by tabulating a correction factor based on the single variable dependence analysis.

2.2.2.2 Generalised linear model

A regression analysis was performed using a GLM (Python, Statsmodels, version 0.14.4) to analyse the FL and DL estimation errors in the global dataset. A GLM assumes linear dependence between the response variable (the FL and DL estimation error) and the input variables (the parameters given to the numerical model, see Table 2.2). However, higher

order terms (of a single parameter and interactions) can be modelled by multiplying multiple parameters together and considering it as another independent variable.

This analysis does not take into account the real analytical expression that leads to the error, but gives an approximation of the error functional shape. The level of detail in this approximation depends only on the number of parameter combinations considered (product, ratio, power). At best, this is an approximation to estimate the first Taylor expansion coefficients of the analytical error functions. The results of the GLM give a list of parameters that influence the model and which need to be considered for improving the result.

To run the GLM, a set of parameters to include must be defined that affect the FL and DL error distribution. A standard approach would be to perform a full analysis of all of the parameters and then perform model reduction by removing one parameter at a time in the order of least significance. This step can be repeated until there is a reduction in model fit (e.g. pseudo-R-square). Due to the size of the training dataset (800 000 points), a full model with complete interactions could not be performed due to limitations of available computing power.

For the low-field methods, up to second order parameters were considered. This gave 105 parameters (primary and interactions) to include. However, at high-field, the fit was poor due to non-linearities and higher-order terms were required to improve the model fit. Within the high-field GLM, all three-way interactions and added two-way interactions with one of the parameters being of higher order (up to 6th order) were included. This brought the number of potential parameters in the model to >1000. For the differential method, rare outliers were strongly influencing the process. Those outliers have been filtered by removing the 0.2% of highest values. Those points corresponded to a value where only the second order anisotropy was present $k_1 \approx 0$. This was not necessary for the high-field method due to the different evaluation of the GLM residual width, which is detailed below.

A genetic algorithm was used to determine parameters and interactions for inclusion within the final model. Here, we define a 'key parameter' as a parameter that will reduce the error distribution significantly. The genetic algorithm was initially designed with a population size set to 30 and up to 150 generations, stopping when the population set was not seen to evolve. This genetic algorithm starts by defining a set of parameters that are selected, each set corresponding to an individual gene, and this individual gene is then used to fit a GLM model on the residual. After this the fitness is calculated for each individual of the generation. This fitness score is given by:

$$\sigma_f = \sigma + N\sigma_0 \,, \tag{2.10}$$

where σ is the width of the GLM residual, N the number of parameters in the set and σ_0 the cost associated with each addition of a parameter. The value of the parameter cost determines the number of parameters that will be selected and considered key.

The width of the GLM residual was determined in two different ways for the different families of methods. For the differential methods, which respond well to the GLM fit, the residual was found to follow a generalised normal distribution (Equation 2.11) which was used to fit the GLM residual. The generalised normal distribution is given by:

$$f(x, \beta, \mu, \sigma) = \frac{\beta}{2\sigma\Gamma(1/\beta)} \exp\left(-\left|\frac{x-\mu}{\sigma}\right|^{\beta}\right), \tag{2.11}$$

where β is the shape parameters, μ the mean of the distribution and σ the standard deviation.

The standard deviation σ of this distribution was then used for the width (σ) of the fitness calculation (e.g. individual fitness). For the high-field method, a distribution was not found that was efficient at fitting the GLM residual. Thus, the width here was defined as the smallest range containing 68.27% of the points. For a normally distributed variable, this range corresponds to twice the standard error. We used the half value of this range

for the individual fitness σ coefficient.

The parameter cost was set for the low-field method to 5×10^{-7} and for the high fill method to 1×10^{-7}. Those two values are relatively low, ensuring that the key parameters are not removed from the model, with the downside of having a larger number of parameters. However, the remanent parameters were then removed from the model using standard model reduction in a subsequent step.

To run the genetic algorithm, we started with an initial population generated by randomly picking 20 interaction parameters and adding the primary parameter for each individual of the set. The GLM was run using those different individual genes and the 10 best individuals based on their fitness score were retained. In addition to the 10 best of the last iteration, the three best of all past generations were also used. This was found to accelerate model convergence. Then, starting from these 13 different individuals, we reconstructed the population of 30 by merging the different sets together, creating new individuals. In this case, two different individuals in the final population were chosen of the 13 reserved. The first individual was chosen by iterating over each individual, which ensures that each individual was represented in the next iteration. The second individual was chosen randomly from the rest of the population. Then, from these two individuals, all the parameters in common between were retained. The parameters that appeared only a single time in one of the individuals were kept with the probability of 50%. Finally, a mutation step was added to bring a new parameter into the population. This was done by adding a parameter randomly to each individual, and removing another parameter randomly at the same time, but this time with a probability of 50%. After a few tests, this method was found to guarantee a good convergence of the iteration process. This process was repeated for 150 generations.

Following the genetic model run, we obtained the parameter set that minimised the width of the distribution of the FL and DL torque estimation error. However, due to the low

parameter cost, this set was large and could be further reduced with standard model reduction. First, all parameters that appeared in interaction terms but were not present as a primary term were included. This ensured a correct description and avoided hiding the potential correlation between a primary parameter with its interaction. Then a model reduction step was performed. As discussed, the parameter cost was set relatively low to ensure inclusion of key parameters. This model reduction was made by systematically removing parameter one at a time with the lowest p-value, based on a symmetric Gaussian. The GLM model was then refitted. The pseudo-R-squared was checked to determine if there was a large variation in the fit quality. This step was reiterated until none of the parameters could be removed without affecting the goodness of fit. In this process, primary parameters appearing in the interaction were retained.

For the high-field method, a slight change to the last selection process was required to accommodate the Lorentzian distribution of the residual (using an absolute error metric), as the assumption of Gaussian a distribution was not met for using the least squared error to fit the residuals. This was not pertinent for the genetic algorithm parameter selection process, as the parameter cost was intentionally set at a lower value, which allowed obtaining an exceedance of parameters. Preliminary testing did not show a large difference in the parameter selection using these two metrics, while it significantly reduced the computing time. For the manual step of the model reduction, the Manhattan distance was used.

The training dataset (800 000 points) was used to develop all models, while the test dataset (200 000 points) was used to present the results in figures. This was performed to determine if any overfitting occurred due to the large number of parameters within models.

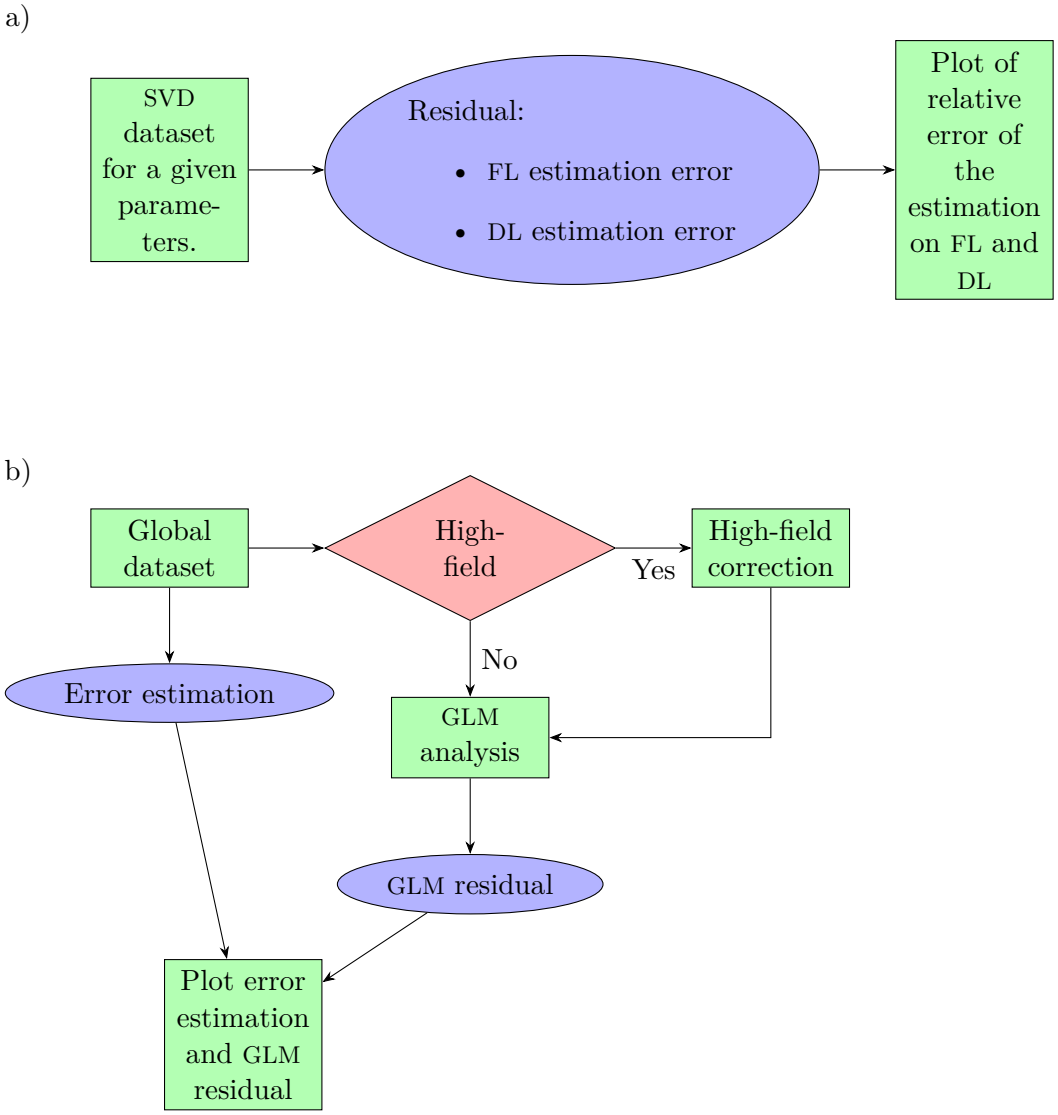

Figure 2.2: Flowchart showing the analysis process for the series of datasets. a) flowchart for the single variable dependence (SVD) analysis where a dataset is created for any individual parameters. b) flowchart for the analysis of the global dataset where the residual error on the FL and DL estimation is represented for both the global dataset and the residual after the GLM analysis.

Table 2.2: Parameters used in the numerical model fit, with parameter name, model default value, maximum and minimum values for the range variation included in the model, if the parameter was varied (denoted with a check mark), and their description included as columns.

Name	Default value	Minimum	Maximum	Vary	Description
$\rho_{xx0}(\Omega\,\mathrm{m})$	1.126×10^{-6}	-	-		Ohm resistance
$\rho_{\mathrm{AHE}}(\Omega\,\mathrm{m})$	-1.268×10^{-8}	-	-		Anomalous Hall effect
$\rho_{\mathrm{HE}}(\Omega\,\mathrm{m})$	0	-3×10^{-9}	3×10^{-9}	✓	Hall effect
$\rho_{\mathrm{AMR}}(\Omega\,\mathrm{m})$	0	-1×10^{-9}	1×10^{-9}	✓	Anisotropic magneto resistance from thin film origin
$\rho_{\mathrm{PHE}}(\Omega\,\mathrm{m})$	0	-2×10^{-9}	2×10^{-9}	✓	Planar Hall effect and associated magneto resistance
$\rho_{LM}(\Omega\,\mathrm{m})$	0	-5×10^{-9}	5×10^{-9}	✓	linear magneto resistance field-dependant
$k_1(\mathrm{T})$	$\frac{1-4k_2}{2}$	0	0.5	✓	first order out of plane anisotropy
$k_2(\mathrm{T})$	0	0	0.25	✓	second order out of plane anisotropy
θ_x (°)	0	-5	5	✓	Euler angle along x
θ_y (°)	0	-5	5	✓	Euler angle along y
θ_z (°)	0	-5	5	✓	Euler angle along z
$\mathrm{FL}(\mathrm{T\,A^{-1}\,m^2})$	1×10^{-14}	-1×10^{-13}	1×10^{-13}	✓	FL coefficient
$\mathrm{DL}(\mathrm{T\,A^{-1}\,m^2})$	3×10^{-14}	-1×10^{-13}	1×10^{-13}	✓	DL coefficient
$\mathrm{ANE}(\Omega\,\mathrm{A^{-1}\,m^3})$	0	-3×10^{-21}	3×10^{-21}	✓	Anomalous Nernst effect
NE $(\Omega\,\mathrm{A^{-1}\,m^3})$	0	-3×10^{-21}	3×10^{-21}	✓	Nernst effect
Distortion (dB)	-140	-140	-70	✓	source quadratic distortion, both positive and negative
σ (a.u.*)	0	{0, 1, 2, 3, 5, 10, 20 }**		✓	Gaussian noise

* The amplitude of noise depends on the harmonic order and type of signal. A multiplying factor of 2×10^{-7} V For the longitudinal first harmonic, 2×10^{-9} V For the longitudinal second harmonic, 1×10^{-7} V for the transverse first harmonic, 1×10^{-9} V for the transverse second harmonic.
** The noise takes only discrete values and is applied to each point.

2.3 Results

2.3.1 Analytical fitting examples of harmonic Hall signals

In order to open the 'black box' of the system described, a set of examples are illustrated demonstrating that it is possible to have a set of harmonic Hall signals for which the fit of the analytical model is poor, while correctly estimating the FL and DL torques, or vice versa (Figure 2.3, 2.4 and 2.5, and Tables 2.3 and 2.4).

No correlation was found between the fit quality represented by the χ^2 value for each analytical method and the accuracy of the FL and DL torque estimation. Here, independence between the fit quality and the FL and DL estimation accuracy was illustrated for both high-field and differential methods.

For the differential method, it was possible to have a significant fit error (Figure 2.3), but still end up with the correct extraction for the FL and DL coefficients. On the other hand, there can be a good agreement between the fit and the model (Figure 2.4); however, the estimated FL and DL torques are incorrect. This is due to the fitting by the model of the thermoelectric effect, as seen in Table 2.3. Which, in general, means that for the differential method, there is no correlation between the goodness of fit and the accuracy of the estimation of the FL and DL torques.

Additionally, agreement decreases as the fitting range starts to get closer to the anisotropy field for the high-field method, even if the fits shown have an overall good agreement (Figure 2.5). Even under conditions where the fit matches the data fairly well, there can still be huge discrepancies between the DL extracted value and the actual DL torque (Table 2.4). The accuracy increases as the lower field values are removed from the fitting process, but the signal-to-noise ratio is also lower, which reduces the extraction precision.

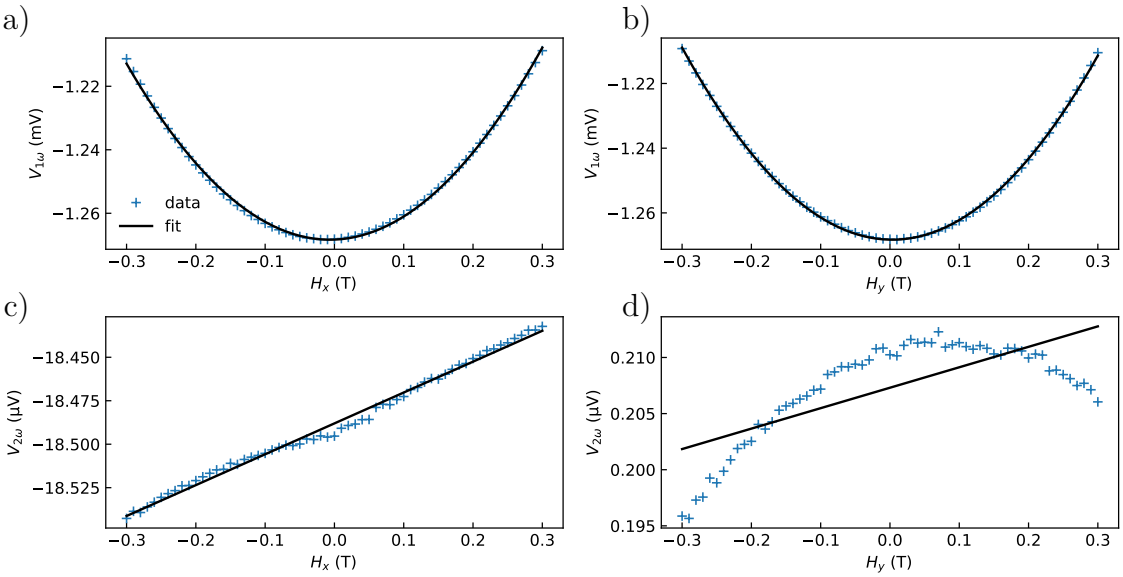

Figure 2.3: Example of fitted data using the differential method. The first harmonic (a, b) and second harmonic (c, d) for a field applied along x (a, c) and y (b, d) direction. The points are the data from the numerical model, while the lines represent the linear and quadratic fit used in the differential method. Despite the presence of a large contribution (due to the distortion) and an overall poor fit in d, the determined values were correct. The even nature of the contributions does not affect the linear fit, resulting in a correct determination of the SOT coefficient.

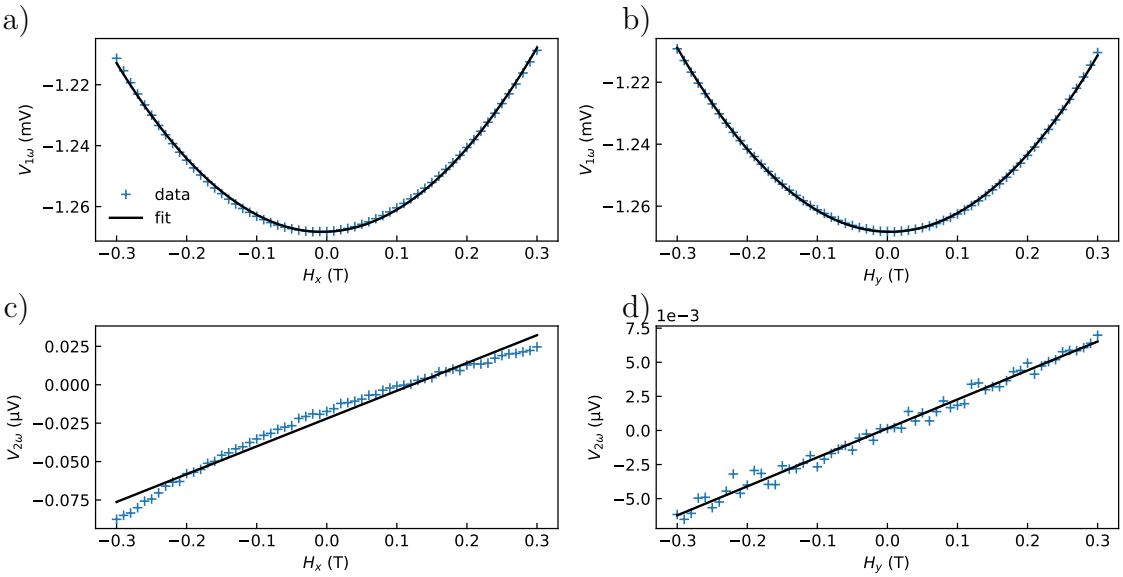

Figure 2.4: Example of high systematic error of fitted data using the differential method, which is the opposite example of Figure 2.3. In this case, the extra contributions follow the same symmetries that are expected from SOT. The fitting coefficients capture all the extra information, leading to an incorrect estimation of the SOT coefficients.

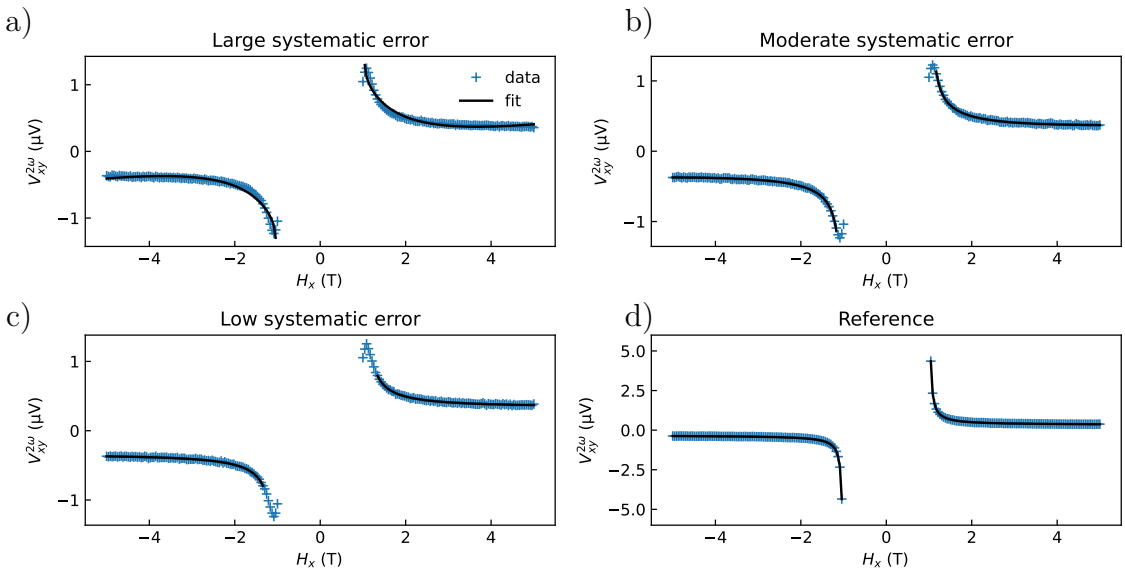

Figure 2.5: High-field method model fits for a small offset of 1.5° *(a-c) and reference value with no offset (d). The fitting starts at* 1.04 T *(a),* 1.16 T *(b),* 1.32 T *(c) and* 1 T *(d). This has a large effect on the determination of the* DL *coefficient, as visible in Table 2.4, despite the agreement appearing correct for each individual fit.*

Table 2.3: Parameters associated with the two examples of the differential method. The experimental FL and DL are reported, along with the relative error estimates.

Parameters	Good model fit, poor accuracy	Poor model fit, good accuracy
ANE ($10^{-22}\,\Omega\,m^3\,A^{-1}$)	20.4	8.4
NE ($10^{-22}\,\Omega\,m^3\,A^{-1}$)	0	0
θ_z (°)	0	0
θ_y (°)	−4.89	−4.89
θ_x (°)	−2.39	−2.39
Distortion (dB)	−140	−75.6
ρ_{xx0} ($10^{-6}\,\Omega\,m$)	1.126	1.126
ρ_{AHE} ($10^{-8}\,\Omega\,m$)	−1.268	−1.268
ρ_{HE} ($10^{-9}\,\Omega\,m$)	1.74	1.74
ρ_{AMR} ($10^{-10}\,\Omega\,m$)	8.00	0
ρ_{PHE} ($10^{-10}\,\Omega\,m$)	−5.2	−6.4
ρ_{LMR} ($10^{-9}\,\Omega\,m$)	5	5
k_1 (T)	0.5	0.5
k_2 (T)	0	0
FL ($10^{-15}\,T\,A^{-1}\,m^2$)	3.7	3.7
DL ($10^{-14}\,T\,A^{-1}\,m^2$)	2.7	2.7
Noise*	0.42	0.42
exp FL ($10^{-15}\,T\,A^{-1}\,m^2$)	4.45	4.22
exp DL ($10^{-14}\,T\,A^{-1}\,m^2$)	2.83	2.78
relative error FL (%)	20.2	14.1
relative error DL (%)	4.81	2.92

* The amplitude of noise depends on the harmonic order and type of signal. A multiplying factor of 2×10^{-7} V For the longitudinal first harmonic, 2×10^{-9} V For the longitudinal second harmonic, 1×10^{-7} V for the transverse first harmonic, 1×10^{-9} V for the transverse second harmonic.

Table 2.4: Parameters used to draw examples of the high-field method fit. The experimental FL and DL are reported, along with the relative error in their estimates.

	Systematic error			
Parameters	Large	Moderate	Low	Reference
ANE ($10^{-22}\,\Omega\,m^3\,A^{-1}$)	6.6	6.6	6.6	6.6
NE ($10^{-22}\,\Omega\,m^3\,A^{-1}$)	0	0	0	0
θ_z (°)	0	0	0	0
θ_y (°)	1.50	1.50	1.50	0
θ_x (°)	0	0	0	0
Distortion (dB)	−80	−80	−80	−80
ρ_{xx0} ($10^{-6}\,\Omega\,m$)	1.126	1.126	1.126	1.126
ρ_{AHE} ($10^{-8}\,\Omega\,m$)	−1.268	−1.268	−1.268	−1.268
ρ_{NHE} ($10^{-9}\,\Omega\,m$)	0	0	0	0
ρ_{AMR} ($10^{-10}\,\Omega\,m$)	0	0	0	0
ρ_{PHE} ($10^{-10}\,\Omega\,m$)	−6	−6	−6	−6
ρ_{LMR} ($10^{-9}\,\Omega\,m$)	5	5	5	5
k_1 (T)	0.5	0.5	0.5	0.5
k_2 (T)	0	0	0	0
FL ($10^{-15}\,T\,A^{-1}\,m^2$)	3.7	3.7	3.7	3.7
DL ($10^{-14}\,T\,A^{-1}\,m^2$)	2.7	2.7	2.7	2.7
Noise*	5.8	5.8	5.8	5.8
H_0	1.04	1.16	1.32	1
exp FL ($10^{-15}\,T\,A^{-1}\,m^2$)	−4640	−1060	−193	18.2
exp DL ($10^{-14}\,T\,A^{-1}\,m^2$)	0.166	1.72	2.40	2.70
relative error FL (%)	−125 000	−28 700	−5310	−391
relative error DL (%)	−93.8	−36.2	−11.1	−0.016

* The amplitude of noise depends on the harmonic order and type of signal. A multiplying factor of 2×10^{-7} V For the longitudinal first harmonic, 2×10^{-9} V For the longitudinal second harmonic, 1×10^{-7} V for the transverse first harmonic, 1×10^{-9} V for the transverse second harmonic.

2.3.2 Single variable measurement analysis

In the perfect scenario, which the analytical methods were developed for, the estimated torque values correspond to the actual values. In this section we describe how the variation of a single parameter affects the estimated values.

For the differential method, the dependencies were predominately linear (Figure 2.6). The parameters that influenced the estimation of the FL and DL torque were the rotation around the z-axis, the PHE (for the methods that do not use the PHE correction), the second-order anisotropy constant (which modifies the anisotropy landscape) and the AMR (for the method using thermal correction, as AMR acts only on the longitudinal signal, V_{xx}). Both thermoelectric effects that were considered here (ANE and NE) show a strong dependence on the method that does not take into account thermal corrections Figure 2.6e, 2.6f). Note that the thermoelectric effects were the largest error observed in the single variable analysis for the parameter range used with this model.

The FL torque was impacted by fewer parameters in the single variable analysis (Figure 2.7), with only the rotation around the z-axis (θ_z), the PHE and the second order anisotropy (k_2) affecting the FL estimation. The amplitude of the variation on the θ_z and PHE was larger than in the case of the DL study, due to the difference between the default value of the FL and DL torques. The AMR, ANE and NE all played a minor role here, as those mainly affect the DL estimation.

In the high-field method, DL determination depends predominately on the sample position (Figure 2.8). The rotation around the z-axis impacts only on the high-field xy determination (Figure 2.8c). The rotation around the x- and y-axes corresponded to the error when the field was applied out-of-plane in relation to the sample plane (Figure 2.8a, 2.8b). The x- and y-axes dependence was strong, reaching $> 80\%$ for all the methods when the fitting started from H_k and the offset was 5° (Figure 2.8a, 2.8b). The dependence was

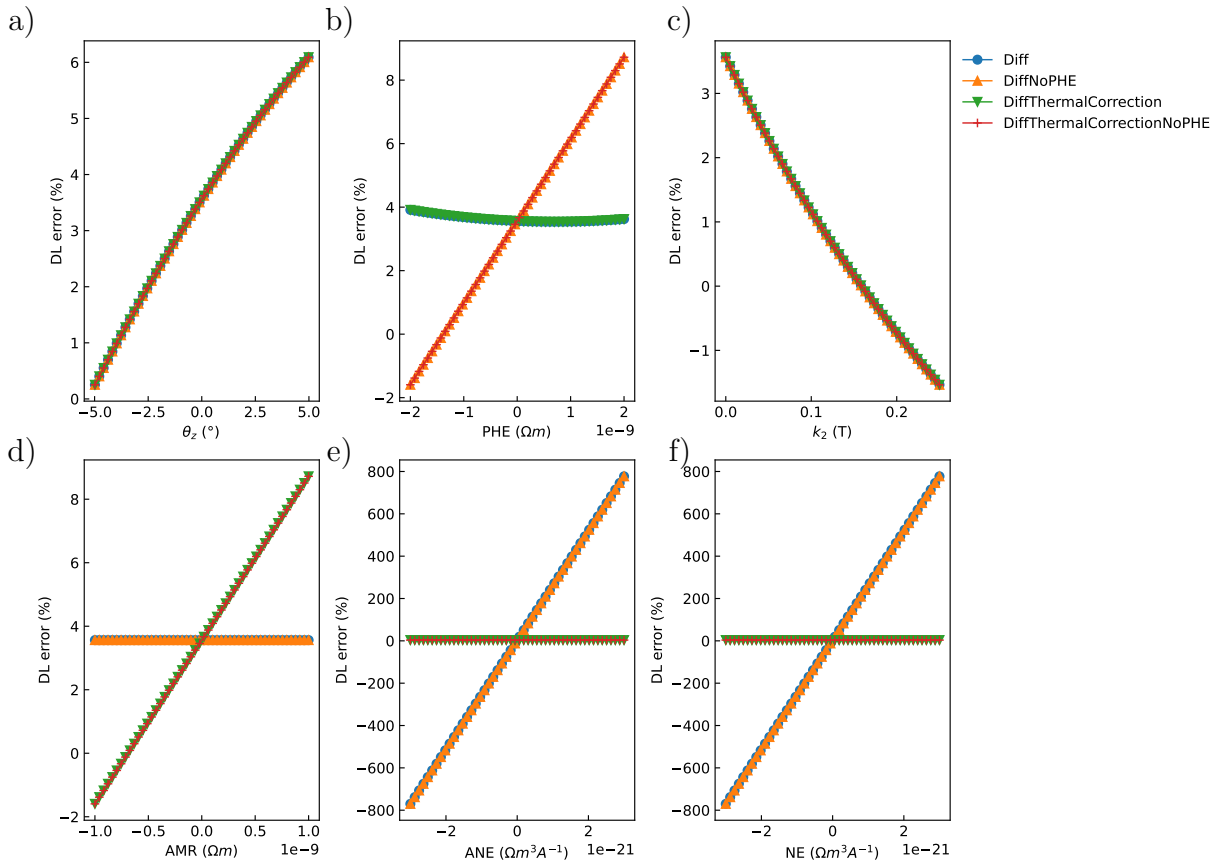

Figure 2.6: Relative error of the DL coefficient for the different differential methods when a single parameter is varied at a time. Variables that are not represented do not show variation. Most of the values were around 4% error, originating from the initial approximation performed in the harmonic Hall method. The PHE correction appeared efficient, with a much smaller dependence on PHE, when applied. The rotation around the z-direction mixed both FL and DL contributions, resulting in an error proportional to the FL terms. The thermal corrections effectively removed the error originating from the NE and ANE; this added a smaller error contribution from AMR due to the inclusion of longitudinal voltage.

also highly non-linear due to the unstable nature of applying the field along the hard axis, which was also illustrated in Figure 2.5. There is no simple analytical expression to model this dependence; thus the values were tabulated to implement a correction, detailed in Section 2.3.3.

From the Equation 2.5, the FL component is captured only when a PHE contribution is present. Thus, it is expected not to see any dependence in the FL estimation expected for the PHE dependence (Figure 2.9). The error in the FL torque estimation was high at low PHE values ($\ll 0.5 \times 10^{-4}$) despite matching all of the assumptions of the analytical

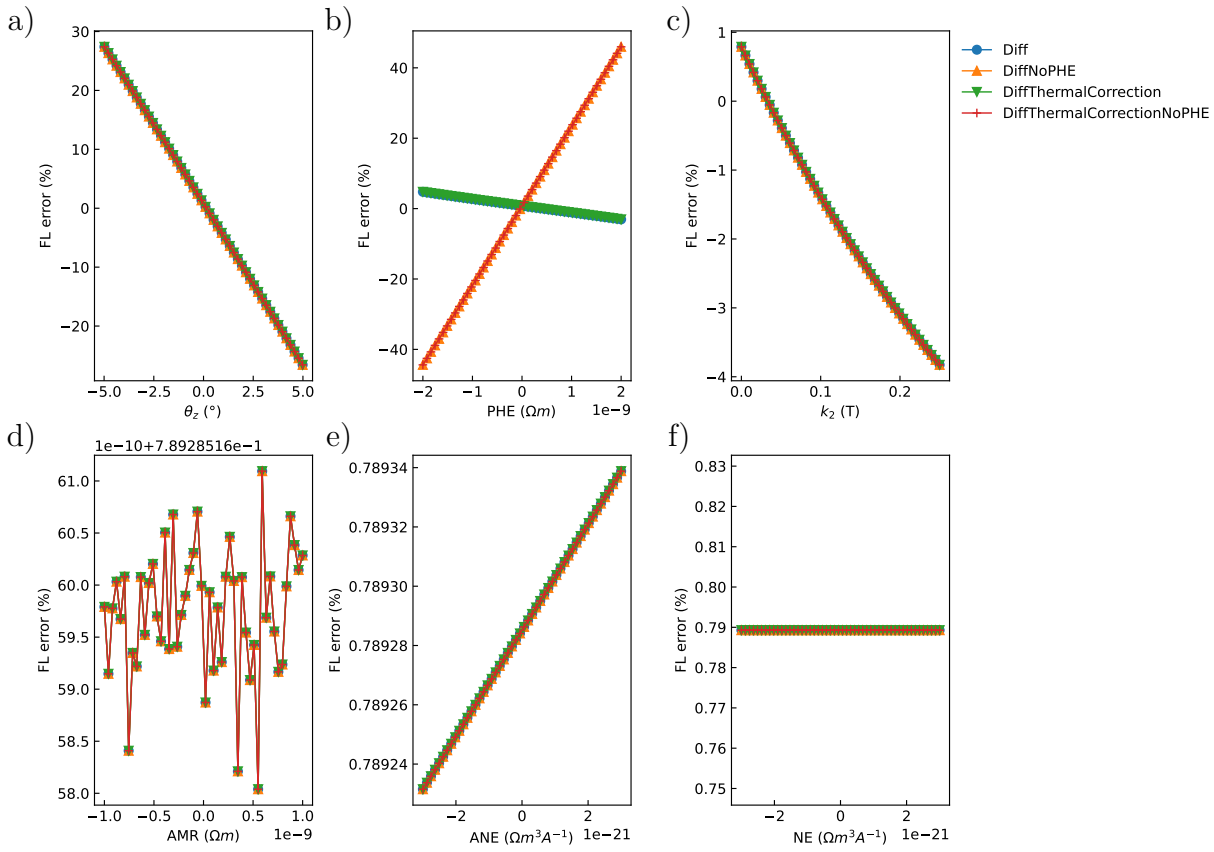

Figure 2.7: Relative error of the FL coefficient for the different differential methods when a single parameter is varied at the time. Variables that are not represented do not show variation. Contributions originating only from mixing the DL and FL effects, such as the rotation around z and PHE, if this is not corrected. The presence of second order anisotropy has a minimal impact on the accuracy. The thermoelectric effect does not influence the FL determination when the other parameters follow the ideal case scenario.

model (Figure 2.9d). The accuracy of the FL torque was high at higher PHE values for the x and x, y analytical methods. For the starting field position at 1 T, the estimation error was lest than 5% for respectively PHE $> 1.2 \times 10^{-9}\,\Omega\,\mathrm{m}$ and PHE $> 0.3 \times 10^{-9}\,\Omega\,\mathrm{m}$ for the x and x, y method. For the xy analytical method, the PHE is never estimated as expected from its Equation 2.5.

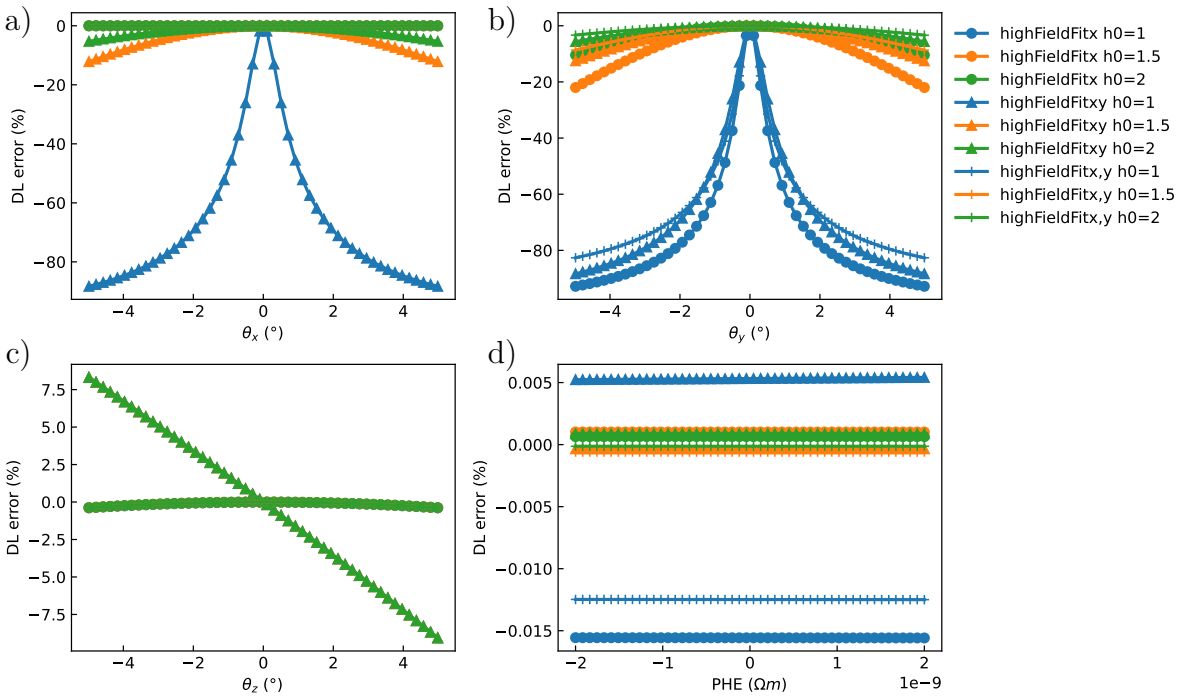

Figure 2.8: Relative error on the DL coefficient for the different high-field methods when a single parameter was varied at the time. Variables that are not represented do not show variation.

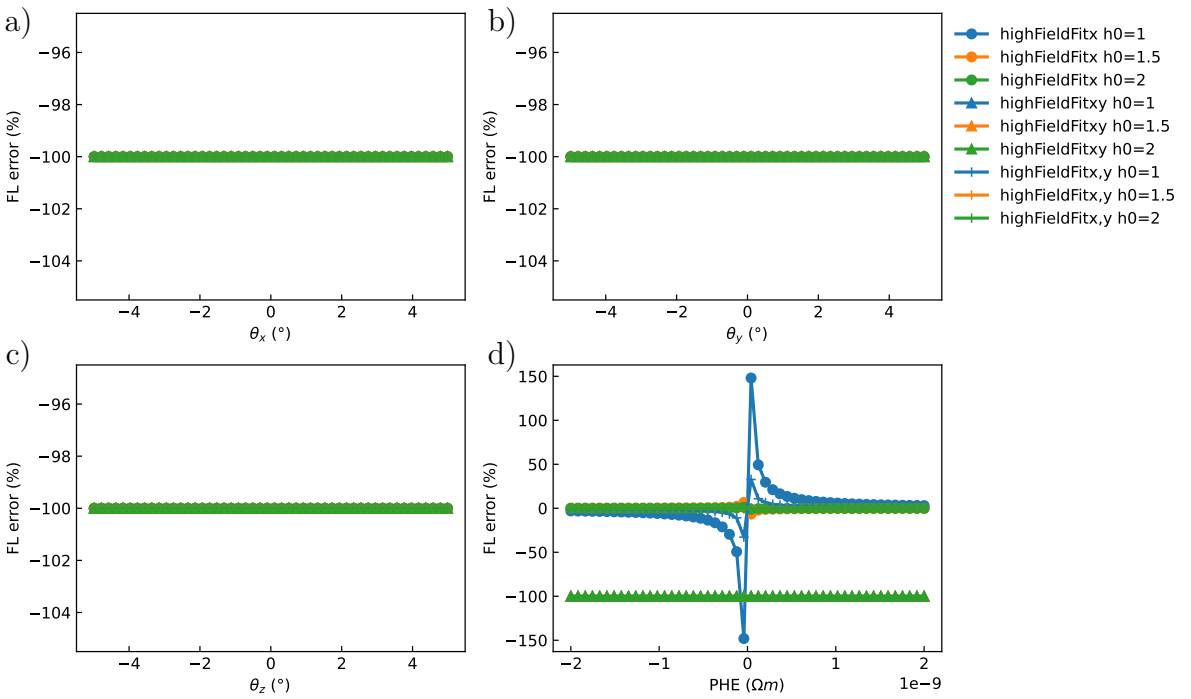

Figure 2.9: Relative error on the FL coefficient for the different high-field methods when a single parameter was varied at the time. Variables that are not represented do not show variation.

2.3.3 High-field correction

The field offset of the high-field method had the strongest and most non-linear impact, as seen in the single variable dependence test (Section 2.3.2). Addressing this was required to see if the tabulated error correction was sound when the global dataset was used (considering all interactions). This error affects all variations of the high-field method (Figure 2.8). This error depended only on the starting fitting position (h_0) and the angular offset value of the sample plane.

A correction factor was tabulated to correct for this highly non-linear dependence. For each value of θ_y and h_0, the DL coefficient was swept, then a straight line was fit to the results, and the offset and slope were tabulated. The residual of the full dataset for the high field x method is shown before and after correction in Figure 2.10.

Before the correction, when the fitting field offset (h_0) was small, i.e. 1.2 T, many points approached -100% relative error. Thus, no DL torque was found despite its presence (Figure 2.10a). A small, sharp peak along zero was attributed to the few points that were close to meeting the zero angle offset requirements. The residual is asymmetric, with the DL value being underestimated, with an estimated value between zero and the real value. After correction, the asymmetry was still present; however, most of the points are now closer to 0% error, while keeping the systematic underestimation of the DL torque (Figure 2.10b). This correction alone, despite the number of parameters involved in the simulation, allowed for a much better estimation of the DL coefficient using all variations of the high-field method. Thus, it was systematically applied in the GLM regression.

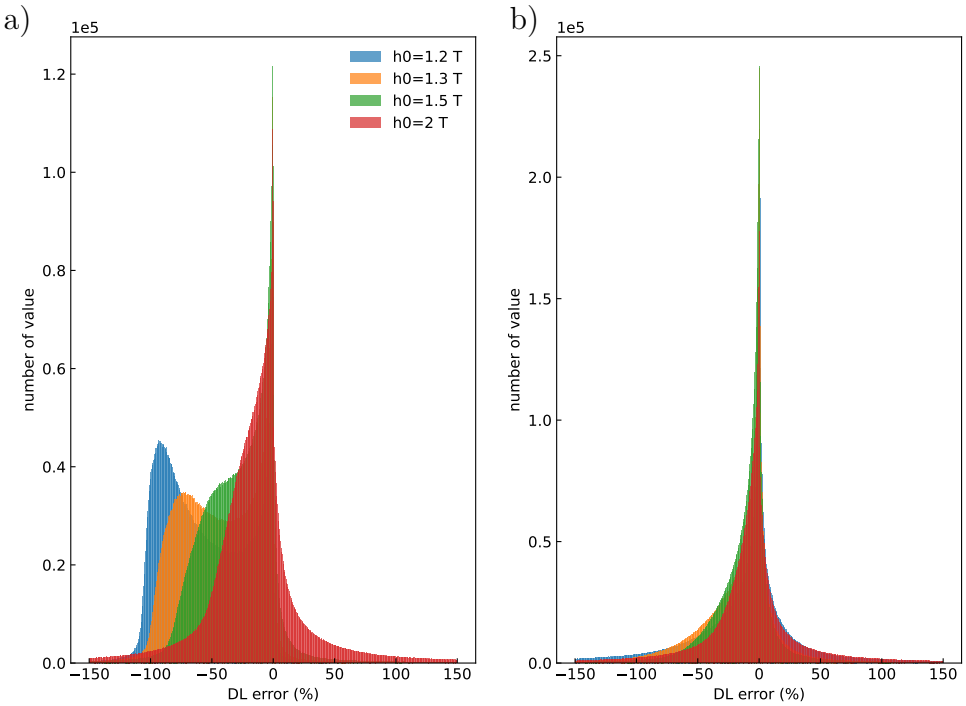

Figure 2.10: Relative percentage error of the DL component for the high-field x method when the full model, including variation of all the parameters, is included. The colours correspond to the different starting fitting ranges: 1.2 T *(blue),* 1.3 T *(orange),* 1.5 T *(green) and* 2 T *(red). On the left graph, the raw value of the error is presented. On the right side graph, the error was corrected on the basis of a correction table determined by the single axis variation Figure 2.8.*

2.3.4 GLM analysis

2.3.4.1 High-field method

For high-field analytical methods, the starting point of the data fit has a large influence on the determination of accuracy (see Section 2.3.1). For each method, three different starting positions of the fit are discussed: 1.2 T, 1.5 T and 2 T.

It was observed that the high-field x method produced the least robust determination of the DL torque, compared to the xy and x, y analytical methods (Figure 2.11). The x, y method showed the lowest error, closely followed by the xy method (Figure 2.11d-i). This was unexpected for the xy method, as the DL effect is reduced by a factor $\cos(45°) \approx 0.71$

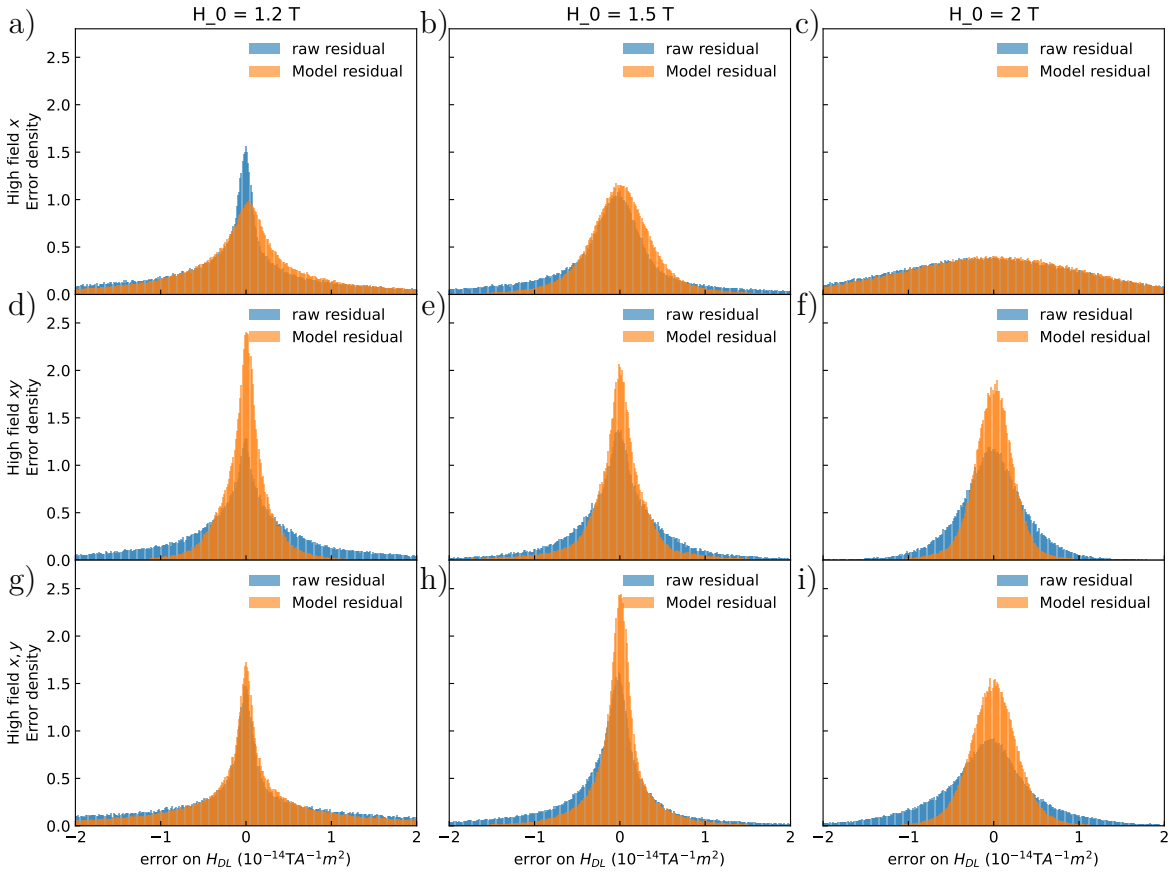

Figure 2.11: Model and corrected residuals for the high-field method, where the three different columns start with a starting fitting point of 1.2 T *(left),* 1.5 T *(middle) and* 2 T *(right). The first line corresponds to the high-field x method, the second line to the high-field xy method and the third to the high-field x, y method. For the whole residual (blue), the field angle correction was applied (Section 2.3.3). The residual after applying the* GLM *is represented in orange.*

(from the analytical expression). However, the systematic error appears to be much lower, which led to better overall accuracy. The addition of the longitudinal signal (V_{xx}) in the x, y method significantly improved the quality of the results, compared to the x method (Figure 2.11a-c and 2.11g-i). This was explained, as the addition of the longitudinal signal fixed the ANE and NE coefficients.

Overall, starting at 1.5 T gave the most accurate result for the xy and x, y methods (Figure 2.11b, e, h). A fitting starting point at 1.2 T was enough to achieve relatively good value for the x method (Figure 2.11a). It should be noted that the correction

detailed in Section 2.3.3 had been implemented using the x method, thus was likely to be more efficient. There was no improvement when using the GLM model for the x method at $h_0 = 2\,\mathrm{T}$ (Figure 2.11c), as most of the information was lost in the extraction and no further improvement could be made.

For the x method, while the model reduces the overall absolute error, the probability density close to zero decreased (Figure 2.11a), indicating that this comes with a trade-off of reducing larger errors but increasing the chance of small errors overall. The analytical method, which demonstrated the largest improvement in error reduction with the GLM analysis, was the x, y method with $h_0 = 1.5\,\mathrm{T}$ (Figure 2.11h), where there was a better prediction of the error and a more centred result was observed. With the xy method, at a starting fitting point set to $h_0 = 1.5\,\mathrm{T}$, the GLM contained five parameters with a P-value lower than 0.5 (Table 2.6), while keeping a large improvement from the GLM model (Figure 2.11e). It appears to be a more straight-forward correction, compared to the x and x, y method, with the same h_0 (Table 2.5 and 2.7 respectively). When the starting point was set to $h_0 = 2\,\mathrm{T}$, there was a tendency to have less parameters (Tables 2.5, 2.6 and 2.7). However, the width of the GLM residual is also larger indicating poorer agreement.

Table 2.5: High-field x method coefficient values determined by GLM, as shown in the tables for starting point: (a) 1.2 T, (b) 1.5 T and (c) 2 T. The units are given as DL field efficiency ($\mathrm{T\,A^{-1}\,m^2}$) in relation to the initial coefficient unit. Colons indicate an interaction.

a) Coefficients for the DL regression with $h_0 = 1.2\,\mathrm{T}$

Name	coef	std err	z	P>|z|
Intercept	-9.06×10^{-16}	1.88×10^{-15}	−0.4814	0.630
ANE	-3.35×10^{5}	-6.33×10^{5}	0.5286	0.597
θ_y	2.99×10^{-17}	5.65×10^{-16}	0.052 99	0.958
k_1	5.39×10^{-16}	6.90×10^{-15}	0.078 01	0.938
χ_{DL}	-7.12×10^{-2}	3.88×10^{-2}	−1.836	0.066
θ_y^6	-2.71×10^{-18}	5.76×10^{-19}	−4.703	<0.001
χ_{DL}^5	-2.61×10^{51}	1.08×10^{51}	−2.421	0.015
θ_y^6:ANE	-1.09×10^{3}	-2.83×10^{2}	3.861	<0.001
θ_y^2:χ_{DL}	-2.65×10^{-2}	4.55×10^{-3}	−5.815	<0.001
k_1^6:χ_{DL}	3.04×10^{1}	1.24×10^{1}	2.448	0.014
χ_{DL}^3:k_1	1.26×10^{26}	3.95×10^{25}	3.187	0.001

b) Coefficients for the DL regression with $h_0 = 1.5\,\mathrm{T}$

Name	coef	std err	z	P>|z|
Intercept	9.36×10^{-17}	1.79×10^{-15}	0.052 18	0.958
ANE	4.55×10^{4}	-6.58×10^{5}	−0.069 24	0.945
θ_z	-9.04×10^{-19}	2.85×10^{-16}	−0.003 173	0.997
θ_y	-7.88×10^{-19}	3.36×10^{-16}	−0.002 343	0.998
distortion	5.69×10^{-20}	4.77×10^{-17}	0.001 192	0.999
k_1	1.87×10^{-16}	5.53×10^{-15}	0.033 76	0.973
χ_{DL}	-5.15×10^{-2}	3.19×10^{-2}	−1.615	0.106
θ_y^2	-2.19×10^{-16}	1.24×10^{-16}	−1.772	0.076
θ_y^2:ANE	-9.41×10^{4}	-7.72×10^{4}	1.219	0.223
θ_y^2:χ_{DL}	-1.77×10^{-2}	8.49×10^{-3}	−2.088	0.037
θ_y^4:χ_{DL}	1.96×10^{-4}	4.30×10^{-4}	0.4556	0.649
θ_y:distortion:k_1	5.77×10^{-17}	6.37×10^{-17}	0.9051	0.365
k_1^4:χ_{DL}	1.14×10^{1}	5.48	2.078	0.038
k_1^6:χ_{DL}	-3.69×10^{1}	2.52×10^{1}	−1.467	0.142

c) Coefficients for the DL regression with $h_0 = 2\,\mathrm{T}$

Name	coef	std err	z	P>|z|
Intercept	-1.09×10^{-15}	2.59×10^{-15}	−0.4211	0.674
ANE	-4.57×10^{5}	-7.32×10^{5}	0.6235	0.533
θ_y	-1.01×10^{-17}	4.93×10^{-16}	−0.020 42	0.984
distortion	-9.17×10^{-19}	8.16×10^{-17}	−0.011 24	0.991
k_1	2.22×10^{-15}	9.56×10^{-15}	0.2325	0.816
χ_{DL}	-6.31×10^{-2}	3.82×10^{-2}	−1.65	0.099
θ_y:distortion	1.57×10^{-17}	2.88×10^{-17}	0.546	0.585
k_1:χ_{DL}	2.43×10^{-1}	1.67×10^{-1}	1.452	0.146
θ_y^4:k_1	-2.00×10^{-17}	2.61×10^{-17}	−0.7641	0.445
θ_y^2:χ_{DL}	-7.75×10^{-3}	3.49×10^{-3}	−2.22	0.026

Table 2.6: High-field xy method coefficient values determined by GLM, as shown in the tables: (a) 1.2 T, (b) 1.5 T and (c) 2 T. The units are given as DL field efficiency ($\mathrm{T\,A^{-1}\,m^2}$) in relation to the initial coefficient unit. Colons indicate an interaction.

Coefficients for the DL regression with $h_0 = 1.2\,\mathrm{T}$

Name	coef	std err	z	P>|z|
Intercept	-6.00×10^{-16}	1.59×10^{-15}	−0.378	0.705
ANE	-3.46×10^{5}	-3.76×10^{5}	0.9219	0.357
θ_z	-1.10×10^{-18}	2.54×10^{-16}	−0.004 342	0.997
θ_y	4.74×10^{-19}	3.03×10^{-16}	0.001 564	0.999
θ_x	-6.47×10^{-19}	2.89×10^{-16}	−0.002 238	0.998
distortion	7.63×10^{-20}	4.11×10^{-17}	0.001 854	0.999
k_1	4.59×10^{-16}	5.33×10^{-15}	0.0861	0.931
χ_{DL}	-1.66×10^{-1}	3.87×10^{-2}	−4.288	<0.001
θ_z:χ_{DL}	-1.58×10^{-2}	5.52×10^{-3}	−2.857	0.004
θ_y:distortion	1.58×10^{-17}	1.53×10^{-17}	1.032	0.302
k_1:χ_{DL}	3.35×10^{-1}	1.07×10^{-1}	3.133	0.002
θ_y^4:χ_{DL}	-2.89×10^{-4}	8.98×10^{-5}	−3.216	0.001
θ_y:θ_x:χ_{DL}	1.41×10^{-2}	2.26×10^{-3}	6.233	<0.001
θ_x^4:χ_{DL}	-2.81×10^{-4}	1.01×10^{-4}	−2.783	0.005
θ_x:distortion:k_1	-4.99×10^{-17}	4.96×10^{-17}	−1.005	0.315

Coefficients for the DL regression with $h_0 = 1.5\,\mathrm{T}$

Name	coef	std err	z	P>|z|
Intercept	-1.99×10^{-16}	1.29×10^{-15}	−0.1544	0.877
ANE	-1.97×10^{5}	-3.76×10^{5}	0.5239	0.600
θ_z	-1.13×10^{-18}	2.21×10^{-16}	−0.005 109	0.996
θ_y	-1.44×10^{-18}	2.49×10^{-16}	−0.005 788	0.995
distortion	-5.53×10^{-20}	3.67×10^{-17}	−0.001 509	0.999
k_1	-7.33×10^{-17}	4.04×10^{-15}	−0.018 15	0.986
χ_{DL}	-5.11×10^{-2}	2.03×10^{-2}	−2.522	0.012
θ_z:χ_{DL}	-1.68×10^{-2}	5.22×10^{-3}	−3.225	0.001
θ_y:distortion	1.56×10^{-17}	1.59×10^{-17}	0.9817	0.326
θ_x:distortion	-1.56×10^{-17}	1.67×10^{-17}	−0.9306	0.352
k_1^4:χ_{DL}	6.71×10^{-1}	7.17×10^{-1}	0.936	0.349

Coefficients for the DL regression with $h_0 = 2\,\mathrm{T}$

Name	coef	std err	z	P>|z|
Intercept	-1.47×10^{-16}	1.36×10^{-15}	−0.1079	0.914
ANE	-1.96×10^{5}	-3.86×10^{5}	0.5091	0.611
θ_z	-2.58×10^{-18}	2.31×10^{-16}	−0.011 15	0.991
distortion	-2.54×10^{-19}	3.84×10^{-17}	−0.006 597	0.995
k_1	-2.36×10^{-16}	4.54×10^{-15}	−0.052 04	0.958
χ_{DL}	-2.33×10^{-2}	1.22×10^{-2}	−1.901	0.057
θ_z:χ_{DL}	-1.71×10^{-2}	4.34×10^{-3}	−3.946	<0.001
θ_y:distortion	1.56×10^{-17}	1.42×10^{-17}	1.1	0.271
θ_x:distortion	-1.56×10^{-17}	1.33×10^{-17}	−1.179	0.238

Table 2.7: High-field x, y method coefficient values determined by GLM, as shown in the tables for starting point: (a) 1.2 T, (b) 1.5 T and (c) 2 T. The units are given as DL field efficiency ($\mathrm{T\,A^{-1}\,m^2}$) in relation to the initial coefficient unit. Colons indicate an interaction.

a) Coefficient for the DL regression with $h_0 = 1.2\,\mathrm{T}$

Name	coef	std err	z	P>|z|
Intercept	-1.15×10^{-16}	7.31×10^{-16}	−0.1578	0.875
ANE	-1.85×10^{5}	-4.26×10^{5}	0.4339	0.664
NE	-2.15×10^{5}	-4.51×10^{5}	0.4771	0.633
θ_y	1.58×10^{-17}	4.43×10^{-16}	0.0357	0.972
χ_{DL}	1.26×10^{-2}	1.82×10^{-2}	0.6922	0.489
θ_y^4	-5.36×10^{-17}	1.23×10^{-17}	−4.345	<0.001
θ_y^6:ANE	-1.11×10^{3}	-3.53×10^{2}	3.162	0.002
θ_y^6:NE	5.77×10^{2}	-3.50×10^{2}	−1.647	0.099
θ_y^2:χ_{DL}	5.79×10^{-2}	7.33×10^{-3}	7.9	<0.001
θ_y^6:χ_{DL}	1.76×10^{-4}	2.18×10^{-5}	8.06	<0.001

b) Coefficient for the DL regression with $h_0 = 1.5\,\mathrm{T}$

Name	coef	std err	z	P>|z|
Intercept	-3.11×10^{-16}	1.04×10^{-15}	−0.2986	0.765
ANE	-6.08×10^{4}	-4.37×10^{5}	0.139	0.889
NE	8.97×10^{3}	-4.47×10^{5}	−0.020 06	0.984
θ_y	-1.47×10^{-18}	3.04×10^{-16}	−0.004 831	0.996
distortion	-1.29×10^{-19}	3.32×10^{-17}	−0.003 877	0.997
NHE	-5.06×10^{-10}	3.55×10^{-7}	−0.001 425	0.999
k_1	-4.16×10^{-17}	4.12×10^{-15}	−0.010 11	0.992
χ_{DL}	5.65×10^{-4}	1.17×10^{-2}	0.048 48	0.961
θ_y^4	-1.10×10^{-17}	4.64×10^{-18}	−2.368	0.018
θ_y^2:ANE	-5.98×10^{4}	-4.37×10^{4}	1.369	0.171
θ_y^2:NE	1.30×10^{5}	-4.52×10^{4}	−2.868	0.004
θ_y^3:distortion	-1.04×10^{-18}	9.80×10^{-19}	−1.063	0.288
θ_y^4:χ_{DL}	5.12×10^{-4}	3.85×10^{-5}	13.31	<0.001
θ_y:distortion:NHE	1.35×10^{-8}	5.90×10^{-9}	2.292	0.022
θ_x^2:NE	-1.05×10^{5}	-3.48×10^{4}	3.02	0.003
k_1^6:χ_{DL}	9.12	4.26	2.141	0.032

c) Coefficient for the DL regression with $h_0 = 2\,\mathrm{T}$

Name	coef	std err	z	P>|z|
Intercept	3.38×10^{-17}	9.46×10^{-16}	0.035 73	0.971
ANE	-2.72×10^{5}	-4.58×10^{5}	0.5937	0.553
NE	-7.37×10^{5}	-6.31×10^{5}	1.168	0.243
θ_y	-1.82×10^{-18}	3.20×10^{-16}	−0.005 676	0.995
θ_x	5.39×10^{-19}	2.45×10^{-16}	0.002 197	0.998
distortion	-1.08×10^{-19}	3.40×10^{-17}	−0.003 171	0.997
NHE	8.12×10^{-10}	4.47×10^{-7}	0.001 816	0.999
χ_{DL}	-1.30×10^{-3}	1.80×10^{-2}	−0.0721	0.943
θ_y^2	-1.43×10^{-16}	8.99×10^{-17}	−1.588	0.112
θ_y:distortion	-4.40×10^{-17}	1.35×10^{-17}	−3.256	0.001
θ_y^2:NE	2.83×10^{5}	-4.90×10^{4}	−5.781	<0.001
θ_y^2:χ_{DL}	2.91×10^{-3}	1.90×10^{-3}	1.531	0.126
θ_y:distortion:NHE	2.94×10^{-8}	7.42×10^{-9}	3.958	<0.001
θ_x^4:NE	-1.14×10^{4}	-2.53×10^{3}	4.511	<0.001

As observed in the correlation matrix, terms that were strongly correlated shared common parameters (Figure 2.12). It is to be expected that interactions that do not share a primary parameter are not correlated, as the initial parameter sampling was fully uncorrelated. The high correlation values present indicated that the non-linear terms are an improper representation of the actual non-linearity present in the estimation error. Generally, there were multiple correlations for all methods. This demonstrated that none of the parameters represented the real dependencies of the estimation error. This is confirmed, as these highly correlated parameters are also associated with a high p-value (Tables 2.5, 2.6 and 2.7).

A notable absence of PHE, and its interactions, was observed for all high-field method GLM models (Tables 2.5, 2.6 and 2.7). Which was expected for the xy method. The anisotropy order influenced the SOT determination even when the field exceeded the anisotropy field ($H > H_k$), as evidenced by k_1's presence (Tables 2.5, 2.6 and 2.7). This suggests that the anisotropy landscape affected SOT determination when the field was applied outside the sample plane. Rotation along θ_z appeared only for the xy method (Table 2.6), as expected, due to the linear dependency of the harmonic Hall signal with θ_z (Equation. 2.5). While the dependency is a second-order effect in the x and x, y methods.

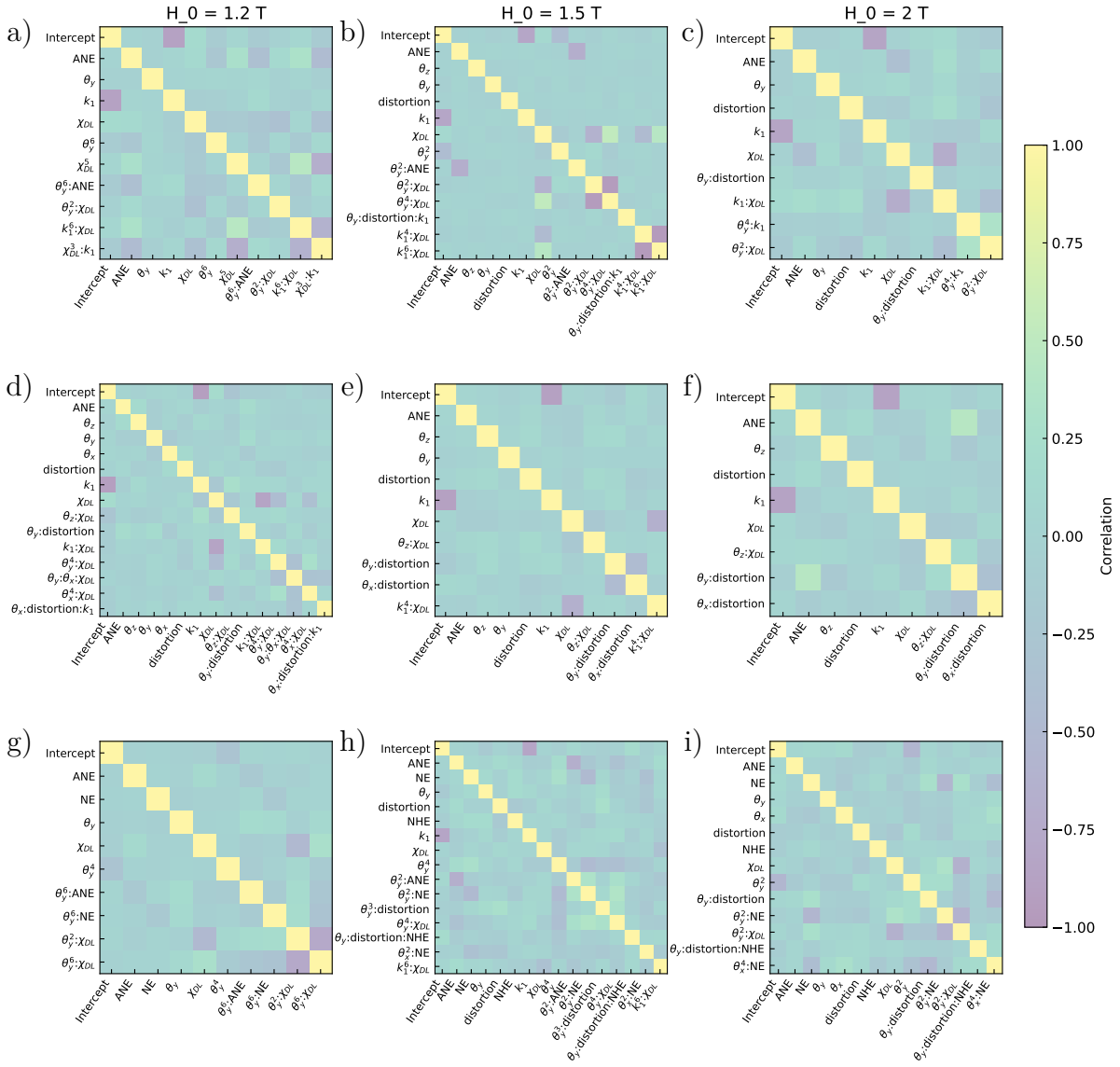

Figure 2.12: High-field method correlation matrices for the linear coefficients determined by the GLM fitting process of Figure 2.11. The columns represent matrices for 1.2 T, 1.5 T and 2 T starting points. The rows correspond respectively to the high-field methods x, xy, and x, y.

2.3.4.2 Differential method

The error estimation was observed to be less peaked, as compared to the high-field method (Figure 2.13). This indicated that low-field methods had a broader distribution. The best estimations were obtained when both PHE and thermoelectric effect corrections were included, with a standard deviation of $1.19 \times 10^{-14}\,\mathrm{T\,A^{-1}\,m^2}$ for the FL determination (Figure 2.13e) and $0.67 \times 10^{-14}\,\mathrm{T\,A^{-1}\,m^2}$ for the DL determination (Figure 2.13f).

The largest estimation error was present on the two methods that did not include a thermal correction (Figure 2.13a-d), where the DL estimation error distribution was the largest, with a standard deviation reaching $\approx 16 \times 10^{-14}\,\mathrm{T\,A^{-1}\,m^2}$. These distributions were dominated by both the ANE and NE parameter distributions. This was expected after observing the single variable dependence in Figure 2.6, where both thermal effects had a strong impact on the DL estimation.

The GLM was able to fit the residual significantly better for the differential method, increasing the accuracy dramatically, as compared with the high-field method (Tables 2.8, 2.9, 2.10 and 2.11). The efficiency of the GLM analysis to capture the estimation error showed its linear dependence on the initial parameters. Each parameter is associated with a small error, but the sum of these broadens the distribution of the overall error.

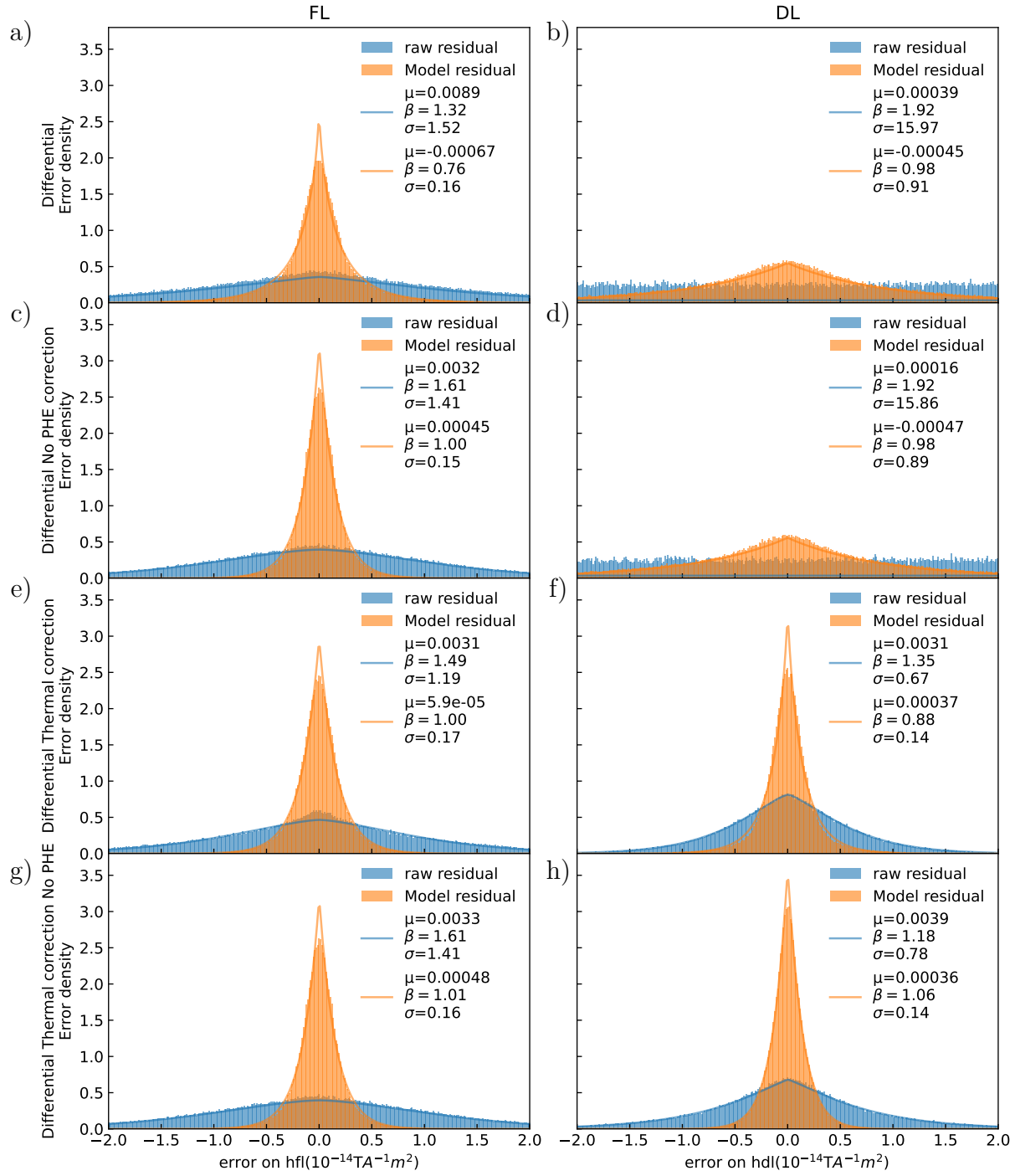

Figure 2.13: The differential model FL absolute error (left column, h_{FL}) and DL absolute error (right column, h_{DL}) distributions, residuals for both without any correction (blue) and after applying a GLM model (orange). The first row corresponds to the differential method, the second row to the differential method with the planar Hall effect correction, the third row to the differential method with the thermal correction, and the fourth row to the differential method with thermal correction and without planar Hall effect correction.

Table 2.8: Differential method (initial) DL and FL coefficient values determined by GLM. The units are given as DL and FL efficiency ($\mathrm{T\,A^{-1}\,m^2}$) in relation to the initial coefficient unit. Colons indicate an interaction.

a) Coefficients for the DL regression

Name	coef	std err	z	P>|z|
Intercept	-8.06×10^{-17}	3.10×10^{-17}	−2.597	0.009
PHE	1.59×10^{-8}	1.34×10^{-8}	1.189	0.234
k_1	3.09×10^{-16}	1.07×10^{-16}	2.873	0.004
θ_z	-1.06×10^{-18}	5.37×10^{-18}	−0.1973	0.844
ANE	-3.63×10^{7}	1.79×10^{4}	−2026	<0.001
NE	-5.02×10^{6}	1.79×10^{4}	−279.9	<0.001
χ_{FL}	1.05×10^{-4}	2.68×10^{-4}	0.3914	0.696
χ_{DL}	-9.51×10^{-2}	5.37×10^{-4}	−177.1	<0.001
PHE:χ_{FL}	-2.01×10^{7}	2.32×10^{5}	−86.69	<0.001
k_1:χ_{DL}	3.12×10^{-1}	1.86×10^{-3}	168	<0.001
θ_z:χ_{FL}	1.54×10^{-2}	9.31×10^{-5}	165.2	<0.001
ANE:k_1	-6.65×10^{7}	6.22×10^{4}	−1070	<0.001
NE:k_1	-1.17×10^{8}	6.21×10^{4}	−1889	<0.001

b) Coefficients for the FL regression

Name	coef	std err	z	P>|z|
Intercept	-3.48×10^{-18}	9.36×10^{-18}	−0.3715	0.710
PHE	4.18×10^{-9}	4.04×10^{-9}	1.035	0.301
k_1	1.04×10^{-17}	3.24×10^{-17}	0.3201	0.749
θ_z	-8.75×10^{-19}	1.62×10^{-18}	−0.5404	0.589
ANE	-6.17×10^{2}	2.69×10^{3}	−0.2292	0.819
NE	6.67×10^{1}	2.69×10^{3}	0.024 79	0.980
χ_{FL}	-2.57×10^{-1}	1.62×10^{-4}	−1588	<0.001
χ_{DL}	-7.75×10^{-5}	8.07×10^{-5}	−0.9604	0.337
k_1:χ_{FL}	6.09×10^{-1}	5.61×10^{-4}	1084	<0.001
θ_z:χ_{DL}	-1.69×10^{-2}	2.80×10^{-5}	−602.7	<0.001
ANE:PHE	-4.22×10^{15}	2.34×10^{12}	−1806	<0.001
ANE:θ_z	9.07×10^{5}	9.36×10^{2}	969.1	<0.001
NE:PHE	-2.74×10^{15}	2.33×10^{12}	−1176	<0.001
NE:θ_z	5.91×10^{5}	9.35×10^{2}	632	<0.001

Table 2.9: Differential method (no PHE correction) DL and FL coefficient values determined by GLM. The units are given as DL and FL efficiency ($\mathrm{T\,A^{-1}\,m^2}$) in relation to the initial coefficient unit. Colons indicate an interaction.

a) Coefficients for the DL regression

Name	coef	std err	z	P>|z|
Intercept	-7.33×10^{-17}	3.04×10^{-17}	−2.409	0.016
PHE	1.30×10^{-8}	1.31×10^{-8}	0.9889	0.323
k_1	2.84×10^{-16}	1.05×10^{-16}	2.698	0.007
θ_z	-6.90×10^{-19}	5.26×10^{-18}	−0.131	0.896
ANE	-3.60×10^{7}	1.76×10^{4}	−2049	<0.001
NE	-4.97×10^{6}	1.76×10^{4}	−282.5	<0.001
χ_{FL}	8.81×10^{-5}	2.62×10^{-4}	0.3358	0.737
χ_{DL}	-9.30×10^{-2}	5.27×10^{-4}	−176.6	<0.001
PHE:χ_{FL}	-9.04×10^{7}	2.28×10^{5}	−397.2	<0.001
k_1:χ_{DL}	3.05×10^{-1}	1.82×10^{-3}	167.4	<0.001
θ_z:χ_{FL}	1.54×10^{-2}	9.12×10^{-5}	168.7	<0.001
ANE:k_1	-6.60×10^{7}	6.09×10^{4}	−1083	<0.001
NE:k_1	-1.16×10^{8}	6.09×10^{4}	−1912	<0.001

b) Coefficients for the FL regression

Name	coef	std err	z	P>|z|
Intercept	-2.29×10^{-18}	5.19×10^{-18}	−0.4424	0.658
PHE	3.45×10^{-9}	2.24×10^{-9}	1.543	0.123
k_1	4.13×10^{-18}	1.79×10^{-17}	0.2304	0.818
θ_z	7.58×10^{-20}	8.98×10^{-19}	0.084 49	0.933
ANE	-1.35×10^{3}	1.49×10^{3}	−0.9051	0.365
NE	-1.34×10^{3}	1.49×10^{3}	−0.8967	0.370
χ_{FL}	-2.51×10^{-1}	8.98×10^{-5}	−2797	<0.001
χ_{DL}	2.25×10^{-5}	4.47×10^{-5}	0.5033	0.615
PHE:χ_{DL}	-8.20×10^{7}	3.87×10^{4}	−2117	<0.001
k_1:χ_{FL}	5.93×10^{-1}	3.11×10^{-4}	1905	<0.001
θ_z:χ_{DL}	-1.69×10^{-2}	1.55×10^{-5}	−1088	<0.001
ANE:θ_z	9.16×10^{5}	5.19×10^{2}	1765	<0.001
NE:θ_z	5.95×10^{5}	5.18×10^{2}	1149	<0.001

Table 2.10: Differential method (with thermal correction) DL and FL coefficient values determined by GLM. The units are given as DL and FL efficiency ($\mathrm{T\,A^{-1}\,m^2}$) in relation to the initial coefficient unit. Colons indicate an interaction.

a) Coefficients for the DL regression

Name	coef	std err	z	P>|z|
Intercept	-1.32×10^{-17}	5.94×10^{-18}	−2.215	0.027
AMR	9.55×10^{-9}	5.12×10^{-9}	1.866	0.062
k_1	4.23×10^{-17}	2.05×10^{-17}	2.062	0.039
θ_z	1.73×10^{-18}	1.03×10^{-18}	1.681	0.093
χ_{FL}	9.36×10^{-6}	5.12×10^{-5}	0.1827	0.855
χ_{DL}	-9.80×10^{-2}	1.03×10^{-4}	−953.1	<0.001
AMR:χ_{FL}	-1.31×10^{8}	8.87×10^{4}	−1473	<0.001
k_1:χ_{DL}	3.22×10^{-1}	3.56×10^{-4}	904.7	<0.001
θ_z:χ_{FL}	1.53×10^{-2}	1.78×10^{-5}	859.2	<0.001

b) Coefficients for the FL regression

Name	coef	std err	z	P>|z|
Intercept	-1.34×10^{-18}	5.56×10^{-18}	−0.2414	0.809
k_1	6.71×10^{-19}	1.92×10^{-17}	0.034 92	0.972
θ_z	1.48×10^{-19}	9.61×10^{-19}	0.1544	0.877
ANE	-7.57×10^{2}	1.60×10^{3}	−0.4737	0.636
NE	-1.78×10^{3}	1.60×10^{3}	−1.117	0.264
χ_{FL}	-2.57×10^{-1}	9.62×10^{-5}	−2675	<0.001
χ_{DL}	-4.28×10^{-6}	4.79×10^{-5}	−0.089 41	0.929
k_1:χ_{FL}	6.09×10^{-1}	3.33×10^{-4}	1827	<0.001
θ_z:χ_{DL}	-1.66×10^{-2}	1.66×10^{-5}	−997.3	<0.001
ANE:θ_z	9.26×10^{5}	5.55×10^{2}	1668	<0.001
NE:θ_z	6.03×10^{5}	5.55×10^{2}	1088	<0.001

Table 2.11: Differential method (with thermal and without PHE correction) DL and FL coefficient values determined by GLM. The units are given as DL and FL efficiency ($\mathrm{T\,A^{-1}\,m^2}$) in relation to the initial coefficient unit. Colons indicate an interaction.

a) Coefficients for the DL regression

Name	coef	std err	z	P>|z|
Intercept	-8.92×10^{-18}	4.33×10^{-18}	-2.062	0.039
AMR	7.33×10^{-9}	3.73×10^{-9}	1.966	0.049
PHE	8.58×10^{-11}	1.87×10^{-9}	0.045 95	0.963
k_1	3.08×10^{-17}	1.50×10^{-17}	2.056	0.040
θ_z	7.56×10^{-19}	7.49×10^{-19}	1.01	0.313
χ_{FL}	4.25×10^{-5}	3.73×10^{-5}	1.138	0.255
χ_{DL}	-9.53×10^{-2}	7.50×10^{-5}	-1271	<0.001
AMR:χ_{FL}	-1.30×10^{8}	6.46×10^{4}	-2005	<0.001
PHE:χ_{FL}	-9.07×10^{7}	3.24×10^{4}	-2803	<0.001
k_1:χ_{DL}	3.12×10^{-1}	2.59×10^{-4}	1205	<0.001
θ_z:χ_{FL}	1.54×10^{-2}	1.30×10^{-5}	1184	<0.001

b) Coefficients for the FL regression

Name	coef	std err	z	P>|z|
Intercept	-1.59×10^{-18}	5.12×10^{-18}	-0.3113	0.756
PHE	3.14×10^{-9}	2.21×10^{-9}	1.422	0.155
k_1	1.91×10^{-18}	1.77×10^{-17}	0.108	0.914
θ_z	1.48×10^{-19}	8.85×10^{-19}	0.1672	0.867
ANE	-1.12×10^{3}	1.47×10^{3}	-0.764	0.445
NE	-1.52×10^{3}	1.47×10^{3}	-1.035	0.301
χ_{FL}	-2.51×10^{-1}	8.86×10^{-5}	-2838	<0.001
χ_{DL}	4.25×10^{-6}	4.41×10^{-5}	0.0965	0.923
PHE:χ_{DL}	-8.20×10^{7}	3.82×10^{4}	-2146	<0.001
k_1:χ_{FL}	5.93×10^{-1}	3.07×10^{-4}	1934	<0.001
θ_z:χ_{DL}	-1.69×10^{-2}	1.53×10^{-5}	-1104	<0.001
ANE:θ_z	9.19×10^{5}	5.11×10^{2}	1797	<0.001
NE:θ_z	5.98×10^{5}	5.10×10^{2}	1172	<0.001

There was a correlation between k_1 and the intercept for all results (Figure 2.14). These parameters were not independent. The intercept parameter was present due to the choice of using k_1 instead of k_2 for the governing parameter. As k_1 and k_2 were linked by an affine relation, the intercept appears to transform the k_1 parameter into k_2.

When significant, the FL, DL, ANE, and NE are highly correlated with their respective k_1 interactions (Figure 2.14). We did not expect a significant FL parameter within the GLM analysis, as there was not a systematic error in the FL determination in the ideal scenario. We expected the DL to be present, due to the 5% systematic error originating from the analytical derivation. However, all the reported values coming from the GLM analysis show a DL value of 10% systematic error (Tables 2.8, 2.9, 2.10 and 2.11), which indicated there were other contributions to this parameter.

For the ANE and NE, the results were more complicated. An interaction with these parameters with k_1 is expected analytically (Section 1.6.3.3). However, the second order anisotropy effect on these parameters was expected to be similar to the effect observed on the DL torque due to the similarity of the ANE, NE and DL contributions to the harmonic Hall signal. The fact that k_2 was established to be a better governing variable than k_1, and that all of these parameters are highly correlated with their interaction with k_1, suggested that the significance of these individual parameters originates from the use of k_1 instead of k_2.

On top of having the best determination, the differential model with both corrections applied demonstrated the largest improvement from the GLM analysis, with the least significant parameters (Table 2.10). θ_z , AMR and k_1 dominate the model. The θ_z parameter mixed the field longitudinal and transverse signals, while the AMR appears due to the addition of the longitudinal signal for the thermal correction. There was no PHE contribution, demonstrating that the correction is only effective when corrections of similar effects are also used, e.g. thermoelectric corrections.

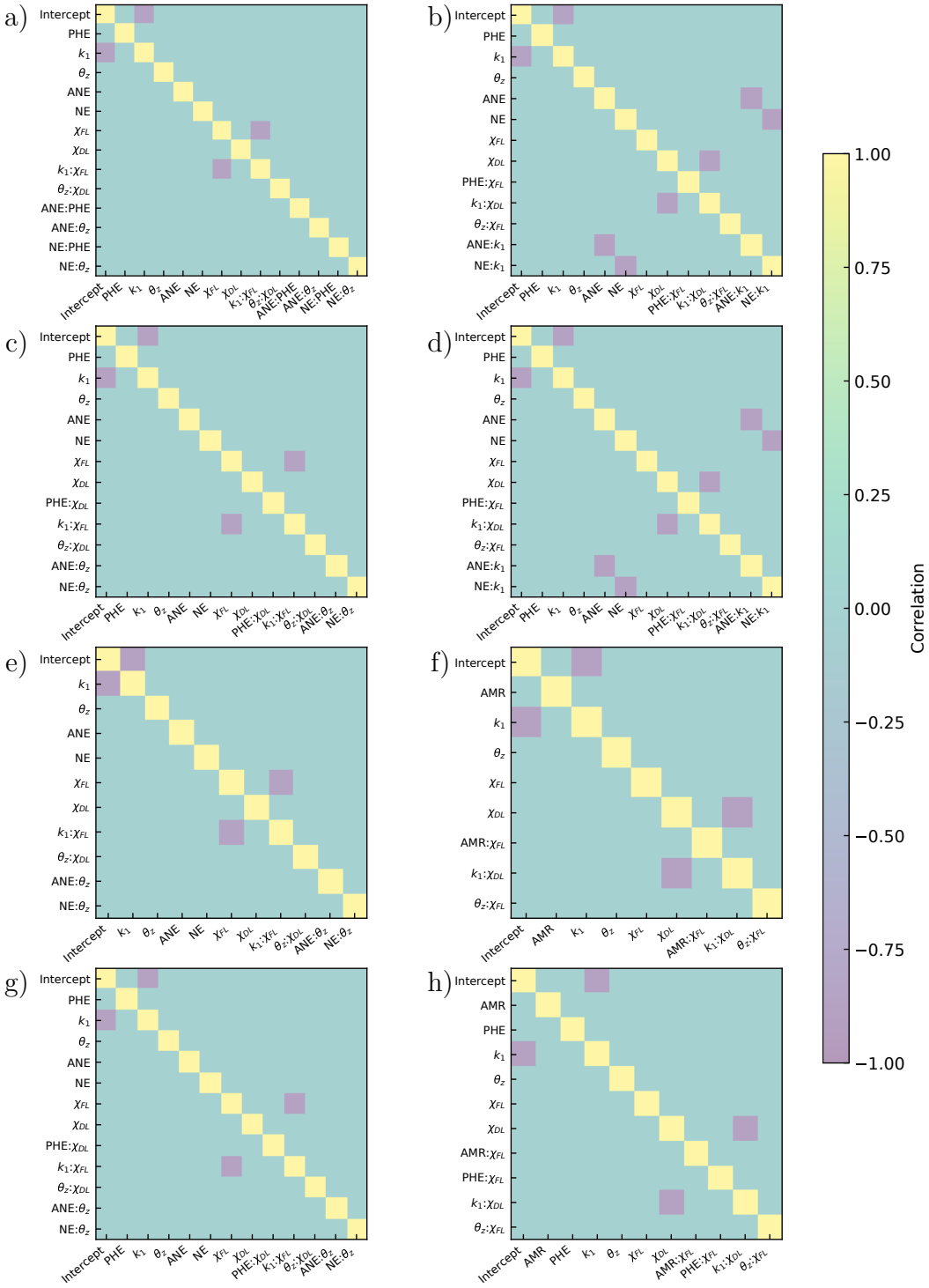

Figure 2.14: Differential method correlation matrices for the linear coefficients determined by the GLM fitting process of Figure 2.13. The columns represent matrices for FL and DL. The rows correspond respectively to the initial, without PHE correction, with thermal corrections, and with thermal and without PHE corrections differential methods.

2.4 Discussion

2.4.1 High-field method

The high-field analytical methods demonstrated relatively high accuracy overall, with increased accuracy in the x, y or xy versions of the method. The thermoelectric contribution developed in [87] was found to separate the SOT and thermoelectric coefficient correctly.

The overall efficiency of the xy method could be at first understood from the particular contribution of the PHE. The 45° field direction corresponds to the maximum value of the PHE, making its contribution to the harmonic Hall signal robust to small variations of the magnetisation vector. However the absence of the PHE in any of the methods contradicts this statement.

The accuracy could be further increased by using the θ_y correction, as described in Section 2.3.3. Ideally, a low angle offset (θ_y) should be used to reduce the error in the model. However, in the real world this is not possible, as magnetic multi-domain states will appear. Thus, the macro-spin approximation is then not met, as required by both analytical methods and the present numerical method. Starting to fit the signal at a value larger than the anisotropy field would lead to better accuracy in the high-field analytical method, but this would be at the expense of precision of the SOT coefficient determination. The anisotropy order and the current source distortion significantly affect this analytical method. The latter must be kept as low as possible to reduce overall error and improve accuracy.

When determining the parameter dependence of the high-field methods by varying only one parameter at a time, only the misalignment affected the error of the DL field estimation. On the other hand, when addressing multiple parameters within the GLM model, most of the errors in the residual were found to be non-linear with high order parameters

for anisotropy, alignment and SOT and/or interactions between different effects, which were not visible in the single variable analysis.

The presence of higher order terms in the fitting coefficient of the error residual comes from the non-linear behaviour and poorly determined approximation of the magnetisation direction as a function of the external field. As a result, an inclusion of sample position, source distortion and anisotropy order is mandatory to ensure accurate (low systematic error) and precise (low random variability) determination of the DL torque. However, these are not usually performed in the literature and are more likely to be fulfilled using numerical models, such as the one presented here or the one given by [112] with the addition of the thermoelectric and field alignment parameters.

2.4.2 Differential method

The differential analytical method was the most accurate when both thermoelectric and PHE corrections were included. There is a gap in reporting the thermoelectric coefficient data for most materials studied in spintronics. Thus, it is challenging to quantify the error due to thermoelectric effects in previously published research. However, this issue has been addressed in the literature and solutions exist [76, 85]. Additionally, measuring the longitudinal voltage to include thermoelectric contributions was systematically required in order to have an accurate estimation of the FL and DL torques. In the future, this should be incorporated as a best practice when using the differential analytical method for the measurement of SOT.

The PHE correction alone did not improve the measurement of the DL torque and marginally decreased the precision of the FL torque measurement, due to the propagation of thermoelectric effects in the FL estimations. This finding concurs with previously published literature, where the PHE correction was significant when the PHE effect was large compared to the AHE [111], or in the case of a small ratio of PHE:AHE the impact of the PHE

correction was small [81]. However, the results of our study contradict the opinion given in [82, 83], where the PHE was systematically neglected. In fact, we found that when both thermoelectric effect and PHE are taken into account, the accuracy of the FL and DL estimation was systematically improved with the PHE correction.

When including PHE corrections, any effect with a similar order of magnitude should also be applied to the model in order to benefit from this single correction. Thus, the results from the GLM analysis demonstrate that the thermoelectric and PHE corrections are not sufficient. An additional correction is required due to the AMR, which can come from the spin Hall magnetoresistance effect occurring in bilayer samples. This additional AMR correction is a consequence of the previous PHE correction, which mixes the transverse and longitudinal signals to remove NE and ANE effects. The AMR results in a change in longitudinal resistance equal to $-\rho^{\mathrm{AMR}}(m_x^2+m_y^2)$ on the first harmonic, which also contributes to the second harmonic due to the effect of the SOT on $\mathbf{m}$. To implement this correction, the longitudinal harmonic Hall signal must be derived following the same procedure as in Sections 1.6.3.1 and 1.6.3.2, including the AMR contribution terms. Note, differential methods are correct only when the first order anisotropy is the only one involved. As the second order anisotropy methodology differential method [77] was not widely cited within the literature, this was not included within our study, thus we cannot draw conclusions to its use. Finally, we suspect that the presence of the primary χ_{FL} and χ_{DL} parameters in the GLM analysis was related to the presence of second order anisotropy, as these parameters are strongly correlated to the $k_1 : \chi_{\mathrm{FL}}$ and $k_1 : \chi_{\mathrm{DL}}$ interactions.

Misalignment of samples along the z-axis significantly reduced the accuracy of FL and DL torque measurements. When measuring the y- (resp. x) direction a small misalignment in θ_z will result in a projection of the x (resp. y) signal. This projection follows a sinusoidal angular dependence; thus a small angle is directly proportional to the misalignment angle. This doesn't solely originate from the FL and DL signals; spurious signals are additionally

contributing, such as the thermoelectric effect. This was demonstrated in the GLM analysis of the differential method with both PHE and thermoelectric corrects (Table 2.10), where the coefficient associated with θ_z:χ_{FL} and θ_z:χ_{DL} are close to unity and the thermoelectric contributions in interaction with θ_z are close to the respective value, in the opposite direction. While misalignment along the z-axis strongly influenced the accuracy of the FL and DL measurements, misalignment of the field along the x- and y-axes was insignificant and thus removed while reducing the model. Thus, great care during the setup of the measurement is required to reduce z-axis misalignment.

When the aforementioned conditions are fulfilled and the AMR correction applied, the differential analytical method is able to produce accurate determinations of the FL and DL torques. It should be noted that a $\approx 5\%$ systematic error occurs on the DL determination, due to the approximation done during the analytical derivation. When these conditions are not fulfilled, a complete model is required, which takes into account all sample and setup-related parameters, e.g. thermoelectric effects, anisotropy order, field misalignment and current source distortion.

In this study, we did not consider experimental errors in the ANE, PHE or anisotropy parameters. It was not determined how an error in one of these would affect the SOT estimation. We assumed that these measurements were carried out using state-of-the-art techniques that are readily available.

2.5 Conclusions

This research has demonstrated under what conditions each of the published analytical methods are effective and the most crucial parameters to consider to ensure high accuracy. In conditions where the analytical methods fail to produce accurate results, we have shown that an appropriate numerical model can be used to produce accurate estimations of the DL and FL torques.

The high-field determination, while being efficient at removing thermoelectric contributions, suffers from the field offset necessary to obtain a single-domain state. This can be mitigated by removing from the fitting process the data close to the anisotropy field (increasing the h_0 parameter), but this comes at the expense of measurement precision. Due to the non-linearity of the orientation of the magnetisation vector as a function of the field, developing an analytical model with a field offset is challenging. The numerical model also requires a single-domain state; however, this model can address any field offsets that are given as a parameter. Thus, the numerical model is appropriate for using with the high-field methodology for SOT measurements.

Thermoelectric correction is necessary for the differential analytical methods. This means that the longitudinal voltage V_{xx} needs to be recorded in addition to the transverse voltage V_{xy}. An AMR correction is necessary and will need to be developed to increase the accuracy of the DL torque determination. The rotation around the z axis (θ_z) has to be kept as low as feasible to reduce the error originating from the mixing of the two signals associated with both the x- and y-directions.

Here, it has been demonstrated that a numerical model, such as the one presented here, is highly recommended to systematically take into account the range of effects which occur within SOT measurements. This method proves to be robust in regards to all artefacts discussed in this study, while allowing the measurement of crucial parameters. Finally, such models should not be used to compensate for the parameters that are controllable during the experiment, such as the misalignment of a sample, which introduced systematic error in the SOT determination. Effort should be undertaken to ensure measurement conditions are as accurate as possible.

CHAPTER 3

Accurate measurement of spin orbit torque in a single layer using Mn_2Ru_xGa as a test candidate

3.1 Introduction

For spintronics applications, scalable manipulation of magnetisation is essential to obtain information density rivalling other device technologies. To date, research has focused on the creation of a spin current that is injected into the adjacent magnetic layer in a 'current perpendicular-to-plane' (spin transfer torque) or 'current parallel-to-plane' (spin orbit torque) configuration [5]. However, this research has limitations. Even in the most efficient bilayer materials (e. g. CoFeB/β-W), switching occurs at high current densities, where Joule heating significantly contributes to switching by reducing the anisotropy barrier[113, 114]. Therefore, the spin current generation efficiency does not correlate with the switching current density [69]. While thicker anti-ferromagnetic (AFM) films can be successfully reversed, thermal heating is still required [71]. This entails high power consumption, making these devices too inefficient for applications, and reduces the device's lifespan [115]. It is therefore necessary to look for new methods of generating spin orbit torque (SOT) that can increase efficiency by multiple orders of magnitude.

We propose investigating *single-layer* SOT in thin films. There, the SOT is intrinsically scalable, and the absence of an interface separating the generation of the spin current and its effect on local magnetisation would lead to larger SOT efficiency. Therefore, we start with a discussion of the theoretical requirements for SOT in a single layer, including which materials could be suitable, and the methods needed to measure their efficiencies accurately.

Symmetry analysis shows that a broken inversion symmetry is required to obtain SOT. In bi- and multilayer stacks, this is ensured by the presence of two, or more, separate and different layers. Ferromagnetic materials, themselves a source of spin currents [116–119], do not produce *self*-spin-orbit torque, as the induced spin current is parallel to the magnetisation direction. Self-torque is possible if mirror symmetry is broken by a spatial change (such as composition gradient [120]) of the properties of a thin film [121–124]. A more enticing prospect is to rely on the lack of crystallographic inversion symmetry in the material [125], which allows the electron wave vector to couple its spin to the lattice as in the Dresselhaus effect [126].

We therefore conclude that suitable materials for single-layer SOT must lack inversion symmetry in their crystallographic structure, and possess relatively strong spin-orbit coupling to ensure efficient spin polarisation of the band structure. For spintronics applications, a large spin polarisation facilitates electrical detection of the magnetisation direction, and a low net moment minimises the detrimental effects of external magnetic perturbations. Using these criteria, Mn_2Ru_xGa is a suitable material for this study [1, 127, 128]. Mn_2Ru_xGa is an inverse Heusler alloy growing in the XA structure with two manganese crystallographic positions, the 4a and 4c sublattices. On MgO (001) substrates, it crystallises in the non-centrosymmetric space group $I\bar{4}m2$ (reduced from $F\bar{4}3m$ by the substrate-induced strain). The two Mn sublattices couple antiferromagnetically to produce a low-moment, high spin polarisation ferrimagnet [46].

Table 3.1: Form of the SOT current to effective field conversion tensors for point group symmetry, $\bar{4}3m$ and ∞m, as determined by symmetry analysis.

Symmetry	Field-like ξ_{FL}	Damping-like ξ_{DL}
$\bar{4}3m$[56]	$\begin{pmatrix} 0 & 0 & 0 \\ 0 & 0 & 0 \\ 0 & 0 & 0 \end{pmatrix}$	$\begin{pmatrix} 0 & x_1 m_z & x_1 m_y \\ x_1 m_z & 0 & x_1 m_x \\ x_1 m_y & x_1 m_x & 0 \end{pmatrix}$
$\bar{4}2m$[56]	$\begin{pmatrix} 1 & 0 & 0 \\ 0 & -1 & 0 \\ 0 & 0 & 0 \end{pmatrix}$	$\begin{pmatrix} 0 & x_3 m_z & x_2 m_y \\ x_3 m_z & 0 & x_2 m_x \\ x_1 m_y & x_1 m_x & 0 \end{pmatrix}$
∞m	$\begin{pmatrix} 0 & 1 & 0 \\ -1 & 0 & 0 \\ 0 & 0 & 0 \end{pmatrix}$	$\begin{pmatrix} x_3 m_z & 0 & x_2 m_x \\ 0 & x_3 m_z & x_2 m_y \\ x_1 m_x & x_1 m_y & x_4 m_z \end{pmatrix}$
literature ∞m	$\begin{pmatrix} 0 & 1 & 0 \\ -1 & 0 & 0 \\ 0 & 0 & 0 \end{pmatrix}$	$\begin{pmatrix} m_z & 0 & -m_x \\ 0 & m_z & -m_y \\ -m_x & -m_y & 0 \end{pmatrix}$

We fabricate thin films of MRG by sputter deposition. The typical film thickness is 26 nm, and they are capped with a protective layer of AlOx to prevent oxidation. The inversion symmetry of these samples is therefore broken by two different mechanisms. First the thin-film geometry allows interface-induced spin-orbit torque. This has ∞m symmetry, and the spin-orbit torque field has both field-like (FL) and damping-like (DL) components, as seen in Table 3.1. The tensor derived from a pure symmetry analysis of the ∞m point group, obtained by assuming a power series dependence on the magnetisation, allows for more free parameters in the damping term than is usually given in the literature [66], but we retain the literature ∞m SOT expression in this study, as experimentally we find that the SOT studied here shows perfect agreement with the reduced parameters tensor expression for the effective field. Second, the crystallographic structure of Mn_2Ru_xGa is $F\bar{4}3m$ in the bulk material, reduced to $I\bar{4}m2$ as mention above. $\bar{4}3m$ allows only DL components, while $\bar{4}m2$ adds a FL component and the coefficients of the DL terms become less constrained. For simplicity, we will consider a FL terms matching $\bar{4}m2$ and DL terms of $\bar{4}3m$. The full SOT tensors are given in Table 3.1.

For all SOT effective fields, the spin efficiency is defined as:

$$\xi = \frac{2e}{\hbar}\frac{\mu_0 H_{\mathrm{DL}} M_s t_M}{j_{tot}}\,, \tag{3.1}$$

where e is the electronic charge, $\hbar$ the reduced Plank constant, μ_0 the magnetic permittivity, H_{DL} the DL fields generated from the SOT, M_s the saturation magnetisation of the magnetic material, t_M the thickness of the magnetic material and j_{tot} the total current density through the sample.

We have seen that broken inversion symmetry is a necessary condition to obtain SOT. In bi- and multilayer stacks, this is reasonably easy to control, as common deposition techniques such as molecular-beam epitaxy (MBE), sputtering and thermal evaporation are able to produce multilayer films where each layer can be sub-nanometric and where the roughness at the interfaces can be inferior to one atomic layer on average.

Relying on the lack of inversion symmetry of the crystallographic cell is another matter. More often than not, the macroscopic sample is made up of a large number of crystallites, which may be non-centrosymmetric, but are often not coherently ordered throughout the sample.

We take MRG in its cubic form ($F\bar{4}m$) as an example. There, inversion of the crystallographic cell, is equivalent to a $\pi/2$ rotation around one of the principal axis (Figure 3.1).

During thin film growth, this rotation is the most likely twinning to occur, as (if we assume the growth axis to be the crystallographic c-axis), the a- and b-axes are of the same length, and the MgO substrate induces no difference between the [110] and [1$\bar{1}$0] directions. They are symmetrically equivalent.

The SOT in the inverted (or rotated by 90°) crystallite is opposite to that of the non-inverted one; hence, for a random 50/50 distribution of the two twins, we expect that macroscopically no SOT can be observed.

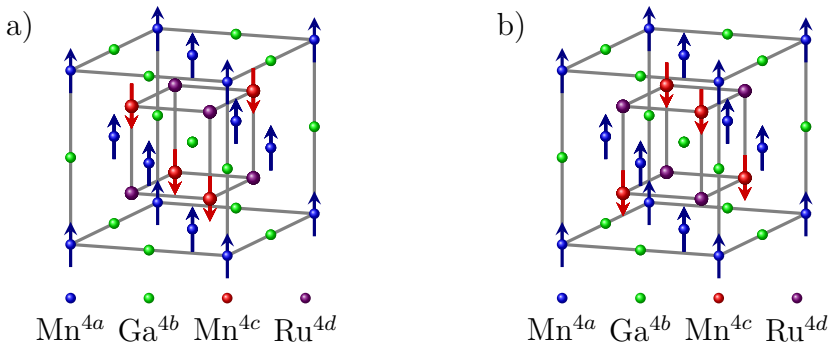

Figure 3.1: Mn_2Ru_xGa inverse Heusler crystal structure. The ordering of Ru and Mn on the 4c and 4d positions distinguishes the non-centrosymmetric XA structure from the symmetric $L2_1$ ($Fm\bar{4}3m$). Figures a and b represent the crystal structure before and after the inversion symmetry operation. We conclude from visual inspection that, in this crystal structure, the inversion and rotation by $\pi/2$ represent the same transformation of the crystallographic structure.

Optimising the growth of these single-layer thin films for SOT is challenging, since laboratory X-ray diffraction can't distinguish between e. g. XA or $L2_1$ structures, nor can it distinguish the [110] from the [1$\bar{1}$0] direction. Therefore the spin-orbit torque observed experimentally is likely much lower than those expected due to e. g. twinning during growth. We need a technique to detect small SOT signals, which can then be used to confirm the degree of sample-wide crystallographic coherence using standard laboratory equipment. This could then be used to implement an iterative cycle, optimising the growth conditions to obtain a single crystal sample and thus a single-layer SOT.

Here we determine the strength and symmetry of the SOT of a single-layer of MRG, considering both interfacial and intrinsic contributions. We will address how to accurately model and measure small SOT signals, considering all transport coefficients, higher order anisotropies and imperfect sample alignment. This model will be used first to model two reference samples: an asymmetric and a symmetric cobalt-platinum multilayer. The fitting of the CoPt multilayer provides confirmation of the validity of our numerical model, and highlights the shortcomings of the commonly used analytical methods. It allows us to isolate magnetothermal effects from the SOT contribution and to give a much-improved numerical estimate of the SOT efficiency.

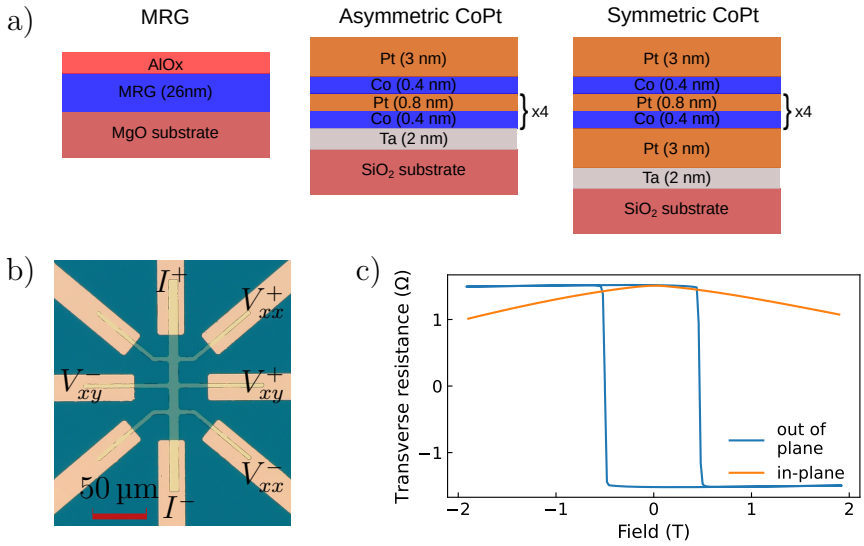

Figure 3.2: a) Three different samples studied. First, a single-layer of Mn_2Ru_xGa, in which the broken inversion symmetry, in principle, originates from the crystallographic structure. We also include a contribution due to the difference between the substrate and the capping layer. Second, a five-layer stack of cobalt platinum, the inversion symmetry is broken by the 3 nm *platinum layer used for capping. Finally, a similar sample to the previous, but with the addition of a Pt layer at the bottom of the stack to make the sample inversion symmetric and cancel the SOT induced by the top layer. b) The standard Hall bar shape with the position of the different electrical contacts. c) The out-of-plane and in-plane field loop recorded by anomalous Hall effect (AHE) in Mn_2Ru_xGa.*

3.2 Method and theory

3.2.1 Sample choice and growth

In order to validate our numerical approach, we produced two sets of CoPt multilayer samples, one structurally asymmetric and one structurally symmetric (see Figure 3.2). Pt is a known efficient material for charge to spin conversion via the spin Hall effect (SHE). Additionally, CoPt multilayers are a convenient structure to achieve robust perpendicular magnetic anisotropy (PMA); the macrospin approximation is valid for these samples (Chapter 1 Section 1.6).

Two CoPt multilayer reference samples were prepared by magnetron sputtering at room temperature on a silicon substrate with 500 nm thermal oxide. A 2 nm buffer layer of tantalum was first deposited on both samples. A 3 nm layer of Pt was deposited on one

of the samples, while the other was kept in the loadlock. Then the second sample was loaded into the chamber and the deposition of the Co and Pt multilayer was commenced. Both samples were kept in vacuum during the full deposition process. The argon flow was kept at the lowest possible value while maintaining a stable plasma during sputtering, ensuring a smooth interface. To calibrate the target deposition rate, a single layer film was deposited and its thickness was measured by X-ray reflectivity. Layer thickness of the final sample was determined from this calibration by controlling the deposition time.

The first sample was structurally symmetric, with 3 nm Pt deposited both before and after the CoPt stack (SiO_2/Ta(2)/Pt(3)/[Co(0.4)Pt(0.8)]$_4$/Co(0.4)/Pt(3)). The second sample was asymmetric, with the first Pt layer omitted while retaining the same capping layer (SiO_2/Ta(2)/[Co(0.4)Pt(0.8)]$_4$/Co(0.4)/Pt(3)). Both stacks are represented on Figure 3.2.a).

The asymmetric multilayer consisted of five layers of cobalt (0.4 nm) separated by a (0.8 nm) platinum layer. The five repetitions of cobalt layers, corresponding to a total thickness of 2 nm, exhibit a strong perpendicular magnetic anisotropy. Both samples (symmetric and asymmetric) were capped by a 3 nm thick platinum layer. For the symmetric sample, a platinum layer with a thickness of 3 nm was inserted between the tantalum buffer layer and the multilayer. This sample should not exhibit SOT.

Magnetron sputtering was used to deposit 26 nm thick Mn_2Ru_xGa films on an MgO substrate in an ultra high vacuum (UHV) system with stoichiometric Mn_2Ga and ruthenium targets. The rate of deposition for the Mn_2Ga and Ru targets were individually established by depositing a single layer and measuring its thickness using X-ray reflectivity. This allowed the composition to be determined, and therefore the x value in Mn_2Ru_xGa as a function of input power on the Mn_2Ga target. The MgO single crystal substrate was annealed at 600 °C in vacuum for 30 min. Then, the Mn_2Ru_xGa was co-sputtered from the Mn_2Ga and Ru targets, maintaining the substrate temperature at 425 °C. A capping

layer of 2.6 nm of aluminium oxide was deposited at room temperature to protect the sample from oxidation. The film's thickness was confirmed using X-ray reflectivity.

Ruthenium deficiency in sputtered Mn_2Ru_xGa has been shown to lead to disorder [1]. In order to stabilise the lack of inversion symmetry, we focused on near-stoichiometric MRG (Mn_2Ru_1Ga). The substrate temperature was kept at 425 °C during deposition to promote a square Hall loop (Figure 3.2.c) that can be described by a single macrospin approximation. This is a requirement for the harmonic Hall analysis [129]. The crystallographic structure was determined by X-ray diffraction Figure 3.2; however, this cannot delineate which disorder was present within the sample, e. g. an XA or a B2 structure. The in-plane coherence length, which denotes the distance over which the crystallographic plane contributes coherently to the diffraction pattern, was determined to be $\approx$ 11.5 nm. O'Brien [130] determined this using reciprocal space mapping and fitting the peak with the Scherrer equation. The deposition temperature of $T_s = 250\,°C$ significantly enhanced the resulting in-plane coherence length, which reached $\approx$ 181 nm. However, this entails an in-plane anisotropy with the sublattice moments being close to in-plane at zero field. The field required to saturate the magnetisation increased to 3 T at 150 K for these samples, and no saturation was obtained at room temperature with an applied field of 5.5 T. The field loop changes from being square to a wasp waist shape [131]. We conclude that samples of high in-plane coherence cannot be modelled as single macrospin, as is required for the harmonic Hall analysis, and thus we do not discuss these further in this thesis.

3.2.2 Spin Orbit torque measurements

The harmonic Hall method has emerged as the standard technique to determine the symmetry and magnitude of the SOT in thin films [5, 75]. Thermoelectric effects, such as the anomalous Nernst effect (ANE), contribute to the harmonic voltages. These con-

tributions can be modelled and corrected for when measuring the SOT signal as shown in [76, 85]. These methods are appropriate for samples with simple uniaxial anisotropy ($E = k_1 \sin^2(\theta)$) and large SOT signals. We discuss this in more detail in the section on thermal effects (Section 1.6.3.3). The low magnetisation of Mn_2Ru_xGa leads to anisotropy fields exceeding several tesla, and the in-equivalence of the two magnetic sublattices of the ferrimagnet entails a complicated anisotropy energy landscape with large first and second order tetragonal terms. These second-order terms increase the complexity when processing the harmonic Hall signal [77] as it changes the field dependence of the magnetisation, and the inclusion of higher-order terms implies there is no analytical solution for the equilibrium position of the magnetisation in an applied field. This remains the case even when the external field is strictly in-plane (Chapter 1 Section 4.3.1.1). As the SOT signal depends directly on the derivative of the magnetisation with respect to the field around its equilibrium position, any errors made here propagate (and amplify) as the SOT signal is determined. Our aim is to capture *any* SOT contribution, even small, present in the single-layer Mn_2Ru_xGa. This is particularly important when using a model based on symmetry arguments, as symmetry only states whose effects are allowed, and not their magnitude. A more accurate approach is thus required. We therefore numerically model the galvano-magnetic response when the magnetisation vector deviates from its equilibrium position.

3.2.2.1 Thermal effects as part of the harmonic Hall measurement

The harmonic Hall method exploits the narrowband character of lock-in amplification to extract the small SOT signal from the much larger AHE contribution. This works, as we have seen, because the amplitude of the SOT signal depends on the current density j, so that its contribution to the signal is proportional to j^2, that is $\sin^2(\omega t) \propto \cos(2\omega t)$.

The applied bias current density j also heats the thin film (joule heating) so that the instantaneous temperature of the sample is $\propto j^2$, and the asymmetric substrate/film/air

then leads to a, oscillating at a frequency of 2ω, vertical temperature gradient. This in turn enables an anomalous Nernst effect $\propto \nabla T \times M$ at that frequency, i. e. with the same symmetry as the DL SOT we aim to observe. It is impossible to separate the two based on a single measurement of the transverse voltage with applied fields lower than the anisotropy field.

Two methods have been proposed to resolve this issue. First, the Nernst effect also contributes to the longitudinal voltage, while the SOT contribution there is expected to be much lower and with a different field dependence. By recording both components (transverse and longitudinal), we are able to separate the Nernst and SOT contributions [85], as described in Chapter 1, Section 1.6.3.3. Second, when the applied field exceeds the anisotropy field, the magnetisation vector aligns with it, and the Nernst contribution saturates. The SOT contribution, on the contrary, is subject to a stronger effective field and therefore decays as $\frac{1}{(H_k - H)}$ for the DL and $\frac{1}{H}$ for the FL component. By recording data with applied fields well above the anisotropy field, we can fit the decay of the signal to obtain the SOT contribution [76], as described in Chapter 1 Section 1.6.3.4.

3.2.2.2 Field configuration choice

The accurate determination of the SOT requires an appropriate choice of which field configuration to use. This choice, in turn, depends on the available field magnitude, the possibility of rotating either the field around some axis of the sample (or the sample around some axis of the field), and crucially the magnetic anisotropy of the sample itself. In Table 3.3, we give the anisotropy parameters for the three sets of samples measured here. They were extracted using the magnetotransport methods described here, but could, at least in principle, have also been obtained by e.g. superconducting quantum interference device (SQUID) magnetometry.

We used two distinct systems for the measurements. The majority were carried out in

a 'Multimag' nested Halbach permanent magnet system where the maximum applied field of $\sim 1.9\,\mathrm{T}$ is in the plane defined by the axis of the Halbach cylinders and can be rotated around this axis. By mounting the sample so that its normal surface is parallel or perpendicular to the axis, the field can be made to rotate in the sample plane, e. g. the xy-, xz-, or yz-planes. The accuracy of the field magnitude in this system is $\sim 50\,\mathrm{mT}$. A second system, based on a Quantum Design 14 T Quantum Design physical property measurement system (PPMS®) equipped with a single-axis rotator, allows measurements in fields near an order of magnitude higher, but this is limited by the number of electrical contacts to the sample, which allows recording only the longitudinal *or* the transverse voltage during a single scan.

Referring again to Table 3.3, the anisotropy of the CoPt multilayer is a simple uniaxial with a first order anisotropy field of $\sim 100\,\mathrm{mT}$. The Multimag system provides sufficient field magnitude to overcome the anisotropy field, and we can accurately record both the transverse and longitudinal voltages for xz and yz (given in the coordinate system of the sample, see Figure 3.3) rotations of the field. This allows us to separate SOT from ANE using both approaches described above. The longitudinal signal allows for an accurate determination of the ANE coefficient, as its contribution is the same as the transverse signal with the in-plane field angle offset by 90°. The SOT contribution differs in the longitudinal signal because it lacks linear effects in $\mathbf{m}$, such as the AHE. As a result, the SOT contribution to the longitudinal signal is small. Therefore, the ANE coefficient can be determined using the longitudinal signal, which can then be set during the fit of the transverse signal.

MRG is different. The first order anisotropy fields is $\sim 0.9\,\mathrm{T}$ and the second order contribution is near equal at $\sim 0.6\,\mathrm{T}$. The 1.9 T available in the Multimag is insufficient to overcome the anisotropy field. We therefore recorded the transverse and longitudinal voltages with the applied field in the sample xy-plane using the Multimag (Figure 3.3),

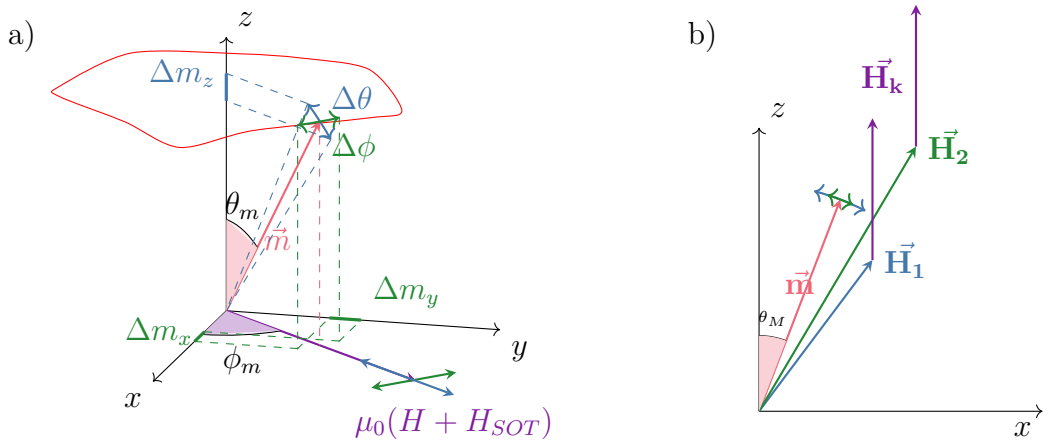

Figure 3.3: Different configurations used for the SOT measurement. (a) In the in-plane scan a new magnetic state is explored as the magnetisation goes more toward the plane's direction with an increasing field. (b) The out-of-plane rotation focuses on only the same position of the magnetisation vector but with different total fields ($\mathbf{H_{ext}} + \mathbf{H_k}$) applied. In this situation the SOT field becomes less effective as the total field increases and the decay of the SOT signal is observed.

followed by a measurement using the PPMS® system up to 14 T, where we scanned the field in the sample xz-plane. Contrary to the xz scan, in the xy configuration with a field lower than the anisotropy field, each new field the position leads to a different magnetisation vector direction. This allowed recording the largest accessible independent value of the magnetisation vector ($\mathbf{M}$), gaining the largest information possible on the magnetisation direction dependence of the SOT and ANE effects.

For the CoPt sample, we can then directly compare the two approaches and confirm their agreement. This then allows us to extract the SOT contribution in MRG with confidence.

3.2.2.3 Choice of numerical solution

The numerical model, introduced in Chapter 2, detailed in Appendix C, is applicable for all combinations of anisotropy and applied field directions. This numerical solution is based on a single macrospin model. In Chapter 2, we have seen that the analytical expressions of [76] and [85] are unsuitable for samples with non-negligible k_2 anisotropy terms. Explicitly, there are no good approximations for the field dependence of the magnetisation vector for a field applied in the plane defined by the easy-axis and a direction

in the hard plane.

Furthermore, analytical methods cannot easily take into account sample misalignment with respect to the axis of the external field, which has a large influence on the recorded signal due to the error made in the equilibrium magnetisation position. Additionally, we required a wide field range to increase the accuracy of SOT measurement. The assumption of [75] that the magnetisation vector is close to the zero-field position is therefore not fulfilled. As shown in Chapter 2, when applying a field higher than the anisotropy field, the relative error can reach 20% with only 5° offset and $H > 1.5H_k$. We therefore used the numerical solution developed within this thesis to model the harmonic Hall signals and to determine the SOT for all materials in this study.

We constructed the numerical model as follows. First, the magnetisation direction was given by minimising the total energy corresponding to the anisotropy and Zeeman energy, as shown in the Equation 3.2. Then we added the spin-orbit torque field. The variation of the magnetisation direction due to the bias current was thus treated as an external field.

This gives the magnetic free energy:

$$E = K_1 \sin^2(\theta) + (K_2 + K_2' \cos(4\phi)) \sin^4(\theta) - \mu_0 \mathbf{M} \cdot \mathbf{H}\,, \tag{3.2}$$

where K_1, K_2, K_2' corresponds to the tetragonal anisotropy, $\mathbf{M}$ to the magnetisation vector and $\mathbf{H} = \mathbf{H}_{\text{ext}} + \mathbf{H}_{\text{SOT}}$ the sum of external and SOT field. The reported anisotropy values are given in terms of anisotropy fields defined as $k_i = \frac{K_i}{\mu_0 M_s}$.

The longitudinal and transverse harmonic voltages are calculated using the tensor detailed in Section 3.2.2.4. This tensor depends solely on the external field and magnetisation vector. The harmonic signals are calculated by demodulating numerically the time-dependent Hall voltage.

Finally, we added the electric field terms corresponding to the magnetothermal effect and

Table 3.2: Different contributions to transport used to model the harmonic Hall voltage. m_i and H_i represent respectively the reduced magnetisation and external applied field along the direction, i, w correspond to the width of the Hall bar geometry, and l to the length between the longitudinal contact probes. The contribution to the transverse (xy) or longitudinal (xx) voltage is given. An absence of contribution is denoted ∘. The last two columns show if a contribution is expected on the first (ω) and second (2ω) harmonic. Noting that in this notation the magnetisation vector m is assumed to be dependent on the current I due to SOT.

	Contributes to:		Visible on harmonic:	
Effect name	V_{xy}	V_{xx}	ω	2ω
Hall	R^H	∘	✓	∘
AHE	$R^{\mathrm{AHE}} m_z I$	∘	✓	✓
PHE	$-R^{\mathrm{PHE}} m_x m_y I$	$R^{\mathrm{PHE}} \left(m_y^2 + m_z^2\right) I$	✓	✓
AMR	∘	$-R^{\mathrm{AMR}}(m_x^2 + m_y^2) I$	✓	✓
LMR	∘	$R^{\mathrm{LMR}} \lvert\mathbf{H}\rvert I$	✓	∘
ANE	$-R^{\mathrm{ANE}}\, w\, m_x\, I^2$	$R^{\mathrm{ANE}}\, l\, m_y\, I^2$	∘	✓
NE	$-R^{\mathrm{NE}}\, w\, H_x\, I^2$	$R^{\mathrm{NE}}\, l\, H_y\, I^2$	∘	✓

included parameters setting the orientation of the sample relative to the external field to take the misalignment into account.

3.2.2.4 Transport properties

The voltage associated with the magnetisation vector can be described by the magnetogalvanic tensor (Equations 3.2). This tensor respects the symmetry of a perfectly isotropic material, and describes effects allowed in any material. A single addition to the isotropic tensor is the anisotropic magnetoresistance (AMR) terms originating from the thin-film geometry with geometry $\propto m$. We recall that the AMR notation in this thesis corresponds to the magnetoresistance effect affecting only the longitudinal resistivity, as defined in Chapter 1, Section 1.3. A lower-symmetry tensor, respecting the $\bar{4}2m$, did not improve the agreement with the experiment at the expense of adding two additional free parameters.

The AHE V_{xy}^{AHE} (Section 1.3.2.1) is the main contribution to the transverse signal in a given sample; it is proportional to m_z. The planar Hall effect (PHE) V_{xy}^{PHE} contributes

significantly in the case of the xy-plane rotation, where the product $m_x m_y$ is maximum. Note that the planar Hall effect additionally contributes to the longitudinal signal with V_{xx}^{PHE}. For the longitudinal voltage, the AMR V_{xx}^{AMR} correspond to the magnetoresistance addition by reducing the symmetry from isotropic to ∞m. A linear magnetoresistance (LMR) term is added V^{LMR} as it is observed empirically. Finally, the thermoelectric contribution, in the form of the Nernst effect (NE) and ANE, is added to the transverse and longitudinal second harmonic signal. The signal correction for the Nernst effect, between the longitudinal and transverse, depends only on the magnetic vector direction and the width w and length l of the Hall bar. The thermoelectric effects, thermal heating and dissipation efficiency are all contracted into the single pre-factor (R^{ANE} dependent on m, and R^{NE} dependent on H).

3.3 Results

Here, we present the results for the control CoPt samples, both asymmetric and symmetric, as well as MRG. For each material, we present the extracted SOT values, as well as results for both the first and second harmonics. The high-field method was used for all materials, while the low-field method was additionally used for the MRG samples. The results shown below are all obtained using the numerical model developed in this thesis.

3.3.1 Cobalt-platinum multilayer

As expected, for both CoPt multilayers, the SOT was found to follow the symmetry of ∞m. The asymmetric CoPt had a strong SOT, while the symmetric CoPt showed a very small SOT value. For the asymmetric CoPt multilayer, the DL value was estimated to be $2.2 \times 10^{-14}\,\mathrm{T\,A^{-1}\,m^2}$ and the FL value was found to be $3.10 \times 10^{-15}\,\mathrm{T\,A^{-1}\,m^2}$. In the symmetric CoPt multilayer, the DL value was found to be $-1.3 \times 10^{-15}\,\mathrm{T\,A^{-1}\,m^2}$ and the FL value was estimated to be $-2.28 \times 10^{-15}\,\mathrm{T\,A^{-1}\,m^2}$. As such, we found the numerical

model to be robust at detecting both strong and weak SOT signals.

3.3.1.1 High-field

Both sample series exhibited simple easy-axis anisotropy with an anisotropy field of $\sim$ 100 mT. The Multimag-based experimental setup was sufficient to carry out scans with the applied field, both in a plane containing the easy axis ('high-field' method). As the field magnitude resolution was only $\sim$ 50 mT (comparable in magnitude to the anisotropy field), we could not use this setup for the differential ('low-field') analytical solution. We recorded experimental data with the applied field in the sample xz and yz-planes.

The *symmetric* sample did not demonstrate a substantial SOT. The signal-to-noise ratio of its contribution to the second harmonic Hall signal was low, significantly lower than the contribution from the ANE. We therefore defer the measurements and analysis of that sample to Appendix D.

The first harmonic transverse and longitudinal signals recorded for the asymmetric sample are shown as points in Figure 3.4, along with the fitted line from the numerical model (solid lines). Their agreement was near perfect. Note that the different field values were fitted together in a single unified model. We found that the transverse signal was dominated by the AHE contribution and that the second-order anisotropy constant was around one order of magnitude less than that found for the first order. For small applied fields (e.g. 0.1 T) the magnetisation vector followed the applied field with a lag of approximately 60°, which reduced to $\sim$ 5° in 1.9 T. This was the origin of the transition from a hysteretic nature in the leftmost top panel of Fig. 3.4 to a sinusoidal behaviour in the rightmost one. The variation of the longitudinal signal was mainly due to AMR. Note that the configurations we have selected here suppress any contribution to the transverse signal from the PHE, as m_x, m_y were zero in the two scans, respectively. We note here that *in this particular case* the dependence on field *magnitude* or *direction* converges to a single solution for the

anisotropy value.

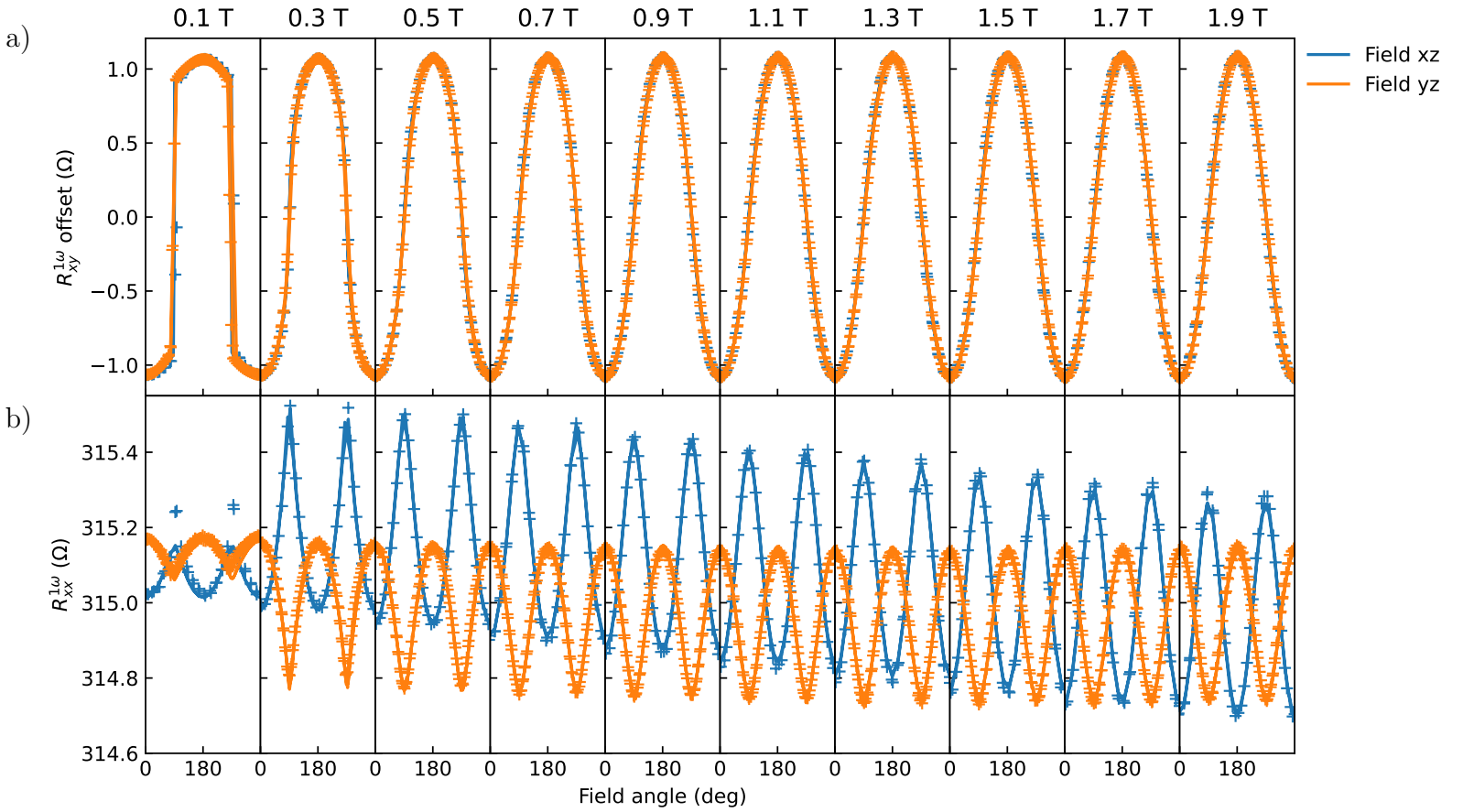

Figure 3.4: CoPt first harmonic signal with field rotated in the xz- (blue) and yz-(orange) planes for both transverse voltages (a) and longitudinal signals (b). The lines are a model fit of the data (crosses) using a single macrospin numerical simulation. The full set of data is fitted simultaneously.

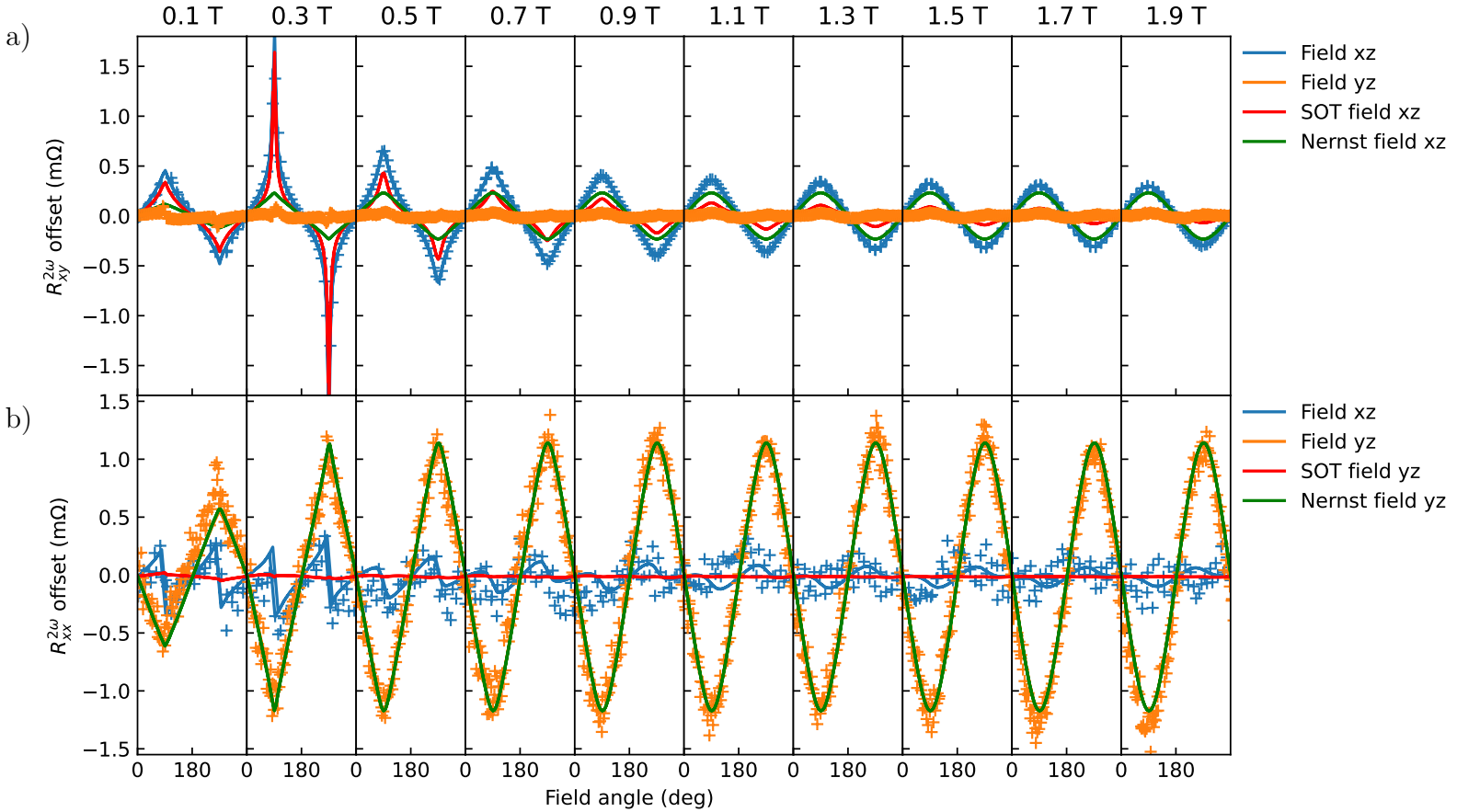

Figure 3.5: CoPt second harmonic signal with field rotation in the xz- (blue) and yz- (orange) planes for both transverse voltages (a) and longitudinal signals (b). The data are represented by points and the line corresponds to the single macrospin numerical simulation reusing the coefficient determined in Figure 3.4 and letting the SOT and ANE parameters free. The full set of data is fitted simultaneously. The fit signal for the xz field rotation is decomposed into the SOT contribution and the ANE contribution, which are represented individually. Lines are the model fit, crosses are data points.

On the basis of the experimentally determined magnetogalvanic tensor, we modelled the second harmonic response, shown in Figure 3.5. In both configurations (xz and yz), the model accurately described the data, and we extracted the SOT and Nernst contributions. As previously reported, the charge to spin conversion in Pt was efficient so that the SOT had a marked contribution to the second harmonic signal. Furthermore, CoPt is a good metal and its low resistivity (i. e. compared to MRG) allows passing substantial current densities without excessive heating. The Nernst contribution is therefore low.

3.3.2 Spin orbit torque in an MRG single-layer

The SOT in MRG was found to follow the symmetry of ∞m layer, without the presence of any SOT coming from the crystallographic structure. The DL value was estimated to be between 2 to $2.3 \times 10^{-14}\,\mathrm{T\,A^{-1}\,m^2}$ and the FL value was found to be ≈ 0 in these measurements. Below, we show a complete experimental characterisation of SOT in PMA Mn_2Ru_xGa, starting with the external field applied in the xy-plane, perpendicular to the easy axis. This is a 'low-field' configuration. We then present the high-field data where the magnitude of the magnetic field allows us to explore the xz-plane defined by the sample normal and the current direction.

3.3.2.1 Low-field

We recorded longitudinal and transverse voltages for an applied field ranging from 0.05 to 1.90 T in steps of 0.05 T. For each field magnitude, we collected data with the angle ϕ_H between the sample x-axis and the applied field from 0 to 360° in steps of 5°. For the first harmonic, a selection of five ϕ_H-scans are shown in Figure 3.6 (points), along with the numerical fit (solid lines). We underline that the model fit was carried out using the entire dataset (both longitudinal and transverse components), and that it is using a *single* set of parameters (the various Rs in Table 3.3, and, in addition, geometrical corrections due to sample mounting). It is clear from Figure 3.6 that the model is an accurate representation

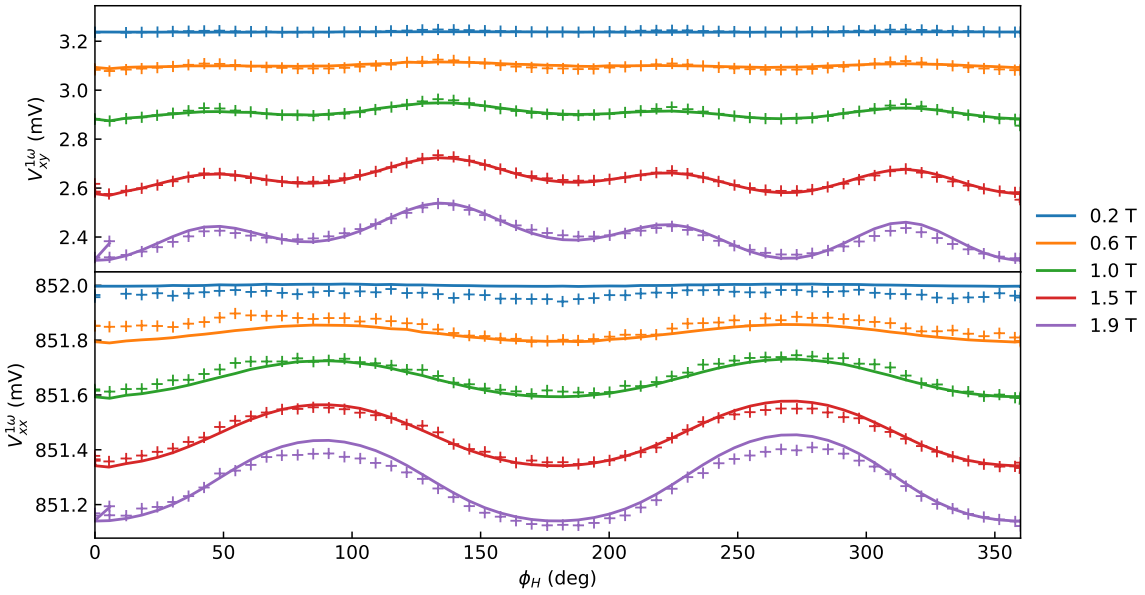

Figure 3.6: Transverse (top panel) and longitudinal (bottom panel) first harmonic signals of Mn_2Ru_xGa. The field was applied in-plane and rotated along the ϕ-direction. The model fit (solid lines) corresponds to the numerical simulation for a single set of parameters, crosses represent data points. The high-field transverse signal (top panel) shows several maxima due to the combination of the tetragonal in-plane anisotropy terms (four-fold symmetry), the PHE (two-fold symmetry) and a slight misalignment of the field with respect to the sample plane (one-fold symmetry).

of the magnetogalvanic tensor of MRG, as the maximum deviation between the data and the model fit is of order 2%. We note in passing that this deviation is mainly due to the sample temperature changing with time during the experiment.

The dominant contribution to the transverse signal is the AHE (R^{AHE}) that, due to the fourfold in-plane anisotropy, results in four maxima/minima in the ϕ_H scan. The PHE (R^{PHE}) is responsible for the two-fold modulation (it is proportional to $m_x m_y \propto \cos 2\phi$). The longitudinal signal is to a large extent constant as a function of ϕ_H, with a small twofold variation due to PHE. We also note a linear-in-applied-field decrease in resistivity due to the term R^{LMR} in Table 3.3, and that the low-field (0.2 to 0.6 T) evolution highlights the initial formation of domains after out-of-plane magnetic saturation of the sample prior to the measurement cycle.

In Figure 3.7, we show the second harmonic voltages as collected (points) along with the numerical fit. Here, only the SOT (H_{DL} and H_{FL}), Nernst contributions and distortion

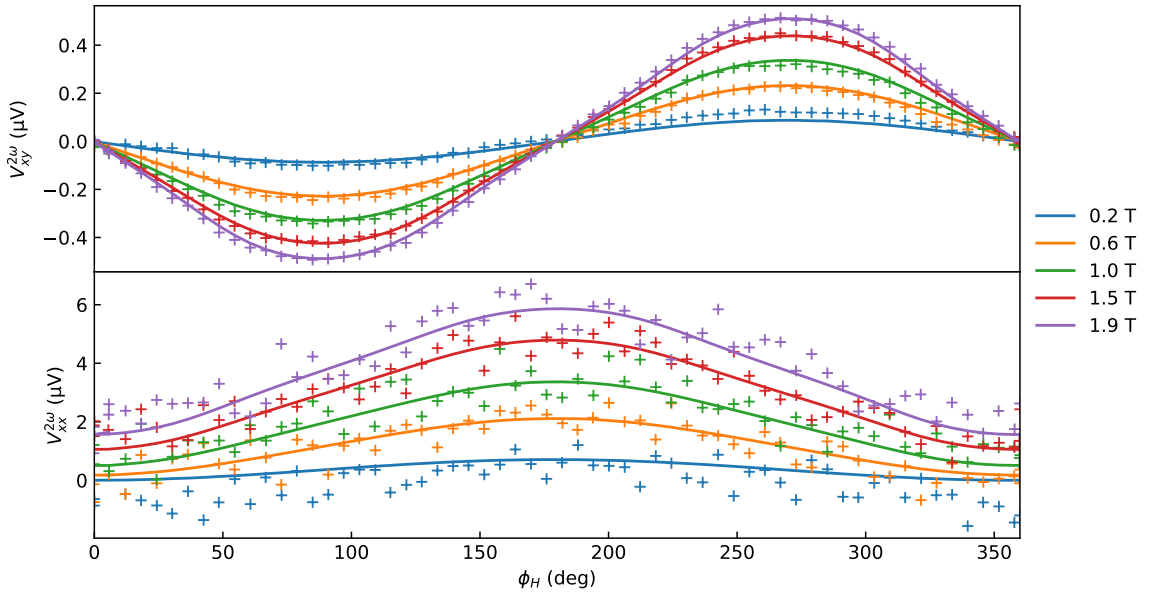

Figure 3.7: Second harmonic field dependence of Mn_2Ru_xGa. The transverse signal (top panel) is composed of the SOT contribution and ANE. The longitudinal (bottom panel) contains only signals originating from the ANE. The longitudinal signal was offset for clarity, solid lines are the model fit and crosses represent data points with correction for distortion

(the bias current supply is not perfect single frequency) were fitted. The remainder of the parameters were fixed at the values obtained from the fit in Figure 3.6. Again, the transverse and longitudinal contributions were fitted simultaneously, which allowed the separation of SOT and Nernst contributions, as described above (Section 3.2.2.4). We note here that the longitudinal signal variation is entirely due to the Nernst contributions, while the transverse is a combination of Nernst and SOT. The SOT contribution is apparent as an 'S' shape (rather than pure sinusoidal), e.g. $\phi_H \approx 180°$.

3.3.2.2 High-field

We now describe the results of the experimental method isolating the SOT contribution from the observed second harmonic signal by applying an external field approximately three times larger than the anisotropy field.

The PPMS® system, described above, allows applying up to 14 T, and to rotate the sample around one axis, parallel to the applied field. Due to experimental limitations, we only

recorded the transverse signal here, but as can be inferred from the description of the method above, this does not impede a reliable analysis of the SOT and Nernst components, as their separation is achieved by analysing the decay of the SOT (and constant nature of the Nernst) in fields exceeding the anisotropy field. The Hall bars measured here are from the same sample coupon as that measured in the 'Low-field' section. We therefore retain the longitudinal components of the conductivity tensor, and also the anisotropy constants.

In Figure 3.8, we show the first harmonic of the transverse signal (points), along with the numerical fit (solid lines). The model accurately describes the non-hysteretic part of V_{xy}, as expected. From this fit we model, in Figure 3.9, the second harmonic signals as a combination of the SOT, and the ordinary and anomalous Nernst effect. The agreement with the experimental data is near perfect. We note that the anomalous Nernst contribution saturates around the anisotropy field ($\sim 3\,\mathrm{T}$), that the ordinary Nernst contribution increases linearly with the applied field, and that the SOT contribution increases as the magnetisation vector tilts away from the easy axis, and then decreases as $1/H$ thereafter. The numerical values extracted from both methods are given in Table 3.3.

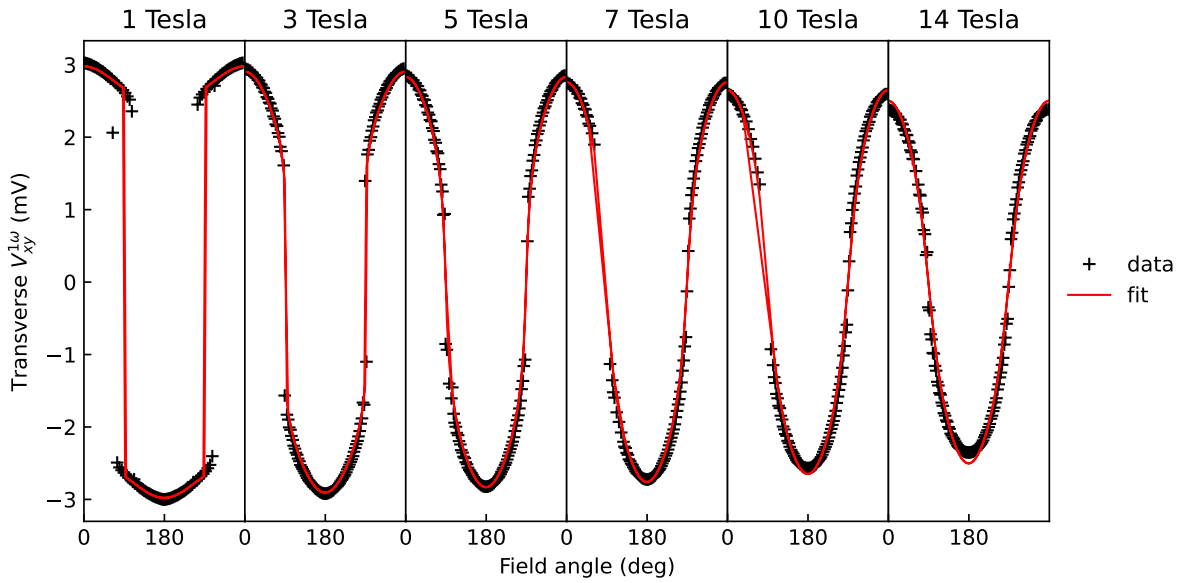

Figure 3.8: First harmonic transverse signal of Mn_2Ru_xGa. The single macrospin model accurately fits the non-hysteretic part of the signal. The different anisotropy coefficients have been fixed from the one found on the in-plane scan.

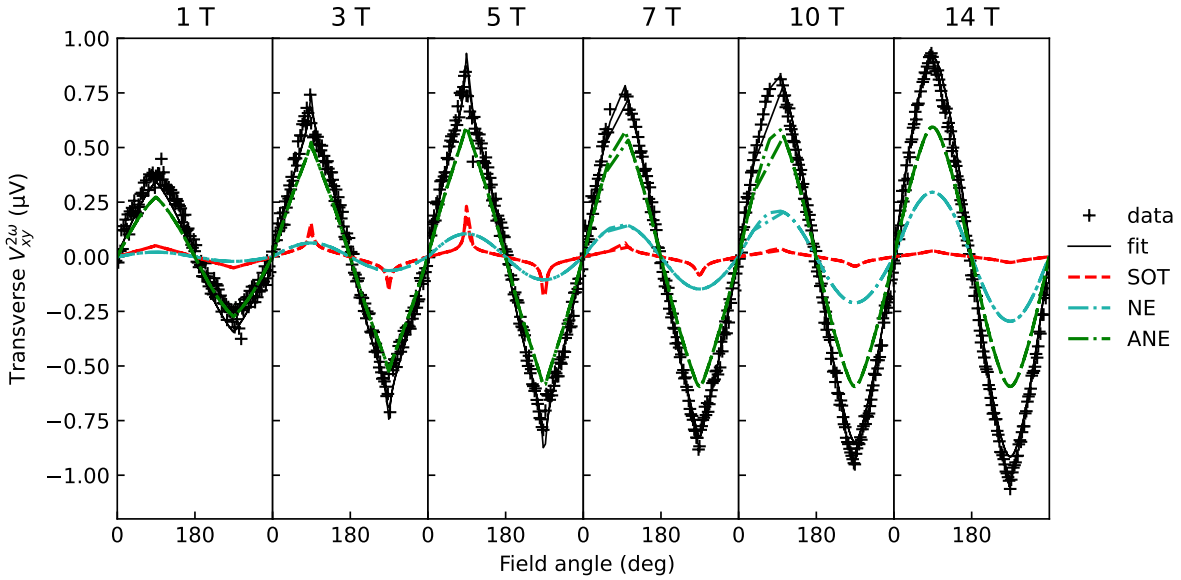

Figure 3.9: Second harmonic transverse signal of Mn_2Ru_xGa, with field rotated in the xz-plane. The signal has three origins: SOT, ANE and NE.

Table 3.3: Fitting coefficients for MRG and CoPt samples.

Coefficient	Low-field MRG	High-field MRG	High-field symmetric CoPt	High-field asymmetric CoPt
$\frac{k_1}{M}$ (T)	0.859	0.859*	0.114	0.0904
$\frac{k_2}{M}$ (T)	0.620	0.620*	0.0036	0.013
$\frac{k_2'}{M}$ (T)	0.0876	-	-	-
ρ_{xx}^0 (Ω m)	2.217×10^{-6}	-	5.90×10^{-7}	6.448×10^{-7}
ρ_{AHE} (Ω m)	4.237×10^{-8}	3.92×10^{-8}	-7.01×10^{-9}	-1.095×10^{-8}
ρ^{AMR} (Ω m)	0	-	4.08×10^{-10}	7.99×10^{-10}
ρ^{PHE} (Ω m)	-1.65×10^{-9}	-	-1.14×10^{-9}	-1.96×10^{-9}
ρ^{HE} (Ω m)	0	-4.75×10^{-10}	-7.73×10^{-11}	-1.24×10^{-10}
Ms(kA m^{-1})	30**	30**	1.325×10^3	1.388×10^3
H_{DL}(T A^{-1} m^2)	2.00×10^{-14}	2.3×10^{-14}	-1.3×10^{-15}	2.2×10^{-14}
H_{FL}(T A^{-1} m^2)	0	0	-2.28×10^{-15}	3.10×10^{-15}
ξ_{DL}	0.047	0.054	-0.01	0.19
ANE	2.10×10^{-21}	2.01×10^{-21}	-2.64×10^{-22}	-4.83×10^{-22}
NE	-	7.13×10^{-23}	-	-

*Anisotropy coefficient for the high-field has been fixed to the same value as obtained by the xy field rotation due to the lack of data in the high-field measurement.
** $M_s = 30 \times 10^3$ is obtained from a different sample at different temperatures

3.4 Discussion

3.4.1 Determination of spin orbit torque in MRG

We found that the SOT in MRG exhibited ∞m symmetry, with $\xi_{\mathrm{DL}} \approx 0.050 \pm 0.004$. This was similar to the $\xi_{\mathrm{DL}} = 0.025 \pm 0.010$ value reported for a Mn_2Ru_xGa/Pt bilayer with similar Mn_2Ru_xGa thickness in [132]. Therefore, we conclude that either spin injection from platinum to Mn_2Ru_xGa was inefficient and/or that thermal effects neglected in that study led to an incorrect determination of the SOT. In Chapter 2, we illustrated how different approximations and data treatment procedures influenced the result of the harmonic Hall method.

The magnitude of the ANE, in terms of an effective R^{ANE} constant, was unusually large and found to be one order of magnitude larger than the value in the CoPt sample. There are multiple reasons for this. First, the large resistivity of Mn_2Ru_xGa leads to a higher Joule dissipation for a given current and thus a high thermal gradient. This increases the heat dissipated in the sample. Second, by Wiedemann-Franz law, we assume that thermal conductivity is proportional to electrical conductivity. Mn_2Ru_xGa is then likely to have lower thermal conductivity than the multilayer of CoPt, which again increases the thermal gradient. Finally, Mn_2Ru_xGa is a half-metal with a lower density of states near the Fermi level. Half-metals have a fully spin-polarised conduction band, resulting in a large variation in the density of states near the Fermi level. The Nernst coefficient depends on the derivative of the conductivity with respect to the electric potential close to the Fermi level [133, 134]. Therefore it is not surprising to find a Nernst coefficient in Mn_2Ru_xGa that is significantly higher than in the CoPt multilayer. All three contribute to a higher NE in Mn_2Ru_xGa, compared to the more electrically conductive material, CoPt. A previous explicit measurement of the ANE in Mn_2Ru_xGa was found to be in the order of 1-5 $\mu\mathrm{V\,K^{-1}}$, Dr Zsolt Gerci (personal communication, Feb 2022). This is consistent with

the signal obtained here.

3.4.1.1 Origins of spin orbit torque

In Section 3.1, we discuss that the SOT in single-layer MRG can originate from either the structural lack of inversion symmetries (thin-film geometry ∞m) or from the absence of crystallographic inversion symmetry ($\bar{4}3m$). First, we will discuss SOT due to thin film geometry followed by an analysis of the effects due to the lack of crystal inversion symmetry.

We found that the SOT associated with the thin film symmetry (∞m) to be of a similar magnitude to a Mn_2Ru_xGa/Pt bilayer system previously reported [132], although thermal effects were neglected in that study. This highlights the importance of thermoelectric effects in Mn_2Ru_xGa in particular, but also generally in harmonic Hall measurement. Moreover, comparing the MRG SOT to that of the asymmetric multilayer CoPt sample used as a reference, here a different picture emerged. Even though the SOT effective fields in CoPt and Mn_2Ru_xGa were of similar magnitude, this is due to Mn_2Ru_xGa having an extremely low net magnetisation rather than a large intrinsic charge-to-spin conversion ratio of the Mn_2Ru_xGa sample. When we compare the SOT *efficiency* of CoPt and Mn_2Ru_xGa the SOT efficiency of the single-layer Mn_2Ru_xGa was much smaller.

Intrinsic SOT from the lack of inversion symmetry ($\bar{4}3m$) in the crystallographic structure was not present in Mn_2Ru_xGa. We explain this as follows: First, even if Mn_2Ru_xGa crystallises in the XA structure, two different orientations of the crystallites are possible. The MgO substrate has a cubic structure; the crystallite can grow as represented in Figure 3.1 or rotated by 90° around the z-axis. There is no energy difference favouring either of these. This rotation is equivalent to an inversion symmetry; thus the two crystallites will have opposite SOT contributions. An equal amount of both crystallite twins throughout the patterned Hall bar results in zero SOT macroscopically.

In theory it is possible to capture this SOT signal on the third harmonic, even in the presence of 50/50 twinning. The third harmonic signal relies on capturing the second order variation of $\mathbf{m}$ due to the SOT field. This variation is proportional to $\mathbf{H}_{\mathrm{SOT}}^2$ and $\frac{\partial^2 \mathbf{m}(\mathbf{H})}{\partial \mathbf{H}^2}$. Due to the $\mathbf{H}_{\mathrm{SOT}}^2$ dependence, the sign of the SOT field, and thus the twinning, will not impact the signal. However, the third harmonic signal also captures other spurious contributions, predominantly thermoelectric effects. These include the change in resistivity and magnetisation due to heating, as well as the contribution from magnetostriction due to thermal lattice expansion [135]. Moreover, we observe that the magnetisation in Mn_2Ru_xGa is decreasing linearly under the application of a hard-axis external field (Figure 3.2.c). As the third harmonic signal is proportional to the second derivative of the magnetisation with respect to the field, we expect a near-zero contribution from the SOT to the third harmonic.

Finally, the absence of SOT of crystallographic origin ($F\bar{4}3m$ symmetry) could be explained by a disordered crystallographic structure, and hence increase symmetry. Initial measurement of the local order was performed using X-ray absorption fine structure spectroscopy (EXAFS), indicated XA order [46]. However, the absence of $\bar{4}3m$ SOT we show here indicates that long-range XA order (several µm) is absent. This hypothesis is supported by using electron diffraction by O'Brien *et al.* (personal communication) . They show that the disordered structure is the only one detectable for higher sample grown temperatures; they observed the absence of pattern in transmission electron microscopy (TEM) associated with the highly crystallographic XA or $L2_1$ structures. Sample growth at $T_S = 225\,^{\circ}\mathrm{C}$ had a higher crystallographic coherence, up to 100 nm in the plane. The magnetic mode of these samples remains to be understood. They cannot be modelled by a simple macrospin nor by a collinear ferrimagnetic model. As we have seen above, a correct model of the magnetic mode is a requirement for SOT measurements.

3.4.2 Spin orbit torque in CoPt

As anticipated, the SOT in the CoPt multilayer conforms to the expected pattern. We found a large spin efficiency of $\xi_{\mathrm{DL}} = 0.19$ in the asymmetric sample, which allows SOT. A low spin efficiency of $\xi_{\mathrm{DL}} = -0.01$ for the DL torque was found for the symmetric CoPt sample.

Despite being small in the symmetric layer, the SOT value was not zero. Imperfections during growth, such as increased roughness as more layers are grown on top of each other, can cause a slight asymmetry in the system, enabling SOT to occur. The model successfully captured this low SOT value, demonstrating that we are able to measure these even in the presence of thermoelectric effects (ANE) on the second harmonic signal. According to the result in the previous chapter (Chapter 2), the uncertainty in the DL field using the differential analytical method with thermoelectric and PHE correction would be close to $0.7 \times 10^{-15}\,\mathrm{T\,A^{-1}\,m^2}$, which is half the extracted value here of $-1.3 \times 10^{-15}\,\mathrm{T\,A^{-1}\,m^2}$. This demonstrates the necessity of using the numerical model when high accuracy is required.

The ANE was lower in the symmetrical sample compared to the asymmetric sample. Potential reasons for this could include a decrease in resistivity due to an increased proportion of Pt, which reduces Joule heating and thus the reduces the thermal gradient. As the galvanomagnetic tensor is set for the entire sample rather than each layer individually, we obtain the average transport coefficient, which increased the Pt contribution further, reducing the coefficient dependent on the magnetisation direction.

The value of the DL SOT in the asymmetric sample is coherent with what was reported previously for a CoPt bilayer [136]. Even if the magnetic volume of the present sample is higher, this should not change the overall SOT value. The exchange averages the torque on the full volume, which is scaled correctly when converted into SOT efficiency via the $M_s t$ product. M_s is the saturation magnetisation and t the thickness of the sample. In general,

thermoelectric effects are less significant when the SOT is larger, since the error will be proportionally lower. However, even in the asymmetric sample, neglecting thermoelectric effects and using a low-field differential method would result in a 30% overestimation of the DL torque, as shown by Equation 1.98. We highlight here that this error is more often than not neglected in the current literature.

3.4.3 Accuracy of the extracted spin orbit torque efficiency

In Section 2 we showed that for the general case, where $\mu_0 H_{\text{applied}}$ is comparable to the combined anisotropy field, and where the energy landscape is more complex than a single uniaxial anisotropy, a numerical solution is required. This offers the added advantage of allowing one to correct for misalignment during the sample positioning. Below, we describe in further detail the approach and reasoning behind the inclusion or not of the different contributions.

The large contribution of the thermal effects in MRG justifies this choice, rather than adapting the analytical expression to each field magnitude and direction. The measurement of the longitudinal resistance ($V_{xx}^{2\omega}$) allowed us to isolate the thermoelectric contributions, while simultaneously fitting both the longitudinal and transverse signals. This led to an accurate estimation of the SOT.

The measurement of SOT in Mn_2Ru_xGa shows that the statistical correlation between the coefficients of the extracted ANE and SOT coefficients decreases when the longitudinal voltages were measured. For example, a similar quality of fit was obtained for the high-field rotation scan, with an SOT field coefficient fixed at a value *twice as large* of what we found in Section 3.3.2.1 (Table 3.3) allowing other contributions such as ANE and NE to be regressed accordingly. This results from the small number of loops recorded below and close to the anisotropy field. The measurement of ANE contribution to the longitudinal signal provides an easy approach to suppress the error of the SOT coefficients due to

thermal effects, as shown in Chapter 2.

An aim of this study was to measure the SOT with sufficient accuracy to use the SOT efficiency as part of an iterative optimisation process for the growth of the Mn_2Ru_xGa thin films with a macroscopic lack of inversion symmetry. Consequently, we focused on detecting small SOT signals that may be present. To ensure this accuracy, all other transport coefficients and small imperfections of the setup have been taken into account in the numerical model.

First, the magnetogalvanic tensor has components dependent on m (and m^2) as well as H (H^2). In the harmonic Hall method, the SOT is expressed as an effective field, which acts only on the magnetisation and does not influence field-dependent transport properties. The analysis must take into account the field-dependent effects to correctly determine the magnetisation dependent ones.

A second consideration is the geometrical imperfection of the experimental setup. It is near-impossible to perfectly align the sample coordinate system with that of the magnetic field. In particular, when the field is applied along a hard axis, its alignment has a significant impact on both the first and second harmonic signals, as shown in the previous Chapter 2. A 5° offset can generate up to 80% error in the determination of the DL coefficients. For low-field measurements, the rotation of the sample around the out-of-plane axis mixes the FL and DL terms with an error proportional to $\sin(\theta_z)$, where θ_z is the magnetisation direction measured from the out-of-plane axis. Small offsets, even when not correlated with errors in the estimation of the FL and DL torque (in the previous studies (Chapter 2)) cause residuals that affect the fitting procedure, as the other transport coefficient cannot be determined as accurately. This is visible in Figure 3.6 where the small one fold signal visible at high-field occurs from a misalignment of approximately 3°.

Our numerical solution takes into account field misalignment in addition to a variety of transport effects (see Table3.1). These were all required to determine the SOT coefficients

(see Chapter 2). We proceed as follows: First, the magnetisation direction (θ, ϕ) was determined by minimising the magnetic free energy for an arbitrary external field, thus taking into account any small geometrical offset present and allowing us to solve for a full range of magnetisation directions. In comparison, the approximations required to obtain an analytical solution to the magnetisation direction as developed in Section 1.6.3 are unable to describe the magnetisation vector when the applied field magnitude is of the same order as the anisotropy field and close to the hard axis direction.

The transport side was then computed with the help of a galvanomagnetic tensor, which used the previously solved magnetisation direction as an input. This naturally decoupled both field and magnetisation effects, as we applied the SOT effective field only to the magnetisation solution. This full procedure allowed measurement of extremely low SOT signals (of the order of $1 \times 10^{-8}\,\mathrm{mT\,A^{-1}\,cm^2}$) and facilitated more accurate modelling of the first and second harmonics; thus, increased the accuracy of the SOT determination.

3.5 Conclusion

SOT of Mn_2Ru_xGa single-layer was determined with high accuracy in this study. The thermoelectric effects (here predominantly the ANE) have been taken into account and confirmed both by taking the contribution to the longitudinal signal and by increasing the total field on the sample. Thermoelectric effects represent a large contribution to the transverse second harmonic single.

Two sources of SOT in MRG thin films were investigated: one due to the thin-film geometry and the other resulting from broken inversion symmetry. The former, though present, was found to be small and contradicts previous literature [132]. The SOT contribution linked to the XA structure has not been observed, supported by recent findings by electron diffraction suggesting that the sizes of the crystallite are too small to induce any coherent diffraction. The transport measurement presented here, which averages over 10 µm, will

aggregate the contribution of both crystallite directions resulting in an overall null SOT signal.

The result presented here does not contradict the possibility of a larger spin-orbit torque in a single-layer due to a crystallographically broken inversion. Initial growth of samples will have a high probability of small SOT due to imperfect crystal growth and possible twining of crystallites. Obtaining data on the order of such crystal structures typically requires the user of resonant X-ray techniques, which are not readily available during sample growth optimisation. The SOT efficiency measurement presented makes it possible to detect small SOT contributions. In this method, field misalignment contributions, thermoelectric effects and transport effects are determined in the most general way possible by applying symmetry arguments. The SOT efficiency can then be used as a proxy parameter to optimise sample production and grow more crystallographically ordered samples using standard laboratory facilities.

CHAPTER 4

Elimination of thermoelectric effects in the harmonic Hall method: a new geometry pattern for measuring spin-orbit torque

4.1 Introduction

The harmonic Hall method is a defacto standard for the measurement of spin orbit torque (SOT) efficiency [5]. A typical measurement performed on a Hall bar device includes contributions beyond the signal originating from the SOT [76, 85]. The most significant of these additional contributions include thermoelectric effects, e.g. anomalous Nernst effect (ANE) and Spin Seebeck effects [137–139].

Thermoelectric contributions can be addressed by applying large magnetic fields, which allows them to be fitted [76, 85, 139]. Another approach involves measuring both contributions along the transverse and longitudinal directions [85]. Alternatively, modifying the configuration of the current/probe setup can be employed [140], but this method addresses only a limited number of contributions. Here, we present a novel geometry for harmonic Hall measurements that eliminates the thermoelectric effect without the need

for additional modelling.

Even in the most precise measurements, where all contributions are meticulously accounted for, a residual signal remains, often approximately 2% of the total signal, as demonstrated in Chapter 3. If the goal is to achieve very high accuracy, it can be challenging to determine whether these residual signals originate from thermoelectric effects or from other phenomena, as they are, by definition, not modelled explicitly, e.g. SOT effects.

The second harmonic response captures all contributions from the SOT. However, this signal is not exclusive to SOT effects and includes any second order (or higher even order) non-linear effects. The most significant additional contribution arises from thermal effects. Since thermal dissipation is proportional to the square of the current, it naturally appears in the second harmonic. Consequently, any thermoelectric and thermal gradient-related effects also appear in the second harmonic.

Thermoelectric and thermal gradient-related effects contribute to the transverse voltage and are both essentially proportional to the magnetisation along the x-axis. Where they generate signals that are very similar to the damping-like (DL) contributions of SOT [76, 139]. However, they have a different symmetry and microscopic origin.

The SOT signal in the harmonic Hall method arises from the perturbation of the magnetisation vector due to the SOT field. This perturbation is highly directional and depends on the SOT field direction, which is influenced by the system's symmetry and current direction, as well as the magnetisation vector direction [4, 56, 66]. In contrast, the Nernst effect (NE) and other thermoelectric effects do not depend on any particular current direction; they depend only on the amount of heat dissipated into the thin film, with the resulting temperature gradient along the z-axis generating a signal that appears similar to the SOT DL field in the standard Hall bar configuration.

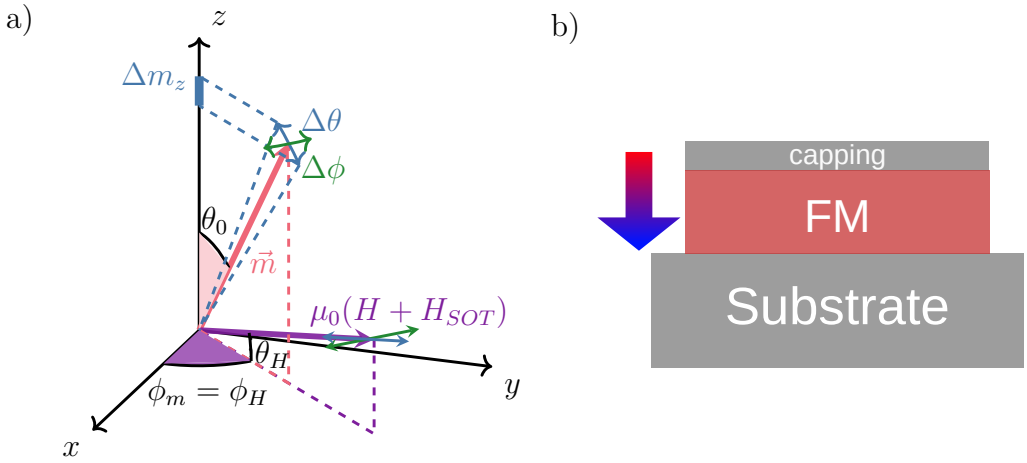

Figure 4.1: Difference between SOT magnetisation variation and Nernst effect contribution, with: a) The applied field (purple) is oriented within the hard plane to tilt the magnetisation to the equilibrium angle θ_0. The SOT field has components both parallel and perpendicular to the applied field. The SOT field aligned with H_{ext} (blue) will generate a variation of $\mathbf{m}_z$. In contrast, when the SOT field is perpendicular (green), there is no change in $\mathbf{m}_z$; only ϕ_m is affected. b) Symmetry of thermal heating with the temperature gradient direction. The ANE depends solely on the equilibrium magnetisation direction and thermal gradient; it does not induce any variation on the magnetisation vector.

By decomposing the problem and examining heat dissipation, it is observed that in most materials, dissipation is isotropic and independent of current direction. This contrasts significantly with the SOT effect, where the SOT field is highly dependent on the direction of the charge current. To address this, a rotating current can be employed instead of one that oscillates:

$$J = J_0 \begin{pmatrix} \cos(\omega t) \\ \sin(\omega t) \\ 0 \end{pmatrix}, \tag{4.1}$$

where J_0 is the current amplitude and ω the frequency used for the Harmonic Hall measurement.

In this case the SOT field will still contribute to variation in the magnetisation angle $\delta\theta$ and $\delta\phi$ (Figure 4.1.a) due to the directional dependence in current. In contrast, the

thermal effects are proportional to the Joule heating dissipation and so:

$$P_{\text{Joule}} = \mathbf{J}(t) \cdot \rho\mathbf{J}(t)\,, \quad \text{assuming } \rho \text{ is a scalar,} \tag{4.2}$$

$$= \rho(J_x^2 + J_y^2) \tag{4.3}$$

$$= \rho J_0^2\,, \tag{4.4}$$

where P_{Joule} is power dissipated by unit of volume, $\mathbf{J}$ is current density and ρ the resistivity. We note that only the main component of the resistivity tensor (noted ρ_{xx0} in the rest of the thesis) is considered here, which allows us to treat it as a scalar.

As the thermal dissipation is time independent, this will be true for the thermal gradient (Figure 4.1.b). All thermoelectric effects proportional to the thermal gradient along z, such as the ANE ($\mathbf{V}_{\text{ANE}} \propto \mathbf{m} \times \nabla\mathbf{T}$), are also time independent and are thus filtered out when recording the first and second harmonic with the lock-in amplifier (LIA).

Two research questions are posed: a) do the field-like (FL) and DL SOT signals persist on the second harmonic when using a rotating current?, and b) can a controlled rotating current be achieved through lithography? These questions were addressed in the following steps:

1. Initially, the first and second harmonic signals were determined analytically for a minimal model that included only the anomalous Hall effect (AHE) in a system with first-order perpendicular magnetic anisotropy.

2. Second, the more common scenario was examined using a macrospin simulation, including both planar Hall effect (PHE) and AHE, for both perpendicular and in-plane anisotropy. The results from a standard Hall bar and the new geometry were compared to determine if all the information was still present despite the difference in the manifestation of the signal.

3. Next, the current distribution of the two proposed geometries was tested using the

finite element method (FEM) discussed and compared to the ideal case of a rotating current.

4. Subsequently, this method was tested experimentally using a multilayer of CoPt patterned in a standard Hall bar and the new geometry proposed. The data were analysed to determine the SOT field and thermoelectric contributions.

5. Finally, a noise analysis was conducted to evaluate if there was a rise in noise caused by the new device's geometry and the additional second current source required for the measurement.

The impact of this research on practical applications is discussed, along with suggestions for future research directions.

4.2 Methodology

4.2.1 Theoretical work

4.2.1.1 Analytical solutions in the case of uniaxial anisotropy

The initial phase of the theoretical work involves considering only the ideal case, with the current following Equation 4.1. This assumes that the current is perfectly controlled in the probing area of the device.

For the transport coefficients, only the anomalous Hall effect and longitudinal resistance terms were considered. The ρ tensor was defined as follows:

$$\rho = \begin{pmatrix} \rho_{xx}^{0} & \rho^{\mathrm{AHE}} m_z \\ -\rho^{\mathrm{AHE}} m_z & \rho_{xx}^{0} \end{pmatrix}, \tag{4.5}$$

where ρ_{xx}^{0} is the isotropic ohmic resistance and ρ^{AHE} is the AHE coefficient.

Only first order perpendicular terms were considered and the field was assumed to be

applied perfectly in the x direction. The magnetic energy for the system corresponds to:

$$E = K_1 \sin^2\theta - \mu_0 M_s H_x \sin(\theta)\,, \tag{4.6}$$

where θ represents the direction of the magnetisation deviation from the z-axis as shown in Figure 4.1. The coefficient K_1 corresponds to the first order anisotropy coefficient and M_s to the saturation magnetisation of the material. The anisotropy was expressed as $k_i = \frac{K_i}{M_s}$, which has the same units as the external applied field.

A small perturbation from the SOT field was assumed, which allowed determination of the second harmonic from a Taylor expansion of the magnetisation vector using the known expression for $\delta\theta$ (see 1.6.2):

$$\delta\theta = -\frac{-\cos\theta(\cos(\phi)\delta H_x + \sin(\phi)\delta H_y) + \sin(\theta)\delta H_z}{2k_1\cos(2\theta) + H_{\parallel}\sin(\theta)}\,. \tag{4.7}$$

The SOT field used here corresponds to the bilayer SOT with:

$$H_{\mathrm{SOT}} = \chi_{\mathrm{FL}}\begin{pmatrix} 0 & 1 & 0 \\ -1 & 0 & 0 \\ 0 & 0 & 0 \end{pmatrix}\mathbf{J} + \chi_{\mathrm{DL}}\begin{pmatrix} m_z & 0 & -m_x \\ 0 & m_z & -m_y \\ -m_x & -m_y & 0 \end{pmatrix}\mathbf{J}\,, \tag{4.8}$$

where χ_{DL} and χ_{FL} are respectively the DL and FL torque coefficient. The electric field $\mathbf{E}$ will be computed in the result section using those postulates. The first and second harmonic responses are derived and discussed further in Section 4.3.1.1.

4.2.1.2 Macrospin simulations

A macrospin simulation was used to compare the standard Hall bar geometry and the new geometry, using standard assumptions commonly reported in the literature. This more general case includes the anomalous Hall effect (AHE) and planar Hall effect (PHE),

yielding a ρ tensor of the form:

$$\rho = \begin{pmatrix} \rho_{xx}^{0} - \rho_{\mathrm{PHE}}(m_y^2 + m_z^2) & \rho^{\mathrm{AHE}} m_z + \rho_{\mathrm{PHE}} m_x m_y \\ -\rho^{\mathrm{AHE}} m_z + \rho_{\mathrm{PHE}} m_x m_y & \rho_{xx}^{0} - \rho_{\mathrm{PHE}}(m_x^2 + m_z^2) \end{pmatrix}. \tag{4.9}$$

For the simulation, $\rho_{xx0} = 1 \times 10^{-7}\,\Omega\,\mathrm{m}$, $\rho_{\mathrm{AHE}} = 1 \times 10^{-9}\,\Omega\,\mathrm{m}$, and $\rho_{\mathrm{PHE}} = -2 \times 10^{-10}\,\Omega\,\mathrm{m}$.

Two different anisotropies were considered, one with perpendicular magnetic anisotropy with $k_1 = 1\,\mathrm{T}$ and one with in-plane anisotropy with $k_1 = -0.1\,\mathrm{T}$. The field was applied along the x direction for the out-of-plane anisotropy and was rotated in-plane with three different field values, $H = 0.1\,\mathrm{T}$, $H = 0.2\,\mathrm{T}$, and $H = 0.5\,\mathrm{T}$, for the in-plane anisotropy.

On both devices, both pairs of probing contacts were located along the x and y directions, respectively. The contact distance was set to 20 µm, which also corresponds to the width of the bar. The film thickness was set at 20 nm. A current of 5 mA was supplied on each current input, resulting in a current density $j_0 = 1.25 \times 10^{10}\,\mathrm{A\,m^{-2}}$. An effective ANE coefficient was defined, containing the heat dissipation coefficient, the gradient generated from the heat dissipation and the ANE coefficient with a value of $8 \times 10^{-22}\,\mathrm{V\,m^{-1}\,A^{-2}\,m^{-4}}$.

The SOT field, as defined in Equation 4.8, has values of $\chi_{\mathrm{FL}} = 1 \times 10^{-13}\,\mathrm{T\,A^{-1}\,m^{-2}}$ and $\chi_{\mathrm{DL}} = 5.6 \times 10^{-13}\,\mathrm{T\,A^{-1}\,m^{-2}}$. Using the current density j_0 this gives respectively an effective field of $h_{\mathrm{FL}} = 1.25\,\mathrm{mT}$ and $h_{\mathrm{DL}} = 7\,\mathrm{mT}$.

The first and second harmonics were solved numerically using the software presented in Chapter 2 and Appendix C. Solutions were obtained for two geometries in the ideal case: 1) for use with a rotating current and 2) the standard Hall bar with a unidirectional current; these were compared descriptively.

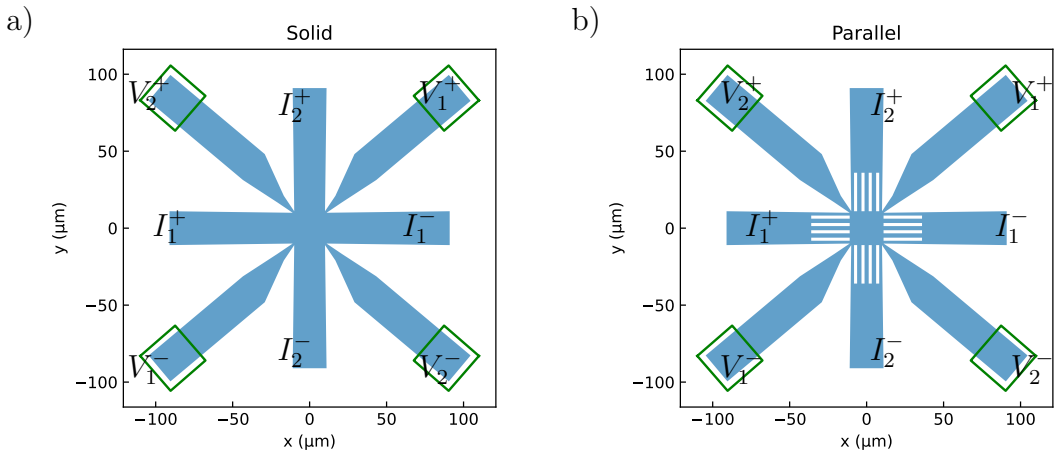

Figure 4.2: Proposed geometry for the new device. The only difference between the solid and parallel geometries was channels in the current leads, which confined the current to the probing area consisting of the middle square. The green rectangle corresponds to the integrating area used to find the contact voltage in the FEM simulation.

4.2.2 Experimental work

4.2.2.1 Finite element method analysis

In a standard Hall bar, the width of the bar (for the current flow) is typically much greater than that of the probing contact, minimising the impact of the probing contact on the current flow [89]. However, when a rotating current is used, both current feeds must be identical, distancing us from the theoretical ideal current scenario. To address, parallel channels were inserted inside the lead current to direct the current along one specific direction (Figure 4.2.b). This design makes the conductivity anisotropic, with conduction only in one direction, preventing current flow in the perpendicular direction.

To study the difference between a trivial design (solid geometry) and the proposed parallel geometry, simulations using Comsol Multiphysics 6.2 software [141] were performed for materials with the following conductivity tensor:

$$\sigma = \begin{pmatrix} \sigma_{xx} & -\sigma_{xy} \\ \sigma_{xy} & \sigma_{xx} \end{pmatrix}, \tag{4.10}$$

with $\sigma_{xx} = 5 \times 10^7\,\Omega\,\mathrm{m}$ and $\sigma_{xy} = 0 \quad \text{or} \quad \pm -5 \times 10^5\,\Omega\,\mathrm{m}$. A voltage source was applied on the perpendicular source contact, with a symmetric source (positive in one extremity and negative at the other). The voltage source followed a cosine wave for the x direction and a sine wave for the y direction.

The simulation used a static model, where the frequency was small enough to justify the quasi-static approximation. The current distribution was computed for 64 time-points, equally spaced over a full period. The current density and direction were reported for the phase equal to 0°, 45°, and 90°. A cross section along $x = 0$ for the 0° phase was plotted for both the solid and parallel geometry.

The simulated design included contact pads, where voltage was computed by averaging the top of the contact for each time-point. This allowed generating the actual contact voltage for each geometry, which could be fitted by sine and cosine functions to compare coefficients with the theoretical ideal case. As only diagonal components are affected by current spreading, a geometrical factor was defined as $g = \frac{V^{\mathrm{FEM}}}{V^{\mathrm{ideal}}} = \frac{\rho_{xx0}^{\mathrm{measured}}}{\rho_{xx0}^{\mathrm{real}}}$ that represents the reduction in diagonal components.

4.2.2.2 Experimental comparisons of new geometry with the standard Hall bar

A CoPt multilayer was patterned with two different geometries: the standard Hall bar geometry (Figure 4.3.b), used as a reference, and the new parallel geometry to allow a rotating current (Figure 4.3.c). The sample corresponds to a repetition of five layers of [Co/Pt]. The sample used was the same one as discussed in Chapter 3, with deposition details found therein. Both the standard Hall bar and the new geometry were patterned using UV lithography and dry argon etch. For both bars, gold contacts were patterned in a second step, using the same mask, to reduce the global device resistance.

For the standard Hall bar geometry, an alternating current (AC) current source (Keithley

K6221) was used to inject the current between the I^+, I^- contact (Figure 4.3.b). For the new geometry, a cosine (between contact I_1^+ and I_1^-) and sine (between contact I_2^+ and I_2^-) AC current were supplied, as shown in Figure 4.3.c. The source consisted of the LIA output and the current was stabilised with a software feedback loop using the circuit in Figure 4.3.d. After each step in-field, the software waited five times the LIA integration time and adjusted the amplitude and phase of the output. This was repeated until convergence was reached. In each scenario, two Zurich instrument MFLI LIA were used to measure the first and second harmonic voltages on the different contact pairs (V_{xy}, V_{xx} for the standard Hall bar geometry; V_1, V_2 for the new geometry). The LIA integration time constant was set to 0.3 s for the standard Hall bar measurement and to 1 s for the new geometry, allowing a larger signal-to-noise ratio, with a filter of order three used in both cases. Data points were recorded after waiting five times the LIA time constant after the field became stable.

The magnetic field was applied using a 'Multimag' system comprising two concentric Halbach cylinders, each generating a field close to 1 T. By changing the relative angle between the cylinders, the field can be varied from 0 T to 1.9 T, while rotating both cylinders together allows us to change the field direction within the plane. This provided control over field intensity and direction, but had relatively large errors (of order 50 mT), limiting the accuracy of films like CoPt used here with an anisotropy coefficient of 100 mT. All measurements were performed at room temperature without temperature control or recording. This caused a small drift in the data due to slow overnight recordings for approximately 8 hours.

To accurately determine the thermoelectric effect in Hall bar geometry, large rotating fields were applied in the xz- and yz-planes to capture and distinguish between thermoelectric and SOT signals. In contrast, for the new geometry, a single scan with the field applied in the xz-plane sufficed due to the rotating current setup capturing both direc-

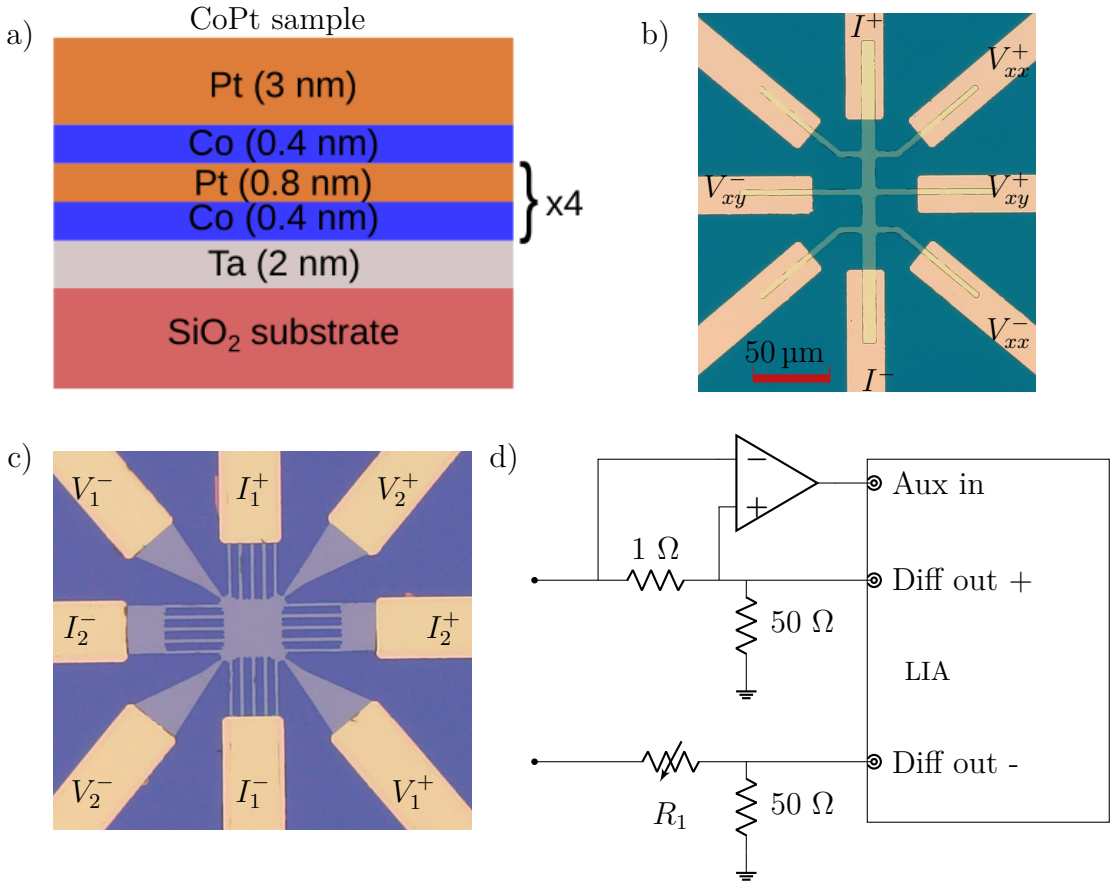

Figure 4.3: Experimental setup for testing the new geometry: a) CoPt multilayer stack used, b) Microscope image of the standard Hall bar geometry used as a reference, c) Microscope image of the new lithography with the different contact positions, and d) Current source using the Zurich Instrument LIA. An instrumental amplifier was used to read the current on a 1 Ω resistor feed in the auxiliary input. Software feedback stabilised both the current intensity and phase.

tions simultaneously. The results were analysed with the software from Appendix C. The fit parameters are detailed below.

The magnetic energy, including anisotropy and Zeeman terms, is:

$$E = K_1 \sin^2(\theta) + K_2 \sin^4(\theta) - \mu_0 M_s \mathbf{H} \cdot \mathbf{m}\,, \tag{4.11}$$

with $\mathbf{H}$ the external field, M_s the saturation magnetisation, $\mathbf{m}$ the reduced magnetisation vector and θ the angle between the magnetisation vector and the z-axis. The anisotropy factors were reported in terms of field, e.g. $k_1 = \frac{K_1}{M_s}$ and $k_2 = \frac{K_2}{M_s}$.

Multiple effects based on symmetry were used. These include the isotropic resistance (ρ_0),

AHE (ρ_{AHE}), PHE (ρ_{PHE}), Hall effect (HE) (ρ_{HE}), and anisotropic magnetoresistance (AMR) (ρ_{AMR}), in addition a linear magnetoresistance (LMR) (ρ_{LMR}) term is incorporated as it is observed experimentally.

The corresponding resistivity (ρ) tensors for an ∞m symmetry were given by:

$$\rho_0 = x_0 \begin{pmatrix} 1 & 0 \\ 0 & 1 \end{pmatrix}, \tag{4.12}$$

$$\rho_{\mathrm{AHE}} = x_0 \begin{pmatrix} 0 & m_z \\ -m_z & 0 \end{pmatrix}, \tag{4.13}$$

$$\rho_{\mathrm{HE}} = x_0 \begin{pmatrix} 0 & H_z \\ -H_z & 0 \end{pmatrix}, \tag{4.14}$$

$$\rho_{\mathrm{PHE}} = x_0 \begin{pmatrix} (m_y^2 + m_z^2) & -m_x m_y \\ -m_x m_y & (m_x^2 + m_z^2) \end{pmatrix}, \tag{4.15}$$

$$\rho_{\mathrm{AMR}} = x_0 \begin{pmatrix} -(m_x^2 + m_y^2) & 0 \\ 0 & -(m_x^2 + m_y^2) \end{pmatrix}, \tag{4.16}$$

$$\rho_{\mathrm{LMR}} = x_0 \begin{pmatrix} \|\mathbf{H}\| & 0 \\ 0 & \|\mathbf{H}\| \end{pmatrix}, \tag{4.17}$$

where x_0 was the reported fit parameter for each term. The Nernst effect was given by:

$$E_{\mathrm{Nernst}} = x_0 \|\mathbf{J}\|^2 \begin{pmatrix} m_y \\ -m_x \end{pmatrix}. \tag{4.18}$$

In the standard geometry, current flows solely along the x-axis. Rotation in the yz-plane caused no variation associated with ρ_{PHE} as $m_y^2 + m_z^2$ remained constant and $m_x m_y = 0$. The AMR coefficient was then determined in the yz scan, while the PHE coefficient was recorded during an xz scan after fixing the AMR coefficient.

In new geometry, the current is supposed to take the form shown in Equation 4.1. How-

ever, the current direction is not fully controlled due to imperfections in the lithography. Instead, the following expression was used for the current:

$$J = J_0 \begin{pmatrix} \cos(\omega t) - \sin(\omega t)\sin(\delta\theta_y) \\ \cos(\delta\theta_y)\sin(\omega t) \end{pmatrix}. \tag{4.19}$$

This fixed the current direction along the x-axis, as the reference axis, and as a result the current along the y direction was not constrained to be fully perpendicular with an associated parameter $\delta\theta_y$. The χ_{FL} and χ_{DL} coefficients are defined as in Equation 4.8. ϕ_{off} is the field angle origin for the rotation of the magnetic field. θ_x, θ_y, and θ_z represent the tilt offset in terms of Euler angles of the field rotation plane compared to the film surface, which originates from the misalignment of the sample plane compared with the field rotation plane. ϕ_{off}, θ_x, θ_y, and θ_z are not independent variables; the three Euler angles are enough to fully define the orientation of the sample in space. However, the presence of ϕ_{off} assists with model convergence. ϕ_{off} can be adjusted manually close to the offset value, then the three Euler angles are fitted for fine adjustment. The offset in this setup corresponds to a few degrees (typically below 2°).

For each channel measured, a contribution from contact offsets with respect to the equipotential was considered. This contribution takes the following form for the first harmonic:

$$V_{x(y)}^{\mathrm{offset}\,A(B)} = V_{x(y)}^{A(B)} - \alpha V_{x(y)}^{B(A)}, \tag{4.20}$$

where A (B) represents the value recorded on the first (second) LIA, and x and y represent the phase of the LIA. This offset was present in all measurements except for the longitudinal signal from the standard Hall bar, due to the significant difference between longitudinal and transverse voltages and the greater distance between V_{xx} contacts.

The second harmonic was initially corrected using the same coefficient as the first harmonic, assuming that any physical offset or current flow alterations would also affect the second harmonic. However, another parameter was added for each output channel of the

second harmonic due to the presence of a constant offset, the origin of which has not been fully determined, but is assumed to arise from the acquisition setup.

The distortion was given by the following mathematical expression:

$$V_{\text{out}} = V\left(1 + 2d\frac{V}{V_{\text{Range}}}\right), \tag{4.21}$$

where V is the initial output without distortion, d the distortion factor and V_{Range} is the maximum value of V.

The distortion on the LIA input was typically too low to require consideration. The manufacture specification specifies at least $-80\,\text{dB}$ and the fitting is optimal when the distortion is set to $-90\,\text{dB}$ or below [142, 143]. Usually, the effect of the distortion in the current source is assumed to be from the ANE with a thermal gradient along the x direction due to the contact acting as a heat sink [139]. However, measurements showed that the typical $-80\,\text{dB}$ distortion present in the source explains the contribution visible in the second harmonic, so an in-plane thermal gradient was not considered.

4.2.2.3 Noise analysis

The use of a more complex geometry, with two current sources, increases the noise in the recorded data. This is considered acceptable if the benefits outweigh the additional noise. This trade-off was analysed by studying different scenarios, including the stability of current sources, electrical noise, and comparing residuals of the fit between the standard Hall bar and the new geometries.

The stability of the current from different sources was investigated. A single $1\,\Omega$ resistor was placed on one branch and was used to provide feedback to the supply voltage, keeping the current intensity and phase constant. To determine whether feedback from only one branch was sufficient, two auxiliary inputs from each LIA and four calibrated $1\,\Omega$ resistors were used to measure simultaneously the current in all the current branches. The current

measurement setup was first calibrated by connecting both resistances in series with the current input measurement of the LIA and, using the same setup of resistors, instrumental amplifiers and LIA auxiliary outputs (Figure 4.3.d) for detection. The current was then varied between 0 and 1.4 mA and a linear fit gives the coefficient between the measured voltage and current with an uncertainty of 0.003% on the fitting coefficient. A new scan was performed similarly to the one of the previous sections (Section 4.2.2.2), but included the four 1 Ω resistance measurement, which was used to verify the current stability.

Electrical noise was investigated by measuring the variation over time and keeping all other parameters constant. The increased impedance of the device and the presence of a longitudinal contribution (V_{xx}) on each LIA increased the noise in the new geometry. Moreover, the use of two independent current sources, each with its own feedback loop, may introduce interference, thereby increasing the noise. The noise was characterised by measuring the first and second harmonics at a constant field of 1.9 T, recording 1000 points with the LIA time constant set to 1 s and the order of filter set to 3. The points were recorded every 5 s to ensure that they were not correlated. This was collected for all combinations of each source being on or off. The source-off state was performed by replacing the current source with a 50 Ω resistance to ground to match the source impedance.

Finally, to assess the new geometry's performance against the standard Hall bar, residuals were compared of each fit of the harmonic Hall signal with varying magnetic fields. Despite systematic patterns in the residuals, a histogram was used to visualise if any error increase was present. Some differences between the recording conditions have an important impact on the amount of noise present in the residual. First, the Hall bar scan had twice as many data points due to field rotation in both directions. Second, the integration time on the LIA was set to 0.3 s for the Hall bar and 1 s for the new geometry.

4.3 Results and discussion

4.3.1 Theoretical work

4.3.1.1 Analytical solutions in the case of uni-axial anisotropy

In this section, the harmonic Hall signal for the new geometry was computed analytically for the simplest case, with a first-order single-axis perpendicular anisotropy. The field was applied perfectly along the x direction. Spherical coordinates for the magnetisation vector and a perturbation from SOT $\delta\theta$ were used; which led to the electric field E of the form:

$$E = \rho J\,, \tag{4.22}$$

$$= J_0 \begin{pmatrix} \rho^0_{xx}\cos(\omega t) + \rho^{\mathrm{AHE}}\cos(\theta)\sin(\omega t) \\ -\rho^{\mathrm{AHE}}\cos(\theta)\cos(\omega t) + \rho^0_{xx}\sin(\omega t) \end{pmatrix} \tag{4.23}$$

$$\approx J_0 \begin{pmatrix} \rho^0_{xx}\cos(\omega t) + \rho^{\mathrm{AHE}}(\cos(\theta) - \sin(\theta)\delta\theta)\sin(\omega t) \\ -\rho^{\mathrm{AHE}}(\cos(\theta) - \sin(\theta)\delta\theta)\cos(\omega t) + \rho^0_{xx}\sin(\omega t) \end{pmatrix}. \tag{4.24}$$

Additionally, the most common SOT field symmetry is given by [66]:

$$\mathbf{H}_{\mathrm{SOT}} = J_0 x_{\mathrm{FL}} \begin{pmatrix} \sin(\omega t) \\ -\cos(\omega t) \\ 0 \end{pmatrix} + J_0 x_{\mathrm{DL}} \begin{pmatrix} \cos(\omega t) m_z \\ \sin(\omega t) m_z \\ -m_x\cos(\omega t) - m_y\sin(\omega t) \end{pmatrix}, \tag{4.25}$$

where x_{DL} and x_{FL} are respectively the DL and FL SOT coefficient.

There are two contributions to the SOT field, one proportional to $\cos(\omega t)$ and the second proportional to $\sin(\omega t)$. As the equation for $\delta\theta$ (Equation 4.7) is linearly dependent on the SOT field, it is possible to separate these into two equations for $\delta\theta$: one proportional

to $\cos(\omega t)$ and the other proportional to $\sin(\omega t)$, as shown here:

$$\delta\theta^{\cos(\omega t)} = -J_0 \frac{-\cos\theta(\cos(\phi)x_{\mathrm{DL}}m_z - \sin(\phi)x_{\mathrm{FL}}) - \sin(\theta)x_{\mathrm{DL}}m_x}{2k_1\cos(2\theta) + H_{\parallel}\sin(\theta)}\,, \tag{4.26}$$

$$\delta\theta^{\sin(\omega t)} = -J_0 \frac{-\cos\theta(\cos(\phi)x_{\mathrm{FL}} + \sin(\phi)x_{\mathrm{DL}}m_z) - \sin(\theta)x_{\mathrm{DL}}m_y}{2k_1\cos(2\theta) + H_{\parallel}\sin(\theta)}\,. \tag{4.27}$$

Finally, the first and second harmonic electric field were computed as:

$$E_x^{\cos(\omega t)} = J_0\rho_{xx}^0\,, \tag{4.28}$$

$$E_x^{\sin(\omega t)} = J_0\rho^{\mathrm{AHE}}m_z\,, \tag{4.29}$$

$$E_y^{\cos(\omega t)} = -J_0\rho^{\mathrm{AHE}}m_z\,, \tag{4.30}$$

$$E_y^{\sin(\omega t)} = J_0\rho_{xx}^0\,, \tag{4.31}$$

$$E_x^{\cos(2\omega t)} = \frac{J_0\rho^{\mathrm{AHE}}}{2}\sin(\theta)\delta\theta^{\sin(\omega t)}\,, \tag{4.32}$$

$$E_x^{\sin(2\omega t)} = -\frac{J_0\rho^{\mathrm{AHE}}}{2}\sin(\theta)\delta\theta^{\cos(\omega t)}\,, \tag{4.33}$$

$$E_y^{\cos(2\omega t)} = \frac{J_0\rho^{\mathrm{AHE}}}{2}\sin(\theta)\delta\theta^{\cos(\omega t)}\,, \tag{4.34}$$

$$E_y^{\sin(2\omega t)} = \frac{J_0\rho^{\mathrm{AHE}}}{2}\sin(\theta)\delta\theta^{\sin(\omega t)}\,. \tag{4.35}$$

On the first harmonic, ρ_{xx}^0 and ρ^{AHE} are independently captured. More generally, the diagonal and off-diagonal components can be separated by their phase and probing direction. On the second harmonic, out of the four recorded harmonic terms, only two are independent with $E_x^{\cos(2\omega t)} = E_y^{\sin(2\omega t)}$ and $E_y^{\cos(2\omega t)} = -E_x^{\sin(2\omega t)}$. Looking at the expression of $\delta\theta$, it is interesting to see that that there is still a separation of FL and DL contributions if one chooses, for example, a field where $\phi = 0$. There are no FL contributions in the $\cos(\omega t)$ terms. The $\sin(\omega t)$ terms, however, contain only FL contributions. These two contributions can be separated based on the relative phase of the harmonic voltage recorded.

4.3.1.2 Macrospin simulations

This section focuses on the results for a macrospin simulation for two separated cases: 1) a first-order anisotropy with perpendicular anisotropy 2) A first-order anisotropy with easy plane anisotropy. For the perpendicular anisotropy, the anisotropy constant is set to $k_1 = 1\,\mathrm{T}$ and the field is applied along the x direction, and for the easy plane anisotropy $k_1 = -0.1\,\mathrm{T}$, the field is rotating in the xy-plane. In terms of transport effects, both AHE and PHE were considered with value for the tensor $\rho_{xx0} = 1 \times 10^{-7}\,\Omega\,\mathrm{m}$, $\rho_{\mathrm{AHE}} = -1 \times 10^{-9}\,\Omega\,\mathrm{m}$, and $\rho_{\mathrm{PHE}} = -2 \times 10^{-10}\,\Omega\,\mathrm{m}$. Signals generated for the new geometry were compared to the signal expected for the standard Hall bar geometry including the ANE.

The first harmonic signals were plotted both from the new geometry and the standard Hall bar geometry for both the diagonal and off-diagonal components (Figure 4.4). The new geometry contains all the signals that were present in the old geometry. In addition, the new geometry also displays the signals that are expected by applying the current at a 90° direction, visible here on the resistance side, where the PHE has an impact on only one term, the others stay constant.

The second harmonic is displayed in Figure 4.5. Similarly, the new geometry contains all the signals present in the traditional Hall bar geometry, with the exception that the ANE does not contribute. The absence of ANE here is obvious by the difference in slope at low applied fields and also by the presence of the offset at high-field for the Hall bar geometry. All SOT present on the Hall bar is also present on the new geometry. Additionally, both the FL and DL components are captured due to the probe in both directions on the new geometry. In Figure (4.5), the FL effect appears similar to that which was observed on the longitudinal signal (V_{xx}) of the Hall bar. The sole difference was that none of the FL effects appeared in the longitudinal signal, as the modulation of the magnetisation vector was not large enough to be captured by the PHE. This longitudinal signal on the Hall bar was caused solely by the product between the DL effect and the PHE. In the

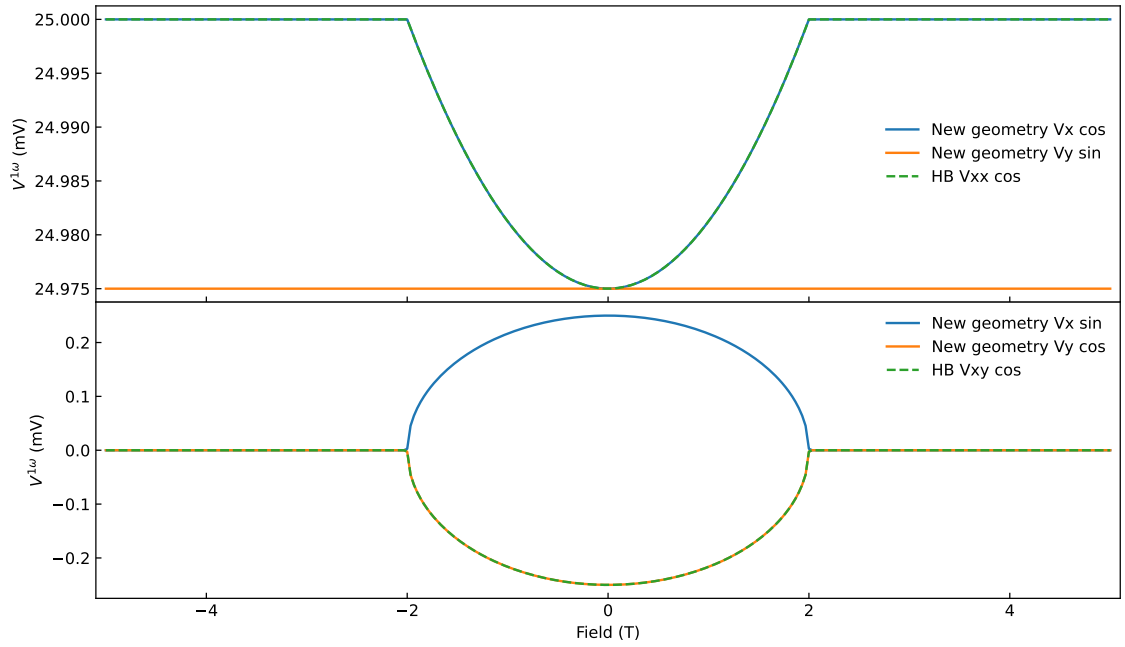

Figure 4.4: First harmonic signal for the Hall bar (HB) and the new geometry. The top panel corresponds to the longitudinal signal and the bottom panel to the transverse signal. Both the new geometry and Hall bar give the same contribution on the transverse signal. The longitudinal signal shows the same contribution for the terms align along the x direction. The new geometry also captures the signal for the current along the y direction of the sin phase. This contribution differs due to the absence of magnetoresistance.

new geometry, the signal still contains contributions from the DL torque and the PHE. However, this contribution was smaller than present in the Hall bar geometry and the signal was mainly dominated by the FL torque effect. Therefore, both FL and DL torques could be recorded without the need to change the direction of the applied field.

The second scenario corresponds to a field applied and rotated in-plane, with an easy plane anisotropy, with the anisotropy coefficient set to $k_1 = -0.1\,\mathrm{T}$. On the first harmonic (Figure 4.6) there was no significant difference between the traditional Hall bar and the new geometry, except for an offset in the field angle for the new geometry, dependent on the current being applied along the x or y direction.

On the second harmonic signal (Figure 4.7), a large difference between the standard Hall bar and new geometry was observed due to the contribution of the anomalous Nernst effect on the standard Hall bar, which gave a contribution to the signal that is independent from

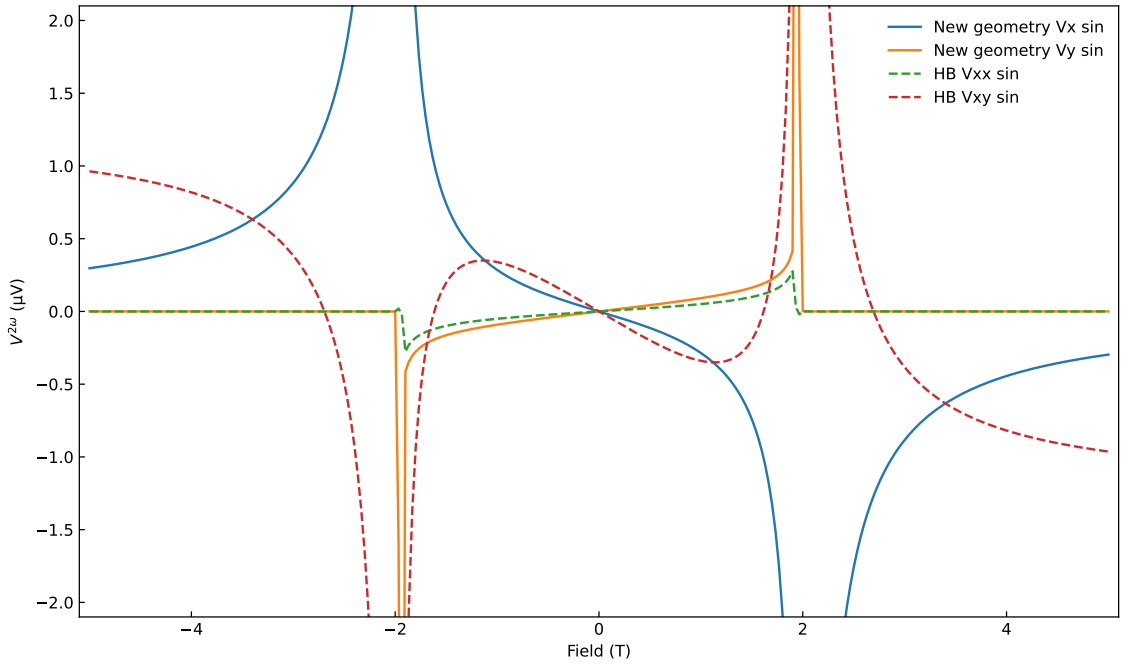

Figure 4.5: Second harmonic signal for the Hall bar (HB) and the new geometry. The DL effect has the same contribution in the new geometry (in blue) and Hall bar (in red). However, the ANE only appears on the Hall bar. The difference in the slope comparing the low-field and the offset high-field methods shows this. Additionally, the two other measured signals (in orange and green) appear similar, but originate from different sources. The signal on the Hall bar (green) originates from the mix of PHE and DL torque. The signal on the new geometry (orange) originates mainly from the FL torque, with a small contribution from the DL torque via the PHE.

the field intensity. Both geometries captured the FL and DL torques. In the new geometry, the FL and DL contributions are separated by their field periodicity, as the FL signal has a two-fold symmetry and the DL signal has a one-fold symmetry.

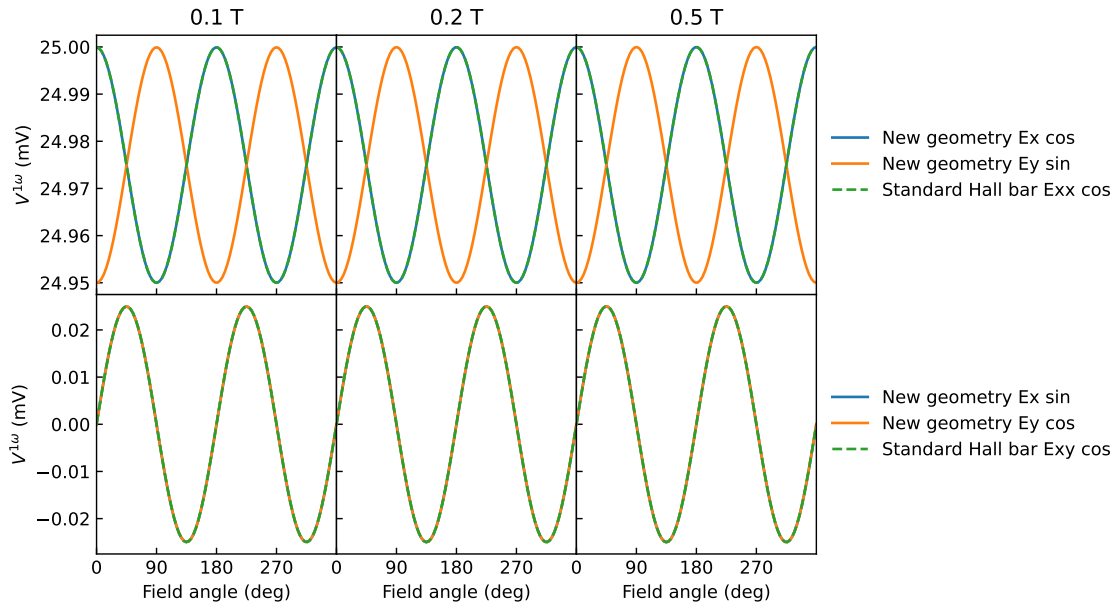

Figure 4.6: First harmonic signal for the Hall bar and new geometry. The longitudinal voltage (upper panel) displays comparable contributions from both the new geometry and the Hall bar, where the Hall bar signal (green) overlap perfectly with the new geometry $E_x \cos$ signal (blue). The distinction is that the new geometry measures currents in both the x and y directions, these differ only by a field angle offset. In contrast, the transverse signals (lower panel) remain consistent across all contributions.

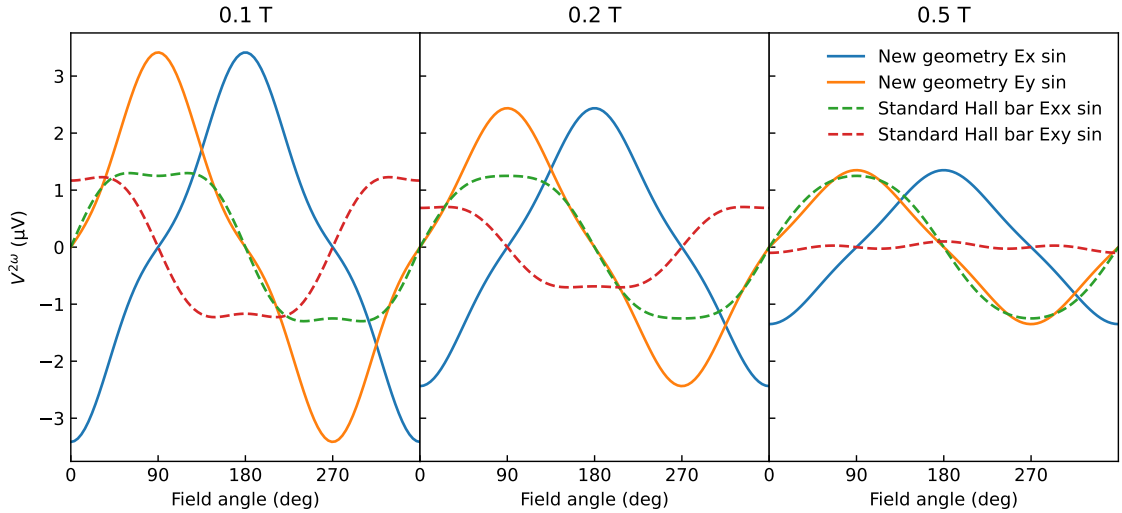

Figure 4.7: Second harmonic signal for the Hall bar and new geometry. Both geometries record both FL and DL torques. The Hall bar E_{xy} corresponds to contributions from the DL torque and ANE, and the Hall bar E_{xx} corresponds to FL torque and ANE. The ANE shows a contribution that does not depend on the field strength. Both FL and DL torques contribute to both signals in the new geometry. However, the DL signal has a periodicity of one for the field angle and the FL signal has a periodicity of two, which makes separating the two contributions easy.

4.3.2 Experimental work

4.3.2.1 Finite element method analysis

Assumptions used in the analytical and macrospin simulation state that the current direction and intensity can be perfectly controlled. Using a rotating current requires sending two currents, one along the x and the other along the y direction within the device. FEM analysis allows us to evaluate the parallel geometry efficacy in confining current compared with a solid design (as in Figure 4.2). The parallel geometry, with inserted channels, effectively confines the current; however, it did not achieve the theoretical ideal case as described by Equation 4.1. From here, we determined a geometrical factor that quantifies the impact of the geometry on the measured diagonal component of the magnetogalvanic tensor.

The current density of the solid geometry is presented in Figure 4.8. The colour represents the intensity and direction of the current for three different time-points corresponding to the phase of the current at 0, 45, and 90 degrees. Globally, the current tends to follow the direction imposed by the phase. However, the current density is reduced by almost half in the probing area of the device (centre) due to the presence of the other current contacts in the perpendicular direction. The current can be seen spreading along the full area, illustrating the lack of uniformity in both intensity and direction on the probing part of the device. This contradicts the previously defined requirements for the single macrospin approximation: i) a uniform and constant current density amplitude and, ii) a current direction exactly following the phases of the input sources.

Figure 4.9 presents the same simulation with the new parallel geometry. Unlike in the solid geometry, the current is now confined in the probing section, the addition of the channels making the path through the contact much less favourable. This has two effects, to stabilise the current intensity in the centre of the probing contact of the bar and to

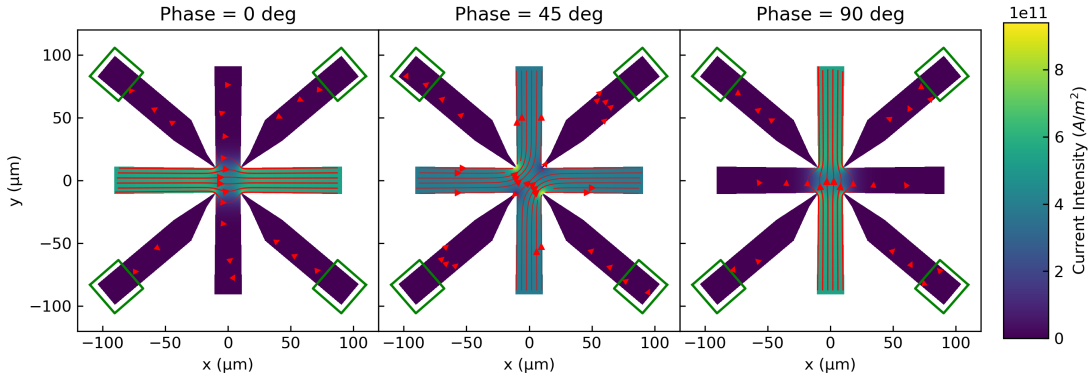

Figure 4.8: Finite elements model of the new geometry with filled contact. The colour corresponds to the norm of the current density, and the lines represent the direction of the current. Due to the increased width of the bar, the current lacks uniform intensity and direction in the centre. The average current direction still follows the direction given by the phase of the input.

stabilise the direction of the current. This is more compatible with the prerequisites used for the single macrospin approximation in Section 4.3.1.1 and 4.3.1.2. However, due to the reduction of the current path, this strongly increases the current density in the contact lead where the channels are present. This limits the maximum current that can be used and increased resistance also leads to additional noise.

A better visualisation of the current leakage can be observed in the cross-section of the current density along $x = 0$ for both geometries (Figure 4.10). This data corresponds to a phase equal to 0, when the current flows along the x direction. This demonstrates the efficiency of the channels inserted on the current contact to concentrate and focus the current on the probing zone. However, an apparent spike in current is still present on the contact lead after the channels, which indicates that these channels are not long enough to reduce the current leakage to a negligible amount. Numerically, one observes that 13% of the current in the parallel version actually flows in the contact lead and thus does not participate equally in the transport, resulting in a reduction of the potential observed on the terminal.

The voltage present was recorded on the probing terminal for all the simulations (Fig-

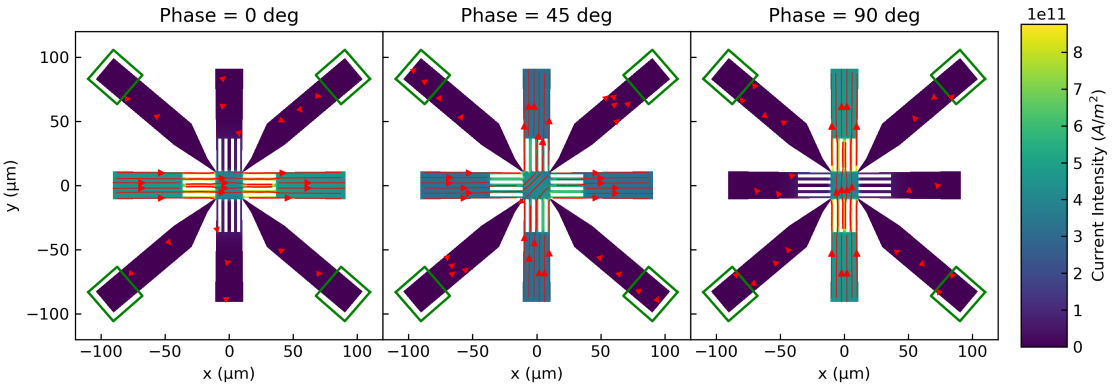

Figure 4.9: Finite elements model of the new geometry, with parallel channels added to the contact. The presence of parallel channels in the contact limits the amount of current that can spread along the transverse contact. This forces a better current density and direction uniformity. The increased resistance of the device and the presence of high current density on the reduced width contact represent a drawback.

ure 4.11). The green rectangles on Figure 4.8 and Figure 4.9 correspond to the average area that was used to determine each voltage. The computation was done for three different values of σ_{xy}: $(-1,\ 0 \text{ and } 1) \times 10^5\,\Omega^{-1}\,\mathrm{m}^{-1}$ The amplitude between the parallel and solid geometries varied greatly, with a smaller amplitude when the current was not confined. The effect of the off-diagonal component (σ_{xy}) appeared to change the phase of the probe voltage, as expected from the analytical expression.

The data represented on Figure 4.11 were fitted with $A\sin(\omega t + \phi)$. The two coefficients, in the form of cos and sin contributions, are reported in Table 4.1. When comparing the

Table 4.1: Extracted signal from the finite element simulation for the solid and parallel geometries compared to the ideal case, where the current is controlled exactly. All the values are normalised by $j_0\sqrt{(2)}w$ with w the width of the bar. Due to the resistance change between the two geometries and the fact that the simulation used the voltage source, we obtained a current density for the parallel geometry of $J_{parallel} = 4.42 \times 10^{11}\,\mathrm{A\,m^{-2}}$ and a current density for solid geometry of $J_{solid} = 5.36 \times 10^{11}\,\mathrm{A\,m^{-2}}$

σ_{xy} $(\Omega^{-1}\,\mathrm{m}^{-1})$	-5×10^5	0	5×10^5
Parallel cos $(10^{-8}\,\mathrm{V\,A^{-1}\,m^{-2}})$	1.6174 ± 0.0002	1.6174 ± 0.0002	1.6174 ± 0.0002
Parallel sin $(10^{-10}\,\mathrm{V\,A^{-1}\,m^{-2}})$	-1.84 ± 0.03	0.03 ± 0.03	1.91 ± 0.03
Solid cos $(10^{-8}\,\mathrm{V\,A^{-1}\,m^{-2}})$	1.1316 ± 0.0002	1.1316 ± 0.0002	1.1316 ± 0.0002
Solid sin $(10^{-10}\,\mathrm{V\,A^{-1}\,m^{-2}})$	1.98 ± 0.03	0.08 ± 0.03	-1.80 ± 0.03
Ideal case cos $(10^{-8}\,\mathrm{V\,A^{-1}\,m^{-2}})$	1.9998	2	1.9998
Ideal case sin $(10^{-10}\,\mathrm{V\,A^{-1}\,m^{-2}})$	-1.9998	0	1.9998

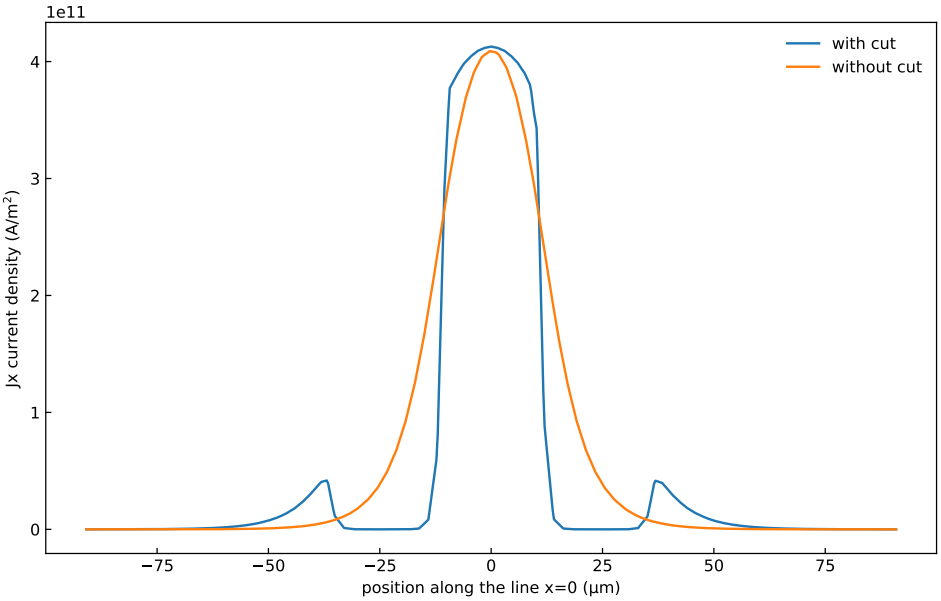

Figure 4.10: Current density from the finite element model simulations. A cross-section of the current along the $x = 0$ position for the 0 phase. The presence of channels in the contact lead increases the uniformity of the current density. The simulation demonstrates that the channels are not long enough to avoid current flowing on the contact lead, with 13% flowing on the contact area for the version with parallel channels, compared to 44% for the solid version.

two values of σ_{xy} there was good agreement globally, with some variation due to error in the finite element modelling (e.g. the sin component should have the same amplitude for negative and positive σ_{xy}). This error was captured and represented partially as the uncertainty of the fitting coefficient. The value between the solid geometry, parallel geometry and ideal case differs on the diagonal value (proportional to $\cos(\omega t)$), due to the lack of uniformity in the current. The observed difference between the solid geometry and the ideal case is much more marked. This demonstrates the efficiency of channelling the current using the parallel geometry to confine it spatially.

The off-diagonal component (proportional to $\sin(\omega t)$) demonstrates better agreement with the theoretical ideal case. This is expected, as the off-diagonal contribution does not depend on the shape and position of the probing contact as long as the current flows between the probing contact points. A geometrical factor was determined to take into

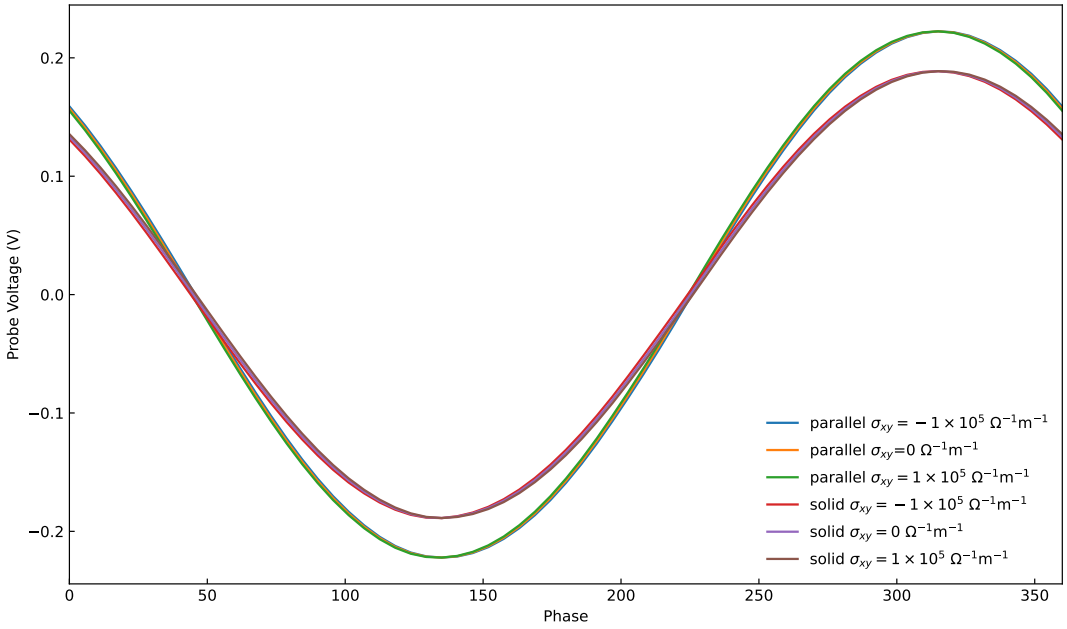

Figure 4.11: Measured voltage on two opposite contact pads of the finite element simulation. The presence of off-diagonal terms σ_{xy} affects the phase of the signal.

account the effect on the diagonal coefficient. The off-diagonal coefficients are not affected and the diagonal values are affected by a factor of 56% for the solid version and 81% for the parallel version, when compared to the value in the ideal case.

4.3.2.2 Experimental comparison of new geometry versus standard Hall bar

Signals recorded from both geometries patterned on a single CoPt multilayer sample were compared. The data from the first harmonic of the standard Hall bar are presented in Figure 4.12, showing a precise fit of both the longitudinal and transverse signals, accounting for contributions from the ANE, PHE, AMR, and HE.

The second harmonic (Figure 4.13) allows for the precise determination of both the SOT and thermoelectric effects. The signal decomposition reveals that the Nernst effect is strong and dominates much of the contribution. Additionally, it is clear that the raw data must first be corrected for a distortion component, proportional to the first harmonic, in order to achieve an accurate fit.

The parallel geometry measurements are shown in Figure 4.14 for the first harmonic and Figure 4.15 for the second harmonic. In the first harmonic, the signals were less distinct due to the mixing of both probing directions as a result of imperfections in the lithography. To address this, three fitting parameters were introduced, two to account for the signal contribution to the projection in the opposite direction, and a third to allow for slight variation in the direction of the y-current (Section 4.2.2.2).

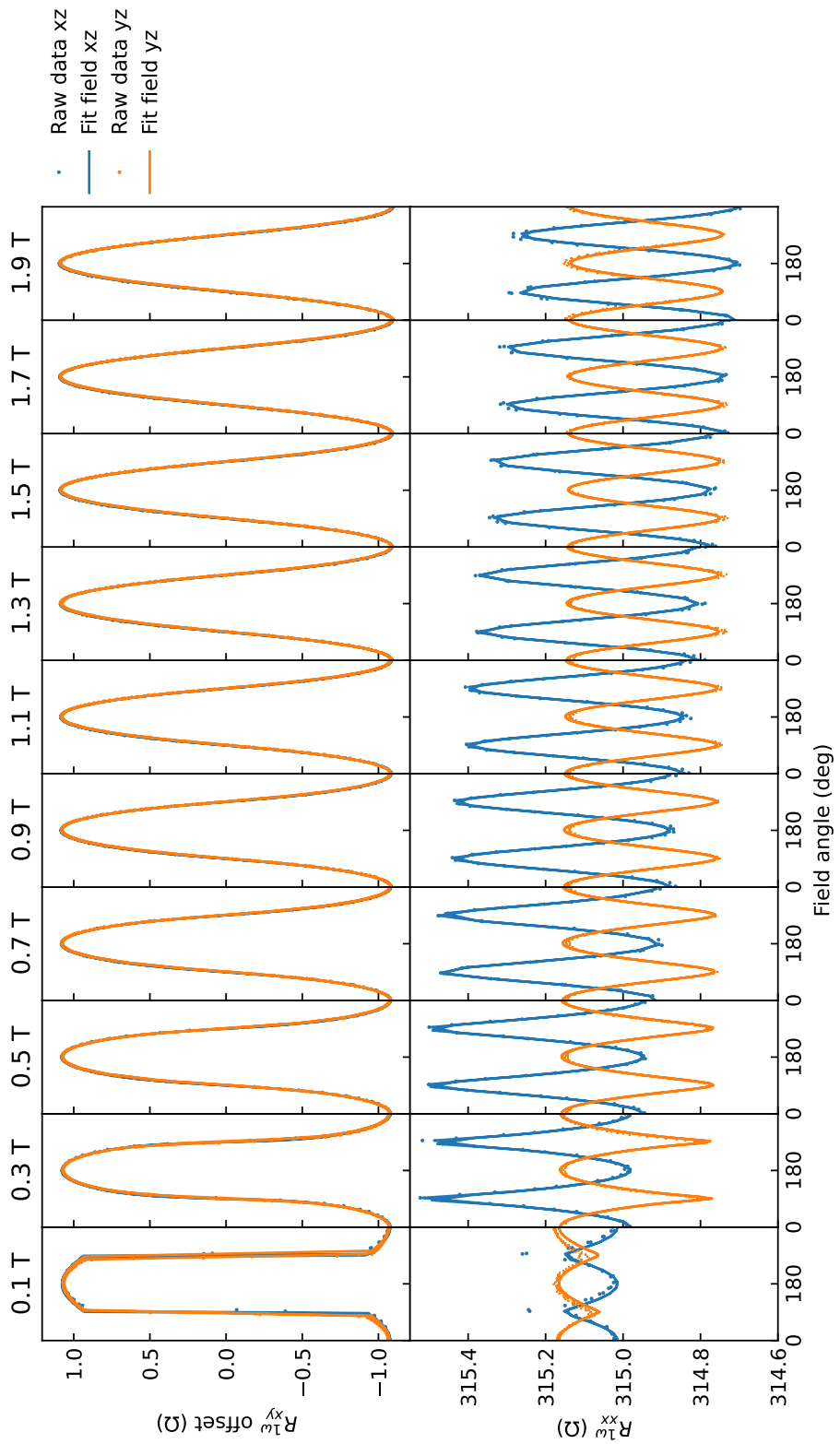

Figure 4.12: First harmonic data and model fit of both signal phases in the Hall bar geometry.

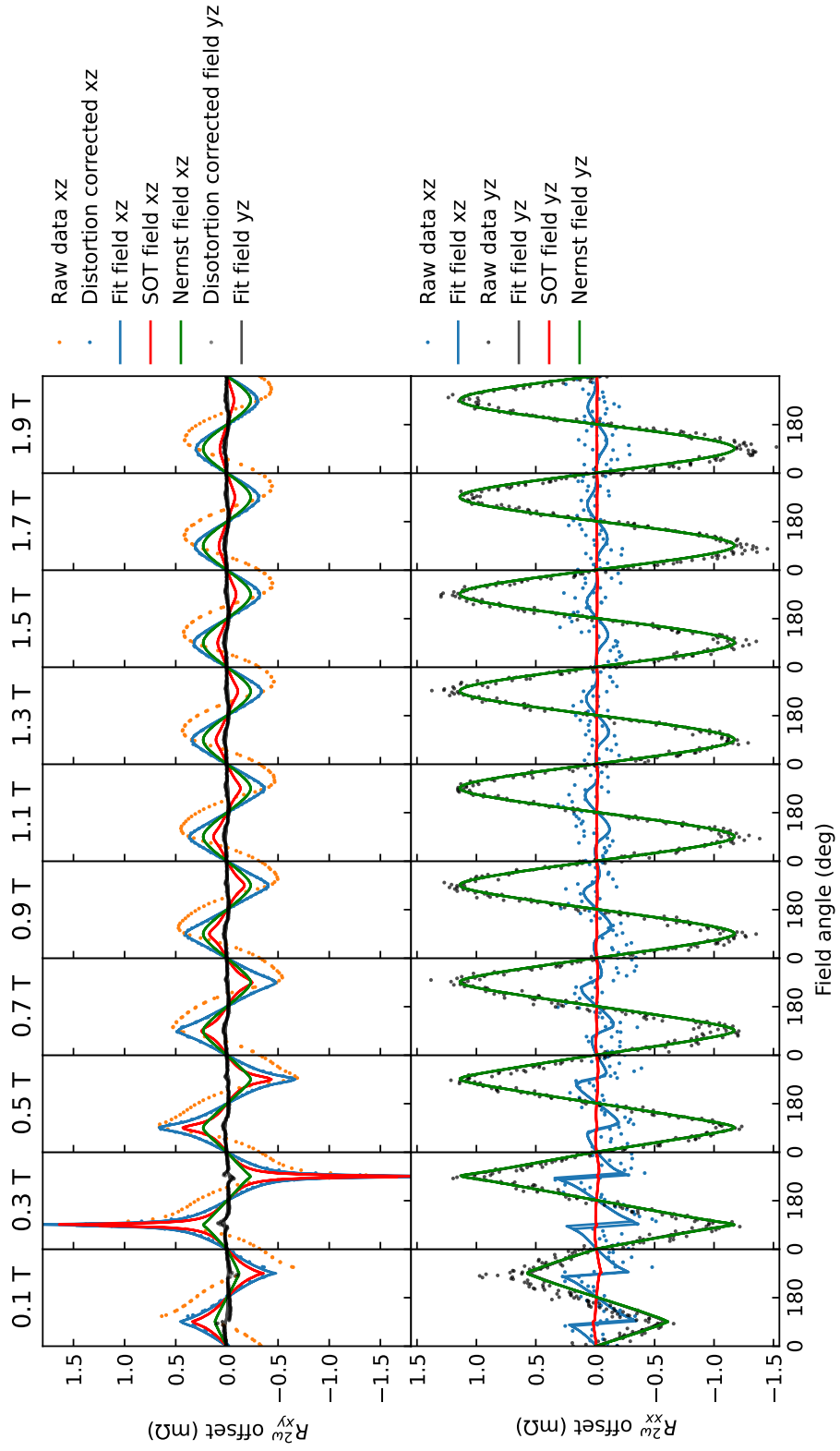

Figure 4.13: Second harmonic data and model fit of both signal phases in the Hall bar geometry.

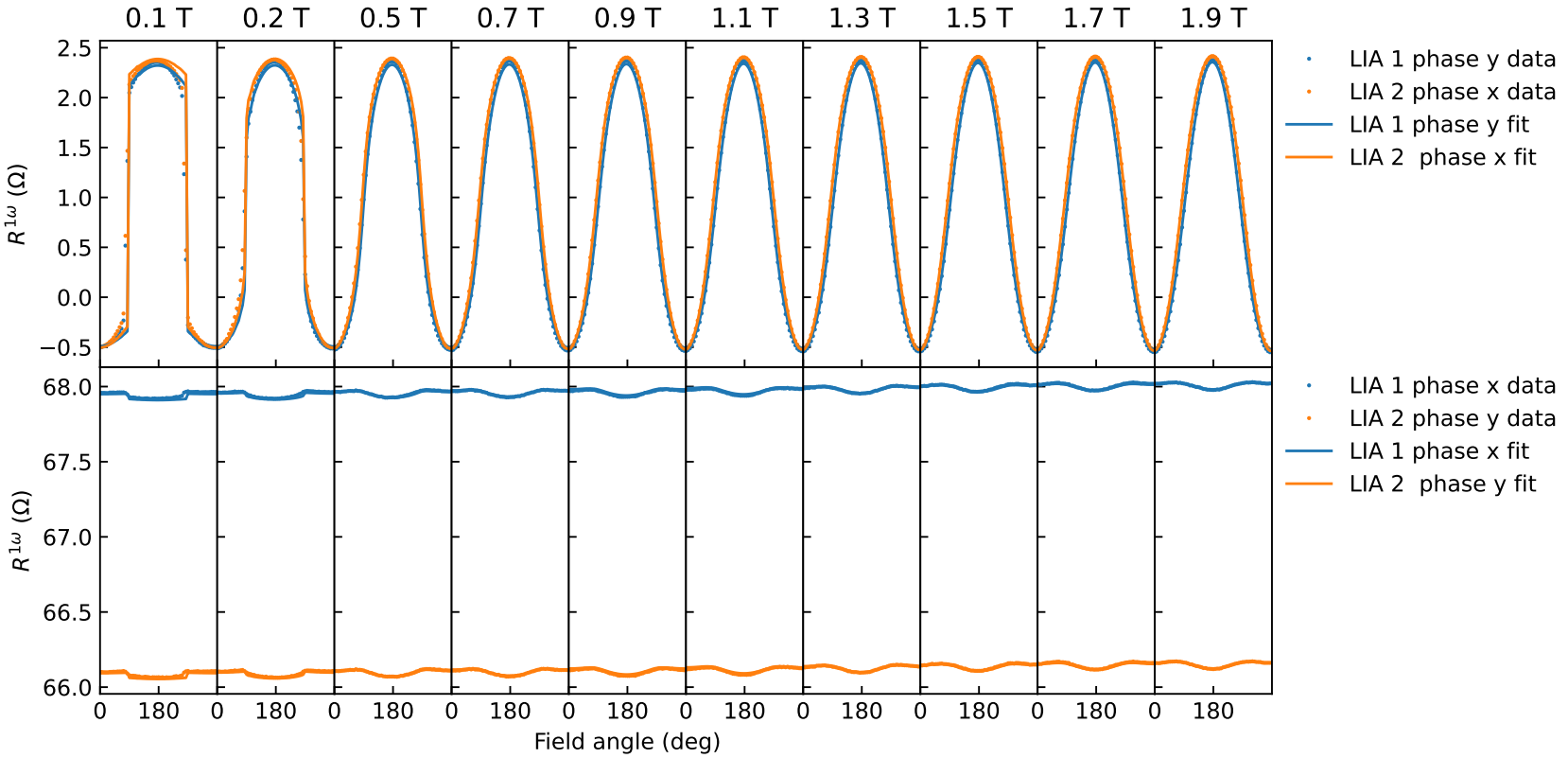

Figure 4.14: First harmonic data and model fit of both phase signals on the new geometry.

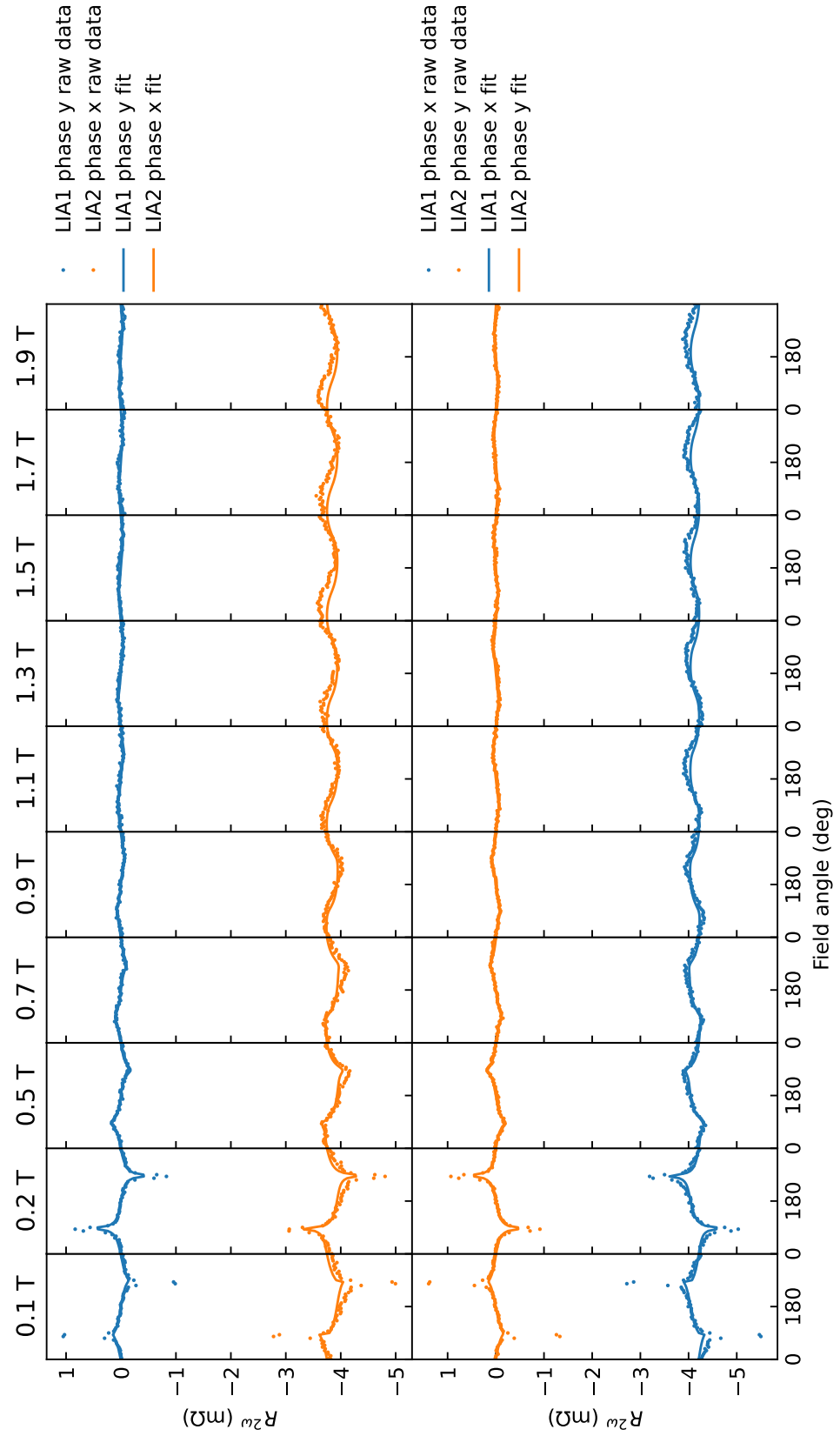

Figure 4.15: Second harmonic data and model fit of both phase signals on the new geometry.

Table 4.2: Fitting coefficients for the traditional Hall bar and new geometry.

Coefficient	Hall bar	New geometry
$\frac{K_1}{M}$ (T)	0.0904	0.097
$\frac{K_2}{M}$ (T)	0.013	0.009
ρ_{xx}^0 (Ω m)	6.448×10^{-7}	4.85×10^{-7}
ρ_{AHE} (Ω m)	-1.095×10^{-8}	-1.03×10^{-8}
ρ^{AMR} (Ω m)	7.99×10^{-10}	7.00×10^{-10}
ρ^{PHE} (Ω m)	-1.96×10^{-9}	-1.71×10^{-9}
ρ^{HE} (Ω m)	-1.24×10^{-10}	-1.38×10^{-10}
Ms(kA m^{-1})	1.388×10^3	1.388×10^3
H_{DL}(T A^{-1} m^2)	2.2×10^{-14}	2.06×10^{-14}
H_{FL}(T A^{-1} m^2)	3.10×10^{-15}	1.18×10^{-15}
ξ_{DL}	0.19	0.17
ANE	-4.83×10^{-22}	-

These imperfections had minimal impact on the second harmonic, as seen in the Figure 4.15. No thermoelectric signals were observed in the second harmonic data. Distortion appeared primarily at 0 phase and was attributed to the current source output, rather than the LIA input. This distortion is expected to be proportional to $\cos^2(\omega t)$ or $\sin^2(\omega t)$, both of which influence the 0 phase of the second harmonic. The theoretical analysis in Section 4.3.1.1 showed that as the FL and DL SOT information is contained in the y-phase signal, the SOT could be extracted solely using the y-phase signal without the need to correct for distortion.

A good overall agreement was observed between the new geometry and the standard Hall bar, when comparing the fitted coefficients, as shown in Table 4.2. The primary difference between these two geometries was found in the resistivity ρ_{xx}, which was 75% of the value of the standard Hall bar. This discrepancy is attributed to current leakage through the perpendicular contacts, previously identified as a geometrical factor. Finite element modelling predicted an effect of approximately 82%. The experimental lithography, with a wider opening of the channel and gold contacts present on the edge of the device, respectively increased and decreased the resistance, leads to a partial cancellation of these

effects. Despite these factors, there was a relatively good agreement between the finite element simulation and the experimental results.

The off-diagonal coefficients were less impacted, with the new geometry's values for the AHE coefficient corresponding to 94% of the value determined in the standard Hall bar. It is important to note that the experiments were conducted without temperature control and significant room temperature variations between the two measurements could also have affected the determined coefficients.

Additionally, current leakage influenced the value of the DL torque coefficient, resulting in a 6% difference between the two geometries. This discrepancy is primarily attributed to the lack of current homogeneity.

4.3.2.3 Noise analysis and noise budget

In the previous section, it appears that the noise level in the new geometry is higher than in the standard Hall bar geometry. This section identifies the noise sources in the new geometry and quantifies the increase. We present the quantified noise increase and demonstrate that it is less significant than initially perceived.

As shown in Figure 4.16, the current amplitude and phase remained highly stable with minimal variation during the scan. Thus, having feedback on only one branch does not appear to impact the system stability. However, an offset was observed between the branches on opposite sides. While this could be attributed to calibration errors, it is unlikely, as the entire system (i.e. $1\,\Omega$ resistor, amplifier and LIA) was recalibrated together. It is more plausible that the offset arises from the $0\,\mathrm{V}$ equipotential not being perfectly centred. The current leakage occurred through the $50\,\Omega$ impedance to the ground of the opposite direction current source. Despite this, the current leakage was relatively constant over time and does not significantly increase the noise in the system, indicating good control of current stability.

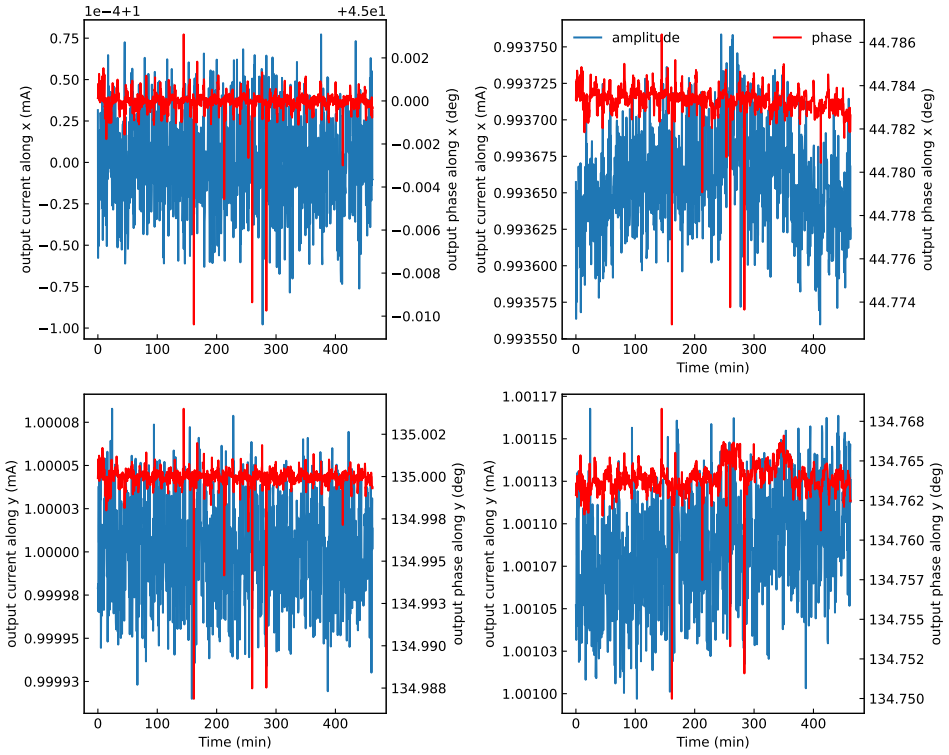

Figure 4.16: Current value and phase measured on the 1 Ω *resistor located on each of the current contacts for the new geometry. The variation of the current on each contact has a standard variation less than* 50 nA*. The difference of current between each axis is at max* 6 µA*. The standard variation on the phase is at most* 0.08°*, and the phase offset between the two branches is no more than* 0.3°*.*

The results for the first harmonic are presented in Figure 4.17. When both current sources were active, the distribution was non-Gaussian and significantly wider than when only one source was active, suggesting technical noise (interference) between the two sources. However, the increase in spread remained below a factor of 3.25, which can be compensated for by increasing the LIA integration time. As expected, the noise originating from the current sources was much higher than the thermal noise observed under the same conditions with both sources off. The thermal noise had a standard deviation of 1 µV.

For the second harmonic, the increase in noise was more than double when both sources were on, indicating some perturbation from the sources. However, the increase was a factor of 2.39, with a more Gaussian distribution, suggesting minimal feedback issues on the second harmonic. Finally, noise from the current source remained dominant, with

a maximum value of approximately 16 nV. In contrast, the standard deviation was only 1.5 nV when solely thermal and electronic detection noise was present, i.e. with the current sources off.

Last, the residual was compared with the fit from Section 4.3.2.2. The histogram of the residual on the second harmonic for both the standard Hall bar and the new geometry can be seen in Figure 4.18. The lowest noise level was observed in the standard Hall bar when measuring the transverse signal, with a standard variation of 11.6 nV. The largest variation occurred in the longitudinal signal of the standard Hall bar (V_{xx}), which can be explained by the difference in LIA integration times and the contact pad spacing (50 µm vs 31 µm, thus the larger range used for the input of the LIA).

In the new geometry, it appears that both contact directions exhibit similar noise levels and distributions. This can be attributed to the fact that in the new geometry, there is always a longitudinal component of the signal present in one of the signal phases, effectively meaning that the longitudinal (V_{xx}) signal is always being measured. Additionally, by increasing the integration time to 1 s, the noise level was reduced to a value comparable to the electronic noise observed in Figure 4.19. This suggests that the residual noise is close to the baseline electrical noise inherent in the setup, with no other significant contributions detected.

These results indicate that the noise was primarily due to the increased input range of the LIA, which is affected by the pickup of the longitudinal voltage. With the longitudinal contribution, the input range is set to 300 mV, and given that the analogue-to-digital converter has a 16-bit resolution, this yields a resolution of 9 µV. In contrast, the Hall voltage is typically much lower, allowing the input range to be set to 10 mV, which provides an input referred resolution of 0.3 µV and therefore better signal-to-noise ratio.

In future experiments, an AC bridge configuration could be employed to reduce the longitudinal voltage contribution. Alternatively, a notch filter at the frequency ω could be

used, bringing the much stronger signal of the first harmonic to a level comparable to the second harmonic signal. Either of these configurations would allow reducing the input range, hence making the best use of the 16 bit analogue-to-digital converters.

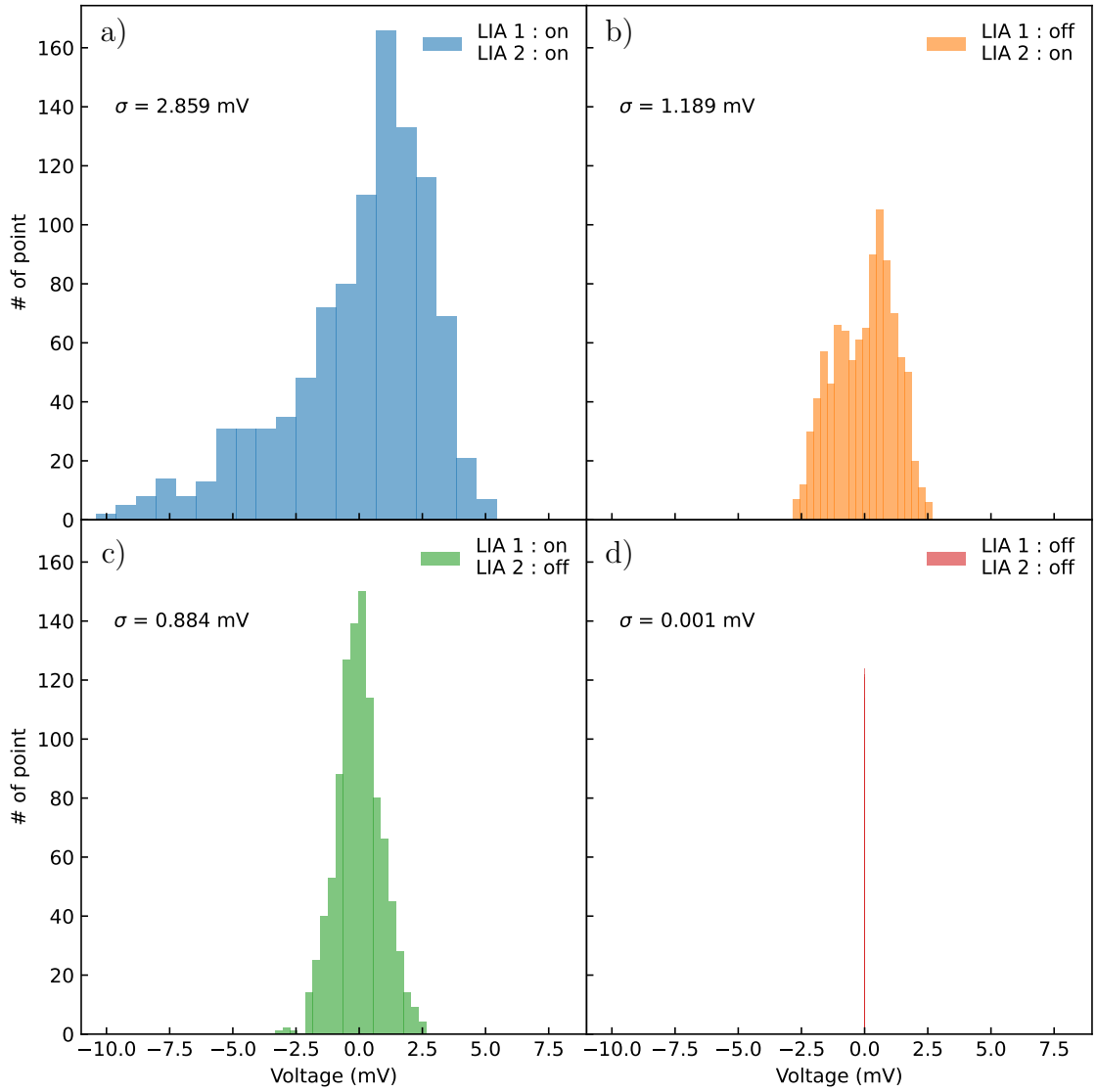

Figure 4.17: Noise on the first harmonic due to electronics in the setup for different configurations:(a) both source on, (b) and (c) one source on and (d) both source off. Having both sources on increases the noise by a factor 3.25 in the worst case, leading to an electrical noise close to 3 mV.

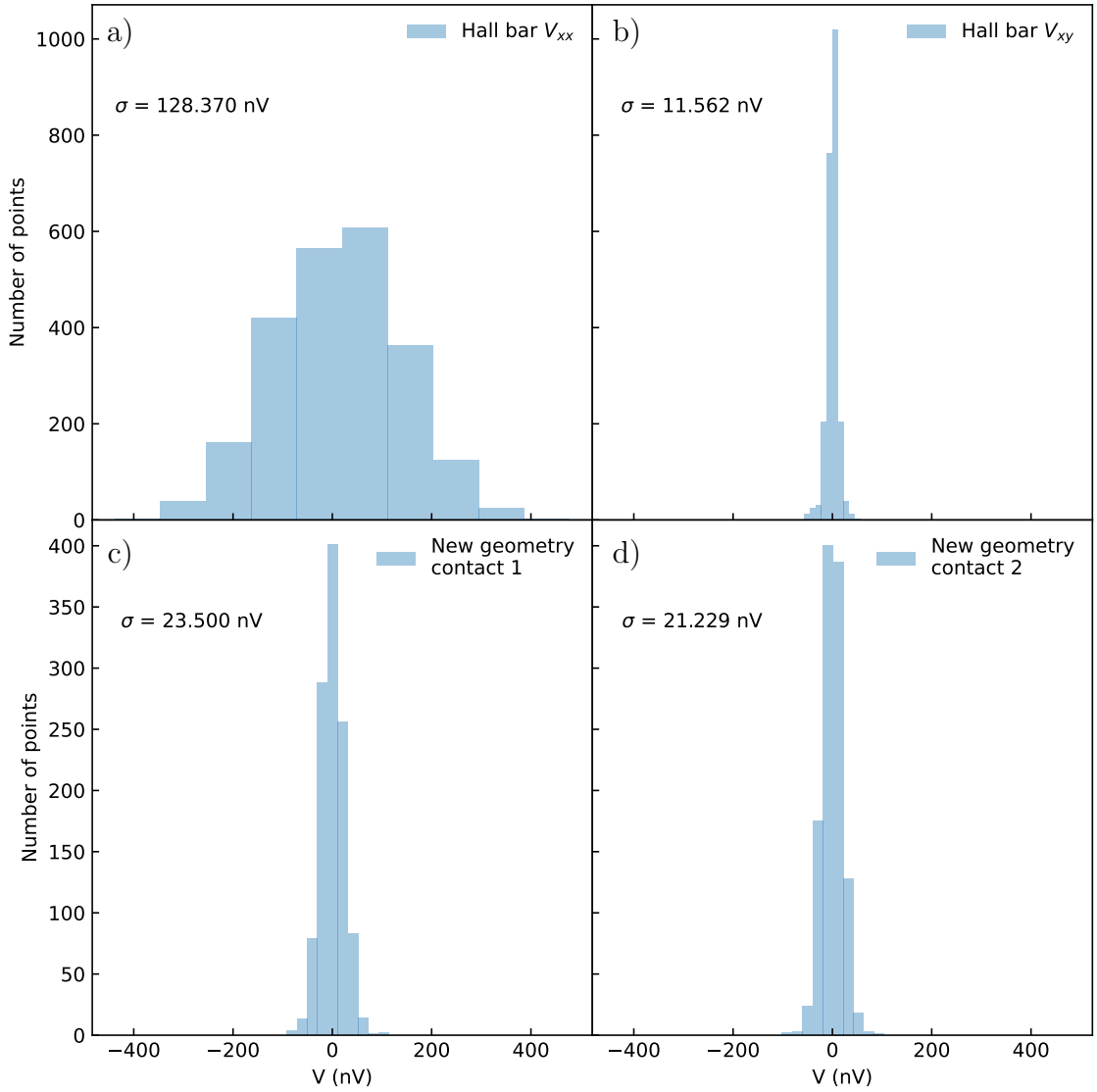

Figure 4.18: Histograms of the residual on the second harmonic for both the Hall bar and the new geometry. The integration time constant differs: 0.3 s *for the Hall bar, and* 1 s *for the new geometry. As shown, (b) the transverse signal V_{xy} of the Hall bar has the lowest noise. (a) The longitudinal signal V_{xx} has the highest noise. (c) and (d) The new geometry always contains a diagonal component on one of its phases for both contact directions, which explains the same level of noise on each component. Increasing the time constant shows that we can reduce this to an acceptable level, and that the noise penalty is negligible for the new geometry.*

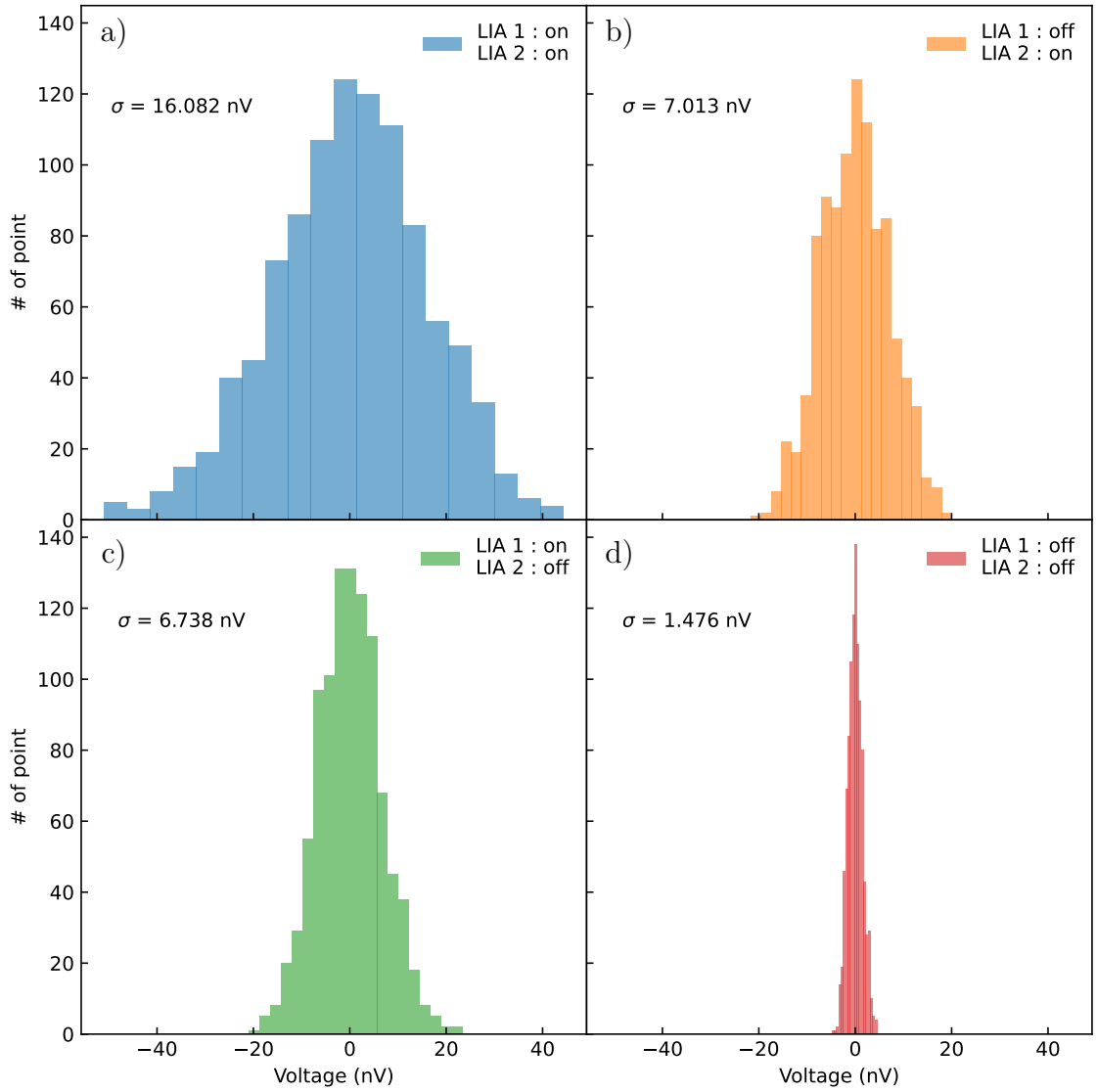

Figure 4.19: Noise on the second harmonic due to the electronics in the setup for different configurations: (a) both sources on, (b) and (c) one source on and (d) both source off. Having both sources on increases the noise by a factor 2.39 in the worst case, leading to an electrical noise close to 16 nV.

4.4 Conclusions

An almost complete elimination of thermoelectric effects was achieved by using a novel harmonic Hall geometry, which enables the use of a rotating current, $\mathbf{J} = J_0 \left(\cos(\omega t), \sin(\omega t), 0\right)$, as opposed to the standard Hall bar methodology. The SOT effect remained present due to the directional dependence of the SOT field.

This new geometry requires higher quality lithography, as imperfectly defined current direction and voltage probing can cause mixing of the terms to occur on the first harmonic.

The addition of parallel channels reduces the current lead width, which increases the potential of a thermal gradient in-plane. However, the second harmonic signal is marginally affected by these imperfections and corresponds solely to the SOT signal. Future research is required to explore different pattern geometries and address both challenges. First, to reduce signal mixing due to imperfections in the lithography and, second, to reduce heating in the channel due to the increased current density. Current control could be improved by using a high-impedance source or isolating the ground (e.g. using a calibrated isolation transformer).

The use of a rotating current enables the measurement of transport effects as a function of the current direction. This makes it ideal for SOT effect measurements as a function of the current direction, which can be complex in samples with symmetry lower than ∞m [92, 144].

By elimination of thermoelectric artifacts, this new geometry facilitates a more direct and robust detection of the SOT fields. This method can be applied to orbital torque measurements, which are particularly challenging due to lower SOT signals and higher thermoelectric effects in these thicker samples when using the standard Hall bar method [145–147]. As the field of orbital torque is an emerging research area, this new geometry could be particularly relevant [148]. For large current analyses using a standard Hall bar, new con-

tributions that do not follow the usual theory have been shown to appear in the harmonic signal [149]. The elimination of thermoelectric effects by using the new geometry could allow us to partition these contributions into SOT and thermoelectric effects.

Finally, in some cases contributions from the SOT are absent on the second harmonic signal, but are theoretically present on the third harmonic (Chapter 3, as well as [150]). However, the analysis of the third harmonic is usually more challenging, as there is a temperature dependence on all magnetogalvanic effects. The use of this new geometry will remove these thermoelectric contributions, allowing straightforward third harmonic signal measurement.

Experimentally, this geometry permits the measurement of SOT at lower fields without the requirement of a rotating magnetic field or fields larger than the anisotropy field. Contrary to the standard Hall bar method, where sample orientation has to be changed to record the FL and DL torques, the new geometry improves time-efficiency by recording these torques simultaneously. These combined advantages decrease the cost and time required to perform SOT measurements.

CHAPTER 5

Conclusions and future work

With a growing interest in discovering new materials with strong spin orbit torque (SOT) and the resulting study of a wider range of magnetic materials, a robust SOT measurement method is required. The new harmonic Hall methods developed in this thesis ensure accurate and high-precision detection of the SOT in single and bilayer films, even when this contribution is small compared to common spurious effects. As a basis for benchmarking, the contemporary harmonic Hall methods were evaluated using numerical simulations and techniques inspired by machine learning. Through this we were able to identify several gaps in the knowledge and highlight fundamental issues concerning the application of these analytical methods. Some of these sample-related problems were already known, such as errors due to thermoelectric contributions. Whereas, systematic errors arising from the experimental setup, such as sample orientation and current source distortion, have not been addressed in the literature. This thesis provides solutions for both the sample and the setup-related issues identified.

Evaluation of the harmonic Hall analytical methods for spin orbit torque measurement

A gap analysis was conducted to identify weaknesses in the current analytical harmonic Hall methods. To do so, a numerical model was developed based on symmetry arguments. Transport properties and the SOT field tensor were defined by symmetry arguments. From this, we could numerically balance the magnetic torques and compute the various harmonic Hall signals. We have used symmetry-based arguments to identify the minimum number of necessary and sufficient parameters to fit the harmonic Hall signal. We note here that this approach naturally groups parameters that obey the same symmetry, and that therefore the analysis carried out here is complementary to the microscopic approach. As an example, the spin Seebeck effect and anomalous Nernst effect are represented by a single parameter; similarly, the Oersted field and field-like (FL) torque are represented by the same parameter. The only approximation made is that of assuming a sample symmetry.

The above evaluation identified the necessary assumptions for preventing significant errors when extracting the SOT with the analytical harmonic Hall method. We show that for the differential method (Chapter 2), both the planar Hall effect (PHE) and thermoelectric contributions must be considered. Recording the longitudinal harmonic Hall signals allows correcting for the thermoelectric effects, as defined in this thesis, Chapter 1, Section 1.6.3.3. For the high-field method, it is essential to apply the field *perfectly* in the sample plane. However, this contradicts the use of the high-field method for samples with perpendicular anisotropy where a bias field needs to be applied out-of-plane to ensure a single magnetic domain. Meeting these requirements allows for relatively high accuracy in determining SOT values with current analytical methods. Even if all the previous assumptions are met, a discrepancy between the analytical methods and the numerical model is still found. To achieve optimal accuracy, it is necessary to use a numerical model that

considers all sample and setup parameters. The gaps in the analytical methods led to the development of a new methodology to measure and analyse harmonic Hall signals.

New methods to measure spin orbit torque and their applications

Above we have summarised how the numerical model was used to evaluate the precision and validity of the analytical harmonic Hall methods. This model can also be applied to the analysis of the harmonic Hall signal directly. It takes into account all transport effects and setup conditions to precisely determine the SOT value. When using this model, erroneous sample positioning can be detected and corrected. We underline here that it is always preferable to align samples correctly from the outset, rather than relying on subsequent correction.

On a more fundamental level, we have shown that the lithography pattern commonly used when recording harmonic Hall signals can be enhanced with a novel design. This allows the acquisition of SOT signals, while effectively eliminating thermoelectric effects at the sample level. This makes our sample geometry suitable for use with samples where thermoelectric modelling is difficult due to complex magnetic or sample structures. This novel Hall geometry requires a numerical model to analyse the SOT signal, as it involves analysing eight independent harmonic Hall signals. It is possible to write out their analytical expressions, but this exercise is of little interest, as the equations become too complex to allow a physical understanding of the effects studied. We speculate that our method will find applications in spin-orbitronics where thicker samples are used, in low-temperature measurements where these thermal gradients are unknown, or for complex thin-film stacks, where modelling the thermoelectric effect can be difficult.

As the derivations for both the numerical model and the new geometry are based on symmetry arguments, their focus is not limited to single or bilayer thin films. Therefore, they can be used for any material that meets the assumptions of the harmonic Hall method: i)

the field dependence on magnetisation must be modellable (numerically if needed), and ii) the measurement is performed in the non-hysteretic region of magnetisation. These conditions are reasonably easy to meet for a wide number of samples and device structures, thereby extending the potential use of the method to a wide array of research challenges.

Numerical method limitations

While the numerical model is central to this thesis, there are caveats that need to be considered. The harmonic Hall method can be more clearly understood through its analytical expression than through the use of a numerical model that effectively hides the sometimes complex interplay between microscopic causes and their effects. Consequently, the numerical model cannot replace the knowledge gained from the analytical approach. Furthermore, the numerical model does not guarantee that overfitting will not occur during data processing. This can lead to inaccurate SOT estimations. To avoid overfitting, it is essential to gather sufficient data from a range of magnetic fields and orientations. A solid understanding of the underlying physics, provided by the analytical method, allows for choosing the correct applied magnetic field magnitude and direction to use in the numerical model. The numerical model will only provide greater accuracy when used to overcome the limitations of the analytical methods.

Future work

The primary aim in developing the numerical model was to address systematic errors, which has been accomplished. The next step would be to estimate the confidence interval of the SOT values obtained, which would address random errors. This is not a trivial task. The harmonic Hall signal fit residuals show systematic patterns, which restrict the use of Gaussian error estimation. While we could increase the complexity of the model to explain these residuals, this would likely require us to abandon the macrospin approximation and use a micro-magnetic model, increasing the number of parameters to

explain a few percent of the signal. A preferable approach would be to use a Bayesian approach to investigate the posterior distribution of the model parameters, e.g. using a Markov-chain Monte Carlo algorithm.

For the new geometry, three potential improvements to the experimental setup have been identified. First, the distortion in the current input could be reduced by adding a frequency filter between the source and the sample. Second, the pattern design in this thesis can be optimised to better resemble an ideal rotating current, i.e. constant in both amplitude and phase across the probing area of the device. This could be achieved through finite element method (FEM) simulations, adapting the design iteratively until it converges on the closest ideal current configuration, while respecting the limitations of lithographic capacity. Finally, the signal-to-noise ratio should be improved to better utilise the detection range of the lock-in amplifier. The signal-to-noise ratio of the second harmonic is limited by the amplitude of the first harmonic longitudinal signal. A better signal-to-noise ratio could be achieved in the future by improving the acquisition chain, taking advantage of the frequency difference between the two signals. These improvements would facilitate the study of lower symmetry materials, whose transport properties depend on the direction between the current and the crystallographic axis.

Wider impacts of this research

The currently available laboratory-grade experimental techniques used to determine crystal structure, e.g. X-ray diffraction, cannot easily detect if inversion symmetry is broken on a sufficiently long real-space range to promote the desired effects. Detecting small SOT signals can serve as an optimisation parameter for sample growth, in line with how optical second harmonic generation has served as a means to detect broken inversion symmetry. This opens up opportunities for the development of non-centrosymmetric magnetic materials by using the SOT as a proxy figure of merit. The novel methods and geometry introduced in this thesis allow for an increase in the throughput of SOT measurements, as

small but finite signals are detected with ease using equipment readily available in most laboratories.

Another advantage of this new geometry is the ability to vary the current direction with respect to the crystallographic axis without the need to pattern different Hall bars for each individual direction. This allows for the measurement of lower symmetry materials for which the current direction matters, such as unidirectional spin magnetoresistance and intrinsic SOT effects.

In the emerging field of orbitronics, orbital torque can originate from a wider variety of materials, as compared to SOT, as these are not limited to heavy metals. This includes materials with large thermoelectric contributions, such as CuO_x [145]. Additionally, orbital torque is expected to have a longer diffusion length [146, 147] and so involves the measurement of thicker samples favouring larger thermal gradients across the film thickness. Combined, these two issues increase the risk of large thermoelectric contributions during measurements. As such, measuring orbital torque using the current analytical harmonic Hall approaches could introduce substantial errors. The new methods introduced in this thesis, such as the numerical model (Chapter 2 and Appendix C) and the novel geometry (Chapter 4), address and solve these challenges.

Bibliography

[1] K. E. Siewierska, G. Atcheson, A. Jha, K. Esien, R. Smith, S. Lenne, N. Teichert, J. O'Brien, J. M. D. Coey, P. Stamenov, and K. Rode, "Magnetic order and magnetotransport in half-metallic ferrimagnetic Mn_yRu_xGa thin films", Phys. Rev. B **104**, 064414 (2021).

[2] G. Ji, Y. Zhang, Y. Chai, and T. Nan, "Recent progress on controlling spin-orbit torques by materials design", npj Spintronics **2** (2024).

[3] Q. Shao, P. Li, L. Liu, H. Yang, S. Fukami, A. Razavi, H. Wu, K. Wang, F. Freimuth, Y. Mokrousov, M. D. Stiles, S. Emori, A. Hoffmann, J. Åkerman, K. Roy, J.-P. Wang, S.-H. Yang, K. Garello, and W. Zhang, "Roadmap of spin-orbit torques", IEEE Transactions on Magnetics **57**, 1 (2021).

[4] A. Manchon, J. Železný, I. M. Miron, T. Jungwirth, J. Sinova, A. Thiaville, K. Garello, and P. Gambardella, "Current-induced spin-orbit torques in ferromagnetic and antiferromagnetic systems", Rev. Mod. Phys. **91**, 035004 (2019).

[5] M.-H. Nguyen and C.-F. Pai, "Spin-orbit torque characterization in a nutshell", APL Materials **9**, 030902 (2021).

[6] R. R. Birss, *Symmetry and magnetism* (North Holland Publishing Company, 1964).

[7] J. Coey, *Magnetism and magnetic materials* (Cambridge University Press, 2010).

[8] A. Einstein and W. J. de Haas, "Experimental proof of the existence of Ampère's molecular currents", Koninklijke Nederlandse Akademie van Wetenschappen Proceedings Series B Physical Sciences **18**, 696 (1915).

[9] S. Blundell, *Magnetism in condensed matter*, Oxford master series in condensed matter physics (Oxford University Press, Oxford, 2001).

[10] K. Yosida, *Theory of magnetism*, 1st ed., Springer Series in Solid-State Sciences (Springer, 1996).

[11] V. Baltz, A. Manchon, M. Tsoi, T. Moriyama, T. Ono, and Y. Tserkovnyak, "Antiferromagnetic spintronics", Rev. Mod. Phys. **90**, 015005 (2018).

[12] J. Finley and L. Liu, "Spintronics with compensated ferrimagnets", Applied Physics Letters **116**, 110501 (2020).

[13] J. Kubler, *Theory of itinerant electron magnetism*, International Series of Monographs on Physics (Oxford University Press, London, England, 2000).

[14] J. F. Janak, "Uniform susceptibilities of metallic elements", Phys. Rev. B **16**, 255 (1977).

[15] K. V. Shanavas, Z. S. Popovi ć, and S. Satpathy, "Theoretical model for rashba spin-orbit interaction in d electrons", Phys. Rev. B **90**, 165108 (2014).

[16] W. Sucksmith and J. E. Thompson, "The magnetic anisotropy of cobalt", R. Soc. Lond. **225** (1954).

[17] Y. Xu, D. D. Awschalom, and J. Nitta, eds., *Handbook of spintronics* (Springer Netherlands, 2016).

[18] J. Stohr and H. C. Siegmann, *Magnetism: from fundamentals to nanoscale dynamics*, Springer Series in Solid-State Sciences (Springer, 2006).

[19] A. Fert and I. A. Campbell, "Two-current conduction in nickel", Phys. Rev. Lett. **21**, 1190 (1968).

[20] S. Kokado, M. Tsunoda, K. Harigaya, and A. Sakuma, "Anisotropic magnetoresistance effects in fe, co, ni, fe4n, and half-metallic ferromagnet: a systematic analysis", Journal of the Physical Society of Japan **81**, 024705 (2012).

[21] V. Baltz, *The basics of electron transport in spintronics* (EDP Sciences, 2023).

[22] I. I. Mazin, "How to define and calculate the degree of spin polarization in ferromagnets", Phys. Rev. Lett. **83**, 1427 (1999).

[23] M. N. Baibich, J. M. Broto, A. Fert, F. N. Van Dau, F. Petroff, P. Etienne, G. Creuzet, A. Friederich, and J. Chazelas, "Giant magnetoresistance of (001)fe/(001)cr magnetic superlattices", Phys. Rev. Lett. **61**, 2472 (1988).

[24] E. H. Hall, "On a new action of the magnet on electric currents", American Journal of Mathematics **2**, 287 (1879).

[25] E. Hall, "Xviii. on the "rotational coefficient" in nickel and cobalt", The London, Edinburgh, and Dublin Philosophical Magazine and Journal of Science **12**, 157 (1881).

[26] N. Nagaosa, J. Sinova, S. Onoda, A. H. MacDonald, and N. P. Ong, "Anomalous hall effect", Rev. Mod. Phys. **82**, 1539 (2010).

[27] H. Chen, Q. Niu, and A. H. MacDonald, "Anomalous hall effect arising from noncollinear antiferromagnetism", Phys. Rev. Lett. **112**, 017205 (2014).

[28] M. Dyakonov and V. Perel, "Current-induced spin orientation of electrons in semiconductors", Physics Letters A **35**, 459 (1971).

[29] Y. K. Kato, R. C. Myers, A. C. Gossard, and D. D. Awschalom, "Observation of the spin hall effect in semiconductors", Science **306**, 1910 (2004).

[30] C. Stamm, C. Murer, M. Berritta, J. Feng, M. Gabureac, P. M. Oppeneer, and P. Gambardella, "Magneto-optical detection of the spin hall effect in pt and w thin films", Phys. Rev. Lett. **119**, 087203 (2017).

[31] J. Sinova, S. O. Valenzuela, J. Wunderlich, C. H. Back, and T. Jungwirth, "Spin hall effects", Rev. Mod. Phys. **87**, 1213 (2015).

[32] A. Hoffmann, "Spin hall effects in metals", IEEE Transactions on Magnetics **49**, 5172 (2013).

[33] K. Behnia and H. Aubin, "Nernst effect in metals and superconductors: a review of concepts and experiments", Reports on Progress in Physics **79**, 046502 (2016).

[34] H. B. Callen, "The application of onsager's reciprocal relations to thermoelectric, thermomagnetic, and galvanomagnetic effects", Phys. Rev. **73**, 1349 (1948).

[35] W. Thomson, "Xix. on the electro-dynamic qualities of metals:—effects of magnetization on the electric conductivity of nickel and of iron", Proceedings of the Royal Society of London **8**, 546 (1857).

[36] P. Ritzinger and K. Výborný, "Anisotropic magnetoresistance: materials, models and applications", Royal Society Open Science **10**, 230564 (2023).

[37] L. Berger, P. P. Freitas, J. D. Warner, and J. E. Schmidt, "On the temperature dependence of the magnetoresistance of ferromagnetic alloys", Journal of Applied Physics **64**, 5459 (1988).

[38] S. Ishio, H. Haga, S. Shindo, and H. Saito, "Anisotropic magnetoresistance in fe-co-ni alloys", Journal of the Magnetics Society of Japan **23**, 427 (1999).

[39] J. Smit, "Magnetoresistance of ferromagnetic metals and alloys at low temperatures", Physica **17**, 612 (1951).

[40] I. A. Campbell, A. Fert, and O. Jaoul, "The spontaneous resistivity anisotropy in ni-based alloys", Journal of Physics C: Solid State Physics **3**, S95 (1970).

[41] L. š. Nádvorník, M. Borchert, L. Brandt, R. Schlitz, K. A. de Mare, K. Výborný, I. Mertig, G. Jakob, M. Kläui, S. T. B. Goennenwein, M. Wolf, G. Woltersdorf,

and T. Kampfrath, “Broadband terahertz probes of anisotropic magnetoresistance disentangle extrinsic and intrinsic contributions”, Phys. Rev. X **11**, 021030 (2021).

[42] Y.-T. Chen, S. Takahashi, H. Nakayama, M. Althammer, S. T. B. Goennenwein, E. Saitoh, and G. E. W. Bauer, “Theory of spin hall magnetoresistance (smr) and related phenomena”, Journal of Physics: Condensed Matter **28**, 103004 (2016).

[43] S. R. Marmion, M. Ali, M. McLaren, D. A. Williams, and B. J. Hickey, “Temperature dependence of spin hall magnetoresistance in thin yig/pt films”, Phys. Rev. B **89**, 220404 (2014).

[44] E. Cogulu, H. Zhang, N. N. Statuto, Y. Cheng, F. Yang, R. Cheng, and A. D. Kent, “Quantifying spin-orbit torques in antiferromagnet–heavy-metal heterostructures”, Phys. Rev. Lett. **128**, 247204 (2022).

[45] H. Nakayama, M. Althammer, Y.-T. Chen, K. Uchida, Y. Kajiwara, D. Kikuchi, T. Ohtani, S. Geprägs, M. Opel, S. Takahashi, R. Gross, G. E. W. Bauer, S. T. B. Goennenwein, and E. Saitoh, “Spin hall magnetoresistance induced by a nonequilibrium proximity effect”, Phys. Rev. Lett. **110**, 206601 (2013).

[46] H. Kurt, K. Rode, P. Stamenov, M. Venkatesan, Y.-C. Lau, E. Fonda, and J. M. D. Coey, “Cubic Mn_2Ga thin films: crossing the spin gap with ruthenium”, Phys. Rev. Lett. **112**, 027201 (2014).

[47] R. A. de Groot, F. M. Mueller, P. G. v. Engen, and K. H. J. Buschow, “New class of materials: half-metallic ferromagnets”, Phys. Rev. Lett. **50**, 2024 (1983).

[48] H. van Leuken and R. A. de Groot, “Half-metallic antiferromagnets”, Phys. Rev. Lett. **74**, 1171 (1995).

[49] C. Felser and A. Hirohata, eds., *Heusler alloys* (Springer International Publishing, 2016).

[50] D. Betto, K. Rode, N. Thiyagarajah, Y.-C. Lau, K. Borisov, G. Atcheson, M. Žic, T. Archer, P. Stamenov, and J. M. D. Coey, "The zero-moment half metal: how could it change spin electronics?", AIP Advances **6**, 055601 (2016).

[51] T. Hahn, ed., *International tables for crystallography* (Springer, 2005).

[52] J. C. Slonczewski, "Current-driven excitation of magnetic multilayers", Journal of Magnetism and Magnetic Materials **159**, L1 (1996).

[53] L. Berger, "Emission of spin waves by a magnetic multilayer traversed by a current", Phys. Rev. B **54**, 9353 (1996).

[54] H. Kurebayashi, J. Sinova, D. Fang, A. C. Irvine, T. D. Skinner, J. Wunderlich, V. Novák, R. P. Campion, B. L. Gallagher, E. K. Vehstedt, L. P. Zârbo, K. Výborný, A. J. Ferguson, and T. Jungwirth, "An antidamping spin-orbit torque originating from the berry curvature", Nature Nanotechnology **9**, 211 (2014).

[55] P. Gambardella and I. M. Miron, "Current-induced spin–orbit torques", Philosophical Transactions of the Royal Society A: Mathematical, Physical and Engineering Sciences **369**, 3175 (2011).

[56] J. Železný, H. Gao, A. Manchon, F. Freimuth, Y. Mokrousov, J. Zemen, J. Ma šek, J. Sinova, and T. Jungwirth, "Spin-orbit torques in locally and globally noncentrosymmetric crystals: antiferromagnets and ferromagnets", Phys. Rev. B **95**, 014403 (2017).

[57] V. Edelstein, "Spin polarization of conduction electrons induced by electric current in two-dimensional asymmetric electron systems", Solid State Communications **73**, 233 (1990).

[58] V. V. Bel'kov and S. D. Ganichev, "Magneto-gyrotropic effects in semiconductor quantum wells", Semiconductor Science and Technology **23**, 114003 (2008).

[59] Y. A. Bychkov and E. I. Rashba, "Oscillatory effects and the magnetic susceptibility of carriers in inversion layers", Journal of Physics C: Solid State Physics **17**, 6039 (1984).

[60] M. Dyakonov, V. Marishchak, V. Perel, and A. Titkov, "The effect of strain on the spin relaxation of conduction electrons in iii-v semiconductors", Journal of Experimental and Theoretical Physics **90**, 1123 (1986).

[61] T. D. Skinner, K. Olejník, L. K. Cunningham, H. Kurebayashi, R. P. Campion, B. L. Gallagher, T. Jungwirth, and A. J. Ferguson, "Complementary spin-hall and inverse spin-galvanic effect torques in a ferromagnet/semiconductor bilayer", Nature Communications **6** (2015).

[62] A. Manchon, H. C. Koo, J. Nitta, S. M. Frolov, and R. A. Duine, "New perspectives for rashba spin-orbit coupling", Nature Materials **14**, 871 (2015).

[63] I. Mihai Miron, G. Gaudin, S. Auffret, B. Rodmacq, A. Schuhl, S. Pizzini, J. Vogel, and P. Gambardella, "Current-driven spin torque induced by the rashba effect in a ferromagnetic metal layer", Nature Materials **9**, 230 (2010).

[64] Y. Du, H. Gamou, S. Takahashi, S. Karube, M. Kohda, and J. Nitta, "Disentanglement of spin-orbit torques in Pt/Co bilayers with the presence of spin hall effect and rashba-edelstein effect", Phys. Rev. Appl. **13**, 054014 (2020).

[65] Y. Du, R. Thompson, M. Kohda, and J. Nitta, "Origin of spin-orbit torque in single-layer CoFeB investigated via in-plane harmonic Hall measurements", AIP Advances **11**, 025033 (2021).

[66] K. Garello, I. M. Miron, C. O. Avci, F. Freimuth, Y. Mokrousov, S. Blügel, S. Auffret, O. Boulle, G. Gaudin, and P. Gambardella, "Symmetry and magnitude of spin-orbit torques in ferromagnetic heterostructures", Nature Nanotechnology **8**, 587 (2013).

[67] A. Manchon and S. Zhang, "Theory of spin torque due to spin-orbit coupling", Physical Review B **79**, 10.1103/physrevb.79.094422 (2009).

[68] C.-F. Pai, M. Mann, A. J. Tan, and G. S. D. Beach, "Determination of spin torque efficiencies in heterostructures with perpendicular magnetic anisotropy", Phys. Rev. B **93**, 144409 (2016).

[69] L. Zhu, D. Ralph, and R. Buhrman, "Lack of simple correlation between switching current density and spin-orbit-torque efficiency of perpendicularly magnetized spin-current-generator–ferromagnet heterostructures", Phys. Rev. Appl. **15**, 024059 (2021).

[70] E. Grimaldi, V. Krizakova, G. Sala, F. Yasin, S. Couet, G. Sankar Kar, K. Garello, and P. Gambardella, "Single-shot dynamics of spin–orbit torque and spin transfer torque switching in three-terminal magnetic tunnel junctions", Nature Nanotechnology **15**, 111 (2020).

[71] B. Pal, B. K. Hazra, B. Göbel, J.-C. Jeon, A. K. Pandeya, A. Chakraborty, O. Busch, A. K. Srivastava, H. Deniz, J. M. Taylor, H. Meyerheim, I. Mertig, S.-H. Yang, and S. S. P. Parkin, "Setting of the magnetic structure of chiral kagome antiferromagnets by a seeded spin-orbit torque", Science Advances **8**, eabo5930 (2022).

[72] X. Han, X. Wang, C. Wan, G. Yu, and X. Lv, "Spin-orbit torques: Materials, physics, and devices", Applied Physics Letters **118**, 120502 (2021).

[73] S. Karimeddiny, J. A. Mittelstaedt, R. A. Buhrman, and D. C. Ralph, "Transverse and longitudinal spin-torque ferromagnetic resonance for improved measurement of spin-orbit torque", Phys. Rev. Appl. **14**, 024024 (2020).

[74] C. Zhang, S. Fukami, K. Watanabe, A. Ohkawara, S. DuttaGupta, H. Sato, F. Matsukura, and H. Ohno, "Critical role of w deposition condition on spin-orbit torque induced magnetization switching in nanoscale w/cofeb/mgo", Applied Physics Letters **109**, 192405 (2016).

[75] M. Hayashi, J. Kim, M. Yamanouchi, and H. Ohno, "Quantitative characterization of the spin-orbit torque using harmonic hall voltage measurements", Phys. Rev. B **89**, 144425 (2014).

[76] C. O. Avci, K. Garello, M. Gabureac, A. Ghosh, A. Fuhrer, S. F. Alvarado, and P. Gambardella, "Interplay of spin-orbit torque and thermoelectric effects in ferromagnet/ normal-metal bilayers", Phys. Rev. B **90**, 224427 (2014).

[77] S. J. Yun, E.-S. Park, K.-J. Lee, and S. H. Lim, "Accurate analysis of harmonic hall voltage measurement for spin-orbit torques", NPG Asia Materials **9**, e449 (2017).

[78] U. H. Pi, K. Won Kim, J. Y. Bae, S. C. Lee, Y. J. Cho, K. S. Kim, and S. Seo, "Tilting of the spin orientation induced by Rashba effect in ferromagnetic metal layer", Applied Physics Letters **97**, 162507 (2010).

[79] J. Kim, J. Sinha, M. Hayashi, M. Yamanouchi, S. Fukami, T. Suzuki, S. Mitani, and H. Ohno, "Layer thickness dependence of the current-induced effective field vector in ta|CoFeB|MgO", Nature Materials **12**, 240 (2012).

[80] T. Schulz, K. Lee, B. Krüger, R. Lo Conte, G. V. Karnad, K. Garcia, L. Vila, B. Ocker, D. Ravelosona, and M. Kläui, "Effective field analysis using the full angular spin-orbit torque magnetometry dependence", Phys. Rev. B **95**, 224409 (2017).

[81] J. Torrejon, J. Kim, J. Sinha, S. Mitani, M. Hayashi, M. Yamanouchi, and H. Ohno, "Interface control of the magnetic chirality in cofeb/mgo heterostructures with heavy-metal underlayers", Nature Communications **5** (2014).

[82] Q. Liu, L. Zhu, X. S. Zhang, D. A. Muller, and D. C. Ralph, "Giant bulk spin-orbit torque and efficient electrical switching in single ferrimagnetic FeTb layers with strong perpendicular magnetic anisotropy", Applied Physics Reviews **9**, 021402 (2022).

[83] L. Zhu, K. Sobotkiewich, X. Ma, X. Li, D. C. Ralph, and R. A. Buhrman, "Strong damping-like spin-orbit torque and tunable dzyaloshinskii-moriya interaction generated by low-resistivity pd1−pt alloys", Advanced Functional Materials **29**, 1805822 (2019).

[84] K. Uchida, M. Ishida, T. Kikkawa, A. Kirihara, T. Murakami, and E. Saitoh, "Longitudinal spin seebeck effect: from fundamentals to applications", Journal of Physics: Condensed Matter **26**, 343202 (2014).

[85] N. Roschewsky, E. S. Walker, P. Gowtham, S. Muschinske, F. Hellman, S. R. Bank, and S. Salahuddin, "Spin-orbit torque and nernst effect in bi-sb/co heterostructures", Phys. Rev. B **99**, 195103 (2019).

[86] M.-G. Kang, J.-G. Choi, J. Jeong, J. Y. Park, H.-J. Park, T. Kim, T. Lee, K.-J. Kim, K.-W. Kim, J. H. Oh, D. D. Viet, J.-R. Jeong, J. M. Yuk, J. Park, K.-J. Lee, and B.-G. Park, "Electric-field control of field-free spin-orbit torque switching via laterally modulated rashba effect in pt/co/alox structures", Nature Communications **12** (2021).

[87] C. O. Avci, A. Quindeau, M. Mann, C.-F. Pai, C. A. Ross, and G. S. D. Beach, "Spin transport in as-grown and annealed thulium iron garnet/platinum bilayers with perpendicular magnetic anisotropy", Phys. Rev. B **95**, 115428 (2017).

[88] A. Ghosh, K. Garello, C. O. Avci, M. Gabureac, and P. Gambardella, "Interface-enhanced spin-orbit torques and current-induced magnetization switching of Pd/Co/AlO_x layers", Phys. Rev. Appl. **7**, 014004 (2017).

[89] L. Neumann and M. Meinert, "Influence of the hall-bar geometry on harmonic hall voltage measurements of spin-orbit torques", AIP Advances **8**, 095320 (2018).

[90] D. M. J. van Elst, M. R. A. Peters, F. Büttner, A. Wittmann, E. A. Tremsina, C. O. Avci, R. Lavrijsen, H. J. M. Swagten, and G. S. D. Beach, "Accurate extraction

of anisotropic spin-orbit torques from harmonic measurements", Applied Physics Letters **118**, 172403 (2021).

[91] Y. Wang, Y.-T. Chan, X. Wang, T. Wang, X. M. Cheng, W. Wu, and J. Q. Xiao, "Second-harmonic signature of chiral spin structures in w/pt/co heterostructures with tunable magnetic anisotropy", Journal of Physics D: Applied Physics **56**, 205002 (2023).

[92] K. Yasuda, A. Tsukazaki, R. Yoshimi, K. Kondou, K. S. Takahashi, Y. Otani, M. Kawasaki, and Y. Tokura, "Current-nonlinear hall effect and spin-orbit torque magnetization switching in a magnetic topological insulator", Phys. Rev. Lett. **119**, 137204 (2017).

[93] S. Kagami, T. Shirokura, and P. N. Hai, "Effects of post-growth annealing in yptbi topological semimetal and co/pt perpendicular magnetization multilayers", Japanese Journal of Applied Physics **63**, 02SP98 (2024).

[94] W. Zhou, H. Yang, M. Tang, and X. Qiu, "Large modulation of spin-orbit torques in irmn/cofeb/mgo heterostructures with optimized perpendicular magnetic anisotropy", Journal of Magnetism and Magnetic Materials **539**, 168311 (2021).

[95] M. S. Gabor, T. Petrisor, M. Nasui, M. A. Nsibi, J. Nath, and I. M. Miron, "Spin-orbit torques and magnetization switching in perpendicularly magnetized epitaxial Pd/Co2FeAl/MgO structures", Phys. Rev. Appl. **13**, 054039 (2020).

[96] Y. Cao, Z. Xie, Z. Zhao, Y. Yang, N. Lei, B. Miao, and D. Wei, "Spin-orbit torque in perpendicularly magnetized [pt/ni] multilayers", Chinese Physics B **32**, 107507 (2023).

[97] W. Skowroński, K. Grochot, P. Rzeszut, S. Łazarski, G. Gajoch, C. Worek, J. Kanak, T. Stobiecki, J. Langer, B. Ocker, and M. Vafaee, "Angular harmonic hall voltage and magnetoresistance measurements of pt/fecob and pt-ti/fecob bilayers

for spin hall conductivity determination", IEEE Transactions on Electron Devices **68**, 6379 (2021).

[98] Y. Deng, M. Yang, Y. Ji, and K. Wang, "Estimating spin hall angle in heavy metal/ferromagnet heterostructures", Journal of Magnetism and Magnetic Materials **496**, 165920 (2020).

[99] H. Ju, X. Zhao, W. Liu, Y. Song, L. Liu, J. Ma, Y. Li, J. Wu, and Z. Zhang, "Enhanced spin-orbit torque and low critical current density in pt100-xrux/[coni]/ru multilayer for spintronic devices", ACS Applied Materials & Interfaces **13**, PMID: 34905352, 61742 (2021).

[100] C. Engel, S. Goolaup, F. Luo, and W. S. Lew, "Quantitative characterization of spin-orbit torques in pt/co/pt/co/ta/bto heterostructures due to the magnetization azimuthal angle dependence", Phys. Rev. B **96**, 054407 (2017).

[101] P. Sethi, S. Krishnia, S. Li, and W. Lew, "Modulation of spin-orbit torque efficiency by thickness control of heavy metal layers in co/pt multilayers", Journal of Magnetism and Magnetic Materials **426**, 497 (2017).

[102] X. P. Zhao, J. Lu, S. W. Mao, Z. F. Yu, D. H. Wei, and J. H. Zhao, "Spin-orbit torque induced magnetization switching in ferrimagnetic Heusler alloy D22-Mn3Ga with large perpendicular magnetic anisotropy", Applied Physics Letters **115**, 142405 (2019).

[103] N. Roschewsky, C.-H. Lambert, and S. Salahuddin, "Spin-orbit torque switching of ultralarge-thickness ferrimagnetic gdfeco", Phys. Rev. B **96**, 064406 (2017).

[104] Z. Wen, J. Kim, H. Sukegawa, M. Hayashi, and S. Mitani, "Spin-orbit torque in Cr/CoFeAl/MgO and Ru/CoFeAl/MgO epitaxial magnetic heterostructures", AIP Advances **6**, 056307 (2016).

[105] H. Xue, S. Chen, D. Wu, W. Zhu, Y. Zhang, C. Duan, J. Chen, Q. Jin, and Z. Zhang, "Temperature-dependent spin-orbit torques in perpendicular magnetic [co/ni]/tbco composite films", Advanced Electronic Materials **5**, 1900014 (2019).

[106] H. Liang, K. Li, M. Xu, Y. Zhang, P. Liu, S. Wang, Z. Sun, R. Yang, G. Yu, and M. Li, "Enhancement of spin-orbit torque and magnetization switching by Pt100-xWx alloy in Co-based films", Journal of Applied Physics **135**, 163901 (2024).

[107] H. Bai, T. Xu, Y. Dong, H.-A. Zhou, and W. Jiang, "Spin-torque switching in rare-earth-free compensated ferrimagnet mn4n films", Advanced Electronic Materials **8**, 2100772 (2022).

[108] S. Chen, D. Li, B. Cui, L. Xi, M. Si, D. Yang, and D. Xue, "Temperature dependence of spin-orbit torques in pt/co/pt multilayers", Journal of Physics D: Applied Physics **51**, 095001 (2018).

[109] L. Liu, X. Zhao, W. Liu, Y. Song, X. Zhao, and Z. Zhang, "Interlayer exchange coupling modulated spin-orbit torque and multi-state switching in gdco/ru/gdco heterostructures", Journal of Physics D: Applied Physics **54**, 505003 (2021).

[110] J. W. Lee, J. Y. Park, J. M. Yuk, and B.-G. Park, "Spin-orbit torque in a perpendicularly magnetized ferrimagnetic Tb-Co single layer", Phys. Rev. Appl. **13**, 044030 (2020).

[111] M. S. Gabor, T. Petrisor, R. B. Mos, A. Mesaros, M. Nasui, M. Belmeguenai, F. Zighem, and C. Tiusan, "Spin-orbit torques and magnetization switching in w/co2feal/mgo structures", Journal of Physics D: Applied Physics **49**, 365003 (2016).

[112] S. Zi ętek, J. Mojsiejuk, K. Grochot, S. Łazarski, W. Skowro ński, and T. Stobiecki, "Numerical model of harmonic hall voltage detection for spintronic devices", Phys. Rev. B **106**, 024403 (2022).

[113] Y. Takeuchi, C. Zhang, A. Okada, H. Sato, S. Fukami, and H. Ohno, "Spin-orbit torques in high-resistivity-w/cofeb/mgo", Applied Physics Letters **112**, 10.1063/1.5027855 (2018).

[114] K. K. Vudya Sethu, S. Ghosh, S. Couet, J. Swerts, B. Sorée, J. De Boeck, G. S. Kar, and K. Garello, "Optimization of tungsten β-phase window for spin-orbit-torque magnetic random-access memory", Phys. Rev. Appl. **16**, 064009 (2021).

[115] Z. Zheng, Z. Zhang, X. Feng, K. Zhang, Y. Zhang, Y. He, L. Chen, K. Lin, Y. Zhang, P. Khalili Amiri, and W. Zhao, "Anomalous thermal-assisted spin-orbit torque-induced magnetization switching for energy-efficient logic-in-memory", ACS Nano **16**, PMID: 35446023, 8264 (2022).

[116] S. Iihama, T. Taniguchi, K. Yakushiji, A. Fukushima, Y. Shiota, S. Tsunegi, R. Hiramatsu, S. Yuasa, Y. Suzuki, and H. Kubota, "Spin-transfer torque induced by the spin anomalous hall effect", Nature Electronics **1**, 120 (2018).

[117] Y. Omori, E. Sagasta, Y. Niimi, M. Gradhand, L. E. Hueso, F. Casanova, and Y. Otani, "Relation between spin hall effect and anomalous hall effect in 3d ferromagnetic metals", Phys. Rev. B **99**, 014403 (2019).

[118] T. Seki, S. Iihama, T. Taniguchi, and K. Takanashi, "Large spin anomalous hall effect in $L1_0-$FePt: symmetry and magnetization switching", Phys. Rev. B **100**, 144427 (2019).

[119] J. D. Gibbons, D. MacNeill, R. A. Buhrman, and D. C. Ralph, "Reorientable spin direction for spin current produced by the anomalous hall effect", Phys. Rev. Appl. **9**, 064033 (2018).

[120] L. Liu, J. Yu, R. González-Hernández, C. Li, J. Deng, W. Lin, C. Zhou, T. Zhou, J. Zhou, H. Wang, R. Guo, H. Y. Yoong, G. M. Chow, X. Han, B. Dupé, J. Železný, J. Sinova, and J. Chen, "Electrical switching of perpendicular magnetization in a single ferromagnetic layer", Phys. Rev. B **101**, 220402 (2020).

[121] T. Seki, Y.-C. Lau, S. Iihama, and K. Takanashi, "Spin-orbit torque in a ni-fe single layer", Physical Review B **104** (2021).

[122] D. Céspedes-Berrocal, H. Damas, S. Petit-Watelot, D. Maccariello, P. Tang, A. Arriola-Córdova, P. Vallobra, Y. Xu, J.-L. Bello, E. Martin, S. Migot, J. Ghanbaja, S. Zhang, M. Hehn, S. Mangin, C. Panagopoulos, V. Cros, A. Fert, and J.-C. Rojas-Sánchez, "Current-induced spin torques on single gdfeco magnetic layers", Advanced Materials **33**, 2007047 (2021).

[123] Y.-C. Lau and M. Hayashi, "Spin torque efficiency of ta, w, and pt in metallic bilayers evaluated by harmonic hall and spin hall magnetoresistance measurements", Japanese Journal of Applied Physics **56**, 0802B5 (2017).

[124] H. Ochoa, R. Zarzuela, and Y. Tserkovnyak, "Self-induced spin-orbit torques in metallic ferromagnets", Journal of Magnetism and Magnetic Materials **538**, 168262 (2021).

[125] M. Jiang, H. Asahara, S. Sato, T. Kanaki, H. Yamasaki, S. Ohya, and M. Tanaka, "Efficient full spin–orbit torque switching in a single layer of a perpendicularly magnetized single-crystalline ferromagnet", Nature Communications **10** (2019).

[126] G. Dresselhaus, "Spin-orbit coupling effects in zinc blende structures", Phys. Rev. **100**, 580 (1955).

[127] J. Winterlik, B. Balke, G. H. Fecher, C. Felser, M. C. M. Alves, F. Bernardi, and J. Morais, "Structural, electronic, and magnetic properties of tetragonal $Mn_{3-x}Ga$: experiments and first-principles calculations", Phys. Rev. B **77**, 054406 (2008).

[128] S. Chatterjee, P. Dutta, P. Singha, S. Giri, A. Banerjee, and S. Majumdar, "Emergence of compensated ferrimagnetic state in mn2-xru1+xga (x = 0.2, 0.5) alloys", Journal of Magnetism and Magnetic Materials **532**, 167956 (2021).

[129] A. Jha, S. Lenne, G. Atcheson, K. Rode, J. M. D. Coey, and P. Stamenov, "Quasistatic magnetization evolution in the compensated ferrimagnetic half-metal Mn_2Ru_xGa", Phys. Rev. B **108**, 224413 (2023).

[130] J. O'Brien, "Novel characterisation and modelling techniques for spintronic materials", PhD thesis (Trinity College Dublin, School of Physics, 2024).

[131] G. Atcheson, J. O'Brien, A. Naden, K. Siewierska, J. M. D. Coey, K. Rode, and P. Stamenov, "Anomalous magnetism in epitaxial mn2ruxga thin films", in 2023 ieee international magnetic conference - short papers (intermag short papers) (2023), pp. 1–2.

[132] J. Finley, C.-H. Lee, P. Y. Huang, and L. Liu, "Spin-orbit torque switching in a nearly compensated heusler ferrimagnet", Advanced Materials **31**, 1805361 (2019).

[133] J. Hu, B. Ernst, S. Tu, M. Kuve ždi ć, A. Hamzi ć, E. Tafra, M. Basleti ć, Y. Zhang, A. Markou, C. Felser, A. Fert, W. Zhao, J.-P. Ansermet, and H. Yu, "Anomalous hall and nernst effects in Co_2TiSn and $Co_2Ti_{0.6}V_{0.4}Sn$ heusler thin films", Phys. Rev. Appl. **10**, 044037 (2018).

[134] L. Salemi and P. M. Oppeneer, "First-principles theory of intrinsic spin and orbital hall and nernst effects in metallic monoatomic crystals", Phys. Rev. Mater. **6**, 095001 (2022).

[135] Q. Zhang, Z. Yan, A. Ying, J. Zhang, B. Zhang, J. Cao, M. Si, L. Xi, D. Xue, and D. Yang, "Measurement of third harmonic voltage in ferromagnet–heavy metal heterostructures", Phys. Rev. B **109**, 064427 (2024).

[136] M.-H. Nguyen, D. C. Ralph, and R. A. Buhrman, "Spin torque study of the spin hall conductivity and spin diffusion length in platinum thin films with varying resistivity", Phys. Rev. Lett. **116**, 126601 (2016).

[137] G. E. W. Bauer, E. Saitoh, and B. J. van Wees, "Spin caloritronics", Nature Materials **11**, 391 (2012).

[138] K. Hasegawa, M. Mizuguchi, Y. Sakuraba, T. Kamada, T. Kojima, T. Kubota, S. Mizukami, T. Miyazaki, and K. Takanashi, "Material dependence of anomalous nernst effect in perpendicularly magnetized ordered-alloy thin films", Applied Physics Letters **106**, 252405 (2015).

[139] H. Yang, H. Chen, M. Tang, S. Hu, and X. Qiu, "Characterization of spin-orbit torque and thermoelectric effects via coherent magnetization rotation", Phys. Rev. B **102**, 024427 (2020).

[140] E.-S. Park, D.-K. Lee, B.-C. Min, and K.-J. Lee, "Elimination of thermoelectric artifacts in the harmonic hall measurement of spin-orbit torque", Phys. Rev. B **100**, 214438 (2019).

[141] C. AB, *Comsol multiphysics®*, version 6.2, Stockholm, Sweden.

[142] I. Keithley Instruments, *Model 6220 dc current source model 6221 ac and dc current source user's manual* (2005).

[143] Z. I. AG, *Mfli user manual* (2017).

[144] J. Železný, Z. Fang, K. Olejník, J. Patchett, F. Gerhard, C. Gould, L. W. Molenkamp, C. Gomez-Olivella, J. Zemen, T. Tichý, T. Jungwirth, and C. Ciccarelli, "Unidirectional magnetoresistance and spin-orbit torque in nimnsb", Phys. Rev. B **104**, 054429 (2021).

[145] S. Ding, A. Ross, D. Go, L. Baldrati, Z. Ren, F. Freimuth, S. Becker, F. Kammerbauer, J. Yang, G. Jakob, Y. Mokrousov, and M. Kläui, "Harnessing orbital-to-spin conversion of interfacial orbital currents for efficient spin-orbit torques", Phys. Rev. Lett. **125**, 177201 (2020).

[146] A. Bose, F. Kammerbauer, R. Gupta, D. Go, Y. Mokrousov, G. Jakob, and M. Kläui, "Detection of long-range orbital-hall torques", Phys. Rev. B **107**, 134423 (2023).

[147] H. Hayashi, D. Jo, D. Go, T. Gao, S. Haku, Y. Mokrousov, H.-W. Lee, and K. Ando, "Observation of long-range orbital transport and giant orbital torque", Communications Physics **6** (2023).

[148] D. Go and H.-W. Lee, "Orbital torque: torque generation by orbital current injection", Phys. Rev. Res. **2**, 013177 (2020).

[149] T. Shiino, P. C. Van, J.-G. Choi, G. Kim, J.-R. Jeong, and B.-G. Park, "Unconventional angular dependence of spin-orbit torque-induced harmonic hall resistance in pt/yig bilayers", npj Spintronics **2** (2024).

[150] Y. Cheng, E. Cogulu, R. D. Resnick, J. J. Michel, N. N. Statuto, A. D. Kent, and F. Yang, "Third harmonic characterization of antiferromagnetic heterostructures", Nature Communications **13** (2022).

[151] J. Nocedal and S. Wright, *Numerical optimization*, 2nd ed., Springer Series in Operations Research and Financial Engineering (Springer, New York, NY, 2006).

APPENDIX A

Third harmonic magnetisation variation

If the inversion symmetry is broken locally but not globally due to disorder in the sample, each SOT contribution cancels out. This results in the absence of the SOT signal at the sample level. However, if the crystallites are large enough, it is possible that the local magnetisation will still oscillate due to the SOT field. Since the anisotropy field is non-linear, the SOT field will result in a contribution to the third harmonic.

At the equilibrium position, we have $\frac{\partial E(\mathbf{H},\theta)}{\partial \theta} = 0$. Where E corresponds to the system's energy, $\mathbf{H}$ corresponds to the magnetic field, and θ represents the angle between the magnetisation and the z-axis. We obtain an equation of the form $F(\mathbf{H}, \theta) = 0$. Next, we address the effect of the variation in the spin orbit torque (SOT) field on θ. To do this, we write $\mathbf{H} = \mathbf{H_0} + \mathbf{H_{eff}}$, where $\mathbf{H_0}$ is the external field and $\mathbf{H_{eff}}$ is the SOT field (which we assume to be small). Directly solving for θ is not feasible, so we will expand the variation around $\mathbf{H_0}$. To accomplish this, we put:

$$\mathbf{H_{eff}} = \begin{pmatrix} \epsilon_{H_x} \\ \epsilon_{H_y} \\ \epsilon_{H_z} \end{pmatrix}, \tag{A.1}$$

and $\theta = \theta_0 + \epsilon_\theta$, where θ_0 corresponds to the equilibrium value in absence of perturbation

field (i.e. $\mathbf{H_{eff}} = 0$). Note that $\frac{\partial^2 F}{\partial H_i \partial H_j} = 0$, as the only term involving energy in the field is $-\mu_0 \mathbf{H} \cdot \mathbf{M}$, which is linear in $\mathbf{H}$. Here we perform the Taylor expansion up to the second-order on $F(\theta, H_x, H_z)$:

$$F(\theta, H_x, H_z) = 0 \approx \overbrace{F(\theta_0, H_{x0}, H_{y0} H_{z0})}^{=0} \tag{A.2}$$

$$\begin{aligned}
][\quad & + \frac{\partial F}{\partial \theta}\epsilon_\theta + \frac{\partial F}{\partial H_x}\epsilon_{H_x} + \frac{\partial F}{\partial H_y}\epsilon_{H_y} + \frac{\partial F}{\partial H_z}\epsilon_{H_z} \\
& + \frac{1}{2}\left(\frac{\partial^2 F}{\partial \theta^2}\epsilon_\theta^2 + 2\frac{\partial^2 F}{\partial \theta \partial H_x}\epsilon_\theta \epsilon_{H_x} + 2\frac{\partial^2 F}{\partial \theta \partial H_y}\epsilon_\theta \epsilon_{H_y} + 2\frac{\partial^2 F}{\partial \theta \partial H_z}\epsilon_\theta \epsilon_{H_z}\right) \\
& = \frac{1}{2}\frac{\partial^2 F}{\partial \theta^2}\epsilon_\theta^2 \\
& + \left(\frac{\partial F}{\partial \theta} + \frac{\partial^2 F}{\partial \theta \partial H_x}\epsilon_{H_x} + \frac{\partial^2 F}{\partial \theta \partial H_y}\epsilon_{H_y} + \frac{\partial^2 F}{\partial \theta \partial H_z}\epsilon_{H_z}\right)\epsilon_\theta \\
& + \frac{\partial F}{\partial H_x}\epsilon_{H_x} + \frac{\partial F}{\partial H_y}\epsilon_{H_y} + \frac{\partial F}{\partial H_z}\epsilon_{H_z}\,.
\end{aligned} \tag{A.3}$$

All derivatives of F are evaluated in $(\theta_0, H_{x0}, H_{y0}, H_{z0})$. From now on, the evaluation point will not be stated. $F(\theta_0, H_{x0}, H_{y0}, H_{z0}) = 0$, as it represents the equilibrium position without a perturbation field. We obtain a second-order equation in θ that we can solve:

$$\begin{aligned}
b^2 - 4ac = & \left(\frac{\partial F}{\partial \theta} + \frac{\partial^2 F}{\partial \theta \partial H_x}\epsilon_{H_x} + \frac{\partial^2 F}{\partial \theta \partial H_y}\epsilon_{H_y} + \frac{\partial^2 F}{\partial \theta \partial H_z}\epsilon_{H_z}\right)^2 \\
& - 2\frac{\partial^2 F}{\partial \theta^2}\left(\frac{\partial F}{\partial H_x}\epsilon_{H_x} + \frac{\partial F}{\partial H_y}\epsilon_{H_y} + \frac{\partial F}{\partial H_z}\epsilon_{H_z}\right)
\end{aligned} \tag{A.4}$$

$$\begin{aligned}
= & \left(\frac{\partial F}{\partial \theta}\right)^2 \\
& + 2\left(\frac{\partial F}{\partial \theta}\frac{\partial^2 F}{\partial \theta \partial H_x} - \frac{\partial^2 F}{\partial \theta^2}\frac{\partial F}{\partial H_x}\right)\epsilon_{H_x} \\
& + 2\left(\frac{\partial F}{\partial \theta}\frac{\partial^2 F}{\partial \theta \partial H_y} - \frac{\partial^2 F}{\partial \theta^2}\frac{\partial F}{\partial H_y}\right)\epsilon_{H_y} \\
& + 2\left(\frac{\partial F}{\partial \theta}\frac{\partial^2 F}{\partial \theta \partial H_z} - \frac{\partial^2 F}{\partial \theta^2}\frac{\partial F}{\partial H_z}\right)\epsilon_{H_z} \\
& + \left(\frac{\partial^2 F}{\partial \theta \partial H_x}\epsilon_{H_x} + \frac{\partial^2 F}{\partial \theta \partial H_y}\epsilon_{H_y} + \frac{\partial^2 F}{\partial \theta \partial H_z}\epsilon_{H_z}\right)^2.
\end{aligned} \tag{A.5}$$

As we have $\frac{\partial F}{\partial \theta} \gg \epsilon_i$, we can perform the Taylor development of the square root in the second-order, neglecting the terms in ϵ^3:

$$\begin{aligned}
\sqrt{b^2-4ac} \approx & \frac{\partial F}{\partial \theta} + \frac{1}{2\frac{\partial F}{\partial \theta}} \Bigg(\\
& 2\left(\frac{\partial F}{\partial \theta}\frac{\partial^2 F}{\partial \theta \partial H_x} - \frac{\partial^2 F}{\partial \theta^2}\frac{\partial F}{\partial H_x}\right)\epsilon_{H_x} \\
& + 2\left(\frac{\partial F}{\partial \theta}\frac{\partial^2 F}{\partial \theta \partial H_y} - \frac{\partial^2 F}{\partial \theta^2}\frac{\partial F}{\partial H_y}\right)\epsilon_{H_y} \\
& + 2\left(\frac{\partial F}{\partial \theta}\frac{\partial^2 F}{\partial \theta \partial H_z} - \frac{\partial^2 F}{\partial \theta^2}\frac{\partial F}{\partial H_z}\right)\epsilon_{H_z} \\
& + \left(\frac{\partial^2 F}{\partial \theta \partial H_x}\epsilon_{H_x} + \frac{\partial^2 F}{\partial \theta \partial H_y}\epsilon_{H_y} + \frac{\partial^2 F}{\partial \theta \partial H_z}\epsilon_{H_z}\right)^2 \Bigg) \\
& - \frac{1}{2\left(\frac{\partial F}{\partial \theta}\right)^3}\Bigg(\left(\frac{\partial F}{\partial \theta}\frac{\partial^2 F}{\partial \theta \partial H_x} - \frac{\partial^2 F}{\partial \theta^2}\frac{\partial F}{\partial H_x}\right)\epsilon_{H_x} \\
& \qquad + \left(\frac{\partial F}{\partial \theta}\frac{\partial^2 F}{\partial \theta \partial H_y} - \frac{\partial^2 F}{\partial \theta^2}\frac{\partial F}{\partial H_y}\right)\epsilon_{H_y} \\
& \qquad + \left(\frac{\partial F}{\partial \theta}\frac{\partial^2 F}{\partial \theta \partial H_z} - \frac{\partial^2 F}{\partial \theta^2}\frac{\partial F}{\partial H_z}\right)\epsilon_{H_z}\Bigg)^2
\end{aligned} \tag{A.6}$$

$$\begin{aligned}
= & \frac{\partial F}{\partial \theta} + \frac{1}{\frac{\partial F}{\partial \theta}}\Bigg(\\
& \left(\frac{\partial F}{\partial \theta}\frac{\partial^2 F}{\partial \theta \partial H_x} - \frac{\partial^2 F}{\partial \theta^2}\frac{\partial F}{\partial H_x}\right)\epsilon_{H_x} \\
& \left(\frac{\partial F}{\partial \theta}\frac{\partial^2 F}{\partial \theta \partial H_y} - \frac{\partial^2 F}{\partial \theta^2}\frac{\partial F}{\partial H_y}\right)\epsilon_{H_y} \\
& + \left(\frac{\partial F}{\partial \theta}\frac{\partial^2 F}{\partial \theta \partial H_z} - \frac{\partial^2 F}{\partial \theta^2}\frac{\partial F}{\partial H_z}\right)\epsilon_{H_z}\Bigg) \\
& - \frac{\frac{\partial^2 F}{\partial \theta^2}}{2\left(\frac{\partial F}{\partial \theta}\right)^2}\left(\frac{\partial F}{\partial H_x}\epsilon_{H_x} + \frac{\partial F}{\partial H_y}\epsilon_{H_y} + \frac{\partial F}{\partial H_z}\epsilon_{H_z}\right)\Bigg(\\
& \qquad \left(2\frac{\partial^2 F}{\partial \theta \partial H_x} - \frac{\partial^2 F}{\partial \theta^2}\frac{\partial F}{\partial H_x}\frac{1}{\frac{\partial F}{\partial \theta}}\right)\epsilon_{H_x} \\
& \qquad + \left(2\frac{\partial^2 F}{\partial \theta \partial H_y} - \frac{\partial^2 F}{\partial \theta^2}\frac{\partial F}{\partial H_y}\frac{1}{\frac{\partial F}{\partial \theta}}\right)\epsilon_{H_y} \\
& \qquad + \left(2\frac{\partial^2 F}{\partial \theta \partial H_z} - \frac{\partial^2 F}{\partial \theta^2}\frac{\partial F}{\partial H_z}\frac{1}{\frac{\partial F}{\partial \theta}}\right)\epsilon_{H_z}\Bigg).
\end{aligned} \tag{A.7}$$

(A.8)

Finally, we obtain the expression for ϵ_θ:

$$\epsilon_\theta = \frac{-b + \sqrt{b^2 - 4ac}}{2a} \tag{A.9}$$

$$= \frac{-\frac{\partial F}{\partial \theta} - \frac{\partial^2 F}{\partial \theta \partial H_x}\epsilon_{H_x} - \frac{\partial^2 F}{\partial \theta \partial H_y}\epsilon_{H_y} - \frac{\partial^2 F}{\partial \theta \partial H_z}\epsilon_{H_z} + \sqrt{b^2 - 4ac}}{\frac{\partial^2 F}{\partial \theta^2}} \tag{A.10}$$

$$= -\frac{1}{\frac{\partial F}{\partial \theta}}(\mathbf{v_1}.\mathbf{H_{eff}}) - \frac{1}{2\left(\frac{\partial F}{\partial \theta}\right)^2}(\mathbf{v_1}.\mathbf{H_{eff}})(\mathbf{v_2}.\mathbf{H_{eff}})\,, \tag{A.11}$$

with:

$$\mathbf{v_1} = \frac{\partial F}{\partial \mathbf{H}} = \begin{pmatrix} \frac{\partial F}{\partial H_x} \\ \frac{\partial F}{\partial H_y} \\ \frac{\partial F}{\partial H_z} \end{pmatrix}, \qquad \mathbf{v_2} = \begin{pmatrix} 2\frac{\partial^2 F}{\partial \theta \partial H_x} - \frac{\partial^2 F}{\partial \theta^2}\frac{\partial F}{\partial H_x}\frac{1}{\frac{\partial F}{\partial \theta}} \\ 2\frac{\partial^2 F}{\partial \theta \partial H_y} - \frac{\partial^2 F}{\partial \theta^2}\frac{\partial F}{\partial H_y}\frac{1}{\frac{\partial F}{\partial \theta}} \\ 2\frac{\partial^2 F}{\partial \theta \partial H_z} - \frac{\partial^2 F}{\partial \theta^2}\frac{\partial F}{\partial H_z}\frac{1}{\frac{\partial F}{\partial \theta}} \end{pmatrix}, \qquad \mathbf{H_{eff}} = \begin{pmatrix} \epsilon_{H_x} \\ \epsilon_{H_y} \\ \epsilon_{H_z} \end{pmatrix}. \tag{A.12}$$

The first term in ϵ_θ corresponds to the already determined linear variation, and contributes to the second harmonic. The second term corresponds to the third harmonic signal and originates entirely from the non-linearity of the magnetisation dependence in the external field.

Multiple attempts to measure the third harmonic signal revealed its limitations. The non-linearity must be strong enough that even a small SOT effective field will be sufficient to obtain a large signal. This was not the case for the material of interest in this thesis (Mn_2Ru_xGa), resulting in a weak signal. Additionally, the third harmonic contains a wider variety of spurious effects, including temperature-dependent changes in net magnetisation, anisotropy constant and resistivity, as well as other parameters. This results in a low efficiency of separating the SOT signal from the other contributions. Nevertheless, this idea could be retested with the new geometry in Chapter 4, which eliminates thermal effects.

APPENDIX B

Mathematical derivations of SOT and the harmonic Hall method

B.1 From the Landau-Lifshitz-Gilbert to the Landau-Lifshitz equation

The Landau-Lifshitz-Gilbert (LLG) equation is given by:

$$\frac{\mathrm{d}\mathbf{m}}{\mathrm{d}t} = -\gamma \mathbf{m} \times \mathbf{B}_{eff} + \alpha \mathbf{m} \times \frac{\mathrm{d}\mathbf{m}}{\mathrm{d}t} + \frac{\gamma}{M_s}\mathbf{T}\,, \tag{B.1}$$

where $\mathbf{m}$ is the magnetisation unit vector, γ is the electron gyromagnetic ratio and α the damping parameter. The SOT in the previous expression $\mathbf{T}$ is given by:

$$\mathbf{T} = \tau_{\mathrm{FL}} \mathbf{m} \times \xi + \tau_{\mathrm{DL}} \mathbf{m} \times (\mathbf{m} \times \xi)\,, \tag{B.2}$$

where τ_{FL} and τ_{DL} are the field-like (FL) and damping-like (DL) parameters, ξ is the direction normal to the plane between the two bilayers.

It is possible to transform the LLG equation to avoid the presence of the $\frac{\mathrm{d}\mathbf{m}}{\mathrm{d}t}$ on the right hand side of the equation. We obtain then the Landau-Lifshitz equation. To do this, we

take the cross product with $\mathbf{m}$ on both sides and use:

$$\mathbf{m} \times \mathbf{m} \times \mathbf{m} \times \mathbf{A} = -\underbrace{\|\mathbf{m}\|^2}_{=1} \mathbf{m} \times \mathbf{A}. \tag{B.3}$$

We then compute:

$$\begin{aligned}
\mathbf{m} \times \frac{\mathrm{d}\mathbf{m}}{\mathrm{d}t} &= -\gamma \mathbf{m} \times \mathbf{m} \times \mathbf{B}_{\text{eff}} + \alpha \mathbf{m} \times \mathbf{m} \times \frac{\mathrm{d}\mathbf{m}}{\mathrm{d}t} + \frac{\gamma}{M_s} \mathbf{m} \times \mathbf{T} \\
&= -\gamma \mathbf{m} \times \mathbf{m} \times \mathbf{B}_{\text{eff}} + \alpha \mathbf{m} \times \mathbf{m} \times \left(-\gamma \mathbf{m} \times \mathbf{B}_{\text{eff}} + \alpha \mathbf{m} \times \frac{\mathrm{d}\mathbf{m}}{\mathrm{d}t} + \frac{\gamma}{M_s} \mathbf{T} \right) \\
&\quad + \frac{\gamma}{M_s} \mathbf{m} \times \mathbf{T} \qquad \text{(B.4)} \\
&= -\gamma \mathbf{m} \times \mathbf{m} \times \mathbf{B}_{\text{eff}} + \alpha\gamma \mathbf{m} \times \mathbf{B}_{\text{eff}} - \alpha^2 \mathbf{m} \times \frac{\mathrm{d}\mathbf{m}}{\mathrm{d}t} \\
&\quad - \frac{\alpha\gamma}{M_s} \mathbf{T} + \frac{\gamma}{M_s} \mathbf{m} \times \mathbf{T} \qquad \text{(B.5)} \\
&= \frac{-\gamma}{1+\alpha^2} \mathbf{m} \times \mathbf{m} \times \mathbf{B}_{\text{eff}} + \frac{\alpha\gamma}{1+\alpha^2} \mathbf{m} \times \mathbf{B}_{\text{eff}} \\
&\quad - \frac{\alpha\gamma}{M_s(1+\alpha^2)} \mathbf{T} + \frac{\gamma}{M_s(1+\alpha^2)} \mathbf{m} \times \mathbf{T}\,, \qquad \text{(B.6)}
\end{aligned}$$

and injecting this expression into Equation B.1:

$$\begin{aligned}
\frac{\mathrm{d}\mathbf{m}}{\mathrm{d}t} &= -\frac{\gamma}{1+\alpha^2} \mathbf{m} \times \mathbf{B}_{\text{eff}} + \frac{\gamma}{M_s(1+\alpha^2)} \mathbf{T} \\
&\quad - \frac{\gamma\alpha}{1+\alpha^2} \mathbf{m} \times \mathbf{m} \times \mathbf{B}_{\text{eff}} + \frac{\alpha\gamma}{M_s(1+\alpha^2)} \mathbf{m} \times \mathbf{T} \qquad \text{(B.7)} \\
&= -\frac{\gamma}{1+\alpha^2} \mathbf{m} \times \left(\mathbf{B}_{\text{eff}} - \frac{\tau_{\text{FL}}\xi - \alpha\tau_{\text{DL}}\xi}{M_s} \right) \\
&\quad - \frac{\gamma\alpha}{1+\alpha^2} \mathbf{m} \times \mathbf{m} \times \left(\mathbf{B}_{\text{eff}} - \frac{\tau_{\text{DL}}\xi + \alpha\tau_{\text{FL}}\xi}{M_s\alpha} \right). \qquad \text{(B.8)}
\end{aligned}$$

We have now obtained the Landau-Lifshitz equation where no derivative terms are present on the right hand side of the equation.

B.2 Derivation of the SOT perturbation for the case of tetragonal anisotropy

We now apply Equation 1.79 to the case of the tetragonal anisotropy. For simplicity in the notation, we set $\mu_0 M = 1$; thus the derivatives along ϕ and θ (Equation 1.75) are:

$$\begin{aligned} F = \frac{\partial E}{\partial \theta} = 0 =& k_1 \sin(2\theta) + 4(k_2 + k_2' \cos(4\phi)) \sin^3(\theta) \cos(\theta) \\ & - H_\parallel \cos(\theta) \cos(\phi - \phi_H) + H_z \sin(\theta)\,, \end{aligned} \tag{B.9}$$

$$G = \frac{\partial E}{\partial \phi} = 0 = -4k_2' \sin(4\phi) \sin^4(\theta) + H_\parallel \sin(\theta) \sin(\phi - \phi_H)\,. \tag{B.10}$$

Similarly, the second derivative of the energy gives:

$$\begin{aligned} \frac{\partial^2 E}{\partial \theta^2} = \frac{\partial F}{\partial \theta} =& 2k_1 \cos(2\theta) + 4(k_2 + k_2' \cos(4\phi)) \sin(\theta) \sin(3\theta) \\ & + H_\parallel \sin(\theta) \cos(\phi - \phi_H) + H_z \cos(\theta)\,, \end{aligned} \tag{B.11}$$

$$\frac{\partial^2 E}{\partial \theta \partial \phi} = \frac{\partial F}{\partial \phi} = \frac{\partial G}{\partial \theta} = -16k_2' \sin(4\phi) \sin^3(\theta) \cos(\theta) + H_\parallel \cos(\theta) \sin(\phi - \phi_H)\,, \tag{B.12}$$

$$\frac{\partial^2 E}{\partial \phi^2} = \frac{\partial G}{\partial \phi} = -16k_2' \cos(4\phi) \sin^4(\theta) + H_\parallel \sin(\theta) \cos(\phi - \phi_H)\,. \tag{B.13}$$

Finally, the last terms of Equation 1.79 can be written as:

$$\frac{\partial F}{\partial H_i} \delta H_i = -\cos(\theta)(\cos(\phi)\delta H_x + \sin(\phi)\delta H_y) + \sin(\theta)\delta H_z\,, \tag{B.14}$$

$$\frac{\partial G}{\partial H_i} \delta H_i = \sin(\theta)(\sin(\phi)\delta H_x - \cos(\phi)\delta H_y)\,. \tag{B.15}$$

From Equation 1.79, we can deduce the variation of $\delta\theta$ and $\delta\phi$, starting with the denom-

inator:

$$
\begin{aligned}
det =& \frac{\partial F}{\partial \theta}\frac{\partial G}{\partial \phi} - \frac{\partial G}{\partial \theta}\frac{\partial F}{\partial \phi} \\
=& \Big(2k_1\cos(2\theta) + 4(k_2 + k_2'\cos(4\phi))\sin(\theta)\sin(3\theta) + H_\parallel \sin(\theta)\cos(\phi - \phi_H) + H_z\cos(\theta)\Big) \\
& \times \Big(-16k_2'\cos(4\phi)\sin^4(\theta)\cos(\phi - \phi_H)\Big) \\
& - \Big(-16k_2'\sin(4\phi)\sin^3(\theta)\cos(\theta) + H_\parallel\cos(\theta)\sin(\phi - \phi_H)\Big)\ .
\end{aligned}
\tag{B.16}
$$

The last step is to inject these calculated terms into Equation 1.79. This is adapted, and recommended, if the aim is to calculate an accurate variation of the magnetisation from the SOT field. However, the result is not an intuitive expression. For this reason, we propose setting $k_2' = 0$, which is a common assumption found in the literature [77]. This approximation is not always justified, as seen in Section 1.2.5 and Section 1.4, as these k_2' terms can originate from the anisotropic cubic terms.

By applying this approximation to Equation B.10, we obtain $\phi = \phi_H$ and $\frac{\partial^2 E}{\partial\theta\partial\phi} = \frac{\partial F}{\partial\phi} = \frac{\partial G}{\partial\theta} = 0$. This simplifies the expression given in [77] to:

$$\delta\theta = -\frac{1}{\frac{\partial F}{\partial\theta}}\frac{\partial F}{\partial H_i}\delta H_i \tag{B.17}$$

$$= -\frac{-\cos\theta(\cos(\phi)\delta H_x + \sin(\phi)\delta H_y) + \sin(\theta)\delta H_z}{2k_1\cos(2\theta) + 4k_2\sin(\theta)\sin(3\theta) + H_\parallel\sin(\theta) + H_z\cos(\theta)}\,, \tag{B.18}$$

$$\delta\phi = -\frac{1}{\frac{\partial G}{\partial\phi}}\frac{\partial G}{\partial H_i}\delta H_i \tag{B.19}$$

$$= -\frac{\sin(\phi)\delta H_x - \cos(\phi)\delta H_y}{H_\parallel}\,. \tag{B.20}$$

B.3 Derivation of the single derivative expression for the harmonic Hall method

Starting from Equation 1.74 and applying the same principle, considering the vector nature of both the external and SOT fields, we can obtain a better expression of the harmonic Hall signal. In this derivation we use the SOT field associated with bilayer system, with ∞m symmetry:

$$\mathbf{H}_{\mathrm{SOT}} = \left(h_{\mathrm{DL}}\cos(\theta), h_{\mathrm{FL}}, -h_{\mathrm{DL}}\sin(\theta)\cos(\phi)\right), \tag{B.21}$$

where h_{DL} and h_{FL} are the SOT coefficients. The equilibrium values of θ and ϕ have analytical expressions:

$$\sin(\theta_0) = \frac{H}{2k_1}, \quad \text{and} \quad \phi_0 = \phi_H\,. \tag{B.22}$$

The first harmonic voltage is given by:

$$V_{xy}^{1\omega} = R_{\mathrm{AHE}}\cos(\theta)I_0 + \frac{R_{\mathrm{PHE}}}{2}\sin^2(\theta)\sin(2\phi)I_0 \tag{B.23}$$

$$= R_{\mathrm{AHE}}\sqrt{1-\left(\frac{H}{2k_1}\right)^2}I_0 + \frac{R_{\mathrm{PHE}}}{2}\left(\frac{H}{2k_1}\right)^2\sin(2\phi_H)I_0\,, \tag{B.24}$$

$$V_{xx}^{1\omega} = R_{xx0}I_0 - R_{\mathrm{PHE}}\left(\sin^2(\theta)\sin^2(\phi)+\cos^2(\theta)\right)I_0 \tag{B.25}$$

$$= R_{xx0}I_0 - R_{\mathrm{PHE}}\left(1-\left(\frac{H}{2k_1}\right)^2\cos^2(\phi_H)\right)I_0\,, \tag{B.26}$$

where R_{AHE} (R_{PHE}) are the AHE (PHE) coefficients, R_{xx0} the isotropic resistance, k_1 the first-order anisotropy constant and H the amplitude of the external field.

The expression of $\delta\theta$ and $\delta\phi$, using

$$\delta\theta = \frac{\cos(\phi_H)h_{\mathrm{DL}} + \sqrt{1-\left(\frac{H}{2k_1}\right)^2}\sin(\phi_H)h_{\mathrm{FL}}}{2k_1\left(1-\left(\frac{H_{\mathrm{ext}}}{2k_1}\right)^2\right)}\,, \tag{B.27}$$

$$\delta\phi = -\frac{h_{\mathrm{DL}}\sin(\phi_H)\sqrt{1-\left(\frac{H}{2k_1}\right)^2} - h_{\mathrm{FL}}\cos(\phi_H)}{H_{\mathrm{ext}}}\,. \tag{B.28}$$

Using these expressions, the second harmonic is expressed as:

$$V_{xy}^{2\omega} = -\frac{1}{2}R_{\mathrm{AHE}}\sin(\theta)\delta\theta I_0^2 \tag{B.29}$$

$$+\frac{1}{2}R_{\mathrm{PHE}}\left(\cos(\theta)\sin(\theta)\sin(2\phi)\delta\theta + \sin^2(\theta)\cos(2\phi)\delta\phi\right)I_0^2 \tag{B.30}$$

$$\begin{aligned}
=&-\frac{1}{2}R_{\mathrm{AHE}}\frac{H}{(2k_1)^2}\left(\frac{\cos(\phi_H)h_{\mathrm{DL}}}{1-(\frac{H}{2k_1})^2} + \frac{\sin(\phi_H)h_{\mathrm{FL}}}{\sqrt{1-\left(\frac{H}{2k_1}\right)^2}}\right)\\
&+\frac{1}{2}R_{\mathrm{PHE}}\sin(2\phi_H)\frac{H}{(2k_1)^2}\left(\frac{\cos(\phi_H)h_{\mathrm{DL}}}{\sqrt{1-\left(\frac{H}{2k_1}\right)^2}} + \sin(\phi_H)h_{\mathrm{FL}}\right)\\
&-\frac{1}{2}R_{\mathrm{PHE}}\frac{H}{(2k_1)^2}\cos(2\phi_H)\left(\sin(\phi_H)h_{\mathrm{DL}}\sqrt{1-\left(\frac{H}{2k_1}\right)^2} - \cos(\phi_H)h_{\mathrm{FL}}\right)\,,
\end{aligned}$$

$$V_{xx}^{2\omega} = \frac{1}{2}R_{\mathrm{PHE}}\left(\sin(2\theta)\cos^2(\phi)\delta\theta - \sin^2(\theta)\sin(2\phi)\delta\phi\right)I_0^2 \tag{B.31}$$

$$\begin{aligned}
=&R_{\mathrm{PHE}}\frac{H_{\mathrm{ext}}}{(2k_1)^2}\left(\frac{\cos^3(\phi_H)h_{\mathrm{DL}}}{\sqrt{1-(\frac{H_{\mathrm{ext}}}{2k_1})^2}} + \cos^2(\phi_H)\sin(\phi_H)h_{\mathrm{FL}}\right)\\
&+\frac{1}{2}R_{\mathrm{PHE}}\frac{H_{\mathrm{ext}}}{(2k_1)^2}\sin(2\phi_H)\left(h_{\mathrm{DL}}\sin(\phi_H)\sqrt{1-\left(\frac{H}{2k1}\right)^2} - h_{\mathrm{FL}}\cos(\phi_H)\right)\,.
\end{aligned} \tag{B.32}$$

The factor $\frac{1}{2}$ ordinates from the demodulation as $\cos^2(\omega t) = 1 + \frac{1}{2}\cos(2\omega t)$, and we set $I_0^2 = 1$ to simplify the notation as this factor is always present on any second harmonic signal.

We can now derive the first harmonic, as suggested by Equation 1.74:

$$\frac{\partial V_{xy}^{1\omega}}{\partial H} = -R_{\mathrm{AHE}}\frac{H}{(2k_1)^2\sqrt{1-\left(\frac{H}{2k_1}\right)^2}} + R_{\mathrm{PHE}}\frac{H}{(2k_1)^2}\sin(2\phi_H)\,, \tag{B.33}$$

$$\frac{\partial V_{xx}^{1\omega}}{\partial H} = 2R_{\mathrm{PHE}}\frac{H}{(2k_1)^2}\cos^2(\phi_H)\,. \tag{B.34}$$

The ratio of the second harmonic over the derivative of the first harmonic is then, when the field is applied along the x- or y-axes, and assuming $\frac{H}{2k_1} \ll 1$:

$$\mathcal{A}_x = 2\left(V_{xy}^{2\omega}\Big/\frac{\partial V_{xy}^{1\omega}}{\partial H}\right)\Bigg|_{\mathbf{H}\parallel x} = \frac{h_{\mathrm{DL}}}{\sqrt{1-\left(\frac{H}{2k_1}\right)^2}} + \xi\sqrt{1-\left(\frac{H}{2k_1}\right)^2}h_{\mathrm{FL}} \tag{B.35}$$

$$\approx h_{\mathrm{DL}} + \xi h_{\mathrm{FL}}\,, \tag{B.36}$$

$$\mathcal{A}_y = 2\left(V_{xy}^{2\omega}\Big/\frac{\partial V_{xy}^{1\omega}}{\partial H}\right)\Bigg|_{\mathbf{H}\parallel y} = h_{\mathrm{FL}} + \xi h_{\mathrm{DL}}\left(1-\left(\frac{H}{2k_1}\right)^2\right) \tag{B.37}$$

$$\approx h_{\mathrm{FL}} + \xi h_{\mathrm{DL}}\,, \tag{B.38}$$

where $\xi = \frac{R_{\mathrm{PHE}}}{R_{\mathrm{AHE}}}$. The value of h_{DL} and h_{FL} are then given by:

$$h_{\mathrm{DL}} = \frac{\mathcal{A}_x - \xi\mathcal{A}_y}{1-\xi^2}\,, \qquad h_{\mathrm{FL}} = \frac{\mathcal{A}_y - \xi\mathcal{A}_x}{1-\xi^2}. \tag{B.39}$$

B.4 Derivation of the second derivative expression for the harmonic Hall method

The second derivative of the first harmonic signal can be expressed as:

$$\frac{\partial^2 V_{xy}^{1\omega}}{\partial H^2} = -R_{\mathrm{AHE}}\left(\frac{1}{(2k_1)^2\sqrt{1-\left(\frac{H}{2k_1}\right)^2}} + \frac{H^2}{(2k_1)^4\sqrt{1-\left(\frac{H}{2k_1}\right)^2}^3}\right) + R_{\mathrm{PHE}}\frac{1}{(2k_1)^2}\sin(2\phi_H)\,, \tag{B.40}$$

$$\frac{\partial^2 V_{xx}^{1\omega}}{\partial H^2} = 2R_{\mathrm{PHE}}\frac{1}{(2k_1)^2}\cos^2(\phi_H)\,. \tag{B.41}$$

The first derivative of the second harmonic signal can be expressed as:

$$\begin{aligned}
\frac{\partial V_{xy}^{2\omega}}{\partial H} =& -\frac{1}{2}R_{\mathrm{AHE}}\frac{1}{(2k_1)^2}\left(\frac{\cos(\phi_H)h_{\mathrm{DL}}}{1-\left(\frac{H}{2k_1}\right)^2}+\frac{\sin(\phi_H)h_{\mathrm{FL}}}{\sqrt{1-\left(\frac{H}{2k_1}\right)^2}}\right)\\
&-\frac{1}{2}R_{\mathrm{AHE}}\frac{H^2}{(2k_1)^4}\left(\frac{2\cos(\phi_H)h_{\mathrm{DL}}}{\left(1-\left(\frac{H}{2k_1}\right)^2\right)^2}+\frac{\sin(\phi_H)h_{\mathrm{FL}}}{\sqrt{1-\left(\frac{H}{2k_1}\right)^2}^3}\right)\\
&+\frac{1}{2}R_{\mathrm{PHE}}\sin(2\phi_H)\frac{1}{(2k_1)^2}\left(\frac{\cos(\phi_H)h_{\mathrm{DL}}}{\sqrt{1-\left(\frac{H}{2k_1}\right)^2}}+\sin(\phi_H)h_{\mathrm{FL}}\right)\\
&+\frac{1}{2}R_{\mathrm{PHE}}\sin(2\phi_H)\frac{H^2}{(2k_1)^4}\frac{\cos(\phi_H)h_{\mathrm{DL}}}{\sqrt{1-\left(\frac{H}{2k_1}\right)^2}^3}\\
&-\frac{1}{2}R_{\mathrm{PHE}}\frac{1}{(2k_1)^2}\cos(2\phi_H)\left(\sin(\phi_H)h_{\mathrm{DL}}\sqrt{1-\left(\frac{H}{2k_1}\right)^2}-\cos(\phi_H)h_{\mathrm{FL}}\right)\\
&+\frac{1}{2}R_{\mathrm{PHE}}\frac{H^2}{(2k_1)^4}\cos(2\phi_H)\frac{\sin(\phi_H)h_{\mathrm{DL}}}{\sqrt{1-\left(\frac{H}{2k_1}\right)^2}}\,, \qquad \text{(B.42)}\\
\frac{\partial V_{xx}^{2\omega}}{\partial H} =& R_{\mathrm{PHE}}\frac{1}{(2k_1)^2}\left(\frac{\cos^3(\phi_H)h_{\mathrm{DL}}}{\sqrt{1-\left(\frac{H}{2k_1}\right)^2}}+\cos^2(\phi_H)\sin(\phi_H)h_{\mathrm{FL}}\right)\\
&+R_{\mathrm{PHE}}\frac{H^2}{(2k_1)^4}\frac{\cos^3(\phi_H)h_{\mathrm{DL}}}{\sqrt{1-\left(\frac{H}{2k_1}\right)^2}^3}\\
&+\frac{1}{2}R_{\mathrm{PHE}}\frac{1}{(2k_1)^2}\sin(2\phi_H)\left(h_{\mathrm{DL}}\sin(\phi_H)\sqrt{1-\left(\frac{H}{2k_1}\right)^2}-h_{\mathrm{FL}}\cos(\phi_H)\right)\\
&-\frac{1}{2}R_{\mathrm{PHE}}\frac{H^2}{(2k_1)^4}\sin(2\phi_H)\frac{h_{\mathrm{DL}}\sin(\phi_H)}{\sqrt{1-\left(\frac{H}{2k_1}\right)^2}}\,. \qquad \text{(B.43)}
\end{aligned}$$

We can then define the ratio of first and second derivatives, as in [75], for the case where the field is applied along x ($\phi = 0°$) or y ($\phi = 90°$). This conveniently eliminates all the terms proportional to $\sin 2\phi$ and separates the others.

Assuming $\frac{H}{2k_1} \ll 1$, we simplify further:

$$\mathcal{B}_x = 2\left(\frac{\partial V_{xy}^{2\omega}}{\partial H}\Big/\frac{\partial^2 V_{xy}^{1\omega}}{\partial H^2}\right)\Bigg|_{\mathbf{H}\parallel x} \tag{B.44}$$

$$= h_{\mathrm{DL}}\frac{1+\left(\frac{H}{2k_1}\right)^2}{\sqrt{1-\left(\frac{H}{2k_1}\right)^2}} - \xi h_{\mathrm{FL}}\left(1-\left(\frac{H}{2k_1}\right)^2\right)^{\frac{3}{2}} \tag{B.45}$$

$$\approx h_{\mathrm{DL}} - \xi h_{\mathrm{FL}}\,, \tag{B.46}$$

$$\mathcal{B}_y = 2\left(\frac{\partial V_{xy}^{2\omega}}{\partial H}\Big/\frac{\partial^2 V_{xy}^{1\omega}}{\partial H^2}\right)\Bigg|_{\mathbf{H}\parallel y} \tag{B.47}$$

$$= h_{\mathrm{FL}} - \xi h_{\mathrm{DL}}\left(1-\left(\frac{H}{2k_1}\right)^2\right)\left(1-2\left(\frac{H}{2k_1}\right)^2\right) \tag{B.48}$$

$$\approx h_{\mathrm{FL}} - \xi h_{\mathrm{DL}}\,, \tag{B.49}$$

where $\xi = \frac{R_{\mathrm{PHE}}}{R_{\mathrm{AHE}}}$. The FL and DL torque can then be obtained by inversing the equations:

$$h_{\mathrm{DL}} = \frac{\mathcal{B}_x + \xi\mathcal{B}_y}{1-\xi^2}\,, \qquad h_{\mathrm{FL}} = \frac{\mathcal{B}_y + \xi\mathcal{B}_x}{1-\xi^2}\,. \tag{B.50}$$

B.5 Derivation of the high-field expression for the harmonic Hall method

From Equation B.9, $\Delta\theta \ll 1$, we can rewrite the expression in terms of $\Delta\theta$ and expand the trigonometric equation, keeping only the terms in the first order of $\Delta\theta$:

$$\begin{aligned} 0 =& k_1(2\Delta\theta\cos(2\theta_H) + \sin(2\theta_H)) + 4k_2(\sin^3(\theta_H)(\cos(\theta_H) - \Delta\theta\sin(\theta_H)) \\ &+ 4\sin^2(\theta_H)\cos^2(\theta_H)\Delta\theta) + H\Delta\theta\,. \end{aligned} \tag{B.51}$$

Thus, we can solve the equation to obtain $\Delta\theta$:

$$\Delta\theta = -\frac{k_1\sin(2\theta_H) + 4k_2\sin^3(\theta_H)\cos(\theta_H)}{2k_1\cos(2\theta_H) + 4k_2\sin(\theta_H)\sin(3\theta_H) + H}\,. \tag{B.52}$$

From Equation 1.81, and injecting the expression for the bilayer SOT:

$$H_{\mathrm{SOT}} = (\cos(\theta)h_{\mathrm{DL}}, h_{\mathrm{FL}}, -\sin(\theta)\cos(\phi)h_{\mathrm{DL}}) \ , \tag{B.53}$$

this can be expressed as:

$$\delta\theta = -\frac{-\cos\theta(\cos(\phi)\delta H_x + \sin(\phi)\delta H_y) + \sin(\theta)\delta H_z}{2k_1\cos(2\theta) + 4k_2\sin(\theta)\sin(3\theta) + H_{\mathrm{ext}}\cos(\Delta\theta)} \tag{B.54}$$

$$= \frac{\cos(\phi)h_{\mathrm{DL}} + \cos(\theta_H + \Delta\theta)\sin(\phi)h_{\mathrm{FL}}}{2k_1\cos(2\theta_H + 2\Delta\theta) + 4k_2\sin(\theta + \Delta\theta)\sin(3\theta + 3\Delta\theta) + H_{\mathrm{ext}}\cos(\Delta\theta)} \tag{B.55}$$

$$\approx \frac{\cos(\phi)h_{\mathrm{DL}} + (\cos(\theta_H) - \Delta\theta\sin(\theta_H))\sin(\phi_H)h_{\mathrm{FL}}}{H_{\mathrm{eff}}\,(1 - 4\Delta\theta\,G)} \tag{B.56}$$

$$\approx \frac{\cos(\phi)h_{\mathrm{DL}} + \cos(\theta_H)\sin(\phi_H)h_{\mathrm{FL}}}{H_{\mathrm{eff}}}\,(1 + 4\Delta\theta\,G) - \Delta\theta\frac{\sin(\theta_H)\sin(\phi_H)}{H_{\mathrm{eff}}} \ , \tag{B.57}$$

$$\delta\phi = -\frac{\sin(\phi)\delta H_x - \cos(\phi)\delta H_y}{H_{\mathrm{ext}}\sin(\theta_H)} \tag{B.58}$$

$$= -\frac{h_{\mathrm{DL}}\cos(\theta)\sin(\phi) - \cos(\phi)h_{\mathrm{FL}}}{H_{\mathrm{ext}}\sin(\theta_H)} \tag{B.59}$$

$$= -\frac{h_{\mathrm{DL}}\,(\cos(\theta_H) - \Delta\theta\sin(\theta_H))\sin(\phi) - \cos(\phi)h_{\mathrm{FL}}}{H_{\mathrm{ext}}\sin(\theta_H)} \ , \tag{B.60}$$

where $H_{\mathrm{eff}} = 2k_1\cos(2\theta_H) + 4k_2\sin(\theta_H)\sin(3\theta_H) + H$ and $G = \frac{k_1\sin(2\theta) + k_2(2\sin(4\theta_H) - \sin(2\theta_H))}{H_{\mathrm{eff}}}$. Two expressions can be now given for $\delta\theta$. First, insert the expression of $\Delta\theta$ (Equation B.52) and G into the equation B.57 and simplify as much as possible. The second option is to consider $\Delta\theta$ small and neglect any terms proportional to it. The two results

are given below:

$$\delta\theta = \frac{\cos(\phi)H_{\mathrm{DL}} - (\cos(\theta_H) - \Delta\theta\sin(\theta_H))\sin(\phi)H_{\mathrm{FL}}}{H_{\mathrm{eff}} - 4\Delta\theta(k_1\sin(2\theta_H) + k_2(2\sin(4\theta_H) - \sin(2\theta_H)))} \tag{B.61}$$

$$= \frac{\cos(\phi)H_{\mathrm{DL}} - (\cos(\theta_H) - \frac{k_1\sin(2\theta_H)+4k_2\sin^3(\theta_H)\cos(\theta_H)}{H_{\mathrm{eff}}}\sin(\theta_H))\sin(\phi)H_{\mathrm{FL}}}{H_{\mathrm{eff}} - 4\frac{(k_1\sin(2\theta_H)+4k_2\sin^3(\theta_H)\cos(\theta_H))(k_1\sin(2\theta_H)+k_2(2\sin(4\theta_H)-\sin(2\theta_H)))}{H_{\mathrm{eff}}}} \tag{B.62}$$

$$\approx \frac{\cos(\phi)H_{\mathrm{DL}}}{H_{\mathrm{eff}}} - \frac{\cos(\theta_H)\sin(\phi)H_{\mathrm{FL}}}{H_{\mathrm{eff}}} \tag{B.63}$$

APPENDIX C

Numerical model

A numerical model was developed for this thesis to analyse the harmonic Hall data, using Python (Version 3.8). The primary objective of this software was to analytically solve the second-order anisotropy equilibrium position, as given in Equation 1.80. The model was then further developed to calculate the full harmonic Hall signal while taking into account arbitrary transport effects. The design of this model aims to facilitate the fitting process of the harmonic Hall signal by separating different inputs into distinct objects that interact (Figure C.1).

Here are the objects from the numerical model and their descriptions:

- **AC Current**: A straightforward sine wave current model that enables the control of current direction and phase. It allows for the generation of a current and demodulation waveform over a single time period.
- **Current**: This function aggregates and sums multiple currents, representing the total current flow in the sample. It includes a distortion control parameter.
- **External field**: This module stores all the fields applied during the experiment, as well as parameters to account for potential sample misalignment.

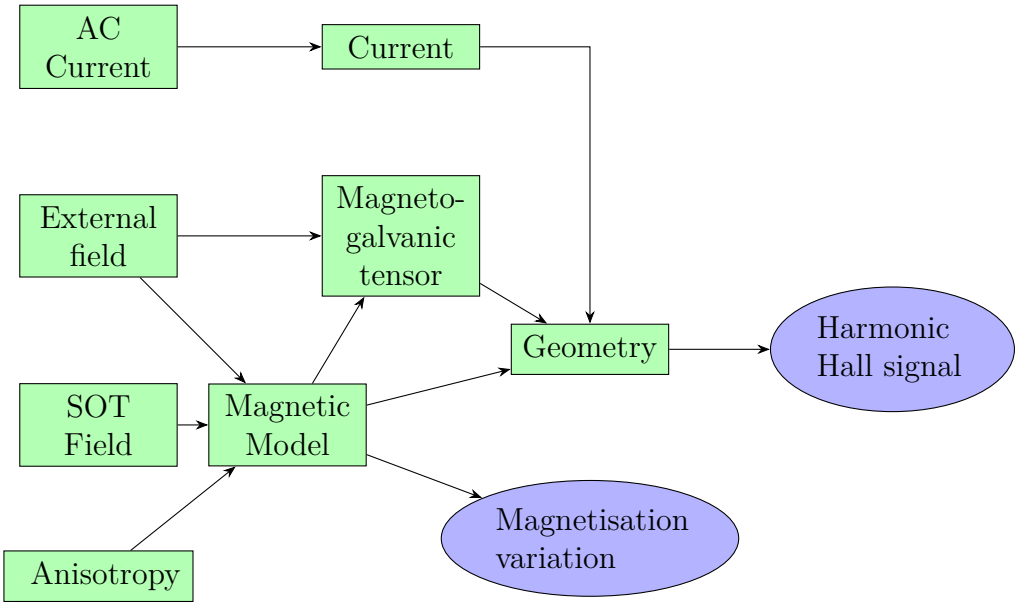

Figure C.1: Illustration of the main objects (green) of the numerical model. The arrows indicate which object is dependent on the other.

- **SOT field**: Includes the SOT tensor and FL and DL parameters.
- **Magnetogalvanic tensor**: Holds the transport coefficients, excluding the thermoelectric effect.
- **Anisotropy**: Includes anisotropy parameters and the solver, determining the magnetisation equilibrium position for any field provided.
- **Magnetic model**: Gathers the external, SOT and anisotropy fields to solve for the magnetisation.
- **Geometry**: Computes the harmonic Hall signal for different geometries; standard Hall bar and new geometry (Chapter 4). The thermoelectric contribution is proportional to J^2, where J is the current density, which is introduced at this stage. The geometry also has parameters that control the distortion level at the input of the lock-in amplifier.

The computation flow follows a different path and we can describe it following the simple diagram in Figure C.2. The majority of the calculations consist of simple matrix

multiplications that are either used directly or summed with the initial data. These transformations allow conversion between different quantities without any involved numerical process. The main computation-intensive step in this package is the minimisation of the anisotropy and Zeeman energy 1.80. This minimisation occurs twice: first, to find the equilibrium magnetisation, and then again to find the new equilibrium position when an SOT field is added to the external field. Contrary to the method described in [90], the computation of the SOT field is performed only once and does not take into account changes in SOT due to the new equilibrium position. It is assumed that the magnetisation change will not significantly affect the spin orbit torque (SOT) field.

Minimising this energy is relatively straightforward, as it has at most only one local and one global minimum, depending on the sign of the magnetisation projection along the z component of the field (H_z). This minimisation can be performed with the Newton conjugate gradient method [151]. Each of these minimisations runs quickly, but the default implementation in the `scipy` library incurs an overhead of around 1 ms. While this may seem insignificant, a typical measurement in this thesis involves 60 different angles and 20 different field values, resulting in 1200 different field configurations. The SOT calculation in this model also includes a new equilibrium computation for the 21 SOT fields associated with the current. As a result, the number of minimisations required for a single measurement is about 25 000, and the overhead cost approaches 25 s. This would limit the interest in using a graphical interface to visualise the harmonic Hall signal. This would also increase the time required to fit the data, as the full minimisation has to be performed each time a user modifies a parameter affecting the effective field. To correct this, we have fully reimplemented the Newton conjugate gradient method using the `numpy` library for array computation. This increases the computation speed by a factor of 70-100, depending on the field configuration. Moreover, previously computed solutions are stored to enhance the smoothness of the graphical user interface.

The demodulation step is given by the integral:

$$V_{\cos}^{n\omega} = \frac{1}{\pi}\int_0^{2\pi} V(t)\cos(nt)\,\mathrm{d}t \tag{C.1}$$

$$V_{\sin}^{n\omega} = \frac{1}{\pi}\int_0^{2\pi} V(t)\sin(nt)\,\mathrm{d}t \tag{C.2}$$

where $n > 1$ is the harmonic of the signal, cos and sin indicates the phase of the demodulation. The number of current sampling points is crucial to prevent computation errors during the demodulation process. Simple test examples show that seven points were sufficient to reach a numerical rounding error. The default sampling number was set at 21 to ensure that there were no errors due to numerical demodulation.

Finally, the different objects allow integration into the `lmfit` Python package. Each object incorporates a `makeParams` and `updateParams` function that returns or updates a `lmfit Parameters` object with parameters controlled by the given object. This allows the simulation package to be integrated into a fitting procedure as visible in Figure C.3.

While other software packages have recently been published [112], allowing users to perform dynamic measurements to analyse ferromagnetic resonance (FMR) signals, these do not take into account spurious contributions, such as thermoelectric effects, current distortion, or easy modification of the sample alignment.

This model provides an efficient framework for understanding and analysing harmonic Hall signals. Its modular design allows for easy modifications and expansions to study different systems. The software focuses on analysing experimental data by considering multiple contributions to the harmonic signal, which does not originate from SOT. Additionally, it allows the user to consider a non-ideal measurement setup by varying the field orientation relative to the sample.

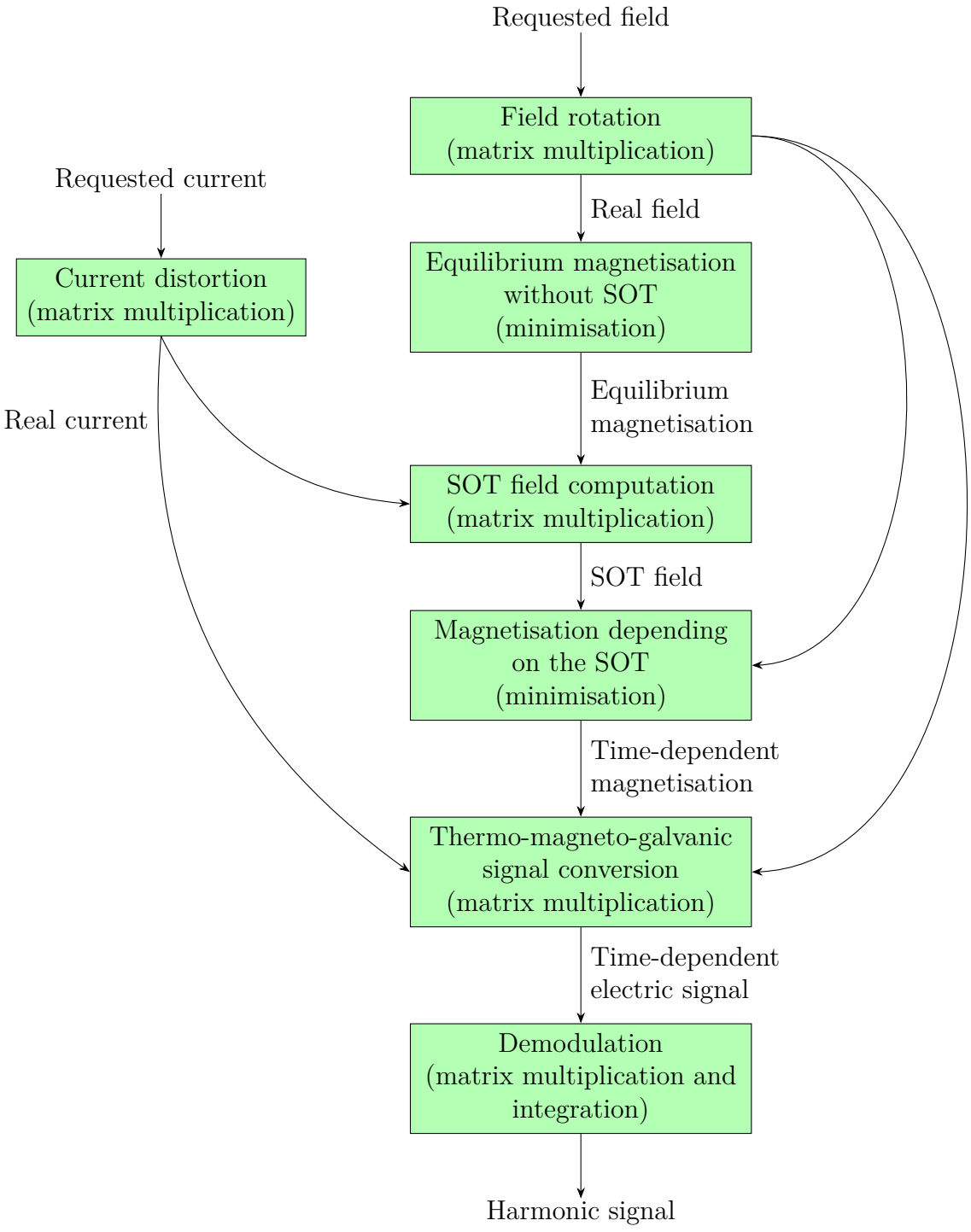

Figure C.2: Computation flow of the harmonic Hall signal. The key steps of the computation are presented in green, including the step of computation and the mathematical operation associated in parentheses. The value on the arrow specifies the content of the data used to perform the next step; the direction of the arrow indicates the direction of the process.

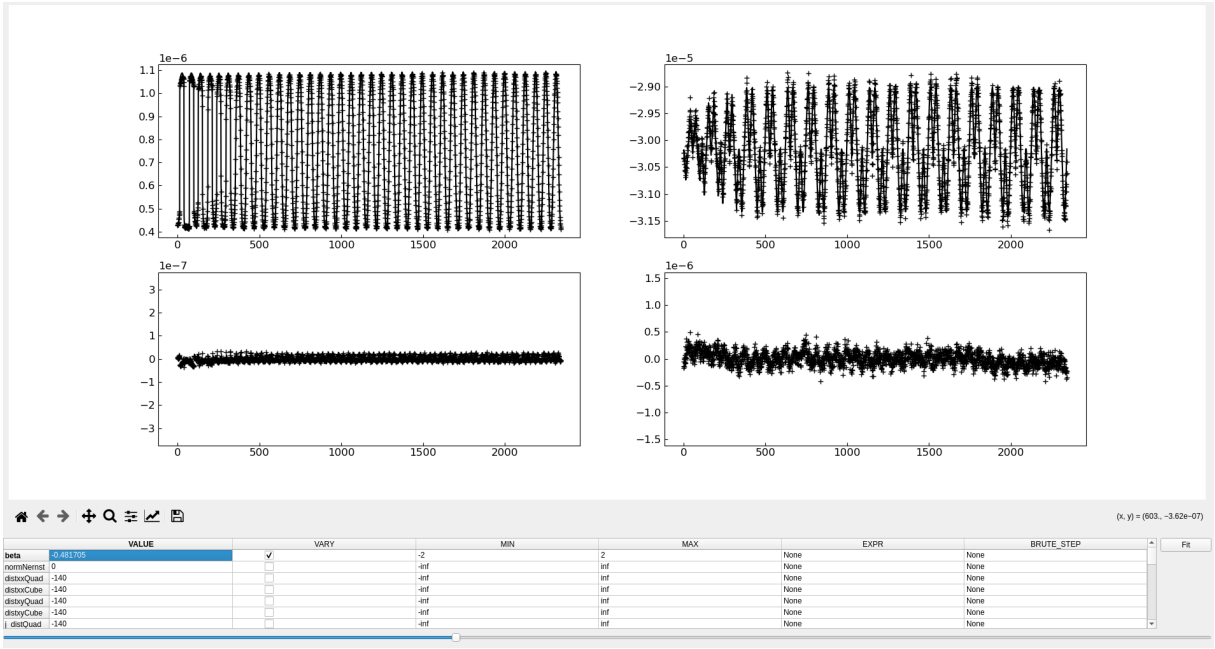

Figure C.3: Graphical user interface for the fitting of harmonic Hall signal. The top row displays the original data and the fit line, while the bottom row shows the corresponding fit residuals. The first column is the transverse signal, and the second is the longitudinal signal. The table at the bottom of the interface allows the user to adjust and test the model's coefficients directly. When the model is close to the result, a fit can be launched on the selected (`vary`) parameter.

APPENDIX D

Symmetric CoPt measurement

The first harmonic signal of the symmetric CoPt sample (Figure D.1) was similar to that of the asymmetric CoPt sample (Figure 3.4). The analysis of the first harmonic coefficient revealed that the anisotropy was slightly higher in the symmetric sample (see Table 3.3). This could be due to the addition of an extra interface between the Co and Pt layers. The transport coefficients were reduced with the additional Pt layer; these do not participate in the magnetotransport effect.

In the second harmonic (Figure D.2), the Nernst contribution dominated, visible on both the longitudinal and transverse signals. The spin orbit torque (SOT) contribution was significantly smaller than the asymmetric sample (Figure 3.5). Nevertheless, it remained present, as small imperfections can break the symmetry of the sample. The details in Table 3.3 indicated that the field-like (FL) contribution was of similar magnitude for both the symmetric and asymmetric samples. In the symmetric sample, The damping-like (DL) contribution almost completely disappeared. The anomalous Nernst effect (ANE) contribution was half the size of that of the symmetric sample. Multiple factors could cause this reduction, such as a decrease in resistivity and thus Joule heating, a reduction in the proportion of magnetic material contributing to the NE, and finally a change in

the current profile through the material, leading to a change in the thermal gradient experienced by the sample.

While the SOT contribution remained small, the quality of the agreement between the data and mobilisation in Figure D.2 suggests that this was still detectable. This confirms the strength of this methodology for detecting small SOT signals in the presence of high thermoelectric contributions.

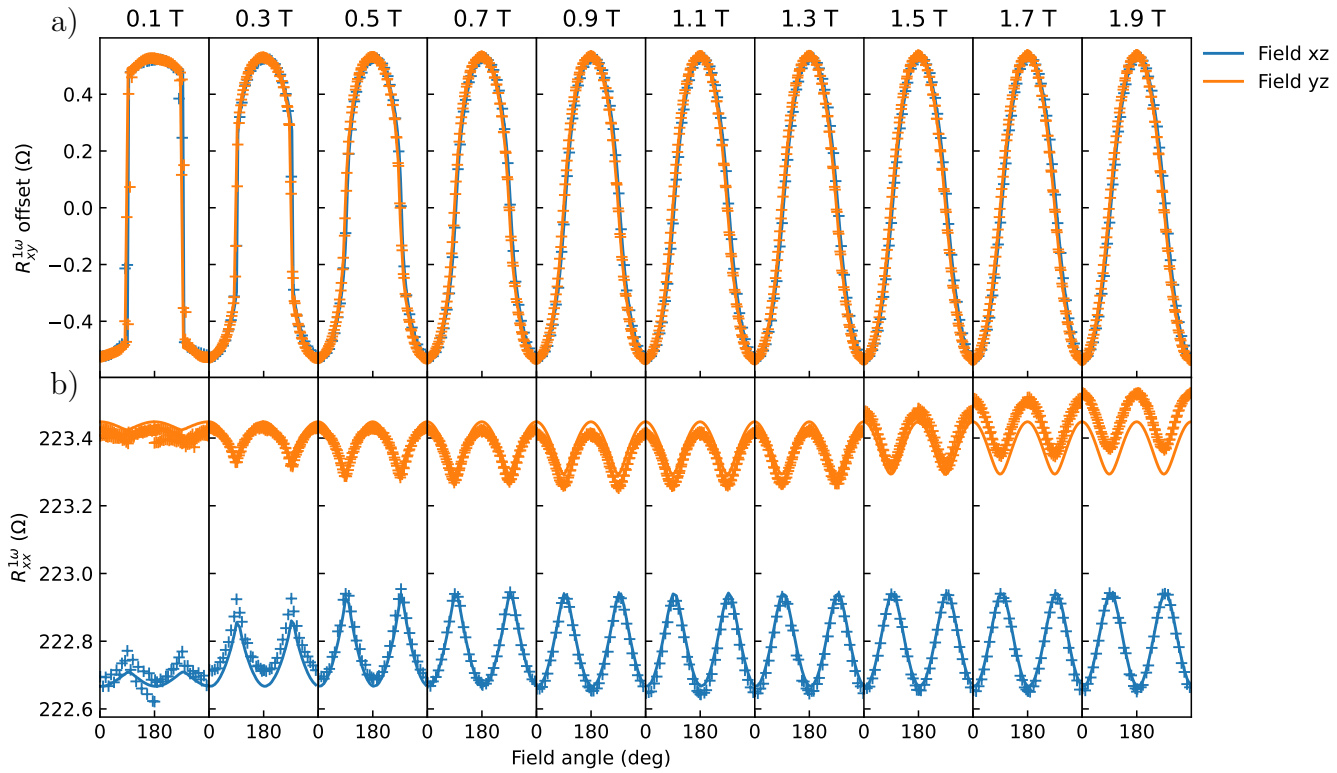

Figure D.1: Symmetric CoPt first harmonic signal with field rotated in the xz- (blue) and yz- (orange) planes for both transverse voltages (a) and longitudinal signal (b). The data are represented by points and the line corresponds to the single macrospin numerical simulation. The full set of data was fit simultaneously.

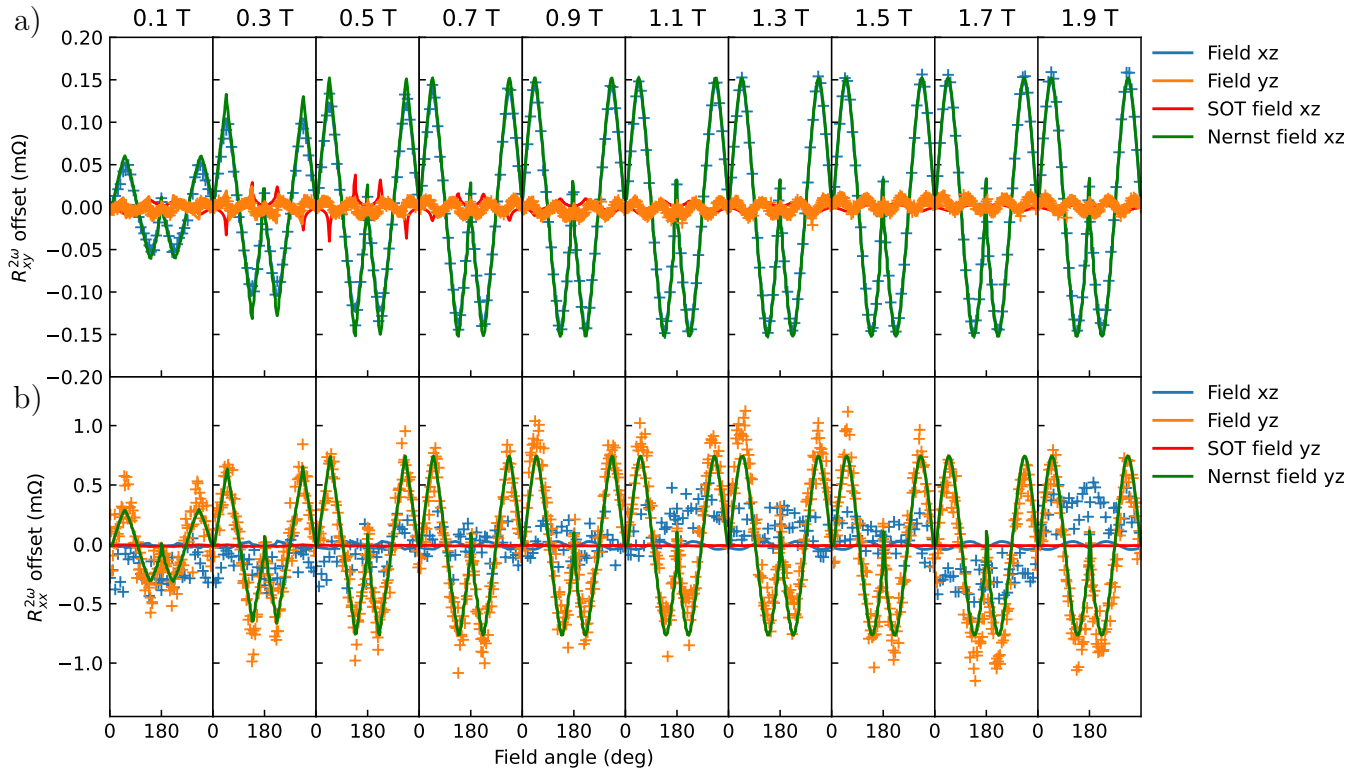

Figure D.2: Symmetric CoPt second harmonic signal with field rotated in the xz- (blue) and yz- (orange) planes for both transverse voltages (a) and longitudinal signal (b). The data are represented by points and the line corresponds to the single macro-spin numerical simulation, reusing the coefficient determined in Figure 3.4 and leaving the SOT and ANE parameters free. The full set of data is fitted simultaneously. The fit signal for the xz field rotation is decomposed into the SOT and ANE contributions, which are represented individually.